University of Alberta
Department of Civil &
Environmental Engineering

# ANALYSIS OF BURIED PIPELINES
# WITH THERMAL APPLICATIONS

by

Nader Yoosef-Ghodsi

and

D.W. Murray

October, 2002

Structural Engineering Report No. 246

# Analysis of Buried Pipelines with Thermal Applications

by

Nader Yoosef-Ghodsi

and

D.W. Murray

Department of Civil and Environmental Engineering

University of Alberta
Edmonton, Alberta
Canada, T6G 2G7

October, 2002

# ABSTRACT

Two of the most important loading conditions for pipelines in operation are ground movement and temperature change. Ground movement is caused by the factors such as fault settlement, slope movement, frost heave, and thaw settlement. The difference between the pipe temperature change in service and the tie-in temperature of the pipeline produces an axial compressive force in the pipeline. With a large enough temperature differential, the resulting compressive axial force can cause the overall buckling of the pipeline, leading to considerable vertical, lateral, or combined movement of the pipe. Many cases of thermal buckling have been recorded for both onshore and offshore pipelines. Pipelines subjected to ground movement or thermal buckling may deform into elastic-plastic range and form wrinkles.

In this research project, a two-dimensional, numerical model is developed for the analysis of pipelines under different loading conditions, and, in particular, under thermal loading. The finite element model features a new elastic-plastic, isoparametric $C^1$ beam element capable of modeling large displacements and finite strains using an updated Lagrangian Formulation. The numerical model can handle highly irregular pipe and ground profiles in order to cover most practical cases. The resulting finite element model was implemented in the computer program ABP (Analysis of Buried Pipelines). The finite element model is verified through several examples by comparing the analytical results to those of closed-form solutions, experimental data, or other finite element programs. Two thermal buckling case studies, stemming from the investigations carried out on actual pipelines, demonstrate the application of the thermal analysis.

# TABLE OF CONTENTS

# LIST OF TABLES

# LIST OF FIGURES

# LIST OF SYMBOLS

## Latin Characters

a      a positive proportionality factor in the Ziegler hardening rule (characteristic for a given material)

$a_i$      coefficients in the fifth order Hermitian polynomial (i = 1, 2, ... , 6)

$a_c$      a parameter used to calculate transverse bearing capacity for clay

$a_q$      a parameter used to calculate transverse bearing capacity for sand

A      pipe cross-sectional area

A      first coefficient of quadratic equation for load factor increment, $d\lambda_{j+1}$

$A_i$      substitute parameters used in strain expressions (i = 1, 2, ... , 13)

B      second coefficient of quadratic equation for load factor increment, $d\lambda_{j+1}$

$B_i$      substitute parameters used in strain expressions (i = 1, 2, ... , 16)

$\langle B^L \rangle$      a vector used in the expression of linear strain

$\langle B_i^L \rangle$      components of $\langle B^L \rangle$ (i = 1, 2)

$\lfloor B^{NL} \rfloor$      a matrix used in the expression of nonlinear strain

$\lfloor B_i^{NL} \rfloor$      components of $\lfloor B^{NL} \rfloor$ (i = 1, 2, 3)

c      soil cohesion or undrained shear strength ($S_u$)

$c_i$      coefficients used to express $\cos\theta$ (i = 1, 2, ... , 6)

C      third coefficient of quadratic equation for load factor increment, $d\lambda_{j+1}$

$C_i$     constants arising from far-field condition differential equations (i = 1, 2, ... , 6)

$C_{ijkl}$     tensor of elastic moduli

$C_{ijpq}^{*}$     components of elastic-plastic constitutive tensor relating true stress and true strain

tensors

$\tilde{C}^{EP}$     elastic-plastic constitutive coefficient relating axial true stress to axial true strain

$C_{ijrs}^{EP}$     components of elastic-plastic constitutive tensor relating $2^{nd}$ Piola-Kirchhoff

stress tensor to Green-Lagrange strain tensor

$_tC^{EP}$     elastic-plastic constitutive coefficient relating axial $2^{nd}$ Piola-Kirchhoff stress to

axial Green-Lagrange strain

$d_{ic}$     a parameter used to calculate transverse bearing capacity for sand

$\Delta d$     a prescribed value determining the size of load step in displacement control

method

D     pipe outside diameter

D     first coefficient of quadratic equation for relaxation factor, $\beta$

$D_i$     integrals of elastic-plastic tangent modulus over pipe cross-section (i = 1, 2, 3)

$e_i$     principal engineering strains

$e_{ij}$     components of linear or engineering strain tensor in global coordinate system

$\tilde{e}_{11}$     linear axial strain (material coordinate system)

E     modulus of elasticity of the pipe material

E     second coefficient of quadratic equation for relaxation factor, $\beta$

$E_{ij}$     components of Green-Lagrange strain tensor in global coordinate system

$\tilde{E}_{11}$     Green-Lagrange axial strain (material coordinate system)

$E_i$     principal Green-Lagrange strains

$E_{ij}^T$     components of thermal strain

$f$     soil friction (force per unit length)

$f_i^B$     components of externally applied forces per unit volume

$f_i^S$     components of externally applied surface traction per unit area

$f(\ )$     yield function

$f_{j+1}(\ )$     function used in linearized constraint equation for thermal analysis

$F$     third coefficient of quadratic equation for relaxation factor, $\beta$

$F_0$     axial force at left end of pipe

$F_L$     axial force at right end of pipe

$F_s$     settlement factor

$\Delta F_s$     increment of settlement factor in a load step

$F_{By}$     ultimate bearing spring resistance

$F_{Uy}$     ultimate uplift spring resistance

$F_{Ly}$     ultimate longitudinal spring resistance

$F_{Hy}$     ultimate horizontal bearing spring resistance

$F_i$     integrals of axial stress over pipe cross-section (i = 1, 2, 3)

$F_T$     resultant of the transverse spring forces

$F_L$     longitudinal spring force

$^t_\tau\mathbf{F}$     deformation gradient at time t with respect to the configuration at time $\tau$

$g(\sigma_{ij})$    plastic potential function

G       gap width

h       h coordinate of pipe material point in local coordinate system

$h_i(r)$     interpolation functions (i = 1, 2, ... , 6)

H       depth of pipe axis measured from ground surface

$H_p$      plastic modulus

$\overline{H}_p$      reduced plastic modulus

$\langle\mathbf{H_u}\rangle$    vector of interpolation functions for x-related DOFs of beam element

$\langle\mathbf{H_v}\rangle$    vector of interpolation functions for y-related DOFs of beam element

I        moment of inertia of pipe cross-section

$I_i$       integrals in virtual work equation (i = 1, 2, 3)

$I_T$      thermal integral in virtual work equation

k       hardening parameter used in yield function

k       foundation modulus in beam on elastic foundation theory

$k_T$      resultant transverse spring stiffness

$k_L$      longitudinal spring stiffness

$k_{ic}$     a parameter used to calculate transverse bearing capacity for clay

$k_{iq}$     a parameter used to calculate transverse bearing capacity for sand

$k_{0c}$    a parameter used to calculate transverse bearing capacity for clay

$k_{0q}$    a parameter used to calculate transverse bearing capacity for sand

$k_0$      a parameter used to calculate transverse bearing capacity for sand

$K_0$      coefficient of soil pressure at rest

$\mathbf{K}$      global stiffness matrix

$\mathbf{K}_j$      stiffness matrix for the pipe configuration at iteration j

$L$      pipe or beam overall length

$L_e$      length of beam element

$L_{TR}$      half-length of transition zone

$\Delta l$      value of arc length in arc-length method

$\Delta l_{old}$      arc length for previous load step respectively

$\Delta l_{new}$      arc length for current load step

$M$      concentrated moment load

$M$      mixed hardening parameter $(0 \leq M \leq 1)$

$M_u$      moment component associated with DOF $\dfrac{du}{ds_0}$

$M_v$      moment component associated with DOF $\dfrac{dv}{ds_0}$

$n$      number of half-waves forming after buckling of a beam on elastic foundation

$N$      axial force

$N_i(r)$      Hermitian shape functions $(i = 1, 2, \ldots, 6)$

$N_{opt}$      optimal number of iterations

$N_{old}$      number of iterations for the previous load step

NPE      number of negative pivot elements in diagonalized tangent stiffness matrix

NSUB    number of sub-increments of inelastic strain increment

$N_c$      a bearing capacity factor for horizontal strip footing

$N_c$      a parameter used to calculate transverse bearing capacity for sand

$N_q$      a bearing capacity factor for horizontal strip footing

$N_\gamma$      a bearing capacity factor for horizontal strip footing

$N_{qv}$      vertical uplift factor for sand

$N_{cv}$      vertical uplift factor for clay

$N_{qh}$      horizontal bearing capacity factor

$N_{cr}$      critical (buckling) axial compressive load for a beam on elastic foundation

p       pipe internal pressure

$P_0$      a parameter substituting $\pi R_i^2 p$

**P**       external force vector

$\hat{\mathbf{P}}$       reference load vector

$\hat{\mathbf{P}}^{th}$      thermal reference load vector

P       Axial load

$P_{cr}$      Euler buckling load

$q_p$      pseudo-transverse load due to internal pressure

$q_x$      total value of distributed load at a given point along an element in the global x direction

$q_y$      total value of distributed load at a given point along an element in the global y direction

| | |
|---|---|
| $q_{xs}$ | distributed load in global x direction per unit of sloped length |
| $q_{ys}$ | distributed load in global y direction per unit of sloped length |
| $q_s^g$ | gravity load per unit of sloped length |
| $q_h^g$ | gravity load per unit of horizontal (global x) length |
| $q_{xi}$ | x component of total distributed load at Node i of the element (i = 1, 2, 3) |
| $q_{yi}$ | y component of total distributed load at Node i of the element (i = 1, 2, 3) |
| $\mathbf{Q}$ | equilibrium force vector |
| Q | fraction of elastic strain increment to total strain increment |
| $\mathbf{Q}_j$ | equilibrating force vector for the pipe configuration at iteration j |
| r | natural coordinate along beam element ($-1 \le r \le 1$) |
| R | a normalizing factor used in thermal solution scheme with non-dimensionalization |
| $R_i$ | pipe internal radius |
| $R_m$ | radius of the midline of pipe cross-section |
| s | local s coordinate of pipe axis |
| $s_0$ | arc-length along beam element in initial configuration |
| $s_i$ | coefficients used to express sinθ (i = 1, 2, ... , 6) |
| $s_{ij}$ | components of deviatoric stress tensor |
| $\bar{s}_{ij}$ | components of reduced deviatoric stress tensor |
| $S_f$ | surface on which external tractions are applied |
| $S_u$ | surface on which displacements are prescribed |
| $S_u$ | undrained shear strength of clay soil |

$S_{ij}$     components of second Piola-Kirchhoff stress tensor in global coordinate system

$_{\tau}^{t}S$     second Piola-Kirchhoff stress tensor measured at time t with respect to the configuration at time $\tau$

$[S_i]$     components of stiffness matrix arising from internal virtual work

t     pseudo-time indicating the progress of a nonlinear solution

t     pipe wall thickness

$[T]$     rotation matrix to convert displacement increments from global to local system

$\Delta T$     temperature change

$\Delta T_i$     initial lift-off temperature change

$\Delta T_{cr}$     critical (buckling) temperature change

$\Delta T_m$     temperature change at the minimum point

$u_i$     components of displacement vector in global coordinate system (i = 1, 2, 3 referring to global direction)

$u_i$     nodal displacements along global x-axis (i = 1, 2, 3 referring to node number)

$u_0$     axial displacement at left end of pipe

$u_L$     axial displacement at right end of pipe

$u^i$     notation used to represent $u_i$ and $\left(\dfrac{du}{ds_0}\right)_i$ degrees of freedom at three nodes of each beam element (i = 1, 2, ... , 6)

$\tilde{u}$     displacement increment of arbitrary point along element axis in local s direction

$\langle \mathbf{u} \rangle$     vector of nodal displacements for beam element

$\bar{\mathbf{u}}$      displacement vector of an arbitrary point on element axis

$\mathbf{u}$      global displacement vector (whole structure)

$\Delta\mathbf{u}_{j+1}$      displacement increment for the load step at the end of iteration j+1

$d\mathbf{u}_{j+1}$      displacement correction for iteration j+1

$d\mathbf{u}_{j+1}^{I}$      first component of displacement correction for iteration j+1

$d\mathbf{u}_{j+1}^{II}$      second component of displacement correction for iteration j+1

$d\hat{u}$      relative longitudinal displacement increment of the pipe with respect to the ground

$\Delta\mathbf{u}_{i}^{mod}$      modified displacement increments in settlement analysis

$U$      displacement of pipe material point in global x direction

$\tilde{U}$      displacement increment of pipe material point along $\tilde{x}$ (or s) axis in material (or local) coordinate system

$\Delta U$      vector of unbalanced forces

$v_i$      nodal displacements along global y-axis (i = 1, 2, 3 referring to node number)

$v^i$      notation used to represent $v_i$ and $\left(\dfrac{dv}{ds_0}\right)_i$ degrees of freedom at three nodes of each beam element (i = 1, 2, ... , 6)

$\tilde{v}$      displacement increment of arbitrary point along element axis in local h direction

$V$      volume of pipe body

$V$      displacement of pipe material point in global y direction

$\tilde{V}$      displacement increment of pipe material point along $\tilde{y}$ (or h) axis in material (or local) coordinate system

$\mathbf{w}$    a vector of weight factors used in displacement control method

$\delta W_{ext}$   external virtual work

$\delta W_\theta^{ext}$   external virtual work due to pressurization

$\delta W_\theta^{int}$   internal virtual work due to pressurization

$\delta W_{soil}^{ext}$   external virtual work done by soil springs

$\delta W_{soil}^{stiff}$   portion of external virtual work done by soil springs contributing to stiffness

$\delta W_{soil}^{load}$   portion of external virtual work done by soil springs contributing to load

$\delta W_{pres}^{ext}$ external virtual work due to transverse loading effect of internal pressure

$\delta W_{pres}^{stiff}$ portion of external virtual work done by the transverse loading effect of internal pressure contributing to stiffness

$\delta W_{pres}^{load}$ portion of external virtual work done by the transverse loading effect of internal pressure contributing to load

$\delta W_q^{ext}$   external virtual work done by distributed load

$\mathbf{W}$    weighting matrix in constraint equation

$x_i$    global coordinates of a material point system (i = 1, 2, 3 referring to global direction)

$x_i$    global coordinates of three nodes of each beam element along global x-axis (i = 1, 2, 3 referring to node number)

$x^i$    notation used to represent $x_i$ and $\left(\dfrac{dx}{ds_0}\right)_i$ at three nodes of each beam element (i = 1, 2, ... , 6)

$\vec{x}$     position vector of an arbitrary point on element axis

$x_{TR}$     global x coordinate of the mid-point of transition zone

$x_{GI}$     global x coordinate of a Gaussian integration point

$x_{int}$     x coordinate of the interception point in gap calculation

$\hat{x}$     shifted x coordinate: $\hat{x} = x - x_{TR}$

$x_0$     length of semi-infinite pipe with plastic soil friction

$X$     coordinate of pipe material point in global x direction

$y_i$     global coordinates of each element nodes along global y-axis (i = 1, 2, 3 referring to node number)

$y^i$     notation used to represent $y_i$ and $\left(\dfrac{dy}{ds_0}\right)_i$ at three nodes of each beam element (i = 1, 2, ... , 6)

$y_{GI}$     global y coordinate of a Gaussian integration point

$y_{int}$     y coordinate of the interception point in gap calculation

$\Delta y_G$     ground settlement at a given point along pipeline

$Y$     coordinate of pipe material point in global Y direction

$z$     a generic variable standing for any of these variables: x, y, u, and v

## Greek Characters

$\alpha$     angle of inclination at fixed support

$\alpha$     adhesion factor for clay

$\alpha$      thermal expansion coefficient of pipe material

$\alpha_i$      roots of quadratic equation for load factor correction (i = 1, 2)

$\alpha_{ij}$      coordinates of the yield surface center in the stress space

$\beta$      relaxation factor used in modified arc-length method

$\beta$      a substitute parameter used in the derivation of elastic-plastic coefficient

$\beta$      angle of ground settlement direction

$\beta$      a substitute parameter: $\beta = \text{sign}(u_L)\dfrac{F_{Ly}}{EA}$

$\gamma$      total soil unit weight

$\gamma$      angle between settlement direction and tangential direction at an integration point

$\bar{\gamma}$      effective soil unit weight

$\delta$      interface angle of friction between soil and pipeline

$\delta$      total differential settlement

$\Delta_{By}$      bearing spring yield displacement

$\Delta_{Uy}$      uplift spring yield displacement

$\Delta_{Ly}$      longitudinal spring yield displacement

$\Delta_{Hy}$      horizontal bearing spring yield displacement

$\Delta_u$      increment of upward pipe displacement with respect to the ground

$\Delta_0$      displacement limit in settlement solution scheme

$d\Delta$      ground settlement increment

$\varepsilon_i$      principal logarithmic (true) strains

$\varepsilon_\theta$      hoop strain due to internal pressure

$\varepsilon_p$      effective strain

$\bar{\varepsilon}_p$      reduced effective strain

$\varepsilon_0$      sum of axial strains due to temperature change and internal pressure

$d\varepsilon_{ij}$      components of strain increment tensor

$d\varepsilon_{ij}^e$      components of elastic strain increment tensor

$d\varepsilon_{ij}^p$      components of plastic strain increment tensor

$d\varepsilon_{ij}^{iso}$      isotropic portions of the components of strain increment tensor

$d\varepsilon_{ij}^{kin}$      kinematic portions of the components of strain increment tensor

$\eta_{ij}$      nonlinear portions of components of Green-Lagrange strain tensor in global coordinate system

$\tilde{\eta}_{11}$      nonlinear portion of axial Green-Lagrange strain (material coordinate system)

$\phi$      pipe curvature

$\phi$      angle of internal friction

$\lambda$      stretch defined as $\lambda = \dfrac{ds}{ds_0}$

$\Delta\lambda_{j+1}$      a scalar load factor whose product with the reference load vector forms the external load increment for the current load step (i.e., $\Delta P = \Delta\lambda_{j+1}\hat{P}$ )

$d\lambda_{j+1}$      load factor correction in the j+1$^{st}$ iteration

$d\lambda$      positive scalar factor of proportionality in flow rule

$d\mu$      a positive proportionality factor in Ziegler kinematic hardening rule

$\nu$      Poisson's ratio for the pipe material

$\theta$      angle specifying position of pipe material point around cross-section

$\theta$      inclination angle of cross-section

$\theta$      reference temperature change

$\theta_F$      final value of reference temperature change

$\rho$      a parameter substituting for $\dfrac{1}{\dfrac{ds}{dr}} = \dfrac{1}{\sqrt{x'^2 + y'^2}}$

$\rho$      mass density

$\sigma_\theta$      hoop stress due to internal pressure

$\sigma_{ij}$      components of Cauchy (true) stress tensor

$\overline{\sigma}_{ij}$      components of reduced stress tensor

$\sigma_i$      principal Cauchy (true) stresses

$\sigma_e$      effective stress

$\overline{\sigma}_e$      reduced effective stress

$\sigma$      Cauchy (true) stress tensor

$\Delta_e \sigma_l$      elastic increment of longitudinal stress required to bring the stress state to von Mises yield ellipse

$\psi$      a substitute parameter: $\psi = \sqrt{\dfrac{k_L}{EA}}$

$\zeta$      constraint equation parameter

$\xi_d$      displacement tolerance

$\xi_f$      force tolerance

# CHAPTER 1. INTRODUCTION AND LITERATURE REVIEW

## 1.1 INTRODUCTION

In the last few decades, buried pipelines have become more widespread as a means of transporting oil and gas. They are replacing other means of transportation in oil and gas industries as the most economical alternative. As new oil and gas resources are explored in remote regions, such as the Arctic and sub-Arctic, pipelines are being extended into new and more severe environments. This requires a better understanding of pipeline behavior and powerful analytical tools capable of analyzing all the potential adverse conditions.

Two important environmental loadings for pipelines are imposed deformation and temperature variation. Imposed deformation can be caused by factors such as slope movement, frost heave, and thaw settlement. The most important effect of imposed deformation is the bending of the pipe due to the imposed curvature. Steel pipelines subjected to imposed deformation may deform into the elastic-plastic range and form wrinkles.

The difference between the pipe temperature in service (close to the fluid temperature) and the tie-in temperature of the pipeline, produces an axial compressive force in the pipeline. If the temperature differential is large enough, the resulting axial force can cause the pipeline to buckle leading to considerable vertical, lateral, or combined movement of the pipe. This may involve elastic-plastic deformation and wrinkling of the pipe. Many cases of thermal buckling have been recorded for both onshore and offshore pipelines.

This research project is an attempt to develop a rigorous, two-dimensional, numerical model capable of analyzing pipelines under different loading conditions, and, in particular, under thermal loading. The finite element model features an elastic-plastic, isoparametric $C^1$ beam element capable of modeling large displacements and finite strains using an updated Lagrangian Formulation. The numerical model can handle highly irregular pipe and ground profiles to cover most practical cases. Two thermal buckling case studies, stemming from the investigations carried out on actual pipelines, demonstrate the application of the thermal analysis.

1

Even though the finite element model developed in this study does not account for wrinkling or tearing of the pipe under severe tensile strains, the results of the analysis are valid up to the first occurrence of either critical tensile or compressive strains. In most practical cases, the pipe should meet the code requirements for specified maximum values of tensile and compressive strain under certain loading conditions. In these situations, the numerical model does not have to be capable of modeling wrinkles and tensile failures. Even in fitness-for-purpose cases, where the actual failure of the pipe is studied, the actual critical strain values can be obtained from the ever growing database of the critical strains in the literature. This database is, to a great degree, due to the research projects undertaken at the University of Alberta since 1990.

## 1.2 OBJECTIVES

The main objective of this research project is to develop a rigorous, two-dimensional, finite element model to study the behavior of buried pipelines, in general, and the thermal buckling of pipelines, in particular. This overall objective can be broken down into the following itemized objectives:

1) To develop a new two-dimensional, elastic-plastic, isoparametric $C^1$ pipe beam element capable of modeling large displacements and finite strains using an updated Lagrangian formulation. This element is expected to improve on the deficiencies of the subparametric $C^1$ pipe beam elements developed by Zhou and Murray (1993). The load and stiffness contributions of internal pressure need to be rigorously derived and implemented in the model.

2) To develop an elastic-plastic material model using the von Mises yield criterion, normality flow rule, and a mixed strain-hardening rule (a mix of isotropic and kinematic hardening rules). The resulting constitutive relationships need to be converted into the constitutive relationships required for the pipeline-beam element in an updated Lagrangian formulation.

3) To develop a pipeline-soil interaction model using soil springs on the basis of the classical Winkler foundation. A nonlinear constitutive relationship is required to model the bearing, uplift, transverse (for a horizontal analysis), and longitudinal soil springs. The constitutive relationship for the uplift spring should take into account the loss of the uplift spring force as the pipe moves drastically upwards in an upheaval buckling analysis.

4) To develop a thermal analysis formulation in order to analyze thermal buckling phenomena such as upheaval buckling and snaking. The formulation should be capable of simulating infinitely long continuations of the pipeline in order to reduce the long length of the model that would otherwise be required.

5) To develop appropriate solution techniques to solve the nonlinear equilibrium equations for each of the loading types: applied loads, settlement, and thermal analysis.

6) To implement the above formulation into a computer program used to generate a variety of example solutions in order to verify different aspects of the finite element formulation developed in this study.

7) To employ the thermal analysis in actual pipe buckling cases to demonstrate the application of thermal analysis in practice.

## 1.3 LITERATURE REVIEW

The literature review has been divided into four categories. They are the pipe beam elements, the pipe-soil interaction model, the analysis of pipelines subjected to settlement, and the thermal buckling analysis of pipelines. These are presented in the following subsections.

### 1.3.1 Pipe Beam Elements

Pipe beam elements are created out of various types of beam elements by augmenting them with internal pressure loading. Therefore, it is only appropriate to review the most common types of beam element available in the literature. From the standpoint of shear deformations, beam elements can be divided into two categories:

- **Euler-Bernoulli beam elements:** these elements are based on the classical Euler-Bernoulli assumption that the cross-sections perpendicular to the beam axis before deformation, remain planar, undistorted, and perpendicular to the deformed beam axis. Consequently, shear deformations, and hence, shear strains and stresses are ignored in the formulation of classical Euler-Bernoulli elements. These elements are suited only for modeling thin (slender) beams, such as pipelines, where the beam cross-sectional dimensions are small compared to typical distances along its axis.

- **Timoshenko Beam Elements:** these elements are based on the Timoshenko beam theory which assumes that the cross-sections perpendicular to the beam axis before deformation, remain planar, undistorted, but not necessarily perpendicular to the deformed beam axis. Thus Timoshenko beam elements allow for transverse shear

3

deformation. These elements can be used for modeling both thick and thin beams. The vast majority of the more recent research on beam elements has focused on $C^0$ Timoshenko beam elements.

The Euler-Bernoulli beam elements are normally two-node elements using cubic Hermitian interpolation functions for transverse displacement and linear interpolation for axial displacements. However, in order to achieve a higher accuracy for the Euler-Bernoulli beam element, a three-node element is sometimes used. Zhou and Murray (1993) adopted such an element in their finite element analysis of buried pipelines. A three-node element uses fifth order Hermitian interpolation functions for transverse displacement and quadratic interpolation functions for axial displacements. The subparametric element by Zhou and Murray occasionally produces undesired oscillations in the axial force and moment responses (as demonstrated in Chapter 4).

The beam elements can also be classified on the basis of the choice of independent unknowns. The oldest and the most widely-used elements are those that use nodal displacements as the independent unknowns. These elements are known as *displacement-based* elements. In contrast, *hybrid* elements are those that use some strain, stress, or internal force components in addition to nodal displacements as independent unknowns. Hybrid elements, introduced by Pian (1964), were rationalized by means of variational formulations by Tong and Pian (1969). Some cases of hybrid beam elements used in pipeline analysis are reviewed in the following.

- The multipurpose finite element program ABAQUS offers hybrid and displacement-based versions of both Euler-Bernoulli and Timoshenko beam elements (Hibbit et al., 2002). The hybrid beam elements in ABAQUS are designed for modeling very slender beams, where the axial stiffness of the beam is very large compared to the bending stiffness. Thus a mixed method, in which the axial force is treated as an independent unknown, is utilized. For Timoshenko beam elements, the transverse shear forces are also treated as independent unknowns.
- Klever et al. (1990) created a two-node hybrid Euler-Bernoulli pipe beam element, where, in addition to the nodal displacements, the beam axial strain, curvature, axial force, and bending moment were treated as independent unknowns. They assumed the axial strain and axial force to be constant over the element. The curvature and bending moment were interpolated linearly over the element. A significant difference was shown between the performance of this element and that of a similar element

4

using a full displacement approach for the post-buckling behavior of an axially compressed Euler beam. The response of the beam as given by the exact elastic solution was followed closely by hybrid elements, whereas displacement-based elements responded much too stiffly.

- Saje (1990) came up with a hybrid beam element based on a new variational principle for initially-straight, elastic beams. The formulation, based on Euler-Bernoulli assumption, was designed for slender beams. In addition to the nodal displacements, the beam axial force, shear force, and bending moment were treated as independent unknowns. Two Lagrange multipliers, enforcing two kinematic relationships between the displacements, angular rotations, and the axial strain, were also independent unknowns in the formulation. Shaw and Bomba (1994) extended this formulation to include nonlinear material behavior in order to study the upheaval buckling response of pipelines. They found that the material nonlinearity had a significant effect on the buckling response. Namely, the pipe buckled at a much lower temperature for an elastic-plastic pipe than for a similar elastic pipe.

As for the pipe beam element adopted in this work, it was decided to create a new isoparametric $C^1$ element based on the Euler-Bernoulli assumption and a displacement approach. This element, as described in Chapter 2, uses fifth order Hermitian interpolation functions for both transverse and axial displacements. The isoparametric element could be considered as a refined version of the subparametric $C^1$ pipe beam element by Zhou and Murray (1993).

### 1.3.2 Pipe-Soil Interaction Model

Due to the highly nonlinear response of soil materials and the possibility of pipe distortion, buried pipe-soil systems have a relatively complex behavior. Two basic approaches are used for numerical modeling of buried pipelines: (1) the simplified model, using specialized beam type elements for the pipe and Winkler type representation of surrounding soil (soil spring structural models), and (2) the complex model, where the soil is modeled using continuum finite element or boundary element methods. Since the focus of this study is on the response of the pipe rather than the soil, a relatively complex model is required for the pipe, while the simplified model using soil springs is considered to be adequate. Some of these models are reviewed in the following.

In lieu of site-specific data on the spring constants, "Guidelines for the Seismic Design of Oil and Gas Pipeline Systems" (CGL, 1984) has been widely used in the industry as the source for obtaining the spring constants from basic soil properties. Elastic-perfectly plastic force-deformation constitutive relationships were used to model the bearing, uplift, transverse (for a horizontal analysis), and longitudinal soil springs (CGL, 1984). Due to the wide scatter in experimental results, the soil spring values given in this reference are not to be viewed as precise values.

Some of the relationships given by the CGL have been questioned by subsequent experimental investigations. Paulin et al. (1997) determined from their full-scale pipe-soil interaction tests that for loose sand, the CGL equations generally overestimate the ultimate lateral (horizontal) resistance of the soil. Furthermore, their experimental results for the soil ultimate axial resistance were generally higher than the values predicted by the CGL for dense sand. However, for loose sand, the experimental values for the ultimate axial resistance were generally lower than the values predicted by the CGL. More importantly, the experimental findings of Rizkalla et al. (1996) and Cappelletto et al. (1998) showed that the CGL highly overestimated the ultimate axial resistance for cohesive soil.

Due to its importance in the upheaval buckling of pipelines, the soil uplift resistance has been the focus of many studies within the past two decades (Trautmann et al., 1985; Finch, 1999; and White et al., 2001). The most important parameters in the uplift models have typically been the cover depth to diameter ratio and the unit weight of the soil. These models generally equate the uplift resistance to a combination of the dead weight from the soil above the pipe and the shearing resistance provided by that segment of soil.

Cyclic thermal loading has been shown to be potentially affecting the soil uplift resistance (Nielsen et al., 1990; and Finch, 1999). Nielsen (1990) suggested that during uplift the cavity forming below the pipe is partially filled with soil particles from around the pipeline. Over a series of heating and cooling cycles of the pipeline, this flow of soil may lead to the migration of the pipe upward through its cover. This upward cyclic movement of the pipe has been known as *cyclic ratcheting*. The results of the tests by Finch (1999) indicate that a large number of thermal cycles result in the pipeline working its way upward to a point where insufficient cover remains.

## 1.3.3 Analysis of Pipelines Subjected to Settlement

Over the past two decades, the analysis of pipelines subjected to ground movement has evolved from simple models using closed-form solutions (Yen et al., 1981) to the use of sophisticated finite element models incorporating pipe and soil material nonlinearities (Zhou and Murray, 1993). The main reason for this development is the expansion of pipelines buried into the Arctic and sub-Arctic regions within the past few decades, which has led to many cases of pipeline failure due to differential thaw settlement and frost heave.

Typically, the relative degrees of complexity of the pipe and soil models depend on the major interest of the investigator. Some of the important studies on the pipelines subjected to ground movement are summarized in the following.

### 1.3.3.1 Model of Nyman

Nyman (1983) used a two-dimensional beam-on-elastic-foundation model to carry out thaw settlement analysis for buried pipelines. The soil surrounding the pipe was modeled by three types of soil springs: bearing, uplift, and longitudinal springs. These springs represent the soil loading above the pipe, the bearing support below the pipe, and the longitudinal friction along the pipe. Equations for ultimate soil resistance and yield displacement were proposed for each type of soil spring. The settlement analyses were carried out using a public-domain program subject to a governing criterion of maximum allowable stress.

### 1.3.3.2 Model of Selvadurai

Selvadurai (1985) proposed a three-dimensional model where elastic beam elements were used to model the pipe and boundary elements were used to model the soil. The strength of the model was in the soil representation, where the soil was modeled as a three-dimensional continuous elastic medium rather than a series of uncoupled soil springs. This would result in a more accurate modeling of the soil behavior. The trade off for the more sophisticated soil model is that the soil had to be discretized two-dimensionally on the exterior surface as well as its interface with the pipe. This would result in a larger scale system, hence limiting the application of the model in practice.

7

### 1.3.3.3 Model in PIPLIN-III

The program PIPLIN-III (SSD, 1989) has been on the market for almost two decades and is widely used by the pipeline industry. The theoretical background of the model used in PIPLIN-III is described in a paper by Row et al. (1983). The two-dimensional model uses elastic-plastic Euler-Bernoulli beam elements using Mroz theory of plasticity (1967) capable of modeling cyclic loading. The model does not account for ovalization or local buckling of the pipe. Thus the wrinkling strain, as an input to the program, is used as a limiting value to detect the onset of failure.

The soil is modeled by discrete nonlinear springs at the nodes between the pipe elements. The transverse spring consists of four components: nonlinear elastic soil spring, primary creep spring, and two creep dashpots to account for creep effects in soil. The transverse spring is capable of modeling the gap development between the soil and the pipeline under reverse loading and seasonal variation of uplift resistance. The longitudinal springs are nonlinear springs similar to the transverse springs except that their response does not depend on the direction of the axial movement of the pipe.

### 1.3.3.4 Model by Zhou and Murray

Zhou and Murray (1993) used a two-dimensional elastic-plastic beam element as described in Section 1.3.1. The soil surrounding the pipe was modeled by three types of soil springs: bearing, uplift, and longitudinal springs. These springs represent the soil loading above the pipe, the bearing support below the pipe, and the longitudinal friction along the pipe. Elastic-perfectly plastic force-deformation constitutive relationships were used to model the bearing, uplift, and longitudinal soil springs. The model was implemented in the program ABP. Using stiffness-property-deformation (SPD) relations, derived from post-buckling analyses of cylindrical shells could be implemented in the beam model in order to account for local buckling effects (Zhou and Murray, 1993 and 1996).

The pipe response was found to be significantly influenced by local buckling, temperature differential, and the strength and stiffness of the uplift and bearing springs. The strength of longitudinal springs and the length of the settlement transition zone were determined to be relatively less influential on the pipe response. The rapid growth of localized deformation was found to be associated with the softening behavior of the pipe.

### 1.3.4 Thermal Buckling Analysis of Pipelines

The main body of research on the thermal buckling of pipelines was fostered by a number of buckling incidents involving the operation of subsea pipelines in 1980's. In particular, the small-diameter pipelines on the bottom of the North Sea carrying hot untreated hydrocarbons from deep wells into adjacent facilities experienced several upheaval buckling failures (Nielsen et al., 1990). A submarine pipeline laid (without trenching) on the seabed normally undergoes lateral buckling (or snaking) as the fluid temperature rises in the pipeline (Miles and Calladine, 1999).

Thermal buckling is not limited to offshore pipelines. Many cases of upheaval buckling have been reported in North America including Alaska's Arctic Coastal Plain (Quimby and Fitzpatrick, 1996). In this case, poor restraint by thawed and saturated cover soil was a major contributor to the problem.

Some of the important numerical and experimental studies on the thermal buckling of pipelines are summarized in the following.

#### 1.3.4.1 Study by Hobbs

Hobbs (1984) addressed both vertical (upheaval) and lateral (snaking) buckling responses of the pipeline to the rising temperature. The classical model for the buckling of continuously welded railroad tracks (Martinet, 1936 and Kerr, 1978) was adopted for the vertical mode of buckling. The governing differential equation for the buckled shape was derived for an infinitely long elastic beam-column resting on a rigid foundation under a lateral load equal to the self-weight. The model also assumed that the slopes were small and that the bending moment at the lift-off point was zero. The model accounted for the reduction in the compressive axial force because of the friction forces developing adjacent to the lift-off point as the ends of the buckled segment move in towards each other.

For the lateral mode of buckling, it was assumed that the initially perfect pipe would buckle into an indefinite number of half-waves. This assumption, partly based on some experimental observations, had the advantage of satisfying the lateral equilibrium. It was also assumed that the lateral frictional force is fully mobilized as the pipe buckles sideways on the foundation. The same differential equation as used for the vertical mode

9

was used here with some change in the boundary conditions. Then the results of the works by Martinet (1936) and Kerr (1978) were presented for the first four modes of lateral buckling (Modes 1 to 4, where the number refers to the number of half-waves forming). Modes 2, 3, and 4 were concluded to be the most likely of all conceivable modes, with the initial imperfection determining which mode would develop in a particular case. Numerical examples showed that lateral modes are possible at smaller temperature change values than the vertical mode for realistic friction coefficients.

The equilibrium paths in terms of the temperature change vs. the buckle length and vs. the buckle amplitude were discussed. The initial out-of-straightness was shown to have a major effect on the temperature rise at which the pipe would actually buckle in reality. The buckling was shown to be a dynamic snap-through when the out-of-straightness were small enough for the equilibrium path to have a minimum point. The temperature change corresponding to the minimum point was called the *safe* temperature change because regardless of the out-of-straightness value, the pipe would be unlikely to buckle below that value of temperature change.

The model has the following limitations:
- Perfect elasticity of the pipe and small slopes were assumed. An elastic solution may lead to unconservative results.
- The model does not apply to buried pipelines.
- Only straight pipes were rigorously examined. The effect of out-of-straightness was not quantitatively determined.

### 1.3.4.2 Study by Hobbs and Liang

Hobbs and Liang (1989) extended the vertical and lateral buckling models by Hobbs (1984) for a semi-infinite line to cover a number of practical cases where a restricted length of line is subjected to temperature increase. The examples of such pipelines discussed include a line between a wellhead and another fixed point, and short exposed segments of pipeline between restraints provided by isolated "spot" rock dumping. The rock dumps were assumed to greatly increase the resistance to axial sliding, reflected by a large friction coefficient. The buckling models were established for both modes of buckling for three different combinations of end restraints: rigid (fixed) restraint at both ends, rock dump at both ends, and rigid restraint at one end and rock dump at the other end.

10

Numerical examples showed that the use of discrete rock dumps or rigid restraints could increase the safe temperature change (as defined in the previous section) for both vertical and lateral buckling modes. In the case of lateral buckling, such restraints also reduced the bending stresses associated with a given temperature change greater than the safe temperature change.

### 1.3.4.3 Study by Ballet and Hobbs

Ballet and Hobbs (1989) expanded the vertical buckling model by Hobbs (1984) for a pipeline encountering a prop imperfection on the otherwise flat seabed. Both symmetric and nonsymmetric buckling were considered. For the symmetric case, the post-buckling upheaval curve, though depending on the prop height, was found to be asymptotic to the upheaval curve for the perfect (straight) pipe at large values of buckle length. It was shown that both upheaval and minimum temperature change values would increase with weight, justifying gravel covering operations.

The nonsymmetric buckling analysis was prompted by the remarkable sharpness of the cusp in the symmetric characteristic curve at upheaval, and the well-known asymmetry found in the buckling of shallow arches under a central load. Many possible asymmetric buckle positions for a given pipe resulted in a broad scatter band mostly under the symmetric upheaval case. This was considered to cast a serious doubt on the stability of the symmetric curve. However, the pre-upheaval parts of the asymmetric and symmetric responses were found close together.

### 1.3.4.4 Study by Ju and Kyriakides

Ju and Kyriakides (1988) studied the thermal vertical buckling of offshore pipelines by modeling the pipeline as a long heavy beam resting on a rigid foundation. They first summarized the results of pervious studies on upheaval buckling phenomenon as described in Section 5.2.

In the upheaval buckling formulation, the foundation could have one of two types of a symmetric imperfection: point imperfection and fully contacting imperfection. The friction between the pipe and the soil was modeled as Coulomb friction. Both elastic and elastic-plastic pipe material were considered in the study.

In the case of small fully contacting imperfection, the temperature change vs. deformation response was found to be characterized by the following temperature change values:

- The temperature change ($\Delta T_U$) corresponding to the first uplift
- The limit (critical) temperature change ($\Delta T_C$) beyond which the pipe is unstable
- The locally minimum temperature change ($\Delta T_M$) occurring after the critical temperature

The first two ($\Delta T_U$ and $\Delta T_C$) were found to be controlled by the amplitude, wavelength, and shape of the imperfection. These temperature change values was found to be dramatically increasing as the initial imperfection decreases in size. However, they were found to be relatively insensitive to frictional effects. In contrast, $\Delta T_M$ was found to be relatively unaffected as imperfection size decreases. For a large enough imperfection size, the response would monotonically increase following the initial uplift, with a severe reduction in resistance to deformation.

The pipe material nonlinearity caused earlier development of the limit temperature ($\Delta T_C$) and lowered the post-buckling response, in general. It was observed that $\Delta T_C$ was reached soon after the yield.

In the case of point imperfection, $\Delta T_U$ and $\Delta T_C$ were found to coincide.

### 1.3.4.5 Study by Raoof and Maschner

Raoof and Maschner (1993 and 1994) started a study on the vertical buckling of heated offshore pipelines by performing a testing program on 7-m long, 16-mm diameter, copper/nickel pipes with a wall thickness of 1.05 mm. These unburied pipe, laid on a flat rigid bed, had a point prop imperfection in the middle with heights ranging from 2 to 15.7 mm. Both gradual and rapid heating were used in the process of heating the pipes.

In gradual heating tests, the buckle had a tendency to seek symmetry both in the pre and post upheaval states. However, in cases where the large deformations during an asymmetric dynamic buckling (or snap) resulted in the plastification of the buckle apex, the tendency to achieve symmetry was significantly reduced. The asymmetry of the dynamic buckle greatly affected the form of the first static buckle after the snap.

According to the terminology used by the authors, the portion of the pipe between the lift-off point *nearer* to the flow inlet and the apex is called Half-wave A, and the portion between the lift-off point *farther* from the flow inlet and the apex is called Half-wave B. In the dynamic buckle, Half-wave A was always longer than Half-wave B. This was due to the temperature gradient, as Half-wave A, being closer to the hot fluid source, experienced higher temperatures than Half-wave B. Then to seek symmetry, the static buckle would move toward Half-wave B as the temperature was increased further.

In gradual heating tests, the pre-upheaval buckle forms were greatly affected by one of the half-waves reducing in length more rapidly right from the initial conditions. This resulted in an asymmetric buckle with respect to the prop position, also asymmetric in overall form. This movement restricted the development of constrained curvature in the pre-upheaval regime, resulting in longer wave lengths and earlier uplift temperatures off the prop. Therefore, a large amount of apex travel before upheaval was associated with a low uplift temperature off the prop. This led to less severe snaps and smaller dynamic buckles than those occurring in similar gradual heating tests. For the majority of the rapid tests, the dynamic buckle generated at the snap had a longer Half-wave B with the apex moving towards Half-wave A. This was not observed in any of the gradual tests. On average, rapid tests showed somewhat lower upheaval temperatures than the gradual tests.

The authors also developed a closed form solution to compare the test results with the theory. They used an approach similar to Hobbs and Liang (1989) to modify the infinite line formulations of Ballet and Hobbs (1992) to cater for the limited length of the test specimens. The theoretical curve for the temperature rise vs. the prop height was shown to be fitting the test data points as an average trend-line.

### 1.3.4.6 Study by Klever et al.

Klever et al. (1990) developed a finite element model for analyzing upheaval buckling response of submarine pipelines. They considered the classical design of protective covers to be over-conservative. The authors also criticize the more recent models that take into account realistic imperfections and the actual, nonlinear response of the cover. However, they considered these models unsuitable for fitness-for-purpose assessments of actual cases because these models consider only idealized, symmetric foundation imperfections. Therefore, they developed a computer model that accounts for all the relevant nonlinear parameters such as elastic-plastic material behavior, axial

friction and sand/clay/rock cover uplift resistance. Moreover, both idealized imperfections and arbitrary foundation profiles could be modeled.

The two-dimensional hybrid beam element they implemented in the model is described in Section 1.3.1. The far-field condition, as an end boundary condition simulating infinitely long continuation of the pipeline, was implemented in the formulation. This would avoid having to use very long models in the analysis. They used an arc-length technique for iterative solution of the equilibrium equations.

Through numerical examples, it was demonstrated that the "effective weight" approach for modeling the uplift force results in unconservative results, and hence it is unreliable. Thus, it was concluded that the it is essential to use realistic, nonlinear uplift resistance behavior of the soil cover.

A major limitation for the model and the resulting computer programs UPBUCK and PLUS-ONE (Andrew Palmer and Associates, 1993) is that their application is confined to offshore pipelines. Thus, the model cannot be applied to onshore pipelines, for which many cases of upheaval buckling have been encountered.

## 1.4 LAYOUT OF THE THESIS

The remainder of this report consists of six Chapters. The major subjects and scope of each of the following chapters are summarized as follows.

Chapter 2 contains the formulation of the two-dimensional, elastic-plastic, isoparametric $C^1$ pipe beam element capable of modeling large displacements and finite strains based on an updated Lagrangian formulation . The load and stiffness contributions of internal pressure were rigorously derived and implemented in the model. Special issues for the element such as moment loading are discussed.

Chapter 3 describes the elastic-plastic material model developed for the finite element formulation. The material model utilizes the von Mises yield criterion, normality flow rule, and a mixed strain-hardening rule. The resulting constitutive relationships are converted into the constitutive relationships required for the pipeline-beam element in an updated Lagrangian formulation.

Chapter 4 describes the pipeline-soil interaction model developed for the finite element formulation. This includes the nonlinear constitutive relationships required to model the bearing, uplift, transverse and longitudinal soil springs. The model is verified using an example and comparison of the results to those of PIPLIN.

Chapter 5 describes the thermal buckling formulation implemented in the finite element model. The thermal formulation is verified through three examples comparing the finite element results with theoretical and/or experimental counterparts.

Chapter 6 presents three case studies to demonstrate the application of thermal analysis. The first case study is an example of a parametric study, whereby the magnitude of initial imperfection is the variant. The second and third case studies stem from the investigations carried out on actual pipelines having undergone thermal buckling. The pipelines investigated in the second and third case studies are onshore and offshore pipelines, respectively.

Chapter 7 summarizes the results of this research project and discusses the areas for future developments.

# CHAPTER 2. FORMULATION OF $C^1$ PIPELINE-BEAM ELEMENT

## 2.1 INTRODUCTION

This chapter contains the finite element formulation developed in this study. A new two-dimensional, isoparametric $C^1$ beam element is presented that is capable of modeling large displacements and finite strains. The element uses a piecewise linear elastic-plastic material model, which is presented in Chapter 3. In order to apply this element to pipeline analysis, it has been equipped with features such as soil springs and internal pressure loading. The pipe-soil interaction model is described in Chapter 4.

This work is an evolution from the element developed by Zhou and Murray (1993) at the University of Alberta. The subparametric $C^1$ element by Zhou and Murray (1993) showed poor performance in regards to the smoothness of the axial force variation, and to a lesser degree, the moment variation along the pipe. The undesired oscillations in the axial force and moment diagrams would normally appear around the peak regions for each variable (for example see Section 4.5). This is believed to be because the subparametric element uses a quadratic interpolation for the axial displacement vs. a fifth-order interpolation for transverse displacement. As a result, very fine meshes (i.e., short elements) are required for a successful analysis. This makes the use of the element computationally expensive.

The reason a $C^1$ element was chosen over a $C^0$ element is that a $C^0$ beam element is normally used to model a beam for which shear deformations need to be accounted for. However the $C^1$ beam element in this study is dedicated to pipelines, which are flexible line structures for which axial and flexural deformations are dominant. Also, where shear deformations can be ignored, a $C^1$ beam element, using higher orders of interpolation, is expected to perform better than a $C^0$ element.

The subsequent sections describe the following: the fundamental assumptions in the new formulation; the element degrees of freedom and interpolation functions; the strain-displacement relations; the virtual work equation and its discretization; and, the load and stiffness contributions of internal pressure.

## 2.2 THE BASIC PROBLEM

In the development to follow, the equations describing the motion of the body of a finite deformable pipeline are derived in a stationary Cartesian coordinate system. It is assumed that the pipe can experience large displacements, large rotations, large strains, and a nonlinear constitutive response. The goal is to evaluate the equilibrium configurations of the pipe at discrete time points 0, $\Delta t$, $2\Delta t$, $3\Delta t$, ... , where $\Delta t$ is an increment in time. To develop a solution strategy, it is assumed that the solutions for the static and kinematic variables for all time steps from time 0 to time t, inclusive, have been obtained. Then the solution procedure for the next equilibrium configuration corresponding to time t + $\Delta t$ is applied repetitively until the solution converges.

The solution requires that all particles of the pipe body be followed in their motion, from the original to the final configuration of the body. This means that a *Lagrangian* (or *material*) formulation needs to be adopted. A Lagrangian formulation stands in contrast to an *Eulerian* formulation, where the motion of material through a stationary control volume is considered. This makes the Eulerian formulation suitable for the analysis of fluid mechanics problems. However, for the analysis of solids and structures, a Lagrangian formulation represents a more natural and efficient approach than does an Eulerian formulation. Hence, a Lagrangian analysis approach is adopted in this study.

## 2.3 VIRTUAL WORK EQUATION

In the Lagrangian incremental analysis approach, the equilibrium of the pipe body at time t + $\Delta t$ can be expressed using the principle of virtual work. This principle can be stated as follows: for any kinematically admissible virtual deformation field, the external virtual work must equal the internal virtual work. Using tensor notation, the principle of virtual work for the equilibrium of the body at time t + $\Delta t$ requires that (Bathe, 1996)

$$\int_{t+\Delta t_V} {}^{t+\Delta t}\sigma_{ij}\ \delta_{t+\Delta t}e_{ij}\ d^{t+\Delta t}V = \int_{t+\Delta t_V} {}^{t+\Delta t}f_i^{B}\ \delta u_i\ d^{t+\Delta t}V + \int_{t+\Delta t_{S_f}} {}^{t+\Delta t}f_i^{S}\ \delta u_i^{S}\ d^{t+\Delta t}S \qquad (2.1)$$

where

$\quad {}^{t+\Delta t}\sigma_{ij} = $ Cartesian components of the *Cauchy stress* tensor (force per unit areas in the deformed geometry)

17

$$\delta_{t+\Delta t}\,e_{ij} = \frac{1}{2}\left(\frac{\partial \delta u_i}{\partial^{t+\Delta t}x_j} + \frac{\partial \delta u_j}{\partial^{t+\Delta t}x_i}\right) = \text{strain tensor corresponding to virtual displacements}$$

$\delta u_i$ = components of virtual displacement vector imposed on configuration at time

$t + \Delta t$, a function of $^{t+\Delta t}x_j$, $\quad j = 1, 2, 3$

$^{t+\Delta t}x_i$ = Cartesian coordinates of material point at time $t + \Delta t$

$^{t+\Delta t}V$ = volume at time $t + \Delta t$

$^{t+\Delta t}f_i^B$ = components of externally applied forces per unit volume at time $t + \Delta t$

$^{t+\Delta t}f_i^S$ = components of externally applied surface traction per unit surface area at

time $t + \Delta t$

$^{t+\Delta t}S_f$ = surface at time $t + \Delta t$ on which external tractions are applied

$\delta u_i^S = \delta u_i$ evaluated on the surface $^{t+\Delta t}S_f$ (the $\delta u_i$ components are zero on

$^{t+\Delta t}S_u$, where displacements are prescribed)

In Eq. (2.1), the left-hand side is the internal virtual work and the right-hand side is the external virtual work. Following Bathe (1996), in the above equation as well as in the rest of this manuscript, the left superscript refers to configuration in which the quantity is evaluated; and the left subscript refers to the configuration with respect to which the quantity is evaluated.

The difficulty in the general application of Eq. (2.1) is that the configuration at the time $t + \Delta t$ is unknown. This is in contrast with linear analysis where it is assumed that the displacements are infinitesimal so that original configuration can be used in Eq. (2.1). To overcome this difficulty in nonlinear analysis, second Piola-Kirchhoff stresses and Green-Lagrange strains, which can be evaluated with respect to a configuration prior to the current one, are used. The choice of the prior configuration has led to two Lagrangian incremental formulations of nonlinear problems. These are total Lagrangian (TL) and updated Lagrangian (UL) formulations (Bathe, 1996). In TL formulation, all static and kinematic variables are referred to the initial configuration at time 0. The UL formulation is based on the same procedures as used in the TL formulation, however, in the solution all static and kinematic variables are referred to the last calculated configuration.

Both the TL and UL formulations can handle large displacements, large rotations, and large strains. Thus, the only advantage of using one formulation rather than the other lies in the greater numerical efficiency it can provide. In general, the incremental strains in the TL formulation contain an initial displacement effect that leads to a more complex

18

strain-displacement matrix than in the UL formulation (Bathe, 1996). Therefore, the UL formulation is deemed more convenient, and hence, adopted in this study. In the context of a UL formulation, the virtual work equation becomes (Bathe, 1996)

$$\int_{{}^{t}V} {}^{t+\Delta t}_{t}S_{ij}\, \delta^{t+\Delta t}_{t}E_{ij}\, d^{t}V = \int_{{}^{t+\Delta t}V} {}^{t+\Delta t}f^{B}_{i}\, \delta u_{i}\, d^{t+\Delta t}V + \int_{{}^{t+\Delta t}S_{f}} {}^{t+\Delta t}f^{S}_{i}\, \delta u^{S}_{i}\, d^{t+\Delta t}S \qquad (2.2)$$

where

$${}^{t+\Delta t}_{t}S_{ij} = \text{Cartesian components of the second Piola-Kirchhoff stress tensor with respect to the configuration at time } t$$

$$\delta^{t+\Delta t}_{t}E_{ij} = \frac{1}{2}\left(\frac{\partial \delta u_{i}}{\partial {}^{t}x_{j}} + \frac{\partial \delta u_{j}}{\partial {}^{t}x_{i}} + \frac{\partial \delta u_{k}}{\partial {}^{t}x_{i}}\frac{\partial \delta u_{k}}{\partial {}^{t}x_{j}}\right) = \text{Green-Lagrange strain increment tensor}$$

corresponding to the virtual displacement increments with respect to the configuration at time t.

Note that the right-hand side of Eq. (2.2) is evaluated based on the most recent configuration during the equilibrium iterations. Thus, at the beginning of the iterations, the configuration at time t, and thereafter, the most recent configuration at time $t + \Delta t$ is used for evaluating the right-hand side of Eq. (2.2).

In the following equations of this chapter, variables without a left superscript signify the increment of that variable from the configuration at time t to time $t + \Delta t$.

Considering the following relationship for stresses

$${}^{t+\Delta t}_{t}S_{ij} = {}^{t}\sigma_{ij} + {}_{t}S_{ij} \qquad \text{(note that } {}^{t}_{t}S_{ij} \equiv {}^{t}\sigma_{ij}\text{)} \qquad (2.3)$$

and the following relationships for strains

$${}^{t+\Delta t}_{t}E_{ij} = {}_{t}E_{ij} \qquad (2.4a)$$

$${}_{t}E_{ij} = {}_{t}e_{ij} + {}_{t}\eta_{ij} \qquad (2.4b)$$

$${}_{t}e_{ij} = \frac{1}{2}\left({}_{t}u_{i,j} + {}_{t}u_{j,i}\right) \qquad (2.4c)$$

$${}_{t}\eta_{ij} = \frac{1}{2}{}_{t}u_{k,i}\, {}_{t}u_{k,j} \qquad (2.4d)$$

the virtual work equation of Eq. (2.2) can be rewritten as

19

$$\int_{^tV} {}_tS_{ij}\,\delta_t E_{ij}\,d^tV + \int_{^tV} {}^t\sigma_{ij}\,\delta_t\eta_{ij}\,d^tV = \delta^{t+\Delta t}W_{ext} - \int_{^tV} {}^t\sigma_{ij}\,\delta_t e_{ij}\,d^tV \qquad (2.5)$$

where $\delta^{t+\Delta t}W_{ext}$, the external virtual work at time $t + \Delta t$, equals the right-hand side of Eq. (2.1).

For the finite element formulation, a linearized version of the virtual work equation is required. Using approximations ${}_tS_{ij} = {}_tC^{EP}_{ijrs}\,{}_t e_{rs}$ (where ${}_tC^{EP}_{ijrs}$ are the elastic-plastic constitutive coefficients derived in Chapter 3) and $\delta_t\varepsilon_{ij} = \delta_t e_{ij}$, Eq. (2.5) is linearized as

$$\int_{^tV} {}_tC^{EP}_{ijrs}\,{}_t e_{rs}\,\delta_t e_{ij}\,d^tV + \int_{^tV} {}^t\sigma_{ij}\,\delta_t\eta_{ij}\,d^tV = \delta^{t+\Delta t}W_{ext} - \int_{^tV} {}^t\sigma_{ij}\,\delta_t e_{ij}\,d^tV \qquad (2.6)$$

The virtual work equation expressed in Eq. (2.6) is the basis for the nonlinear finite element formulation developed in this investigation.

## 2.4 FUNDAMENTAL ASSUMPTIONS

The isoparametric pipe beam element is developed based on the following mathematical and physical assumptions:

(1) Euler-Bernoulli assumption: all cross-sections perpendicular to the pipe axis before the deformation, remain planar, undistorted, and perpendicular to the deformed pipe axis. This assumptions has the following implications:

    (a) Shear deformations, and hence, shear strains and stresses are ignored. This is justified because pipelines are flexible line structures where axial and flexural deformations are dominant. Thus they fit into the category of thin beams.

    (b) Any distortion of the pipe cross-section is ignored. Therefore ovalization and local shell buckling are not accounted for. The local shell effects are outside of the scope of this study. Future studies need to be carried out for the inclusion of these effects.

(2) The radial stresses are insignificant, and hence, are ignored. This is because for a typical pipeline the pipe wall thickness is much smaller than the pipe diameter.

(3) The pipe material yields according to the von Mises criterion. After yielding, plastic flow occurs according to the normality rule of the theory of plasticity.

(4) In the elastic-plastic material model, the strain-hardening of the material is represented by a mixed hardening formulation. The ratio between isotropic and kinematic hardening can be appropriately chosen and used in the analysis.

20

(5) The residual stresses due to pipe manufacturing procedure and transverse girth welds are not taken into account in this investigation.

(6) The soil support is modeled by distributed elastic-plastic soil springs. This, in the case of lateral springs, corresponds to an elastic-plastic *Winkler* foundation. Thus, the surrounding soil can be divided into infinitesimal slices, where the interaction of each slice with the pipe is represented by soil springs. The Winkler's hypothesis implies that the interaction between the hypothetical soil slices can be ignored. This assumption is generalized herein to apply to the longitudinal springs. Therefore, the longitudinal springs are also assumed to be independent of each other (i.e., decoupled). The Winkler's hypothesis might introduce some inaccuracy since the interaction between slices can sometimes be important. However, given the low accuracy of the available soil properties in practice, this assumption is appropriate.

(7) In the scope of this study, it is assumed that the internal pressure, if any, is applied to the initial pipe configuration prior to any other loading. Moreover, it is assumed that during and at the end of pressurization, the pipe remains elastic.

## 2.5 ELEMENT DOF'S AND SHAPE FUNCTIONS

The global and local coordinate systems for the two-dimensional isoparametric curved pipe beam element are shown in Fig. 2.1. The s-axis of the local coordinate system passes through the centroidal axis of the cross-section. The local h-axis remains always normal to the s-axis. As shown in Fig. 2.1, the x-y plane defines the plane of bending deformation. The element nodes and degrees of freedom are also shown in Fig. 2.1. The non-dimensional longitudinal ordinate, r, varies from −1 at Node 1 to 1 at Node 3. At Node 2, r has a value of 0 regardless of the exact position of the node. Thus, the middle node does not have to be exactly at the midspan of the element.

There are four degrees of freedom per node. These are $u_i$, $\left(\dfrac{du}{ds_0}\right)_i$, $v_i$, and $\left(\dfrac{dv}{ds_0}\right)_i$ for Node i (i = 1, 2, 3), where $u_i$ and $v_i$ are nodal displacements along the global x and y-axes, respectively. Here $s_0$ is the arc-length along the element in the initial configuration[1].

---

[1] See Section 2.13 for a more detailed description of the derivative DOFs.

21

Notations $u^i$ and $v^i$ ($i$ = 1, 2, ... , 6) are used to represent the nodal degrees of freedom as follows:

$$u^1 = u_1 \tag{2.7a}$$

$$u^2 = u_2 \tag{2.7b}$$

$$u^3 = u_3 \tag{2.7c}$$

$$u^4 = \left( \frac{du}{ds_0} \right)_{\!1} \tag{2.7d}$$

$$u^5 = \left( \frac{du}{ds_0} \right)_{\!2} \tag{2.7e}$$

$$u^6 = \left( \frac{du}{ds_0} \right)_{\!3} \tag{2.7f}$$

$$v^1 = v_1 \tag{2.8a}$$

$$v^2 = v_2 \tag{2.8b}$$

$$v^3 = v_3 \tag{2.8c}$$

$$v^4 = \left( \frac{dv}{ds_0} \right)_{\!1} \tag{2.8d}$$

$$v^5 = \left( \frac{dv}{ds_0} \right)_{\!2} \tag{2.8e}$$

$$v^6 = \left( \frac{dv}{ds_0} \right)_{\!3} \tag{2.8f}$$

Similarly, notations $x^i$ and $y^i$ ($i$ = 1, 2, ... , 6) are used to represent the nodal coordinates corresponding to the degrees of freedom:

$$x^1 = x_1 \tag{2.9a}$$

$$x^2 = x_2 \tag{2.9b}$$

$$x^3 = x_3 \tag{2.9c}$$

$$x^4 = \left( \frac{dx}{ds_0} \right)_{\!1} \tag{2.9d}$$

$$x^5 = \left( \frac{dx}{ds_0} \right)_{\!2} \tag{2.9e}$$

$$x^6 = \left(\frac{dx}{ds_0}\right)_{/3} \tag{2.9f}$$

$$y^1 = y_1 \tag{2.10a}$$

$$y^2 = y_2 \tag{2.10b}$$

$$y^3 = y_3 \tag{2.10c}$$

$$y^4 = \left(\frac{dy}{ds_0}\right)_{/1} \tag{2.10d}$$

$$y^5 = \left(\frac{dy}{ds_0}\right)_{/2} \tag{2.10e}$$

$$y^6 = \left(\frac{dy}{ds_0}\right)_{/3} \tag{2.10f}$$

Hermitian shape functions, which provide $C^1$ continuity across element boundaries, are used to interpolate the displacements u and v and the coordinates x and y of any given point along the element as a function of its position, represented by the non-dimensional coordinate r. In order to derive these shape functions, a generic variable, z, is introduced that can stand for any of the variables x, y, u, and v. The value of z at an arbitrary coordinate r along an element is expressed as

$$z(r) = N_1(r)\,z_1 + N_2(r)\,z_2 + N_3(r)\,z_3 + N_4(r)\left(\frac{dz}{dr}\right)_{/1} + N_5(r)\left(\frac{dz}{dr}\right)_{/2} + N_6(r)\left(\frac{dz}{dr}\right)_{/3} \tag{2.11}$$

Where the Hermitian shape functions $N_i(r)$ (i = 1, 2, ... , 6) are to be determined. Since there are six constraints involved here associated with the value of z and its derivative at the three nodes, a fifth order polynomial is used to evaluate z(r), with six unknown coefficients to be found:

$$z(r) = a_5\,r^5 + a_4\,r^4 + a_3\,r^3 + a_2\,r^2 + a_1\,r + a_0 \tag{2.12}$$

The six constraint equations can be expressed as

$$z_1 = z(-1) = -a_5 + a_4 - a_3 + a_2 - a_1 + a_0 \tag{2.13a}$$

$$z_2 = z(0) = a_0 \tag{2.13b}$$

$$z_3 = z(-1) = a_5 + a_4 + a_3 + a_2 + a_1 + a_0 \tag{2.13c}$$

$$\left(\frac{dz}{dr}\right)_{/1} = z_1' = z'(-1) = 5a_5 - 4a_4 + 3a_3 - 2a_2 + a_1 \tag{2.13d}$$

$$\left(\frac{dz}{dr}\right)_2 = z'_2 = z'(0) = a_1 \tag{2.13e}$$

$$\left(\frac{dz}{dr}\right)_3 = z'_3 = z'(1) = 5a_5 + 4a_4 + 3a_3 + 2a_2 + a_1 \tag{2.13f}$$

Hence, the coefficients $a_i$ $(i = 1, 2, \ldots, 6)$ are obtained as

$$a_5 = \frac{3}{4}(z_1 - z_3) + \frac{1}{4}(z'_1 + z'_3) + z'_2 \tag{2.14a}$$

$$a_4 = -\frac{1}{2}(z_1 + z_3) + \frac{1}{4}(-z'_1 + z'_3) + z_2 \tag{2.14b}$$

$$a_3 = \frac{5}{4}(-z_1 + z_3) - \frac{1}{4}(z'_1 + z'_3) - 2z'_2 \tag{2.14c}$$

$$a_2 = z_1 + z_3 - 2z_2 + \frac{1}{4}(z'_1 - z'_3) \tag{2.14d}$$

$$a_1 = z'_2 \tag{2.14e}$$

$$a_0 = z_2 \tag{2.14f}$$

The Hermitian shape functions $N_i(r)$ $(i = 1, 2, \ldots, 6)$ are obtained by substituting the coefficients $a_i$ $(i = 1, 2, \ldots, 6)$ from Eqs. (2.14) into Eq. (2.12) and corresponding the resulting equation to Eq. (2.11). This yields the shape functions as

$$N_1(r) = \frac{3}{4}r^5 - \frac{1}{2}r^4 - \frac{5}{4}r^3 + r^2 \tag{2.15a}$$

$$N_2(r) = r^4 - 2r^2 + 1 \tag{2.15b}$$

$$N_3(r) = -\frac{3}{4}r^5 - \frac{1}{2}r^4 + \frac{5}{4}r^3 + r^2 \tag{2.15c}$$

$$N_4(r) = \frac{1}{4}(r^5 - r^4 - r^3 + r^2) \tag{2.15d}$$

$$N_5(r) = r^5 - 2r^3 + r \tag{2.15e}$$

$$N_6(r) = \frac{1}{4}(r^5 + r^4 - r^3 - r^2) \tag{2.15f}$$

These equations are plotted in Fig. 2.2 for the range of $-1 \le r \le 1$. Equations (2.15) can be rewritten as

$$N_1(r) = \frac{3}{4}r^2(1-r)^2\left(r + \frac{4}{3}\right) \tag{2.16a}$$

24

$$N_2(r) = \left(1 - r^2\right) \tag{2.16b}$$

$$N_3(r) = -\frac{3}{4} r^2 (1+r)^2 \left(r - \frac{4}{3}\right) \tag{2.16c}$$

$$N_4(r) = \frac{1}{4} r^2 (1-r)^2 (1+r) \tag{2.16d}$$

$$N_5(r) = r \left(1 - r^2\right)^2 \tag{2.16e}$$

$$N_6(r) = -\frac{1}{4} r^2 (1+r)^2 (1-r) \tag{2.16f}$$

Before the shape functions are applied to the degrees of freedom, it is noted that the derivatives in the DOFs are with respect to $s_0$ (e.g., $u^4 = \left(\dfrac{du}{ds_0}\right)_1$), whereas in the derivation of the Hermitian shape functions, the derivatives are with respect to r. Thus, to reconcile the two, the derivatives $\left(\dfrac{ds_0}{dr}\right)_i$ ($i = 1, 2, 3$) are introduced at the element nodes. The chain rule results in

$$\left(\frac{dz}{dr}\right)_i = \left(\frac{dz}{ds_0}\right)_i \left(\frac{ds_0}{dr}\right)_i \qquad (i = 1, 2, 3) \tag{2.17}$$

Hence, Eq. (2.11) can be rewritten as

$$z(r) = N_1(r)\, z_1 + N_2(r)\, z_2 + N_3(r)\, z_3 + N_4(r) \left(\frac{ds_0}{dr}\right)_1 \left(\frac{dz}{ds_0}\right)_1 + N_5(r) \left(\frac{ds_0}{dr}\right)_2 \left(\frac{dz}{ds_0}\right)_2$$

$$+ N_6(r) \left(\frac{ds_0}{dr}\right)_3 \left(\frac{dz}{ds_0}\right)_3 \tag{2.18}$$

Therefore, the last three shape functions (i.e., $N_4$, $N_5$, and $N_6$) can be combined with the corresponding $\left(\dfrac{ds_0}{dr}\right)_i$ to give the interpolation functions for the DOFs adopted in this work. Thus, the final form of the interpolation functions, $h_i(r)$ ($i = 1, 2, \ldots, 6$), can be written as (not to be confused with the local coordinate h, which, in contrast, does not bear any right subscripts in this work)

$$h_1(r) = N_1(r) = \frac{3}{4} r^2 (1-r)^2 \left(r + \frac{4}{3}\right) \tag{2.19a}$$

$$h_2(r) = N_2(r) = \left(1 - r^2\right) \tag{2.19b}$$

$$h_3(r) = N_3(r) = -\frac{3}{4} r^2 (1+r)^2 \left( r - \frac{4}{3} \right) \tag{2.19c}$$

$$h_4(r) = N_4(r) \left( \frac{ds_0}{dr} \right)_1 = \frac{1}{4} r^2 (1-r)^2 (1+r) \left( \frac{ds_0}{dr} \right)_1 \tag{2.19d}$$

$$h_5(r) = N_5(r) \left( \frac{ds_0}{dr} \right)_2 = r (1-r^2)^2 \left( \frac{ds_0}{dr} \right)_2 \tag{2.19e}$$

$$h_6(r) = N_6(r) \left( \frac{ds_0}{dr} \right)_3 = -\frac{1}{4} r^2 (1+r)^2 (1-r) \left( \frac{ds_0}{dr} \right)_3 \tag{2.19f}$$

Hence, z(r) can finally be expressed as

$$z = \sum_{i=1}^{6} h_i(r) z^i \tag{2.20}$$

Since z is a generic variable representing x, y, u, and v, Eq. (2.20) is used to express these variable as

$$u = \sum_{i=1}^{6} h_i(r) u^i \tag{2.21a}$$

$$v = \sum_{i=1}^{6} h_i(r) v^i \tag{2.21b}$$

$$x = \sum_{i=1}^{6} h_i(r) x^i \tag{2.21c}$$

$$y = \sum_{i=1}^{6} h_i(r) y^i \tag{2.21d}$$

## 2.6 STRESS AND STRAIN COMPONENTS IN VIRTUAL WORK EQUATION

It is important to first establish what components of strain need to be worked out for the formulation. As a result of the first two assumptions mentioned in Section 2.4, the only stress components that need to be considered are the longitudinal (i.e., axial) and hoop stresses. The first assumption also implies that the only strain component that can be computed based on the kinematic assumptions is the longitudinal strain. However, the hoop strain is, in general, nonzero because even due to longitudinal action only, the Poisson effect results in a change in the hoop strain. Therefore, hoop as well as longitudinal stress and strain must be considered for the internal virtual work.

According to the seventh assumption of Section 2.4, the internal pressure, and hence the hoop stress, remain constant throughout the analysis. It is shown below that the contribution of hoop stress and strain to the internal virtual work equals the contribution of internal pressure and radial displacement of the pipe wall to the external virtual work. This holds true for a varying internal pressure as well. However, the following demonstration is carried out for constant internal pressure.

Figure 2.3 shows an infinitesimal element of pipe shell with a length of dx and subtending an angle $d\theta$. The pipe is assumed to have an internal radius of $R_i$ and a wall thickness of t. The hoop stress due to an internal pressure value of p is

$$\sigma_\theta = \frac{pR_i}{t} \tag{2.22}$$

The virtual hoop strain can be related to the virtual variation in the internal radius as

$$\delta\varepsilon_\theta = \frac{\delta R_i}{R_i} \tag{2.23}$$

Assuming a small $\dfrac{t}{R_i}$ ratio, the internal virtual work due to the hoop stress and strain for the element can be written as

$$d\delta W_\theta^{int} = \sigma_\theta \, \delta\varepsilon_\theta \, t \, R_i \, d\theta \, dx \tag{2.24}$$

which can be simplified using Eqs. (2.22) and (2.23) as

$$d\delta W_\theta^{int} = P \, \delta R_i \, R_i \, d\theta \, dx \tag{2.25}$$

The external virtual work due to the internal pressure and radial displacement of pipe wall for the element can be written as

$$d\delta W_\theta^{ext} = P \, \delta R_i \, R_i \, d\theta \, dx \tag{2.26}$$

Thus, the contribution of hoop stress and strain in internal virtual work equals the contribution of internal pressure and radial displacement of pipe wall in the external virtual work. This implies that the hoop effects are decoupled from the longitudinal effects in the virtual work equation. Therefore the hoop strain and the radial displacement contributions can be dropped from the internal and external virtual work, respectively, leaving only the longitudinal effects. As a result, only the longitudinal stress

and strain need to be considered in the virtual work equation of this finite element formulation.

## 2.7 STRAIN-DISPLACEMENT RELATIONSHIPS

For this section and the following sections of this chapter, the following notation is used: The variables without a left superscript signify the increment of that variable from the configuration at time t to time $t + \Delta t$. Quantities with left superscripts are the total values at the configuration time specified by the superscript.

Figure 2.4 shows the pipe configuration at a general time t. The global coordinate system is represented by the x and y axes. For a generic point of the pipe body, shown by P in the figure, there is a pipe cross-section perpendicular to the pipe axis. The center of the cross-section is indicated by A in Fig. 2.4. The local element coordinate system denoted by h and s has already been described in Section 2.5. For each material point, such as Point P in Fig. 2.3, a material coordinate system is defined with axes originating from that point and parallel to the local axes h and s. These axes, denoted by $\tilde{x}$ and $\tilde{y}$ in Fig. 2.4, are used to express the longitudinal stress and strain quantities at the material point.

From Fig. 2.4, the coordinates of Point P in the global coordinates system, $^tX$ and $^tY$, can be expressed in terms of the coordinates of point A in the global system, $^tx$ and $^ty$, and the h coordinate of Point P in the local element system as

$$^tX = {}^tx - h\sin{}^t\theta \tag{2.27a}$$

$$^tY = {}^ty + h\cos{}^t\theta \tag{2.27b}$$

Where $^t\theta$ is the inclination angle of the cross-section as shown in Fig. 2.4.

Thus, the displacements of Point P in the global coordinate system, $^tU$ and $^tV$, become

$$^tU = {}^tX - {}^0X = {}^tx - {}^0x - h\left(\sin{}^t\theta - \sin{}^0\theta\right) = {}^tu - h\left(\sin{}^t\theta - \sin{}^0\theta\right) \tag{2.28a}$$

$$^tV = {}^tY - {}^0Y = {}^ty - {}^0y + h\left(\cos{}^t\theta - \cos{}^0\theta\right) = {}^tv + h\left(\cos{}^t\theta - \cos{}^0\theta\right) \tag{2.28b}$$

Where $^tu$ and $^tv$ are the displacements of Point A in the global coordinate system.

The material point displacements, $^tU$ and $^tV$, need to be expressed in terms of the nodal displacements $^tu^i$ and $^tv^i$. Substituting for $^tu$ and $^tv$ from Eqs. (2.21a) and (2.21) yields

$$^tU = \sum_{i=1}^{6} h_i(r) \, ^tu^i - h\left(\sin{}^t\theta - \sin{}^0\theta\right) \qquad (2.29a)$$

$$^tV = \sum_{i=1}^{6} h_i(r) \, ^tv^i + h\left(\cos{}^t\theta - \cos{}^0\theta\right) \qquad (2.29b)$$

Thus, the displacement increments, U and V, become

$$U = {}^{t+\Delta t}U - {}^tU = \sum_{i=1}^{6} h_i(r) u^i - h\left(\sin{}^{t+\Delta t}\theta - \sin{}^t\theta\right) \qquad (2.30a)$$

$$V = {}^{t+\Delta t}V - {}^tV = \sum_{i=1}^{6} h_i(r) v^i + h\left(\cos{}^{t+\Delta t}\theta - \cos{}^t\theta\right) \qquad (2.30b)$$

The challenge now is to express the sin and cos terms in Eqs. (2.30) in terms of the increments of the nodal displacements $u^i$ and $v^i$. This is done through the $\dfrac{d^tx}{d^ts} (= \cos{}^t\theta)$ and $\dfrac{d^ty}{d^ts} (= \sin{}^t\theta)$ terms as follows:

$$\cos{}^t\theta = \frac{d^tx}{d^ts} = \frac{\dfrac{d^tx}{dr}}{\dfrac{d^ts}{dr}} = \frac{\dfrac{d^tx}{dr}}{\sqrt{\left(\dfrac{d^tx}{dr}\right)^2 + \left(\dfrac{d^ty}{dr}\right)^2}} = \frac{{}^tx'}{\sqrt{{}^tx'^2 + {}^ty'^2}} \qquad (2.31a)$$

$$\sin{}^t\theta = \frac{d^ty}{d^ts} = \frac{\dfrac{d^ty}{dr}}{\dfrac{d^ts}{dr}} = \frac{\dfrac{d^ty}{dr}}{\sqrt{\left(\dfrac{d^tx}{dr}\right)^2 + \left(\dfrac{d^ty}{dr}\right)^2}} = \frac{{}^ty'}{\sqrt{{}^tx'^2 + {}^ty'^2}} \qquad (2.31b)$$

where $x'$ and $y'$ are the derivatives of x and y with respect to r, respectively. In general, the prime superscript signifies a derivative with respect to r for any given variable for the rest of this chapter unless otherwise is specified. Using Eq. (2.31a), the cos terms of Eq. (2.30b) can be expressed as

29

$$\cos^{t+\Delta t}\theta - \cos^{t}\theta = \frac{d^{t+\Delta t}x}{d^{t+\Delta t}s} - \frac{d^{t}x}{d^{t}s} = \frac{^{t+\Delta t}x'}{\sqrt{^{t+\Delta t}x'^{2} + ^{t+\Delta t}y'^{2}}} - \frac{^{t}x'}{\sqrt{^{t}x'^{2} + ^{t}y'^{2}}} \qquad (2.32)$$

From there,

$$\cos^{t+\Delta t}\theta - \cos^{t}\theta = \frac{^{t}x' + x'}{\sqrt{\left(^{t}x' + x'\right)^{2} + \left(^{t}y' + y'\right)^{2}}} - \frac{^{t}x'}{\sqrt{^{t}x'^{2} + ^{t}y'^{2}}} \qquad (2.33)$$

Hence,

$$\cos^{t+\Delta t}\theta - \cos^{t}\theta = \frac{^{t}x' + x'}{\sqrt{^{t}x'^{2} + ^{t}y'^{2}}\sqrt{1 + \dfrac{a}{^{t}x'^{2} + ^{t}y'^{2}}}} - \frac{^{t}x'}{\sqrt{^{t}x'^{2} + ^{t}y'^{2}}} \qquad (2.34)$$

where

$$a = 2^{t}x' x' + 2^{t}y' y' + x'^{2} + y'^{2} \qquad (2.35)$$

Assuming small enough increments, $\dfrac{a}{^{t}x'^{2} + ^{t}y'^{2}} < 1$. Thus, Binomial expansion can

be applied to the term $\dfrac{1}{\sqrt{1 + \dfrac{a}{^{t}x'^{2} + ^{t}y'^{2}}}} = \left(1 + \dfrac{a}{^{t}x'^{2} + ^{t}y'^{2}}\right)^{-\frac{1}{2}}$ in Eq. (2.34):

$$\cos^{t+\Delta t}\theta - \cos^{t}\theta = \frac{^{t}x' + x'}{\sqrt{^{t}x'^{2} + ^{t}y'^{2}}}\left(1 - \frac{a}{2\left(^{t}x'^{2} + ^{t}y'^{2}\right)} + \frac{3a^{2}}{8\left(^{t}x'^{2} + ^{t}y'^{2}\right)^{2}}\right) - \frac{^{t}x'}{\sqrt{^{t}x'^{2} + ^{t}y'^{2}}} \qquad (2.36)$$

where only the first three terms of the Binomial have been maintained. This is because the higher order terms lead to cubic and higher order incremental terms, which do not play any role in the linearized equation of virtual work.

Defining $^{t}\rho = \dfrac{1}{\dfrac{d^{t}s}{dr}} = \dfrac{1}{\sqrt{^{t}x'^{2} + ^{t}y'^{2}}}$, Eq. (2.36) becomes

$$\cos^{t+\Delta t}\theta - \cos^{t}\theta = {}^{t}\rho\, x' - \frac{{}^{t}\rho^{3}}{2}\left(^{t}x' + x'\right)a + \frac{3}{8}\,{}^{t}\rho^{5}\,{}^{t}x'\, a^{2} \qquad (2.37)$$

Keeping up to quadratic incremental terms, Eq. (2.37) reduces to

$$\cos^{t+\Delta t}\theta - \cos^{t}\theta = {}^{t}c_{1}\, x' + {}^{t}c_{2}\, y' + {}^{t}c_{3}\, x'^{2} + {}^{t}c_{4}\, y'^{2} + {}^{t}c_{5}\, x'y' \qquad (2.38)$$

where

$${}^t c_1 = {}^t \rho \left(1 - {}^t \rho^2 \, {}^t x'^2\right) \tag{2.39a}$$

$${}^t c_2 = -{}^t \rho^3 \, {}^t x' \, {}^t y' \tag{2.39b}$$

$${}^t c_3 = -\frac{3}{2} \, {}^t \rho^3 \, {}^t x' \left(1 - {}^t \rho^2 \, {}^t x'^2\right) \tag{2.39c}$$

$${}^t c_4 = -\frac{1}{2} \, {}^t \rho^3 \, {}^t x' \left(1 - 3 \, {}^t \rho^2 \, {}^t y'^2\right) \tag{2.39d}$$

$${}^t c_5 = -{}^t \rho^3 \, {}^t y' \left(1 - 3 \, {}^t \rho^2 \, {}^t x'^2\right) \tag{2.39e}$$

Similarly, it can be shown that

$$\sin {}^{t+\Delta t}\theta - \sin {}^t \theta = {}^t s_1 \, x' + {}^t s_2 \, y' + {}^t s_3 \, x'^2 + {}^t s_4 \, y'^2 + {}^t s_5 \, x'y' \tag{2.40}$$

where

$${}^t s_1 = -{}^t \rho^3 \, {}^t x' \, {}^t y' \tag{2.41a}$$

$${}^t s_2 = {}^t \rho \left(1 - {}^t \rho^2 \, {}^t y'^2\right) \tag{2.41b}$$

$${}^t s_3 = -\frac{1}{2} \, {}^t \rho^3 \, {}^t y' \left(1 - 3 \, {}^t \rho^2 \, {}^t x'^2\right) \tag{2.41c}$$

$${}^t s_4 = -\frac{3}{2} \, {}^t \rho^3 \, {}^t y' \left(1 - {}^t \rho^2 \, {}^t y'^2\right) \tag{2.41d}$$

$${}^t s_5 = -{}^t \rho^3 \, {}^t x' \left(1 - 3 \, {}^t \rho^2 \, {}^t y'^2\right) \tag{2.41e}$$

Substituting the sin and cos terms from Eqs. (2.38) and (2.40) into Eqs. (2.30) yields the displacement increments for the material point P as

$$U = \sum_{i=1}^{6} h_i(r) \, {}^t u^i - h\left({}^t s_1 \, x' + {}^t s_2 \, y' + {}^t s_3 \, x'^2 + {}^t s_4 \, y'^2 + {}^t s_5 \, x'y'\right) \tag{2.42a}$$

$$V = \sum_{i=1}^{6} h_i(r) \, {}^t v^i + h\left({}^t c_1 \, x' + {}^t c_2 \, y' + {}^t c_3 \, x'^2 + {}^t c_4 \, y'^2 + {}^t c_5 \, x'y'\right) \tag{2.42b}$$

Noting that

$$x' = {}^{t+\Delta t} x' - {}^t x' = ({}^{t+\Delta t} x' - {}^0 x') - ({}^t x' - {}^0 x') = {}^{t+\Delta t} u' - {}^t u' = u' = \sum_{i=1}^{6} h_i'(r) \, u^i \tag{2.43a}$$

$$y' = {}^{t+\Delta t}y' - {}^{t}y' = ({}^{t+\Delta t}y' - {}^{0}y') - ({}^{t}y' - {}^{0}y') = {}^{t+\Delta t}v' - {}^{t}v' = v' = \sum_{i=1}^{6} h_i'(r)\, v^i \qquad (2.43b)$$

The displacement increments for the material point P can finally be written, by substituting Eqs. (2.43) into Eqs. (2.42), as

$$U = \sum_{i=1}^{6} h_i(r)\, u^i - h \left( \begin{array}{l} {}^{t}s_1 \sum_{i=1}^{6} h_i'\, u^i + {}^{t}s_2 \sum_{i=1}^{6} h_i'\, v^i + {}^{t}s_3 \left( \sum_{i=1}^{6} h_i'\, u^i \right)^2 \\[2mm] + {}^{t}s_4 \left( \sum_{i=1}^{6} h_i'\, v^i \right)^2 + {}^{t}s_5 \left( \sum_{i=1}^{6} h_i'\, u^i \right)\left( \sum_{i=1}^{6} h_i'\, v^i \right) \end{array} \right) \qquad (2.44a)$$

$$V = \sum_{i=1}^{6} h_i(r)\, v^i + h \left( \begin{array}{l} {}^{t}c_1 \sum_{i=1}^{6} h_i'\, u^i + {}^{t}c_2 \sum_{i=1}^{6} h_i'\, v^i + {}^{t}c_3 \left( \sum_{i=1}^{6} h_i'\, u^i \right)^2 \\[2mm] + {}^{t}c_4 \left( \sum_{i=1}^{6} h_i'\, v^i \right)^2 + {}^{t}c_5 \left( \sum_{i=1}^{6} h_i'\, u^i \right)\left( \sum_{i=1}^{6} h_i'\, v^i \right) \end{array} \right) \qquad (2.44b)$$

Here U and V are the displacement increments in the global coordinate system. They need to be converted into the material coordinate system (denoted by axes $\tilde{x}$ and $\tilde{y}$ in Fig. 2.4). This conversion is carried out through a rotation transformation:

$$\left\{ \begin{array}{c} \tilde{U} \\ \tilde{V} \end{array} \right\} = \left[ {}^{t}T \right] \left\{ \begin{array}{c} U \\ V \end{array} \right\} \qquad (2.45)$$

where $\tilde{U}$ and $\tilde{V}$ are the displacement increments in the material coordinate system and $\left[ {}^{t}T \right]$ is the rotation matrix:

$$\left[ {}^{t}T \right] = \begin{bmatrix} \cos {}^{t}\theta & \sin {}^{t}\theta \\ -\sin {}^{t}\theta & \cos {}^{t}\theta \end{bmatrix} \qquad (2.46)$$

And the sin and cos terms can be expressed as

$$\cos {}^{t}\theta = \frac{d^t x}{d^t s} = \frac{{}^{t}x'}{\sqrt{{}^{t}x'^2 + {}^{t}y'^2}} = {}^{t}\rho \; {}^{t}x' \qquad (2.47a)$$

$$\sin {}^{t}\theta = \frac{d^t y}{d^t s} = \frac{{}^{t}y'}{\sqrt{{}^{t}x'^2 + {}^{t}y'^2}} = {}^{t}\rho \; {}^{t}y' \qquad (2.47b)$$

Hence, the rotation matrix becomes

$$\left[ {}^{t}T \right] = {}^{t}\rho \begin{bmatrix} {}^{t}x' & {}^{t}y' \\ -{}^{t}y' & {}^{t}x' \end{bmatrix} \qquad (2.48)$$

As concluded in Section 2.6, the only strain component required for the formulation is the longitudinal or axial strain. The Green-Lagrange strain at the generic material point, P, with respect to the configuration at time t can be expressed as

$$_t\tilde{E}_{11} = {}_t\tilde{U}_{,\tilde{x}} + \frac{1}{2}\left( {}_t\tilde{U}_{,\tilde{x}}^2 + {}_t\tilde{V}_{,\tilde{x}}^2 \right) \tag{2.49}$$

where

$$_t\tilde{U}_{,\tilde{x}} = \frac{\partial \tilde{U}}{\partial^t \tilde{x}} = \frac{\partial \tilde{U}}{\partial^t s} = {}_t\tilde{U}_{,s} \tag{2.50a}$$

$$_t\tilde{V}_{,\tilde{x}} = \frac{\partial \tilde{V}}{\partial^t \tilde{x}} = \frac{\partial \tilde{V}}{\partial^t s} = {}_t\tilde{V}_{,s} \tag{2.50b}$$

Hence,

$$_t\tilde{E}_{11} = {}_t\tilde{U}_{,s} + \frac{1}{2}\left( {}_t\tilde{U}_{,s}^2 + {}_t\tilde{V}_{,s}^2 \right) \tag{2.51}$$

Note that in taking the derivatives $_t\tilde{U}_{,s}$ and $_t\tilde{V}_{,s}$ using Eq. (2.45), the $\sin^t\theta$ and $\cos^t\theta$ terms are treated as constants. This is because for any given point, the axes $\tilde{x}$ and $\tilde{y}$ at the configuration time t remain constant. Hence, Eq. (2.45) yields

$$\begin{Bmatrix} {}_t\tilde{U}_{,s} \\ {}_t\tilde{V}_{,s} \end{Bmatrix} = \begin{bmatrix} {}^tT \end{bmatrix} \begin{Bmatrix} {}_tU_{,s} \\ {}_tV_{,s} \end{Bmatrix} \tag{2.52}$$

In order to work out the derivatives of Eq. (2.52), the chain rule is applied:

$$_tU_{,s} = \frac{\partial U}{\partial^t s} = \frac{\dfrac{\partial U}{\partial^t r}}{\dfrac{\partial^t s}{\partial^t r}} = \frac{{}_tU_{,r}}{\sqrt{{}^tx'^2 + {}^ty'^2}} = {}^t\rho \; {}_tU_{,r} \tag{2.53a}$$

And similarly,

$$_tV_{,s} = {}^t\rho \; {}_tV_{,r} \tag{2.53b}$$

Substituting for $_tU_{,s}$ and $_tV_{,s}$ in Eq. (2.52) from Eqs. (2.53) yields

$$\begin{Bmatrix} {}_t\tilde{U}_{,s} \\ {}_t\tilde{V}_{,s} \end{Bmatrix} = {}^t\rho \begin{bmatrix} {}^tT \end{bmatrix} \begin{Bmatrix} {}_tU_{,r} \\ {}_tV_{,r} \end{Bmatrix} \tag{2.54}$$

Substituting for $\begin{bmatrix} {}^tT \end{bmatrix}$ from Eq. (2.48) gives

$$\begin{Bmatrix} {}_t\tilde{U}_{,s} \\ {}_t\tilde{V}_{,s} \end{Bmatrix} = {}^t\rho^2 \begin{bmatrix} {}^tx' & {}^ty' \\ -{}^ty' & {}^tx' \end{bmatrix} \begin{Bmatrix} {}_tU_{,r} \\ {}_tV_{,r} \end{Bmatrix} \tag{2.55}$$

Substituting for ${}_t\tilde{U}_{,s}$ and ${}_t\tilde{V}_{,s}$ from Eq. (2.55) into Eq. (2.51) yields

$$
{}_t\tilde{E}_{11}={}^t\rho^2\left({}^tx'\,{}_tU'+{}^ty'\,{}_tV'\right)+\frac{1}{2}{}^t\rho^4\left[\left({}^tx'\,{}_tU'+{}^ty'\,{}_tV'\right)^2+\left(-{}^ty'\,{}_tU'+{}^tx'\,{}_tV'\right)^2\right] \quad (2.56)
$$

where the alternate notations of ${}_tU'={}_tU_{,r}$ and ${}_tV'={}_tV_{,r}$ have been used.

The longitudinal strain, ${}_t\tilde{E}_{11}$, is expressed as a sum of linear and nonlinear (i.e., quadratic) components. In other words,

$$
{}_t\tilde{E}_{11}={}_t\tilde{e}_{11}+{}_t\tilde{\eta}_{11} \quad (2.57)
$$

Where ${}_t\tilde{e}_{11}$ and ${}_t\tilde{\eta}_{11}$ are the linear and nonlinear strains, respectively from Eqs. (2.4c) and (2.4d). Substituting for ${}_tU$ and ${}_tV$ from Eqs. (2.44) into Eqs. (2.56) leads to the following expressions for the linear and nonlinear strains:

$$
{}_t\tilde{e}_{11}={}^t\rho^2\left({}^tx'\sum_{i=1}^{6}h'_i\,u^i+{}^ty'\sum_{i=1}^{6}h'_i\,v^i\right)+h\left({}^tA_1\sum_{i=1}^{6}h''_i\,u^i+{}^tA_2\sum_{i=1}^{6}h''_i\,v^i+{}^tA_8\sum_{i=1}^{6}h'_i\,u^i+{}^tA_9\sum_{i=1}^{6}h'_i\,v^i\right) \quad (2.58)
$$

$$
_t\tilde{\eta}_{11} = \frac{{}^t\rho^2}{2}\left(\left(\sum_{i=1}^{6} h_i' \, u^i\right)^2 + \left(\sum_{i=1}^{6} h_i' \, v^i\right)^2\right) +
$$

$$
h\left(\begin{array}{l}
\dfrac{{}^tB_8}{2}\left(\displaystyle\sum_{i=1}^{6} h_i' \, u^i\right)^2 + \dfrac{{}^tB_9}{2}\left(\displaystyle\sum_{i=1}^{6} h_i' \, v^i\right)^2 + {}^tA_{14}\left(\displaystyle\sum_{i=1}^{6} h_i' \, u^i\right)\left(\displaystyle\sum_{i=1}^{6} h_i' \, v^i\right) + \\[3ex]
{}^tB_1\left(\displaystyle\sum_{i=1}^{6} h_i' \, u^i\right)\left(\displaystyle\sum_{i=1}^{6} h_i'' \, u^i\right) + {}^tB_2\left(\displaystyle\sum_{i=1}^{6} h_i' \, v^i\right)\left(\displaystyle\sum_{i=1}^{6} h_i'' \, v^i\right) + \\[3ex]
{}^tB_3\left(\displaystyle\sum_{i=1}^{6} h_i' \, u^i\right)\left(\displaystyle\sum_{i=1}^{6} h_i'' \, v^i\right) + {}^tB_4\left(\displaystyle\sum_{i=1}^{6} h_i' \, v^i\right)\left(\displaystyle\sum_{i=1}^{6} h_i'' \, u^i\right)
\end{array}\right) +
$$

$$
h^2\left(\begin{array}{l}
\dfrac{{}^tB_{10}}{2}\left(\displaystyle\sum_{i=1}^{6} h_i' \, u^i\right)^2 + \dfrac{{}^tB_{11}}{2}\left(\displaystyle\sum_{i=1}^{6} h_i' \, v^i\right)^2 + \dfrac{{}^tB_5}{2}\left(\displaystyle\sum_{i=1}^{6} h_i'' \, u^i\right)^2 + \\[3ex]
\dfrac{{}^tB_6}{2}\left(\displaystyle\sum_{i=1}^{6} h_i'' \, v^i\right)^2 + \\[3ex]
{}^tB_{12}\left(\displaystyle\sum_{i=1}^{6} h_i' \, u^i\right)\left(\displaystyle\sum_{i=1}^{6} h_i' \, v^i\right) + {}^tB_7\left(\displaystyle\sum_{i=1}^{6} h_i'' \, u^i\right)\left(\displaystyle\sum_{i=1}^{6} h_i'' \, v^i\right) + \\[3ex]
{}^tB_{13}\left(\displaystyle\sum_{i=1}^{6} h_i' \, u^i\right)\left(\displaystyle\sum_{i=1}^{6} h_i'' \, u^i\right) + {}^tB_{14}\left(\displaystyle\sum_{i=1}^{6} h_i' \, v^i\right)\left(\displaystyle\sum_{i=1}^{6} h_i'' \, v^i\right) + \\[3ex]
{}^tB_{15}\left(\displaystyle\sum_{i=1}^{6} h_i' \, u^i\right)\left(\displaystyle\sum_{i=1}^{6} h_i'' \, v^i\right) + {}^tB_{16}\left(\displaystyle\sum_{i=1}^{6} h_i' \, v^i\right)\left(\displaystyle\sum_{i=1}^{6} h_i'' \, u^i\right)
\end{array}\right)
\tag{2.59}
$$

Where $A_i$ and $B_i$ are defined as follows.

$$
{}^tA_1 = {}^t\rho^2\left(-{}^tx' \, {}^ts_1 + {}^ty' \, {}^tc_1\right)
\tag{2.60a}
$$

$$
{}^tA_2 = {}^t\rho^2\left(-{}^tx' \, {}^ts_2 + {}^ty' \, {}^tc_2\right)
\tag{2.60b}
$$

$$
{}^tA_3 = 2 \, {}^t\rho^2\left(-{}^tx' \, {}^ts_3 + {}^ty' \, {}^tc_3\right)
\tag{2.60c}
$$

$$
{}^tA_4 = 2 \, {}^t\rho^2\left(-{}^tx' \, {}^ts_4 + {}^ty' \, {}^tc_4\right)
\tag{2.60d}
$$

$$
{}^tA_5 = {}^t\rho^2\left(-{}^tx' \, {}^ts_5 + {}^ty' \, {}^tc_5\right)
\tag{2.60e}
$$

$$
{}^tA_6 = {}^t\rho^2\left({}^ty' \, {}^ts_1 + {}^tx' \, {}^tc_1\right)
\tag{2.60f}
$$

$$^tA_7 = {}^t\rho^2 \left( {}^ty'\; {}^ts_2 + {}^tx'\; {}^tc_2 \right) \qquad\qquad (2.60g)$$

$$^tA_8 = {}^t\rho^2 \left( -{}^tx'\; {}^ts_1' + {}^ty'\; {}^tc_1' \right) \qquad\qquad (2.60h)$$

$$^tA_9 = {}^t\rho^2 \left( -{}^tx'\; {}^ts_2' + {}^ty'\; {}^tc_2' \right) \qquad\qquad (2.60i)$$

$$^tA_{10} = {}^t\rho^2 \left( {}^ty'\; {}^ts_1' + {}^tx'\; {}^tc_1' \right) \qquad\qquad (2.60j)$$

$$^tA_{11} = {}^t\rho^2 \left( {}^ty'\; {}^ts_2' + {}^tx'\; {}^tc_2' \right) \qquad\qquad (2.60k)$$

$$^tA_{12} = {}^t\rho^2 \left( -{}^tx'\; {}^ts_3' + {}^ty'\; {}^tc_3' \right) \qquad\qquad (2.60l)$$

$$^tA_{13} = {}^t\rho^2 \left( -{}^tx'\; {}^ts_4' + {}^ty'\; {}^tc_4' \right) \qquad\qquad (2.60m)$$

$$^tA_{14} = {}^t\rho^2 \left( -{}^tx'\; {}^ts_5' + {}^ty'\; {}^tc_5' \right) \qquad\qquad (2.60n)$$

$$^tB_1 = {}^tA_3 + {}^t\rho^2\; {}^tx'\; {}^tA_1 \qquad\qquad (2.61a)$$

$$^tB_2 = {}^tA_4 + {}^t\rho^2\; {}^ty'\; {}^tA_2 \qquad\qquad (2.61b)$$

$$^tB_3 = {}^tA_5 + {}^t\rho^2\; {}^tx'\; {}^tA_2 \qquad\qquad (2.61c)$$

$$^tB_4 = {}^tA_5 + {}^t\rho^2\; {}^ty'\; {}^tA_1 \qquad\qquad (2.61d)$$

$$^tB_5 = {}^tA_1{}^2 \qquad\qquad (2.61e)$$

$$^tB_6 = {}^tA_2{}^2 \qquad\qquad (2.61f)$$

$$^tB_7 = {}^tA_1\; {}^tA_2 \qquad\qquad (2.61g)$$

$$^tB_8 = 2\left[ {}^tA_{12} + {}^t\rho^2 \left( {}^tx'\; {}^tA_8 - {}^ty'\; {}^tA_{10} \right) \right] \qquad\qquad (2.61h)$$

$$^tB_9 = 2\left[ {}^tA_{13} + {}^t\rho^2 \left( {}^ty'\; {}^tA_9 + {}^tx'\; {}^tA_{11} \right) \right] \qquad\qquad (2.61i)$$

$$^tB_{10} = {}^tA_8{}^2 + {}^tA_{10}{}^2 \qquad\qquad (2.61j)$$

$$^tB_{11} = {}^tA_9{}^2 + {}^tA_{11}{}^2 \qquad\qquad (2.61k)$$

$$^tB_{12} = {}^tA_8\; {}^tA_9 + {}^tA_{10}\; {}^tA_{11} \qquad\qquad (2.61l)$$

$${}^{t}B_{13} = {}^{t}A_1 \ {}^{t}A_8 \tag{2.61m}$$

$${}^{t}B_{14} = {}^{t}A_2 \ {}^{t}A_9 \tag{2.61n}$$

$${}^{t}B_{15} = {}^{t}A_2 \ {}^{t}A_8 \tag{2.61o}$$

$${}^{t}B_{16} = {}^{t}A_1 \ {}^{t}A_9 \tag{2.61p}$$

In order to express Eqs. (2.58) and (2.59) in a matrix form, the following vectors are introduced

$$\langle \mathbf{H_u} \rangle = \langle h_1 \quad h_2 \quad h_3 \quad h_4 \quad h_5 \quad h_6 \quad 0 \quad 0 \quad 0 \quad 0 \quad 0 \quad 0 \rangle \tag{2.62a}$$

$$\langle \mathbf{H_v} \rangle = \langle 0 \quad 0 \quad 0 \quad 0 \quad 0 \quad 0 \quad h_1 \quad h_2 \quad h_3 \quad h_4 \quad h_5 \quad h_6 \rangle \tag{2.62b}$$

$$\langle \mathbf{H_u'} \rangle = \langle h_1' \quad h_2' \quad h_3' \quad h_4' \quad h_5' \quad h_6' \quad 0 \quad 0 \quad 0 \quad 0 \quad 0 \quad 0 \rangle \tag{2.62c}$$

$$\langle \mathbf{H_v'} \rangle = \langle 0 \quad 0 \quad 0 \quad 0 \quad 0 \quad 0 \quad h_1' \quad h_2' \quad h_3' \quad h_4' \quad h_5' \quad h_6' \rangle \tag{2.62d}$$

$$\langle \mathbf{H_u''} \rangle = \langle h_1'' \quad h_2'' \quad h_3'' \quad h_4'' \quad h_5'' \quad h_6'' \quad 0 \quad 0 \quad 0 \quad 0 \quad 0 \quad 0 \rangle \tag{2.62e}$$

$$\langle \mathbf{H_v''} \rangle = \langle 0 \quad 0 \quad 0 \quad 0 \quad 0 \quad 0 \quad h_1'' \quad h_2'' \quad h_3'' \quad h_4'' \quad h_5'' \quad h_6'' \rangle \tag{2.62f}$$

and the vector of nodal displacement increments for the element is defined as

$$\langle \mathbf{u} \rangle = \langle u^1 \quad u^2 \quad u^3 \quad u^4 \quad u^5 \quad u^6 \quad v^1 \quad v^2 \quad v^3 \quad v^4 \quad v^5 \quad v^6 \rangle \tag{2.63}$$

In Matrix expressions, bold characters represent matrices and vectors, while plain characters represent their components. Moreover, the notations { }, < >, and [ ] represent a column vector, a row vector, and a matrix, respectively.

Equations (2.58) and (2.59) can be written in a matrix form as

$${}_{t}\tilde{e}_{11} = \langle {}^{t}\mathbf{B^L} \rangle \{\mathbf{u}\} = \langle \mathbf{u} \rangle \{ {}^{t}\mathbf{B^L} \} \tag{2.64}$$

$${}_{t}\tilde{\eta}_{11} = \langle \mathbf{u} \rangle [ {}^{t}\mathbf{B^{NL}} ] \{\mathbf{u}\} \tag{2.65}$$

Where

$$\langle {}^{t}\mathbf{B^L} \rangle = {}^{t}\rho^2 \left( {}^{t}x' \langle \mathbf{H_u'} \rangle + {}^{t}y' \langle \mathbf{H_v'} \rangle \right) + h \left( {}^{t}A_1 \langle \mathbf{H_u''} \rangle + {}^{t}A_2 \langle \mathbf{H_v''} \rangle + {}^{t}A_8 \langle \mathbf{H_u'} \rangle + {}^{t}A_9 \langle \mathbf{H_v'} \rangle \right) \tag{2.66}$$

$$\left[{}^t\mathbf{B}^{NL}\right]=\left({}^t\rho^2+h\,{}^t B_8+h^2\,{}^t B_{10}\right)\!\{H'_u\}\langle H'_u\rangle+\left({}^t\rho^2+h\,{}^t B_9+h^2\,{}^t B_{11}\right)\!\{H'_v\}\langle H'_v\rangle+$$

$$\left(h\,{}^t A_{14}+h^2\,{}^t B_{12}\right)\!\left(\{H'_u\}\langle H'_v\rangle+\{H'_v\}\langle H'_u\rangle\right)+$$

$$\left(h\,{}^t B_1+h^2\,{}^t B_{13}\right)\!\left(\{H'_u\}\langle H''_u\rangle+\{H''_u\}\langle H'_u\rangle\right)+$$

$$\left(h\,{}^t B_2+h^2\,{}^t B_{14}\right)\!\left(\{H'_v\}\langle H''_v\rangle+\{H''_v\}\langle H'_v\rangle\right)+$$

$$\left(h\,{}^t B_3+h^2\,{}^t B_{15}\right)\!\left(\{H'_u\}\langle H''_v\rangle+\{H''_v\}\langle H'_u\rangle\right)+ \tag{2.67}$$

$$\left(h\,{}^t B_4+h^2\,{}^t B_{16}\right)\!\left(\{H'_v\}\langle H''_u\rangle+\{H''_u\}\langle H'_v\rangle\right)+$$

$$\left(h^2\,{}^t B_5\right)\!\{H''_u\}\langle H''_u\rangle+\left(h^2\,{}^t B_6\right)\!\{H''_v\}\langle H''_v\rangle+$$

$$\left(h^2\,{}^t B_7\right)\!\left(\{H''_u\}\langle H''_v\rangle+\{H''_v\}\langle H''_u\rangle\right)$$

Since, in the virtual work equation, $\left\langle{}^t\mathbf{B}^L\right\rangle$ and $\left[{}^t\mathbf{B}^{NL}\right]$ are integrated over the volume of the element, they need to be sorted out in terms of the local coordinate h:

$$\left\langle{}^t\mathbf{B}^L\right\rangle=\left\langle{}^t\mathbf{B}_1^L\right\rangle+h\left\langle{}^t\mathbf{B}_2^L\right\rangle \tag{2.68}$$

where

$$\left\langle{}^t\mathbf{B}_1^L\right\rangle={}^t\rho^2\left({}^t x'\langle H'_u\rangle+{}^t y'\langle H'_v\rangle\right) \tag{2.69a}$$

$$\left\langle{}^t\mathbf{B}_2^L\right\rangle={}^t A_1\langle H''_u\rangle+{}^t A_2\langle H''_v\rangle+{}^t A_8\langle H'_u\rangle+{}^t A_9\langle H'_v\rangle \tag{2.69b}$$

and

$$\left[{}^t\mathbf{B}^{NL}\right]=\left[{}^t\mathbf{B}_1^{NL}\right]+h\left[{}^t\mathbf{B}_2^{NL}\right]+h^2\left[{}^t\mathbf{B}_3^{NL}\right] \tag{2.70}$$

where

$$\left[{}^t\mathbf{B}_1^{NL}\right]={}^t\rho^2\left(\{H'_u\}\langle H'_u\rangle+\{H'_v\}\langle H'_v\rangle\right) \tag{2.71a}$$

$$\left[{}^t\mathbf{B}_2^{NL}\right]=h\begin{pmatrix}{}^t B_8\{H'_u\}\langle H'_u\rangle+{}^t B_9\{H'_v\}\langle H'_v\rangle+{}^t A_{14}\left(\{H'_u\}\langle H'_v\rangle+\{H'_v\}\langle H'_u\rangle\right)+\\[4pt]{}^t B_1\left(\{H'_u\}\langle H''_u\rangle+\{H''_u\}\langle H'_u\rangle\right)+{}^t B_2\left(\{H'_v\}\langle H''_v\rangle+\{H''_v\}\langle H'_v\rangle\right)+\\[4pt]{}^t B_3\left(\{H'_u\}\langle H''_v\rangle+\{H''_v\}\langle H'_u\rangle\right)+{}^t B_4\left(\{H'_v\}\langle H''_u\rangle+\{H''_u\}\langle H'_v\rangle\right)\end{pmatrix} \tag{2.71b}$$

$$\left[{}^t\mathbf{B}_3^{NL}\right]=h^2\begin{pmatrix}{}^t B_{10}\{H'_u\}\langle H'_u\rangle+{}^t B_{11}\{H'_v\}\langle H'_v\rangle+{}^t B_{12}\left(\{H'_u\}\langle H'_v\rangle+\{H'_v\}\langle H'_u\rangle\right)+\\[4pt]{}^t B_{13}\left(\{H'_u\}\langle H''_u\rangle+\{H''_u\}\langle H'_u\rangle\right)+{}^t B_{14}\left(\{H'_v\}\langle H''_v\rangle+\{H''_v\}\langle H'_v\rangle\right)+\\[4pt]{}^t B_{15}\left(\{H'_u\}\langle H''_v\rangle+\{H''_v\}\langle H'_u\rangle\right)+{}^t B_{16}\left(\{H'_v\}\langle H''_u\rangle+\{H''_u\}\langle H'_v\rangle\right)+\\[4pt]{}^t B_5\{H''_u\}\langle H''_u\rangle+\left(h^2\,{}^t B_6\right)\{H''_v\}\langle H''_v\rangle+{}^t B_7\left(\{H''_u\}\langle H''_v\rangle+\{H''_v\}\langle H''_u\rangle\right)\end{pmatrix} \tag{2.71c}$$

The above equations will be used in derivation of the element stiffness matrix.

## 2.8 FINITE ELEMENT EXPANSION OF VIRTUAL WORK

There are several components involved in the equation of virtual work that need to be expressed in matrix form in order to establish the equilibrium equations. All of the three integrals in Eq. (2.6) pertain to the internal virtual work. The matrix form of these integrals are derived in Section 2.8.1 using the strain-displacement relations developed in Section 2.7.

The external virtual work, represented by $\delta^{t+\Delta t} W_{ext}$ in Eq. (2.6), includes the virtual work done by all of the loads and soil springs. The work done by the soil springs, internal pressure, and distributed loads is derived in the following subsections. The thermal load and the associated virtual work component will be discussed at length in Chapter 5.

### 2.8.1 Finite Element Expansion of Internal Virtual Work

The internal virtual work expressed in Eq. (2.6) consists of three integrals. These are

$$I_1 = \int_{{}^t V} {}_t C_{ijrs}^{EP} \, {}_t e_{rs} \, \delta_t e_{ij} \, d^t V \tag{2.72a}$$

$$I_2 = \int_{{}^t V} {}^t \sigma_{ij} \, \delta_t \eta_{ij} \, d^t V \tag{2.72b}$$

$$I_3 = \int_{{}^t V} {}^t \sigma_{ij} \, \delta_t e_{ij} \, d^t V \tag{2.72c}$$

where integrals $I_1$ and $I_2$ contribute to the stiffness matrix and integral $I_3$ contributes to the load vector. Here the integrals are taken over the volume that the body of the whole pipe model occupies at time t.

As concluded in Section 2.6, only the longitudinal stress and strain need to be considered in the virtual work equation, and hence, in this finite element formulation. Thus, the integrals of Eqs. (2.72) can be simplified to

$$I_1 = \int_{{}^t V} {}_t C_{1111}^{EP} \, {}_t \tilde{e}_{11} \, \delta_t \tilde{e}_{11} \, d^t V \tag{2.73a}$$

$$I_2 = \int_{{}^t V} {}^t \tilde{\sigma}_{11} \, \delta_t \tilde{\eta}_{11} \, d^t V \tag{2.73b}$$

39

$$I_3 = \int_{^tV} {}^t\tilde{\sigma}_{11} \, \delta_t \tilde{e}_{11} \, d^tV \tag{2.73c}$$

where, as the notations indicate, the stress and strain measures in Eqs. (2.73) are in the material coordinate system. The sole elastic-plastic constitutive coefficient, ${}_tC_{1111}^{EP}$, will be shown as ${}_tC^{EP}$ from here on for simplicity. The procedure of calculating this coefficient is described in Chapter 3.

Substituting for ${}_t\tilde{e}_{11}$ in Eqs. (2.73a) and (2.73c) using Eqs. (2.64) and (2.68) yields $I_1$ and $I_3$ as follows

$$I_1 = \sum_e \langle \delta \mathbf{u} | \left( \int_{^tL_e} \left( {}^tD_1 \left[ {}^tS_1 \right] + {}^tD_2 \left[ {}^tS_2 \right] + {}^tD_3 \left[ {}^tS_3 \right] \right) d^ts \right) \{ \mathbf{u} \} \tag{2.74}$$

$$I_3 = \sum_e \langle \delta \mathbf{u} | \left( \int_{^tL_e} \left( {}^tF_1 \left\{ {}^t\mathbf{B}_1^L \right\} + {}^tF_2 \left\{ {}^t\mathbf{B}_2^L \right\} \right) d^ts \right) \tag{2.75}$$

where

$$\left[ {}^tS_1 \right] = \left\{ {}^t\mathbf{B}_1^L \right\} \langle {}^t\mathbf{B}_1^L | \tag{2.76a}$$

$$\left[ {}^tS_2 \right] = \left\{ {}^t\mathbf{B}_1^L \right\} \langle {}^t\mathbf{B}_2^L | + \left\{ {}^t\mathbf{B}_2^L \right\} \langle {}^t\mathbf{B}_1^L | \tag{2.76b}$$

$$\left[ {}^tS_3 \right] = \left\{ {}^t\mathbf{B}_2^L \right\} \langle {}^t\mathbf{B}_2^L | \tag{2.76c}$$

$$^tD_1 = \int_{^tA} {}_tC^{EP} d^tA \tag{2.77a}$$

$$^tD_2 = \int_{^tA} {}_tC^{EP} \, h \, d^tA \tag{2.77b}$$

$$^tD_3 = \int_{^tA} {}_tC^{EP} \, h^2 \, d^tA \tag{2.77c}$$

$$^tF_1 = \int_{^tA} {}_t\tilde{\sigma}_{11} \, d^tA \tag{2.78a}$$

$$^tF_2 = \int_{^tA} {}_t\tilde{\sigma}_{11} \, h \, d^tA \tag{2.78b}$$

Substituting for $_t\tilde{\eta}_{11}$ in Eq. (2.73b) using Eqs. (2.65) and (2.70) yields $I_2$ as

$$I_2 = \sum_e 2\langle \delta u \rangle \left( \int_{{}^tL_e} ({}^tF_1 [{}^tB_1^{NL}] + {}^tF_2 [{}^tB_2^{NL}] + {}^tF_3 [{}^tB_3^{NL}]) d {}^ts \right) \{u\} \qquad (2.79)$$

where

$$^tF_3 = \int_{{}^tA} {}_t\tilde{\sigma}_{11} h^2 d {}^tA \qquad (2.80)$$

The procedures for obtaining the longitudinal stress, $_t\tilde{\sigma}_{11}$, and the constitutive coefficient, $_tC^{EP}$, in the integrals expressed by Eqs. (2.77), (2.78), and (2.80), are described in the next chapter. These integrals are calculated using a number of Newton-Cotes integration points over the cross-sections that correspond to the Gauss integration points along the pipeline-beam element. The number of the equally-distanced integration points around the cross-section can be specified by the user of the program ABP. Ten to Twenty sampling points are recommended for one half of the cross-section.

## 2.8.2 Virtual Work Done by Soil Springs

The pipe-soil interaction and the constitutive relations for soil springs are described, in detail, in Chapter 4. The final action of the soil springs on the pipe, however, is considered here for the purpose of obtaining the stiffness and load contributions of the soil springs.

As Fig. 2.5 shows, the soil springs are considered to be oriented in the local coordinate system as distributed (or continuous) entities along the element. There are three types of springs modeling the reaction from soil surrounding the pipeline. Transverse support from the soil beneath and above the pipe are modeled by bearing and uplift springs, respectively (see Fig. 2.5). The interface frictional reaction along the pipeline is modeled using longitudinal springs.

The resultant of the transverse spring forces (i.e., the bearing and uplift springs) at time $t + \Delta t$, noted by $^{t+\Delta t}F_T$, and the longitudinal spring force at time $t + \Delta t$, noted by $^{t+\Delta t}F_L$, can be expressed as

$$^{t+\Delta t}F_T = {}^tF_T - {}^tk_T \tilde{v} \qquad (2.81a)$$

41

$$^{t+\Delta t}F_L = {}^tF_L - {}^tk_L\,\tilde{u} \tag{2.81b}$$

where

$^tF_T$ = the resultant of the transverse spring forces at time t

$^tF_L$ = the longitudinal spring force at time t

$^tk_T$ = the resultant transverse spring stiffness at time t

$^tk_L$ = the longitudinal spring stiffness at time t

Note that because of the distributed nature of the springs, the above force and stiffness values (for any given point along the axis of the pipeline) are measured per unit length of the pipe.

The external virtual work done by the soil springs can be expressed as

$$\delta W_{soil}^{ext} = \sum_e \int_{{}^tL_e} \left( {}^{t+\Delta t}F_T\,\delta\tilde{v} + {}^{t+\Delta t}F_L\,\delta\tilde{u} \right) d^ts \tag{2.82}$$

The reason for the virtual work done by the soil springs being external is that the reference body for the virtual work equation has been assumed to be the pipe body. The same transformation matrix as used in Eq. (2.45) can be used to obtain $\tilde{u}$ and $\tilde{v}$, the displacement increments of the arbitrary point A in Fig. 2.4 in the local coordinate system. Hence,

$$\begin{Bmatrix} \tilde{u} \\ \tilde{v} \end{Bmatrix} = \begin{bmatrix} {}^tT \end{bmatrix} \begin{Bmatrix} u \\ v \end{Bmatrix} = {}^t\rho \begin{bmatrix} {}^tx' & {}^ty' \\ -{}^ty' & {}^tx' \end{bmatrix} \begin{Bmatrix} u \\ v \end{Bmatrix} \tag{2.83}$$

Substituting for by $^{t+\Delta t}F_T$ and $^{t+\Delta t}F_L$ from Eq. (2.81), substituting for $\tilde{u}$ and $\tilde{v}$ from Eq. (2.83) into Eq. (2.82), and incorporating vectors of Eqs. (2.62) yield:

$$\delta W_{soil}^{ext} = \sum_e \left( \begin{array}{l} \int_{{}^tL_e} {}^t\rho\langle\delta u\rangle\left(-{}^ty'\{H_u\}+{}^tx'\{H_v\}\right)\left[{}^tF_T - {}^tk_T\,{}^t\rho\left(-{}^ty'\langle H_u\rangle+{}^tx'\langle H_v\rangle\right)\{u\}\right]d^ts + \\ \int_{{}^tL_e} {}^t\rho\langle\delta u\rangle\left({}^tx'\{H_u\}+{}^ty'\{H_v\}\right)\left[{}^tF_L - {}^tk_L\,{}^t\rho\left({}^tx'\langle H_u\rangle+{}^ty'\langle H_v\rangle\right)\{u\}\right]d^ts \end{array} \right) \tag{2.84}$$

This leads to the following stiffness matrix and load vector contributions:

$$\delta W_{soil}^{stiff} = \sum_e \langle\delta u\rangle \left( \begin{array}{l} \int_{{}^tL_e} {}^t\rho^2\,{}^tk_T\left(-{}^ty'\{H_u\}+{}^tx'\{H_v\}\right)\left(-{}^ty'\langle H_u\rangle+{}^tx'\langle H_v\rangle\right)d^ts + \\ \int_{{}^tL_e} {}^t\rho^2\,{}^tk_L\left({}^tx'\{H_u\}+{}^ty'\{H_v\}\right)\left({}^tx'\langle H_u\rangle+{}^ty'\langle H_v\rangle\right)d^ts \end{array} \right) \{u\} \tag{2.85}$$

$$\delta W_{soil}^{load} = \sum_e \langle \delta u \rangle \left\{ \begin{array}{l} \int_{{}^{t}L_e} {}^{t}\rho\,{}^{t}F_T \left(-{}^{t}y'\{H_u\}+{}^{t}x'\{H_v\}\right)d^{t}s + \\[2mm] \int_{{}^{t}L_e} {}^{t}\rho\,{}^{t}F_L \left({}^{t}x'\{H_u\}+{}^{t}y'\{H_v\}\right)d^{t}s \end{array} \right\} \qquad (2.86)$$

Note that a sign change has been applied to the stiffness contribution of Eq. (2.85). This is because the stiffness contribution of Eq. (2.84) is considered to have moved to the left hand side of the virtual work equation.

### 2.8.3 Virtual Work Done by Internal Pressure

From the work carried out by Yoosef-Ghodsi et. al (1994), the effect of internal pressure on a bent pipe is a transverse distributed load in the direction from the intrados to the extrados of the pipe. This equivalent transverse load can be expressed as

$$q_p = P_0\,\phi \qquad (2.87)$$

where $\phi$ is the pipe curvature and $P_0 = \pi R_i{}^2\,p$, in which $R_i$ is the pipe internal radius and $p$ is the internal pressure.

Using a vector notation the virtual work done by the equivalent transverse load at time $t+\Delta t$ can be written as

$$\delta W_{pres}^{ext} = \sum_e \int_{{}^{t}L_e} -P_0\left(\frac{d^2\left({}^{t+\Delta t}\bar{\mathbf{x}}\right)}{d^{t}s^2}\cdot\delta\bar{\mathbf{u}}\right) d^{t}s \qquad (2.88)$$

where, ${}^{t+\Delta t}\bar{\mathbf{x}} = {}^{t+\Delta t}x\,\bar{\mathbf{i}}+{}^{t+\Delta t}y\,\bar{\mathbf{j}}$, $\bar{\mathbf{u}} = u\,\bar{\mathbf{i}}+v\,\bar{\mathbf{j}}$, and $\dfrac{d^2\left({}^{t+\Delta t}\bar{\mathbf{x}}\right)}{d^{t}s^2}\cdot\delta\bar{\mathbf{u}}$ signifies a *dot product*. Here $\bar{\mathbf{i}}$ and $\bar{\mathbf{j}}$ are the base unit vectors for the global coordinate system in the x and y direction, respectively. The vector $\dfrac{d^2\left({}^{t+\Delta t}\bar{\mathbf{x}}\right)}{d^{t}s^2}$ approximately matches the curvature vector at time $t+\Delta t$, and hence, $\dfrac{d^2\left({}^{t+\Delta t}\bar{\mathbf{x}}\right)}{d^{t}s^2}$ is almost perpendicular to the pipe axis at time $t+\Delta t$ (the reason $\dfrac{d^2\left({}^{t+\Delta t}\bar{\mathbf{x}}\right)}{d^{t}s^2}$ does not exactly equal the curvature vector at time $t+\Delta t$ is that the derivative is taken with respect to s at time t rather than $t+\Delta t$). Therefore in Eq. (2.88),

$$-P_0 \frac{d^2\left(^{t+\Delta t}\bar{x}\right)}{d^t s^2}$$ constitutes the equivalent lateral force, and because of the dot product, only the projection of $\delta\bar{u}$ normal to the pipe axis plays a role.

Integration by parts yields Eq. (2.76) as

$$\delta W_{pres}^{ext} = -P_0 \sum_e \left( \left[ \frac{d\left(^{t+\Delta t}\bar{x}\right)}{d^t s}(L_e) \cdot \delta\bar{u}(L_e) - \frac{d\left(^{t+\Delta t}\bar{x}\right)}{d^t s}(0) \cdot \delta\bar{u}(0) \right] - \int_{L_e} \left( \frac{d\left(^{t+\Delta t}\bar{x}\right)}{d^t s} \cdot \frac{d(\delta\bar{u})}{d^t s} \right) d^t s \right)$$

(2.89)

where 0 and $L_e$ represent the beginning and end of each element. Figure 2.6 shows the physical interpretation of the force components present in Eq. (2.89). It is noted that the derivative $\frac{d\left(^{t+\Delta t}\bar{x}\right)}{d^t s}$ at any point along the pipe axis closely approximates the unit vector tangent to the pipe axis at that point ($^{t+\Delta t}s \approx {}^t s$). Therefore all of the three forces shown in Fig. 2.6 are tangent to the pipe with a magnitude of $P_0$. Thus only the projection of $\delta\bar{u}$ tangent to the pipe axis plays a role in Eq. (2.89). It is also noted that for any two consecutive elements, the term $\frac{d\left(^{t+\Delta t}\bar{x}\right)}{d^t s} \cdot \delta\bar{u}$ for the common node appears with opposite signs in the expressions for the two respective elements in Eq. (2.89). Hence for a single-branch pipeline structure the first two terms on the right hand side of Eq. (2.89) are cancelled out except for the very ends of the model. Thus Eq. (2.89) becomes

$$\delta W_{pres}^{ext} = -P_0 \left[ \frac{d\left(^{t+\Delta t}\bar{x}\right)}{d^t s}(L) \cdot \delta\bar{u}(L) - \frac{d\left(^{t+\Delta t}\bar{x}\right)}{d^t s}(0) \cdot \delta\bar{u}(0) \right] + P_0 \sum_e \left( \int_{^t L_e} \left( \frac{d\left(^{t+\Delta t}\bar{x}\right)}{d^t s} \cdot \frac{d(\delta\bar{u})}{d^t s} \right) d^t s \right)$$

(2.90)

where 0 and L represent the beginning and end of the model.

Noting that $^{t+\Delta t}\bar{x} = {}^t\bar{x} + \bar{u}$, Eq. (2.90) can be rewritten as

$$\delta W_{pres}^{ext} = -P_0 \left[ \left( \frac{d\left(^t\bar{x}\right)}{d^t s}(L) + \frac{d\bar{u}}{d^t s}(L) \right) \cdot \delta\bar{u}(L) - \left( \frac{d\left(^t\bar{x}\right)}{d^t s}(0) + \frac{d\bar{u}}{d^t s}(0) \right) \cdot \delta\bar{u}(0) \right] +$$

$$P_0 \sum_e \int_{^t L_e} \left( \frac{d\left(^t\bar{x}\right)}{d^t s} + \frac{d\bar{u}}{d^t s} \right) \cdot \frac{d(\delta\bar{u})}{d^t s} d^t s$$

(2.91)

Equation (2.91) results in the following stiffness matrix and load vector contributions:

$$\delta W_{pres}^{stiff} = P_0 \left[ \frac{d\bar{u}}{d^t s}(L) \cdot \delta\bar{u}(L) - \frac{d\bar{u}}{d^t s}(0) \cdot \delta\bar{u}(0) \right] - P_0 \sum_e \int_{{}^tL_e} \frac{d\bar{u}}{d^t s} \cdot \frac{d(\delta\bar{u})}{d^t s} d^t s \qquad (2.92)$$

$$\delta W_{pres}^{load} = -P_0 \left[ \frac{d({}^t\bar{x})}{d^t s}(L) \cdot \delta\bar{u}(L) - \frac{d({}^t\bar{x})}{d^t s}(0) \cdot \delta\bar{u}(0) \right] + P_0 \sum_e \int_{{}^tL_e} \frac{d({}^t\bar{x})}{d^t s} \cdot \frac{d(\delta\bar{u})}{d^t s} d^t s \qquad (2.93)$$

The first two terms of the expression for the stiffness contribution in Eq. (2.92), involving only the end nodes of the model, result in non-symmetricity of the stiffness matrix. Because the solution techniques for solving the equilibrium equations depend on the symmetricity of the stiffness matrix, the first two terms on the right hand side of Eq. (2.92) are neglected. This type of approximation is valid for an iterative solution scheme as employed herein, though it might delay the solution convergence to some degree. The stiffness contribution is, thus, taken to be

$$\delta W_{pres}^{stiff} = -P_0 \sum_e \int_{{}^tL_e} \frac{d\bar{u}}{d^t s} \cdot \frac{d(\delta\bar{u})}{d^t s} d^t s \qquad (2.94)$$

Expanding the dot product of the integrand in Eq. (2.94) and applying the chain rule similar to that of Eq. (2.53a) result in the stiffness contribution as

$$\delta W_{pres}^{stiff} = -P_0 \sum_e \int_{{}^tL_e} {}^t\rho^2 \left( {}_t u_{,r} \delta_t u_{,r} + {}_t v_{,r} \delta_t v_{,r} \right) d^t s \qquad (2.95)$$

Using the vectors of Eqs. (2.62), Equation (2.95) can be expressed in a matrix form as

$$\delta W_{pres}^{stiff} = -P_0 \sum_e \langle \delta u | \left( \int_{{}^tL_e} {}^t\rho^2 \left( \{H'_u\}\langle H'_u\rangle + \{H'_v\}\langle H'_v\rangle \right) d^t s \right) \{u\} \qquad (2.96)$$

Similarly, the load contribution in Eq. (2.92) can be expressed as

$$\delta W_{pres}^{load} = -P_0 {}^t\rho \left[ \left( {}^tx'(L)\delta u(L) + {}^ty'(L)\delta v(L) \right) - \left( {}^tx'(0)\delta u(0) + {}^ty'(0)\delta v(0) \right) \right] +$$

$$P_0 \sum_e \langle \delta u | \left( \int_{{}^tL_e} {}^t\rho^2 \left( {}^tx'\{H'_u\} + {}^ty'\{H'_v\} \right) d^t s \right) \qquad (2.97)$$

Note that according to Eq. (2.97), the end nodes of the model will have loads in the global x and y direction arising from the internal pressure. There is also a typical load vector for each element of the model, given by the integral in Eq. (2.97).

## 2.8.4 Virtual Work Done by Distributed Loads

Overburden load and the pipe self-weight are the most common examples of distributed loads. However, a general distributed load, with components specified in the global x and y directions, is also considered herein.

It is assumed that the magnitude of the distributed load is given or evaluated at the three nodes of each element. In addition, the gravity is assumed to act in the global y direction. The total values of distributed load for a given point along an element at time t in the global x and y direction, noted by $^t q_x$ and $^t q_y$, respectively, are as follows:

$$^t q_x = {}^t q_{xs} \tag{2.98a}$$

$$^t q_y = {}^t q_{ys} + {}^t q_s^g + {}^t q_h^g \cos{}^t \theta \tag{2.98b}$$

where

$^t q_{xs}$ = distributed load in the global x direction per unit of sloped length

$^t q_{ys}$ = distributed load in the global y direction per unit of sloped length

$^t q_s^g$ = gravity load per unit of sloped length (used for self weight)

$^t q_h^g$ = gravity load per unit of horizontal (global x) length (used for overburden load)

$^t \theta$ = slope angle as shown in Fig. 2.4. Note that $\cos {}^t \theta = \dfrac{^t x'}{\sqrt{^t x'^2 + {}^t y'^2}} = {}^t \rho \; {}^t x'$.

Having known the x and y components of total distributed load at the three nodes of each element, a quadratic interpolation is used to obtain the respective values at any point along the element. Hence,

$$^t q_x(r) = \left( \frac{^t q_{x1} + {}^t q_{x3}}{2} - {}^t q_{x2} \right) r^2 + \left( \frac{^t q_{x3} - {}^t q_{x1}}{2} \right) r + {}^t q_{x2} \; r \tag{2.99a}$$

$$^t q_y(r) = \left( \frac{^t q_{y1} + {}^t q_{y3}}{2} - {}^t q_{y2} \right) r^2 + \left( \frac{^t q_{y3} - {}^t q_{y1}}{2} \right) r + {}^t q_{y2} \; r \tag{2.99b}$$

where $^t q_{xi}$ and $^t q_{yi}$ are the x and y components of total distributed load at Node i of the element (i = 1, 2, 3).

The external virtual work done by the distributed load at time $t+\Delta t$ can be expressed as

$$\delta W_q^{ext} = \sum_e \int_{{}^tL_e} \left( {}^{t+\Delta t}q_x \ \delta u + {}^{t+\Delta t}q_y \ \delta v \right) d{}^ts \tag{2.100}$$

Using the vectors of Eqs. (2.62), Equation (2.100) can be expressed in a matrix form as

$$\delta W_q^{ext} = \sum_e \langle \delta u \rangle \left( \int_{{}^tL_e} \left( {}^{t+\Delta t}q_x \{H_u\} + {}^{t+\Delta t}q_y \{H_v\} \right) d{}^ts \right) \tag{2.101}$$

Note that in the iterative solution scheme, ${}^tq_x$ and ${}^tq_y$ are used for ${}^{t+\Delta t}q_x$ and ${}^{t+\Delta t}q_y$ in the first iteration, respectively. From the second iteration onward, the latest values of ${}^{t+\Delta t}q_x$ and ${}^{t+\Delta t}q_y$ are used based on the latest pipe configuration.

## 2.8.5 Finite Element Equilibrium Equations

Based on the derivations carried out in Sections 2.8.1 to 2.8.4, the virtual work equation expressed in Eq. (2.6) can be expanded using Eqs. (2.74), (2.75), (2.79), (2.85), (2.86), (2.96), (2.97), and (2.101). This results in

$$\sum_e \langle \delta u | \left( \int_{{}^tL_e} ({}^tD_1[{}^tS_1]+{}^tD_2[{}^tS_2]+{}^tD_3[{}^tS_3])d^ts \right) \{u\} +$$

$$\sum_e 2\langle \delta u | \left( \int_{{}^tL_e} ({}^tF_1[{}^tB_1^{NL}]+{}^tF_2[{}^tB_2^{NL}]+{}^tF_3[{}^tB_3^{NL}])d^ts \right) \{u\} +$$

$$\sum_e \langle \delta u | \left( \begin{array}{l} \int_{{}^tL_e} {}^t\rho^2\, {}^tk_T \left(-{}^ty'\{H_u\}+{}^tx'\{H_v\}\right)\left(-{}^ty'\langle H_u \rangle + {}^tx'\langle H_v \rangle \right)d^ts + \\ \int_{{}^tL_e} {}^t\rho^2\, {}^tk_L \left({}^tx'\{H_u\}+{}^ty'\{H_v\}\right)\left({}^tx'\langle H_u \rangle + {}^ty'\langle H_v \rangle \right)d^ts \end{array} \right) \{u\} +$$

$$-P_0 \sum_e \langle \delta u | \left( \int_{{}^tL_e} {}^t\rho^2 \left(\{H_u'\}\langle H_u'\rangle + \{H_v'\}\langle H_v'\rangle \right)\, d^ts \right) \{u\} =$$

$$\sum_e \langle \delta u | \left( \int_{{}^tL_e} ({}^tF_1 \{{}^tB_1^L\}+{}^tF_2 \{{}^tB_2^L\})d^ts \right) + \sum_e \langle \delta u | \left( \begin{array}{l} \int_{{}^tL_e} {}^t\rho\, {}^tF_T \left(-{}^ty'\{H_u\}+{}^tx'\{H_v\}\right)d^ts + \\ \int_{{}^tL_e} {}^t\rho\, {}^tF_L \left({}^tx'\{H_u\}+{}^ty'\{H_v\}\right)d^ts \end{array} \right) +$$

$$-P_0\, {}^t\rho \left[ \left({}^tx'(L)\delta u(L)+{}^ty'(L)\delta v(L)\right)-\left({}^tx'(0)\delta u(0)+{}^ty'(0)\delta v(0)\right) \right] +$$

$$P_0 \sum_e \langle \delta u | \left( \int_{{}^tL_e} {}^t\rho^2 \left({}^tx'\{H_u'\}+{}^ty'\{H_v'\}\right)\, d^ts \right) + \sum_e \langle \delta u | \left( \int_{{}^tL_e} \left({}^{t+\Delta t}q_x\{H_u\}+{}^{t+\Delta t}q_y\{H_v\}\right)\, d^ts \right)$$

$$(2.102)$$

The incremental finite element equilibrium equations are obtained by direct assembly procedure in the global coordinate system. The integrations along the length of the elements are carried out using Gauss quadrature. A minimum of five Gauss quadrature points are required for the element to prevent rank deficiency. However, a six-point Gauss integration is recommended.

## 2.9 SPECIAL ISSUES FOR $C^1$ BEAM ELEMENT

Unlike traditional beam elements, the $C^1$ beam element does not use rotation as a degree of freedom. This makes the application of concentrated moments and modeling of fixed supports (i.e., moment constraints) not as straight-forward as they are in the case of traditional beam elements. The following subsections address these two issues.

## 2.9.1 Application of Concentrated Moment

It is not usual for a pipeline to be subjected to, and thus analyzed under, external moment loading. However, for the sake of completeness and noting that the element might be used for purposes other than pipeline analysis, this problem is discussed herein.

As Fig. 2.7 shows, a concentrated moment of M is considered to be applied at a node with an angle of inclination ${}^t\theta$ corresponding to the configuration at time t. The objective is to find the force components associated with the degrees of freedom $\dfrac{du}{ds_0}$ and $\dfrac{dv}{ds_0}$ at the node. The two equations required to obtain the two force components are derived from the following two constraints:

a) Assuming there is an infinitesimal rotation increment of $d\theta$ at the node, the sum of the work done by the two force components associated with the rotational components of $\dfrac{du}{ds_0}$ and $\dfrac{dv}{ds_0}$ must equal $Md\theta$.

b) The sum of the work done by the two force components associated with the stretching components of $\dfrac{du}{ds_0}$ and $\dfrac{dv}{ds_0}$ must be zero.

By defining stretch at time t as ${}^t\lambda = \dfrac{d^t s}{ds_0}$ then, $\dfrac{d^t x}{ds_0}$ and $\dfrac{d^t y}{ds_0}$ can be written as

$$\frac{d^t x}{ds_0} = \frac{d^t x}{d^t s}\frac{d^t s}{ds_0} = \frac{d^t x}{d^t s}\,{}^t\lambda = \cos {}^t\theta\,\,{}^t\lambda \tag{2.103a}$$

$$\frac{d^t y}{ds_0} = \frac{d^t y}{d^t s}\frac{d^t s}{ds_0} = \frac{d^t y}{d^t s}\,{}^t\lambda = \sin {}^t\theta\,\,{}^t\lambda \tag{2.103b}$$

It is assumed that the infinitesimal displacement increments occur within times t and t+dt. The corresponding increment of the degrees of freedom $\dfrac{du}{ds_0}$ and $\dfrac{dv}{ds_0}$ can be expressed using Eqs. (2.103) as

$$\frac{du}{ds_0} = \frac{d^{t+dt} x}{ds_0} - \frac{d^t x}{ds_0} = \cos {}^{t+dt}\theta\,\,{}^{t+dt}\lambda - \cos {}^t\theta\,\,{}^t\lambda = \cos({}^t\theta + d\theta)({}^t\lambda + d\lambda) - \cos {}^t\theta\,\,{}^t\lambda \tag{2.104a}$$

$$\frac{dv}{ds_0} = \frac{d^{t+dt} y}{ds_0} - \frac{d^t y}{ds_0} = \sin {}^{t+dt}\theta\,\,{}^{t+dt}\lambda - \sin {}^t\theta\,\,{}^t\lambda = \sin({}^t\theta + d\theta)({}^t\lambda + d\lambda) - \sin {}^t\theta\,\,{}^t\lambda \tag{2.104b}$$

Expanding the sin and cos terms in Eqs. (2.104) and neglecting quadratic and higher orders of infinitesimal terms result in

$$\frac{du}{ds_0} = \cos{}^t\theta \, d\lambda - \sin{}^t\theta \, {}^t\lambda \, d\theta \qquad (2.105a)$$

$$\frac{dv}{ds_0} = \sin{}^t\theta \, d\lambda + \cos{}^t\theta \, {}^t\lambda \, d\theta \qquad (2.105b)$$

It is quite obvious that in Eqs. (2.105) the stretching components of the DOFs are the first term in each equation, containing the term $d\lambda$, and the rotational components of the DOFs are the second term in each equation, containing the term $d\theta$. Using these components, the constraints (a) and (b) of the previous page result in the following two equations, respectively:

$$M_u(-\sin{}^t\theta \, {}^t\lambda \, d\theta) + M_v(\cos{}^t\theta \, {}^t\lambda \, d\theta) = M \, d\theta \qquad (2.106a)$$

$$M_u(\cos{}^t\theta \, d{}^t\lambda) + M_v(\sin{}^t\theta \, d{}^t\lambda) = 0 \qquad (2.106b)$$

where $M_u$ and $M_v$ are the force components associated with the DOFs $\dfrac{du}{ds_0}$ and $\dfrac{dv}{ds_0}$, respectively. Equations (2.106) yield $M_u$ and $M_v$ as

$${}^t M_u = -\frac{M}{{}^t\lambda} \sin{}^t\theta \qquad (2.107a)$$

$${}^t M_v = \frac{M}{{}^t\lambda} \cos{}^t\theta \qquad (2.107b)$$

At the beginning of the analysis, ${}^0\lambda = 1$, and thus, $M_u$ and $M_v$ become

$${}^0 M_u = -M \sin{}^0\theta \qquad (2.108a)$$

$${}^0 M_v = M \cos{}^0\theta \qquad (2.108b)$$

In a small-deformation analysis, the values of $M_u$ and $M_v$, as given by Eqs. (2.108), can be maintained throughout the analysis.

## 2.9.2 Fixed Supports

Figure 2.8 shows a fixed support with an angle of inclination $\alpha$ (i.e., the value of $\theta$ at the support remaining constant throughout the analysis). Unlike traditional beam

elements, neither of the two rotational DOFs (i.e., $\dfrac{du}{ds_0}$ and $\dfrac{dv}{ds_0}$) is zero at the node. However, with $d\theta$ being zero at the support, Eqs. (2.105) reduce to

$$\frac{du}{ds_0} = \cos\alpha \, d\lambda \qquad (2.109a)$$

$$\frac{dv}{ds_0} = \sin\alpha \, d\lambda \qquad (2.109b)$$

Hence,

$$\frac{du}{ds_0} = \cot\alpha \, \frac{dv}{ds_0} \qquad (2.110a)$$

$$\frac{dv}{ds_0} = \tan\alpha \, \frac{du}{ds_0} \qquad (2.110b)$$

Either of the Eqs. (2.110) can provide the constraint equation required for eliminating one of the two rotational DOFs and maintaining the other one. For $\alpha \approx 0$ or $\pi$, Eq. (2.110b) and for $\alpha \approx \dfrac{\pi}{2}$ or $\dfrac{3\pi}{2}$, Eq. (2.110a) should be used to avoid numerical difficulties. For other values of $\alpha$, either of the two equations is sufficient as the boundary constraint equation.

## 2.10 SOLUTION TECHNIQUES

Depending on the type of the main loading in an analysis, a particular solution technique is usually more appropriate than others. There are three main loading conditions considered in this study. These are:

a) applied loads
b) ground settlement
c) thermal loading

The 'ground settlement' and 'thermal loading' conditions are discussed in Chapters 4 and 5, respectively.

The applied loads are defined as loading conditions where no settlement or advanced thermal loading are involved. In short, the loading is limited to fixed internal pressure, fixed temperature differential, and varying nodal and distributed loads. The nodal and

distributed loads are varied in an *incremental-iterative* solution using an arc-length method. The arc-length solution technique adopted here is the scheme proposed by Bellini and Chulya (1987) and implemented by Zhou and Murray (1993). A description of the method is presented in the following subsections.

### 2.10.1 Incremental-Iterative Solution Procedure

A difficulty is nonlinear structural analysis is the dependence of the stiffness and internal forces on the displacements. A nonlinear finite element formulation generally ends up with the following set of equations

$$\mathbf{K}\,\mathbf{u} = \mathbf{P} - \mathbf{Q} \tag{2.111}$$

where $\mathbf{K}$ is the stiffness matrix, $\mathbf{u}$ is the nodal displacement vector, and $\mathbf{P}$ and $\mathbf{Q}$ are the external and the equilibrium force vectors, respectively. In a nonlinear analysis, $\mathbf{K}$ and $\mathbf{Q}$ depend on the displacements and stresses in the structure. When a structure reaches equilibrium, the difference between the equilibrating forces and the external loads vanishes.

Although it is possible to apply the entire external load in a single step, it is not appropriate in practical applications because iterative procedures usually do not lead to convergence for large load steps. In general, path-dependent material behavior requires small strain increments to ensure the accuracy of the prediction. Therefore, the total external load should be applied in a number of small loading steps (or increments). Such a procedure is called an *incremental procedure*. Starting from an equilibrium configuration at time t, an incremental displacement vector, $\Delta\mathbf{u}$, can be calculated by

$$^{t}\mathbf{K}\,\Delta\mathbf{u} = \Delta\mathbf{P} + {}^{t}\mathbf{P} - {}^{t}\mathbf{Q} \tag{2.112}$$

where the total external load is comprised of $^{t}\mathbf{P}$, that is already present at the beginning of the load step and a load increment $\Delta\mathbf{P}$.

In an incremental solution procedure that is non-iterative, a significant drifting of the predicted path from the true equilibrium path may occur. This is fundamentally because the linearized equations that are solved in the solution procedure are only an approximation of the original nonlinear equilibrium equations. The linearized equations, such as Eqs. (2.112), are valid, strictly speaking, at the very beginning of the loading step. Consequently, the unbalanced loads at the end of each loading step will be carried

along in all subsequent loading steps. This implies that the error will likely be accumulated and cause a significant drift. This drift can be prevented or at least significantly reduced by performing equilibrium iterations within each loading step. The resulting solution procedure is called an *incremental-iterative procedure*.

There are many incremental-iterative solution procedures, each one being appropriate for a certain type of loading and analysis. Among these solution procedures are the Newton-Raphson procedures and control techniques such as displacement and arc-length control. The advantage of the arc-length control technique over the classical Newton-Raphson procedure that the arc-length method is capable of reaching limit loads, such as buckling loads, and tracing down the postbuckling equilibrium paths by decreasing the external load when necessary. The arc-length control method, which is the basis for the solution procedure for 'applied loads', is presented in the following.

## 2.10.2 Arc-Length Control Method

One of the most robust procedures for nonlinear analysis of structures is known as *arc-length control* (Wempner, 1971, Riks, 1972, 1979, and Ramm, 1980). To describe the method, Equation (2.112) is considered as the starting point. Assuming that the solution, having converged at time t, is at iteration i+1 through the next load step, Equation (2.112) yields

$$d\mathbf{u}_{j+1} = \mathbf{K}_j^{-1} \left( \Delta\lambda_{j+1} \hat{\mathbf{P}} + {}^t\mathbf{P} - \mathbf{Q}_j \right)$$

(2.113)

where

$d\mathbf{u}_{j+1}$ = displacement correction for iteration j+1

$\mathbf{K}_j$ = stiffness matrix for the pipe configuration at iteration j

$\mathbf{Q}_j$ = equilibrating force vector for the pipe configuration at iteration j

$\hat{\mathbf{P}}$ = a reference load vector

$\Delta\lambda_{j+1}$ = a scalar load factor whose product with the reference load vector comprises the external load increment for the current load step (i.e., $\Delta\mathbf{P} = \Delta\lambda_{j+1}\hat{\mathbf{P}}$);

The relationship between the load factor increment for the load step, $\Delta\lambda_{j+1}$, and the load factor correction in the j+1$^{st}$ iteration, $d\lambda_{j+1}$, can be written as

$$\Delta\lambda_{j+1} = \Delta\lambda_j + d\lambda_{j+1}$$

(2.114)

53

Similarly, the relationship between the displacement increment for the load step, $\Delta \mathbf{u}_{j+1}$, and the displacement correction in the $j+1^{st}$ iteration, $d\mathbf{u}_{j+1}$, can be written as

$$\Delta \mathbf{u}_{j+1} = \Delta \mathbf{u}_j + d\mathbf{u}_{j+1} \qquad (2.115)$$

The essence of the arc-length control is that the displacement correction is taken to be the sum of two separate contributions. The first part, denoted by $d\mathbf{u}_{j+1}^I$, represents the contribution of the external load components that are being incremented within this load step. This contribution is defined by

$$d\mathbf{u}_{j+1}^I = \mathbf{K}_j^{-1} \hat{\mathbf{P}} \qquad (2.116)$$

The second part is the response to the unbalanced forces, that is the difference between the sum of all external loads and equilibrating forces at the end of iteration j. Denoted by $d\mathbf{u}_{j+1}^{II}$, this contribution can be expressed as

$$d\mathbf{u}_{j+1}^{II} = \mathbf{K}_j^{-1} \left( \Delta \lambda_j \hat{\mathbf{P}} + {}^t\mathbf{P} - \mathbf{Q}_j \right) \qquad (2.117)$$

From Eqs. (2.113), (2.116), and (2.117), it can be concluded that

$$d\mathbf{u}_{j+1} = d\lambda_{j+1} \, d\mathbf{u}_{j+1}^I + d\mathbf{u}_{j+1}^{II} \qquad (2.118)$$

In the arc-length control, the increment of the scalar load factor, $\Delta \lambda$, is considered as an additional variable, which is determined by an additional equation called the *constraint equation*. A very common constraint is that the Euclidean norm of the accumulated incremental displacement vector, $\Delta \mathbf{u}_{j+1}$, and the accumulate increment of the load factor, $\Delta \lambda_{j+1}$, in a load step remains constant during the load step. Hence,

$$\Delta \mathbf{u}_{j+1}^T \, \Delta \mathbf{u}_{j+1} + \Delta \lambda_{j+1}^2 = \Delta l^2 \qquad (2.119)$$

where $\Delta l$ is a prescribed reference length. Substituting Eqs. (2.114), (2.115), and (2.118) into Eq. (2.119) and ignoring second order terms result in

$$\Delta \mathbf{u}_j^T \, d\mathbf{u}_{j+1} + \Delta \lambda_j \, d\lambda_{j+1} = 0 \qquad (2.120)$$

This equation implies that the increment in iteration j+1 in the load-displacement space, $(d\mathbf{u}_{j+1}, d\lambda_{j+1})$, is perpendicular to the accumulated increment up to iteration j, $(\Delta \mathbf{u}_j, \Delta \lambda_j)$. Substituting Eq. (2.118) into Eq. (2.120) yields $d\lambda_{j+1}$ as

$$d\lambda_{j+1} = -\frac{\Delta \mathbf{u}_j^T \, d\mathbf{u}_{j+1}^{II}}{\Delta \mathbf{u}_j^T \, d\mathbf{u}_{j+1}^I + \Delta\lambda_j}$$ (2.121)

The form of equation expressed by Eq. (2.120) is called a *linear constraint equation* because of the linear relationship between the incremental load factor and the displacement increments due to the unbalanced forces. The quadratic constraint equation expressed by Eq. (2.119) is called a *spherical constraint equation* because it defines the iteration on a sphere in the load-displacement space and converges to the intersection of the sphere and the equilibrium path.

The spherical constraint equation can be generalized into a general quadratic equation as

$$\Delta \mathbf{u}_{j+1}^T \, \Delta \mathbf{u}_{j+1} + \zeta \Delta\lambda_{j+1}^2 = \Delta l^2$$ (2.122)

where $\zeta$ is a constant which allows different weights to be assigned to the values of displacement and load factor increments . When $\zeta$ equals one, Eq. (2.122) defines the spherical constraint equation. When $\zeta$ equals zero, the equation is referred to as a *cylindrical constraint equation*. For other values of $\zeta$, the equation becomes a *ellipsoidal constraint equation*.

Bellini and Chulya (1987) studied and compared these three forms of quadratic constraint equations, namely, the spherical, cylindrical, and ellipsoidal constraint equations. Based on six case studies including several benchmark problems, the cylindrical constraint equation was recommended for snap-through behavior. Moreover, it was concluded that for snap-back behavior and paths with very stiff loading and unloading, an ellipsoidal constraint equation would be more effective.

Arc-length methods might fail in cases that involve highly localized failure or bifurcation modes (de Borst, 1988) because the norm of the global displacement increment may not be sensitive enough to control highly localized displacement increments. To remedy this problem, the *indirect displacement control* technique was developed (de Borst, 1988). The basic idea of indirect displacement control is that the norm of displacement increment in the constraint equation is replaced by the norm of a weighted displacement increment. Thus, Eq. (2.122), for instance, changes to

$$\Delta \mathbf{u}_{j+1}^T \, \mathbf{W} \, \Delta \mathbf{u}_{j+1} + \zeta \Delta\lambda_{j+1}^2 = \Delta l^2$$ (2.123)

where **W** is a weighting matrix. By assigning higher weight values to certain displacement components associated with the localized failure area, the norm of the weighted displacement increment will be more sensitive to selected localized failure or bifurcation modes. Because the failure or bifurcation modes are problem-dependent, the selection of the weight matrix **W** rests on the analyst's understanding of the individual problem. As a result, the application of the indirect displacement control is limited.

## 2.10.3 Modified Arc-Length Method

The process of iteration with linear constraint equation, expressed by Eq. (2.120), is to find iteratively the intersection of a plane normal to the previous increment in the load-displacement space and the equilibrium path. If this intersection does not exist, the linearized arc-length control leads to divergence. In other cases, the size of the load step should be kept extremely small in order to achieve convergence. Therefore a better arc-length constraint equation is required to prevent the failure of the solution process associated with the linear constraint equation. The basic problem is that the linear constraint restricts only the direction of the subsequent displacement increments without limiting the magnitude of the accumulated displacement increment in the load step. This problem can be remedied by a quadratic arc-length equation.

The general form of quadratic arc-length constraint equation is defined by Eq. (2.122). Substituting Eq. (2.118) into Eq. (2.122) results in a quadratic equation in terms of the load factor increment, $d\lambda_{j+1}$, as (Zhou and Murray, 1993)

$$A\, d\lambda_{j+1}^2 + B\, d\lambda_{j+1} + C = 0 \tag{2.124}$$

where

$$A = du_{j+1}^{I}{}^{T} du_{j+1}^{I} + \zeta \tag{2.125a}$$

$$B = 2(du_{j+1}^{I}{}^{T} du_{j+1}^{II} + \Delta u_{j}{}^{T} du_{j+1}^{I} + \zeta \Delta\lambda_{j}) \tag{2.125b}$$

$$C = du_{j+1}^{II}{}^{T} du_{j+1}^{II} + 2\Delta u_{j}{}^{T} du_{j+1}^{II} + \Delta u_{j}{}^{T} \Delta u_{j} + \zeta \Delta\lambda_{j}^{2} - \Delta l^{2} \tag{2.125c}$$

In order for Eq. (2.124) to have a real root the following condition has to be satisfied

$$B^2 - 4\,A\,C \geq 0 \tag{2.126}$$

Numerical examples indicate that the above condition cannot be satisfied when the contribution of the displacement increment from unbalanced forces, $du_{j+1}^{I}$, is significantly greater than the contribution from reference load, $du_{j+1}^{II}$. To prevent the failure of the solution process, a relaxation factor $\beta$ is introduced into Eq. (2.118) as

$$du_{j+1} = d\lambda_{j+1}\, du_{j+1}^{I} + \beta\, du_{j+1}^{II} \qquad 0 \leq \beta \leq 1 \tag{2.127}$$

Mathematically, the relaxation factor is used to satisfy the condition in Eq. (2.126). The physical interpretation of the relaxation factor, $\beta$, is that only a fraction of the unbalanced forces are considered in some of the iterations. In other words, an iterative procedure based on Eq. (2.127) is one where the unbalanced forces are applied partly. This usually increases the number of iterations, however, the stability of the iterative process can be improved. Substituting Eq. (2.127) into Eq. (2.122) gives

$$B = 2(\beta du_{j+1}^{I}{}^{T}\, du_{j+1}^{II} + \Delta u_{j}{}^{T}\, du_{j+1}^{I} + \zeta \Delta \lambda_{j}) \tag{2.128a}$$

$$C = \beta^{2} du_{j+1}^{II}{}^{T}\, du_{j+1}^{II} + 2\,\beta \Delta u_{j}{}^{T}\, du_{j+1}^{II} + \Delta u_{j}{}^{T}\, \Delta u_{j} + \zeta \Delta \lambda_{j}^{2} - \Delta l^{2} \tag{2.128b}$$

With a proper value for $\beta$, the real roots of Eq. (2.124) can be solved as

$$\alpha_{1,2} = \frac{-B \pm \sqrt{B^{2} - 4\,A\,C}}{2\,A} \tag{2.129}$$

Only one of the two roots can be chosen as the load factor increment. The following criterion is utilized for this selection (Bellini and Chulya, 1987).

$$d\lambda_{j+1} = \alpha_{1} \quad \text{if} \quad \Delta u_{j}\,(\alpha_{2}\, du_{j+1}^{I} + \beta du_{j+1}^{II}) < \Delta u_{j}\,(\alpha_{1}\, du_{j+1}^{I} + \beta du_{j+1}^{II}) \tag{2.130a}$$

$$d\lambda_{j+1} = \alpha_{2} \quad \text{if} \quad \Delta u_{j}\,(\alpha_{1}\, du_{j+1}^{I} + \beta du_{j+1}^{II}) < \Delta u_{j}\,(\alpha_{2}\, du_{j+1}^{I} + \beta du_{j+1}^{II}) \tag{2.130b}$$

The acceptable range for the relaxation factor $\beta$ is determined by substituting A, B, and C, defined in Eqs. (2.128) into Eq. (2.126) and setting it equal to zero. This results in the following quadratic equation in terms of the relaxation factor $\beta$.

$$D\,\beta^{2} + E\,\beta + F = 0 \tag{2.131}$$

where

$$D = (du_{j+1}^{I}{}^{T}\, du_{j+1}^{II})^{2} - 2(du_{j+1}^{I}{}^{T}\, du_{j+1}^{I})(du_{j+1}^{II}{}^{T}\, du_{j+1}^{II}) - \zeta du_{j+1}^{II}{}^{T}\, du_{j+1}^{II} \tag{2.132a}$$

$$E = 2\,(\Delta \mathbf{u}_j^{\mathrm{T}}\, d\mathbf{u}_{j+1}^{\mathrm{I}})(d\mathbf{u}_{j+1}^{\mathrm{I}}{}^{\mathrm{T}}\, d\mathbf{u}_{j+1}^{\mathrm{II}}) + 2\,\zeta\,\Delta\lambda_j\,(d\mathbf{u}_{j+1}^{\mathrm{I}}{}^{\mathrm{T}}\, d\mathbf{u}_{j+1}^{\mathrm{II}})$$
$$- 2\,(d\mathbf{u}_{j+1}^{\mathrm{I}}{}^{\mathrm{T}}\, d\mathbf{u}_{j+1}^{\mathrm{I}})(\Delta\mathbf{u}_j^{\mathrm{T}}\, d\mathbf{u}_{j+1}^{\mathrm{II}}) - 2\,\zeta\,\Delta\mathbf{u}_j^{\mathrm{T}}\, d\mathbf{u}_{j+1}^{\mathrm{II}} \tag{2.132b}$$

$$F = (\Delta\mathbf{u}_j^{\mathrm{T}}\, d\mathbf{u}_{j+1}^{\mathrm{I}} + \zeta\,\Delta\lambda_j)^2 - (d\mathbf{u}_{j+1}^{\mathrm{I}}{}^{\mathrm{T}}\, d\mathbf{u}_{j+1}^{\mathrm{I}} + \zeta)(\Delta\mathbf{u}_j^{\mathrm{T}}\,\Delta\mathbf{u}_j + \zeta\,\Delta\lambda_j^2 - \Delta l^2) \tag{2.132c}$$

Equation (2.131) is guaranteed to have real roots because $B^2 - 4\,A\,C \geq 0$ is always satisfied. This can be proved as follows. Using Eq. (2.109), the second term in Eq. (2.132c) vanishes and $F \geq 0$ under all conditions. The first term in Eq. (2.132a) can be expressed as

$$(d\mathbf{u}_{j+1}^{\mathrm{I}}{}^{\mathrm{T}}\, d\mathbf{u}_{j+1}^{\mathrm{II}})^2 = (d\mathbf{u}_{j+1}^{\mathrm{I}}{}^{\mathrm{T}}\, d\mathbf{u}_{j+1}^{\mathrm{I}})(d\mathbf{u}_{j+1}^{\mathrm{II}}{}^{\mathrm{T}}\, d\mathbf{u}_{j+1}^{\mathrm{II}})\cos^2\theta \tag{2.133}$$

where $\theta$ is the angle between vectors $d\mathbf{u}_{j+1}^{\mathrm{I}}$ and $d\mathbf{u}_{j+1}^{\mathrm{II}}$, and $\zeta$ is a positive number. Therefore, D is always a non-positive number. Consequently, the condition $E^2 - 4\,D\,F \geq 0$ is satisfied all the time. Thus, the real roots of Eq. (2.131) are

$$\beta_{1,2} = \frac{-E \pm \sqrt{E^2 - 4\,D\,F}}{2\,E} \tag{2.134}$$

where $\beta_1 \leq 0$ and $\beta_2 \geq 0$. Since the condition in Eq. (2.126) is satisfied when the value of $\beta$ is between these two roots, the acceptable range for $\beta$ can be expressed as

$$0 \leq \beta \leq \beta_{\max} \tag{2.135}$$

where
$$\beta_{\max} = \min(1, \beta_2) \tag{2.136}$$

It is very difficult to develop a universal method to choose a generally applicable value of reference arc-length, $\Delta l$, because the optimum value depends on the response of the structure in its current state. Therefore, the reference arc-length, $\Delta l$, should be adjusted as iteration proceeds to achieve maximum efficiency. The automatic adjustment proposed by Zhou and Murray (1993) is implemented in this work:

$$\Delta l_{\mathrm{new}} = \sqrt[4]{\frac{N_{\mathrm{opt}}}{N_{\mathrm{old}}}}\,\Delta l_{\mathrm{old}} \tag{2.137}$$

where $\Delta l_{\mathrm{old}}$ and $\Delta l_{\mathrm{new}}$ are the arc length for the previous and current load step, respectively, $N_{\mathrm{opt}}$ is the optimal number of iterations (prescribed), and $N_{\mathrm{old}}$ is the number of iterations for the previous load step.

Note that a good initial value of the reference arc-length is hard to obtain for a new problem to be analyzed. Thus, there may be a situation where the iterative procedure converges very slowly, or does not converge within the specified maximum number of iterations. In these cases, the reference arc-length is reduced by a factor of 0.3 to 0.5, and the iterative procedure is restarted from the previous equilibrium configuration.

## 2.10.4 Loading Criterion

The loading criterion is particularly important for the predictive iteration (j = 0) in the loading step. At the beginning of the loading step, $du_{j+1}^{ll}$, $\Delta u_j$, and $\Delta \lambda_j$ are zero and Eq. (2.129) gives

$$\alpha_{1,2} = \pm \frac{\Delta l}{\sqrt{du_1^{1^T} du_1^1 + \zeta}} \tag{2.138}$$

In order to determine which root should be used, the criterion in Eqs. (2.130) cannot be utilized because the accumulated displacement increment in the load step is zero for the predictive iteration. The displacement increment for the predictive iteration can be expressed as

$$\Delta u_1 = \Delta \lambda_1 \, du_1^1 \tag{2.139}$$

where $\Delta \lambda_1$ is one of the two roots expressed by Eq. (2.138). The direction of the displacement increment depends on the loading criterion that is yet to be determined.

The loading criterion is established based on the fact that the main loading system, represented by the reference loads, always does positive work on the increments of the principal deformation pattern. The only exception to this rule is in a snap-back behavior, which can be distinguished from elastic unloading by checking the positive-definiteness of the tangent stiffness matrix. In general, the tangent stiffness matrix is positive-definite for elastic unloading, and is not positive-definite for a snap-back. The loading criterion is established such that the structure remains in a state of loading along the entire equilibrium path. This leads to the following loading criterion.

$$\Delta \lambda_1 = \alpha_1 \qquad \text{if } \left( \hat{P}^T \, du_1^1 > 0 \quad \text{and} \quad NPE = 0 \right) \tag{2.140a}$$

$$\Delta \lambda_1 = \alpha_2 \qquad \text{if } \left( \hat{P}^T \, du_1^1 > 0 \quad \text{and} \quad NPE > 0 \right) \tag{2.140b}$$

$$\Delta\lambda_1 = \alpha_2 \qquad \text{if } \hat{\mathbf{P}}^T \, d\mathbf{u}_1^1 < 0 \tag{2.140c}$$

where $\hat{\mathbf{P}}$ is the reference load and NPE is the *number of negative pivot elements* in the diagonalized tangent stiffness matrix.

For iterations subsequent to the predictive (i.e., the first) iteration, the state of loading is ensured by the selection criterion expressed in Eqs. (2.130).

## 2.10.5 Convergence Criteria

Two convergence criteria are implemented to ensure that the solution is closely following the equilibrium path. These are the displacement and force criteria. In displacement criterion, the convergence of the iteration is measured by the ratio of the norm of the displacement increment at iteration j to the norm of the accumulated displacement increment up to iteration j. This can be expressed as

$$\frac{\left\|d\mathbf{u}_j\right\|}{\left\|\Delta\mathbf{u}_j\right\|} \le \xi_d \tag{2.141}$$

where $\xi_d$ is a specified displacement tolerance. A typical value of $\xi_d$ is about 0.001 in the elastic ascending region, but can be relaxed somewhat in the region with significant nonlinearity and in the post-peak region.

The force convergence criterion adopted in this study can be expressed as

$$\frac{\left\|\Delta\mathbf{U}\right\|}{\left\|\hat{\mathbf{P}}\right\|} \le \xi_f \tag{2.142}$$

where $\Delta\mathbf{U}$ is the vector of unbalanced forces and $\xi_f$ is a specified force tolerance. The recommended value for $\xi_f$ is 0.01, but can be relaxed somewhat in the regions where solution has difficulty to converge.

## 2.11 DEVELOPMENT OF PROGRAM ABP

A computer program has been developed based on the finite element formulation of pipeline-beam element using the $C^1$ beam element. This program, called ABP (Analysis of Buried Pipe), and was written in FORTRAN 90 language. This program has evolved from a program by the same name (ABP) developed by Zhou and Murray (1993).

However, due to many limitations of the original program, such as its data structure, many subroutines have been rewritten and the language was upgraded from FORTRAN 77 to FORTRAN 90. Moreover, the implementation of the formulations presented in this study required a substantial amount of code to be added to the program.

The program ABP can perform either as an stand-alone tool or as an analysis engine for the program ABPipe, which is an integrated analysis system with user-friendly preprocessor and postprocessor. The ABPipe program was developed at the University of Alberta and was partially sponsored by the pipeline industry.

The program ABP is capable of analyzing pipelines under applied loads, ground settlement, and thermal buckling analysis. Analysis under applied loads was described in this chapter. The ground settlement and thermal buckling analysis, as well as fundamental issues such as pipe-soil interaction and elastic-plastic material model, are discussed in the future chapters.

## 2.12 NUMERICAL EXAMPLES

In order to verify the implementation of the $C^1$ beam element and to illustrate the performance of the arc-length control solution procedure, two numerical examples are presented in this section.

The elastic buckling of cantilever pipes is modeled in both examples. The pipes are subjected to a concentric axial load, which is applied in the analysis as a reference load. The examples are an approximation of the classical *elastica* problem, where an inextensible, flexible elastic bar is subjected to an axial load. The main difference between the finite-element models and the classical elastica is that in the finite-element models, the pipe beam is extensible. However, the axial stiffness of the pipes in the numerical examples is much greater than the bending stiffness of the pipes. Thus, except for the advanced stages of the load-deformation response, similar load-deformation characteristics are expected from the finite-element and classical solutions. Therefore, the responses from the two solutions can be compared together.

### 2.12.1 Example One

Figure 2.9 shows the layout of the pipe considered in this example. The pipe is 324 mm in diameter, 6.35 mm in wall thickness and 1500 mm in length. The model

consists of three 500-mm elements and seven nodes as shown in Fig. 2.9. The pipe is fixed at one end (i.e. all the DOFs constrained) and free at the other end, where the axial load is applied. The pipe is assumed to be elastic with an elastic modulus of 200,000 MPa. Since this is a buckling problem being analyzed by a finite-element procedure, an initial imperfection needs to be applied to the model. To that purpose, the pipe is assumed to have an out-of-straightness rising linearly from zero at the fixed end to 0.01 mm at the free end of the model.

Some of the analysis results are presented in Figs. 2.10, 2.11, and 2.12, where the analytical results are compared to those of the classical closed-form solution by Timoshenko (1936). Figures 2.10 and 2.11 show the load vs. the end *axial* displacement response and the load vs. the end *transverse* displacement response, respectively. Figure 2.12 shows the deformed shape of the pipe obtained from the analysis for different values of $\frac{P}{P_{cr}}$ throughout the response. Here P is the axial load applied to the model and $P_{cr}$ is the Euler buckling load given by

$$P_{cr} = \frac{\pi^2\,EI}{4\,L^2} \tag{2.143}$$

It should be noted that the pipe deformed shapes in Fig. 2.12 are generated by connecting the nodes with straight lines. Thus, unlike their representations in the figure, the actual deformed shapes are smooth.

As Figures 2.10 and 2.11 show, there is a good agreement between the two solutions, especially at the earlier stages of the response. However, at the later stages of the response, the two solutions start to separate somewhat. This is due to the fact that, later on in the finite-element solution, the axial deformation of the pipe becomes significant. Whereas, as mentioned above, the classical solution does not account for the axial deformation of the pipe.

### 2.12.2 Example Two

Example 2 has been devised with the motivation to investigate the effect of increasing the axial stiffness of the pipe relative to the bending stiffness. To that aim, while the pipe cross-section of Example 1 is a realistic one used in the industry, a hypothetical cross-section is assumed for this example. An outside diameter of 200 mm

and thickness of 100 mm are assumed in Example 2. The only difference between the two examples is in cross-sectional geometry. Thus, Example 2 has the same layout and boundary conditions as those of Example 1

In the finite element formulation, the integration over the cross-section is performed as if the entire area of the cross-section is concentrated on the midline of the pipe cross-section. Therefore, the section properties as considered by the formulation, and hence, the computer program ABP, are as follows.

$$A = 2\pi R_m t = 2\pi(50)(100) \tag{2.144a}$$

$$I = \pi R_m^3 t = \pi(50)^3(100) \tag{2.144b}$$

Where A is the cross-sectional area, $R_m$ is the radius of the cross-section midline, I is the moment of inertia, and t is the pipe thickness.

In order to have a measure of the axial stiffness of the pipes relative to their bending stiffness, the following non-dimensional ratio is introduced.

$$\kappa = \frac{\dfrac{EA}{L}}{\dfrac{3EI}{L^3}} = \frac{AL^2}{3I} \tag{2.145}$$

This ratio has a value of 59.5 for Example 1 and a value of 600 for Example 2. Therefore, the objective of having a higher relative axial stiffness is met by the choice of the cross-section for Example 2.

The results for Example 2 are presented in Figs. 2.13, 2.14, and 2.15, where the analytical results are compared to those of the classical closed-form solution. Figures 2.13 and 2.14 show the load vs. the end axial displacement response and the load vs. the end transverse displacement response, respectively. Figure 2.15 shows the deformed shape of the pipe obtained from the analysis for different values of $\dfrac{P}{P_{cr}}$ throughout the response.

As Figures 2.13 and 2.14 show, there is a good agreement between the analytical and classical solutions throughout the response. This is in contrast to the response of Example 1 where, at the later stages of the response, the analytical solution departs from

the classical solution. Thus, as expected, the increase in the relative axial stiffness, which brings the model closer to the assumption of inextensibility, results in better agreement with the classical elastica solution.

As Figure 2.12 and 2.15 indicate, the finite element solution is able to represent the large deformation and large strain response of the pipe using a relatively coarse mesh. The large bending deformation is especially noted for the first element (that attached to the fixed support) at the $\frac{P}{P_{cr}}$ value of 16.2 in Fig. 2.12 and 18.5 in Fig. 2.15. A significant stretching of the pipe is also evident for the deformed shape corresponding to the $\frac{P}{P_{cr}}$ value of 16.22 in Fig. 2.12.

## 2.13 DESCRIPTION OF DERIVATIVE DEGREES OF FREEDOM

The derivative DOFs, $\frac{du}{ds_0}$ and $\frac{dv}{ds_0}$, are functions of the rotation and stretch at a given node. This is demonstrated in the following.

Using the chain rule and noting that ${}^t u = {}^t x - {}^0 x$, the derivative $\frac{d^t u}{ds_0}$ can be expressed as

$$\frac{d^t u}{ds_0} = \frac{d^t u}{d^t s} \frac{d^t s}{ds_0} = \left( \frac{d^t x}{d^t s} - \frac{d^0 x}{d^t s} \right) \frac{d^t s}{ds_0} = \left( \cos {}^t \theta - \cos {}^0 \theta \right) \frac{d^t s}{ds_0} \qquad (2.146)$$

Similarly, the derivative $\frac{d^t v}{ds_0}$ can be expressed as

$$\frac{d^t v}{ds_0} = \frac{d^t v}{d^t s} \frac{d^t s}{ds_0} = \left( \frac{d^t y}{d^t s} - \frac{d^0 y}{d^t s} \right) \frac{d^t s}{ds_0} = \left( \sin {}^t \theta - \sin {}^0 \theta \right) \frac{d^t s}{ds_0} \qquad (2.147)$$

It is evident from Eqs. (2.146) and (2.147) that the derivative DOFs, $\frac{d^t u}{ds_0}$ and $\frac{d^t v}{ds_0}$, are each a function of the rotation, ${}^t \theta$, and the stretch, $\frac{d^t s}{ds_0}$ (note that $s_0 \equiv {}^0 s$), at a given node. Furthermore, it can be seen that the choice of $\frac{d^t u}{d^t s}$ and $\frac{d^t v}{d^t s}$ as the derivative

DOFs would not have been viable because both $\dfrac{d^t u}{d^t s}$ and $\dfrac{d^t v}{d^t s}$ are functions of the rotation only, and thus dependent.
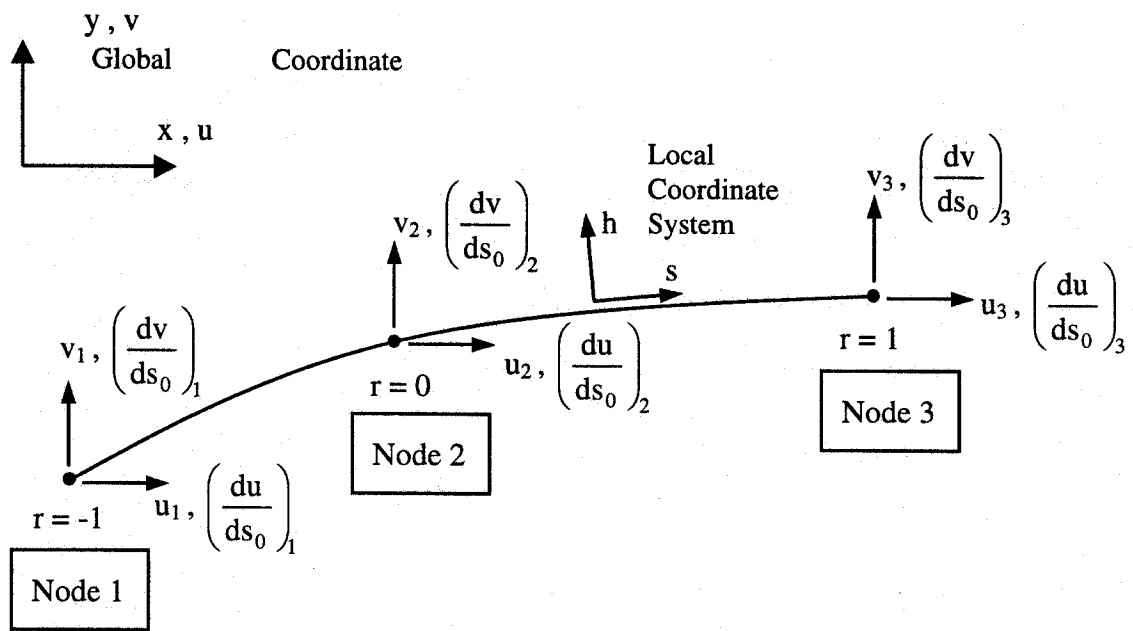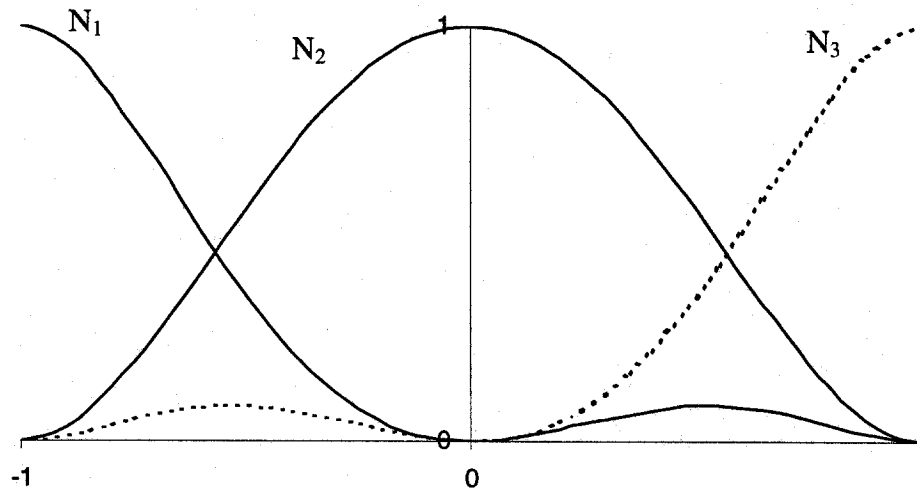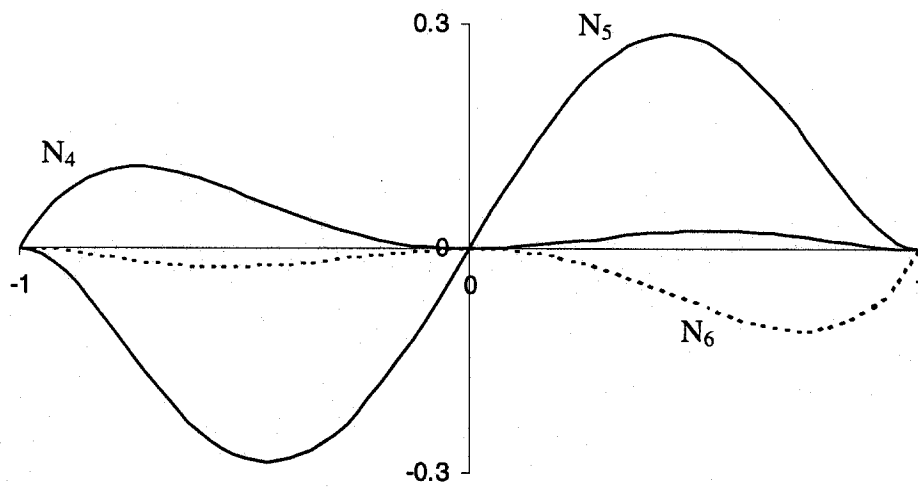
Fig. 2.1  Element Nodes and DOFs

(a) Hermitian Shape Functions $N_1$, $N_2$, and $N_3$



(b) Hermitian Shape Functions $N_4$, $N_5$, and $N_6$

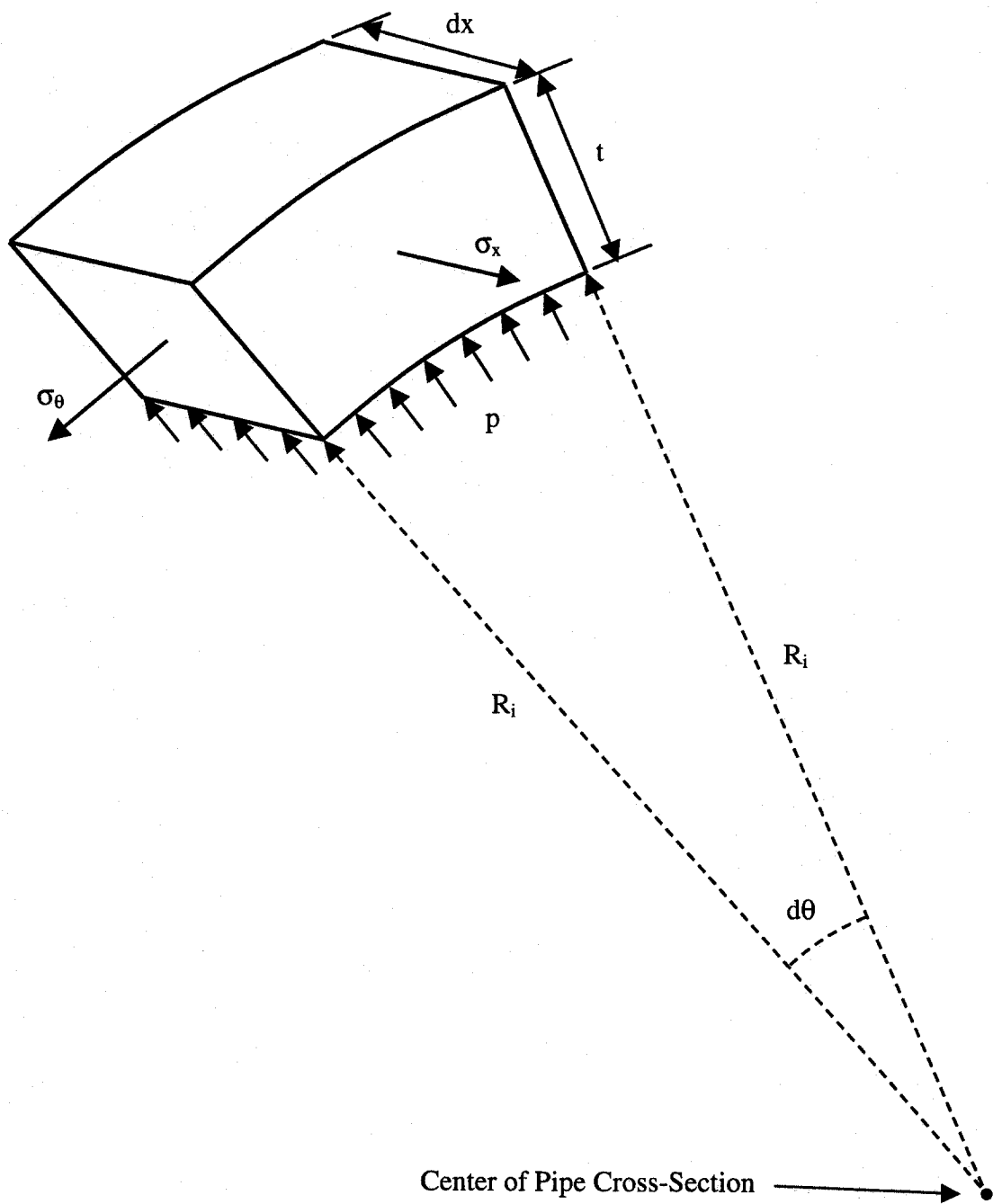Fig. 2.2 Fifth Order Hermitian Shape Functions
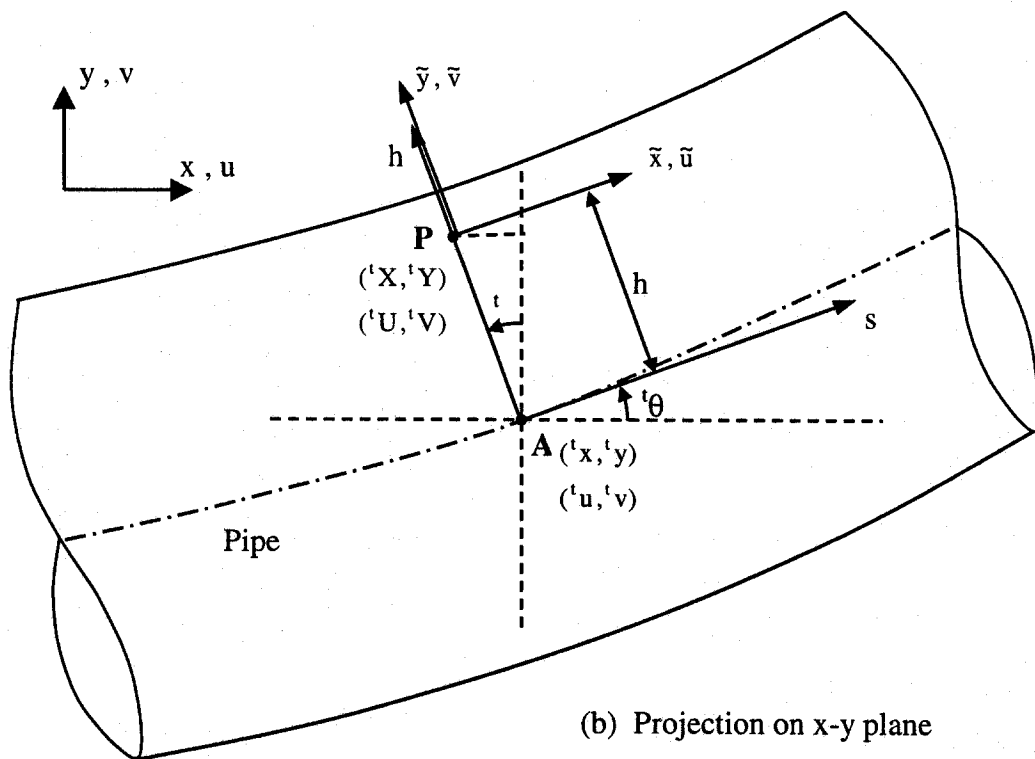
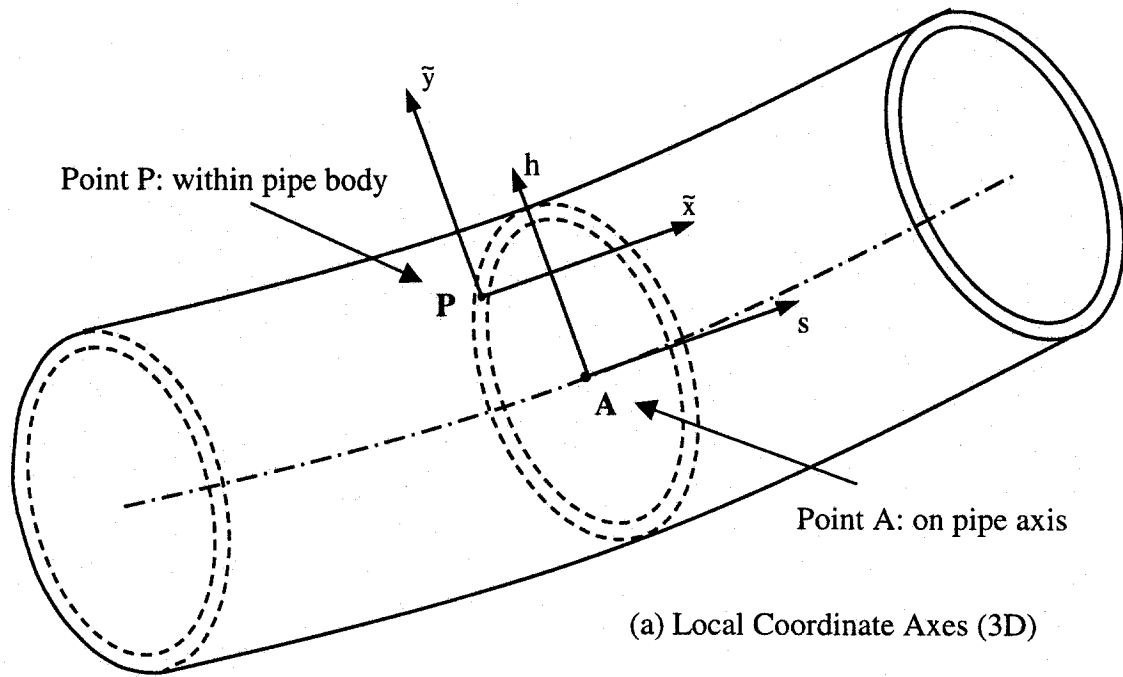Fig. 2.3  An Infinitesimal Element of Pipe

Point P: within pipe body

$\tilde{y}$

h

$\tilde{x}$

P

s

A

Point A: on pipe axis

(a) Local Coordinate Axes (3D)

y , v

x , u

$\tilde{y}, \tilde{v}$

h

$\tilde{x}, \tilde{u}$

P

$({}^{t}X, {}^{t}Y)$

$({}^{t}U, {}^{t}V)$

t

h

s

${}^{t}\theta$

A $({}^{t}x, {}^{t}y)$

$({}^{t}u, {}^{t}v)$

Pipe

(b) Projection on x-y plane

Fig. 2.4 Pipe Geometry at Time t: Material point P vs. Axis point A
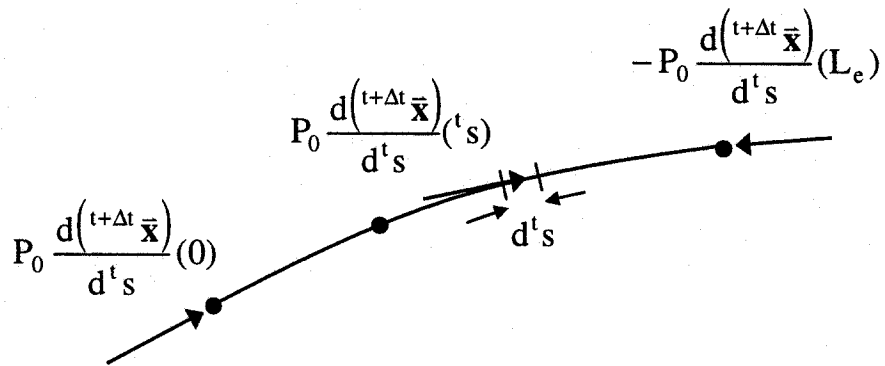
69
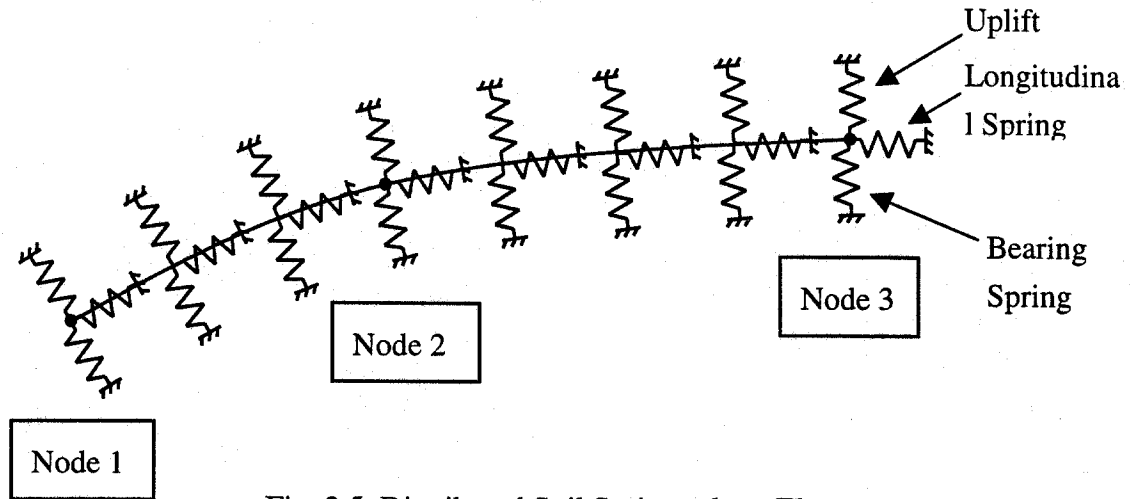
Fig. 2.5 Distributed Soil Springs along Element



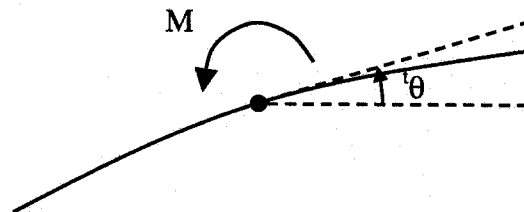Fig. 2.6 Force Components of Eq. (2.89) along Element



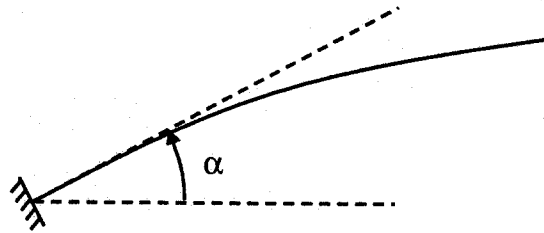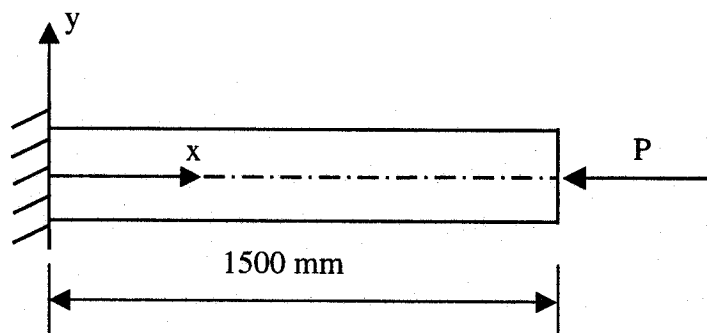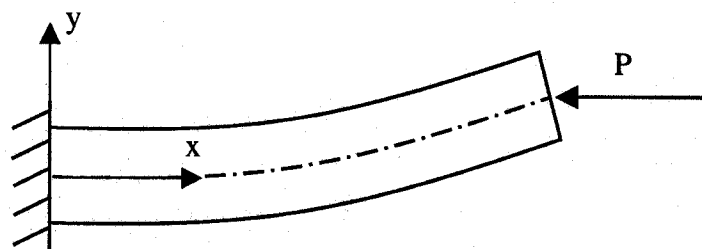Fig. 2.7 Concentrated Moment Applied at a Node

Fig. 2.8 Fixed Support with Angle of inclination α



(a) Initial Layout



(b) Deformed Shape

Fig. 2.9 Layout of Elastic Cantilever Pipe of Examples 1 & 2

71

Fig. 2.10 Load vs. End Axial Displacement for Example 1
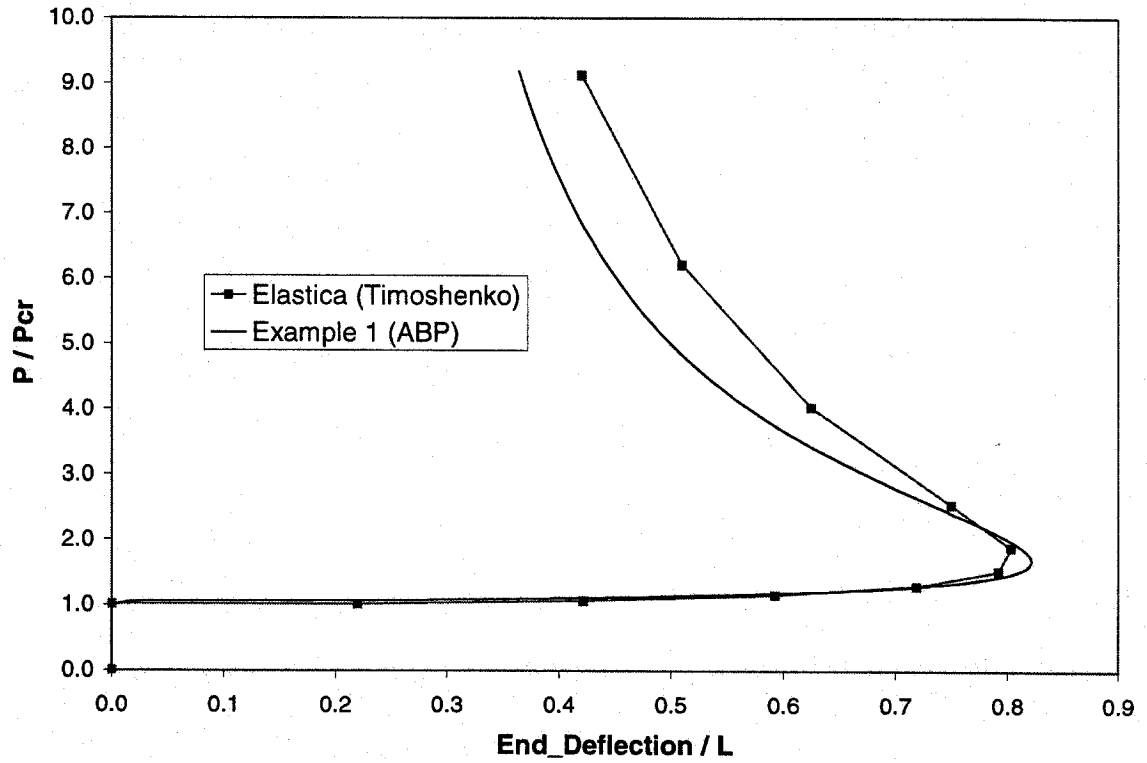


Fig. 2.11 Load vs. End Transverse Displacement for Example 1

72

The value next to each curve is the corresponding P / Pcr

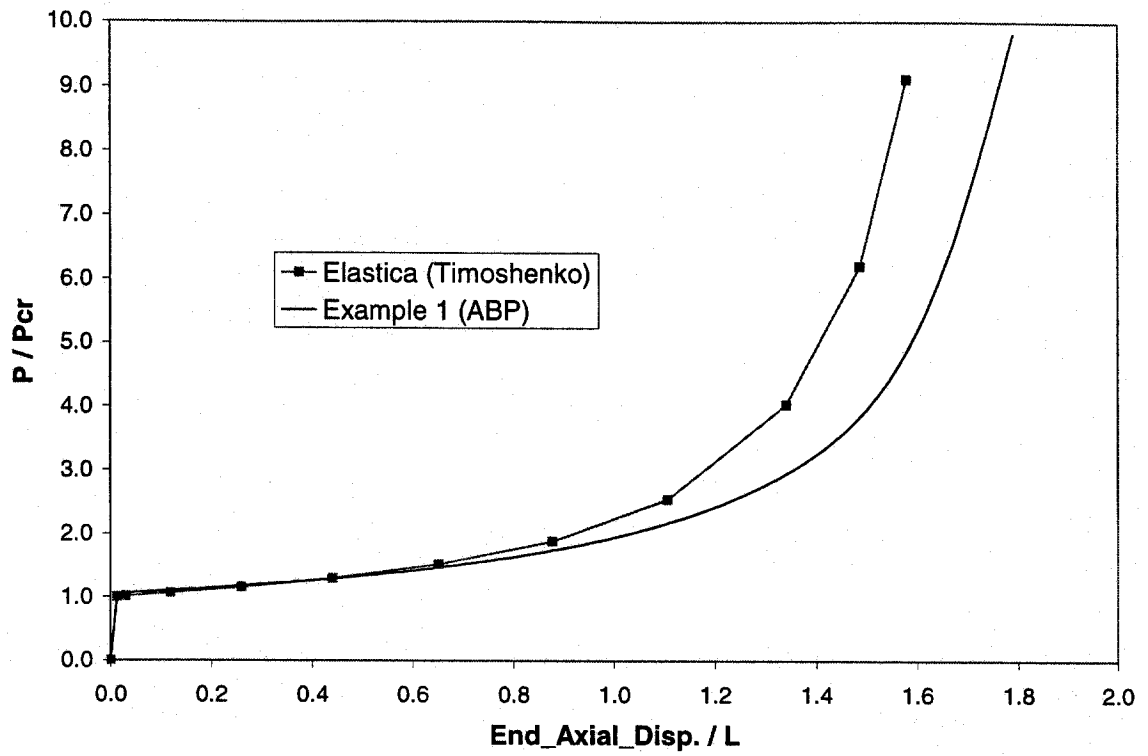Fig. 2.12 Deformed Shapes of Cantilever Pipe of Example 1 for Different Values of P / Pcr

73

Fig. 2.13  Load vs. End Axial Displacement for Example 2



Fig. 2.14  Load vs. End Transverse Displacement for Example 2

**The value next to each curve is the corresponding P / Pcr**
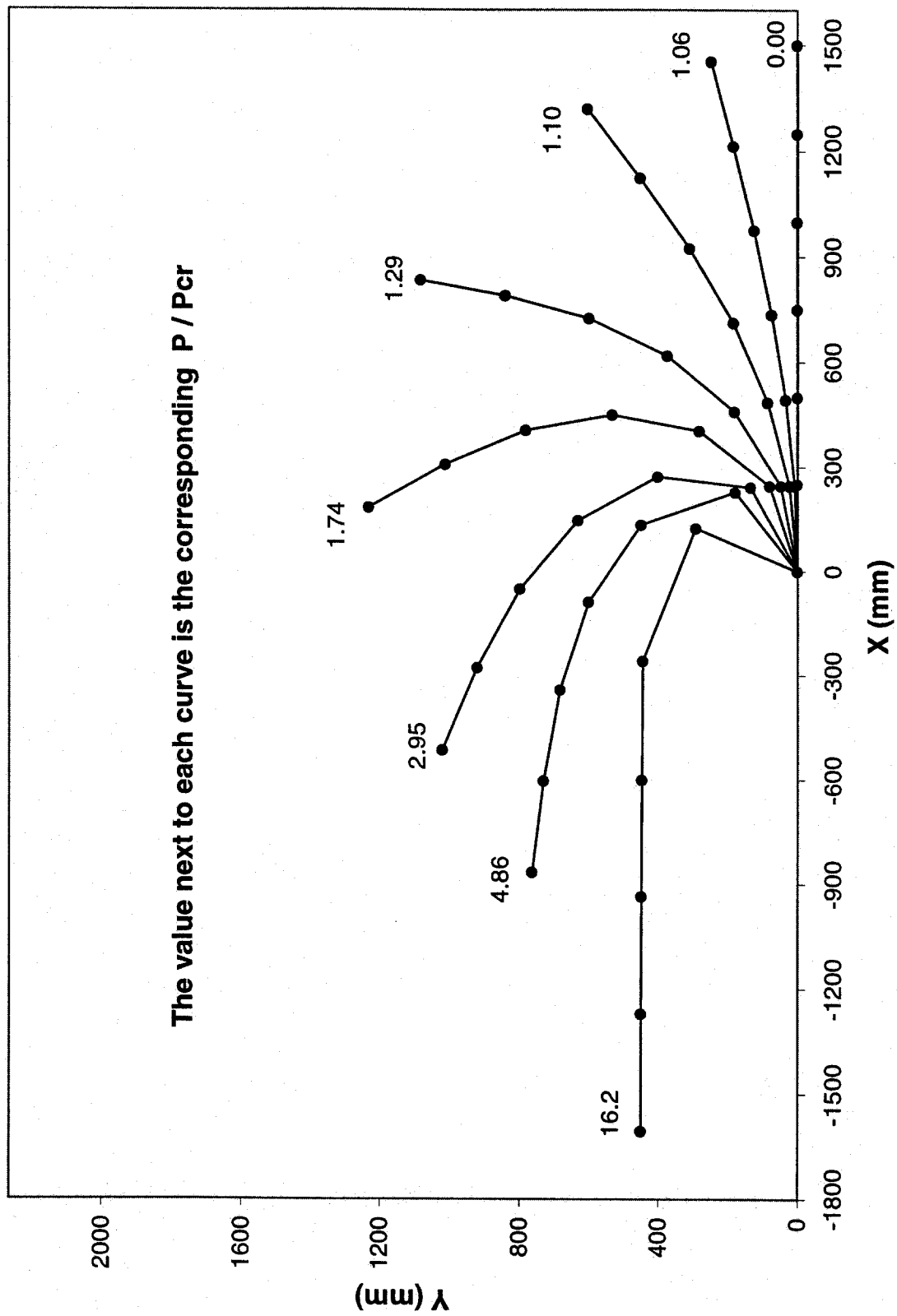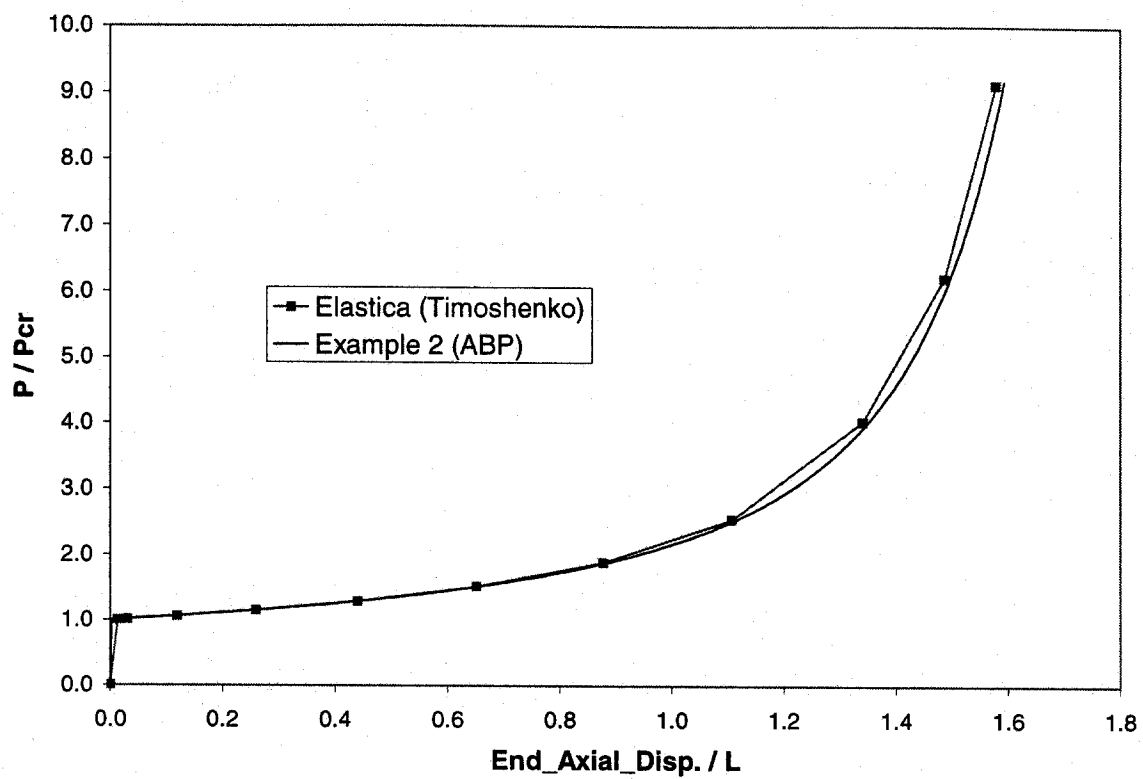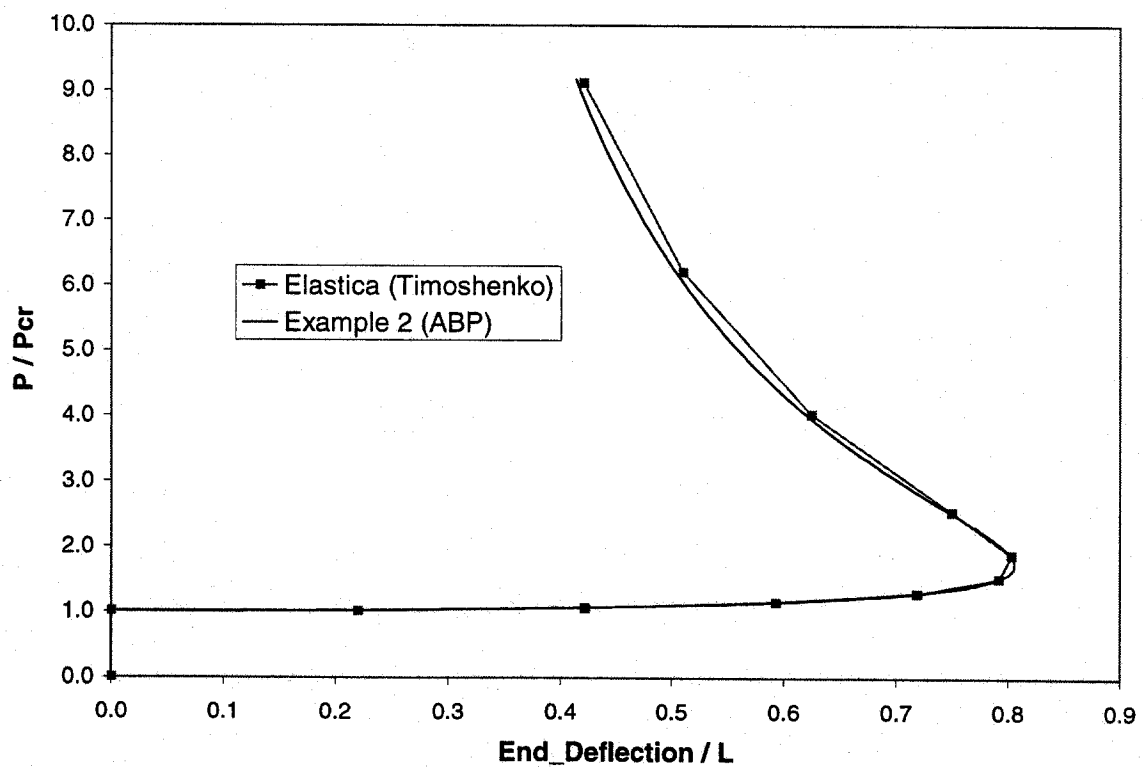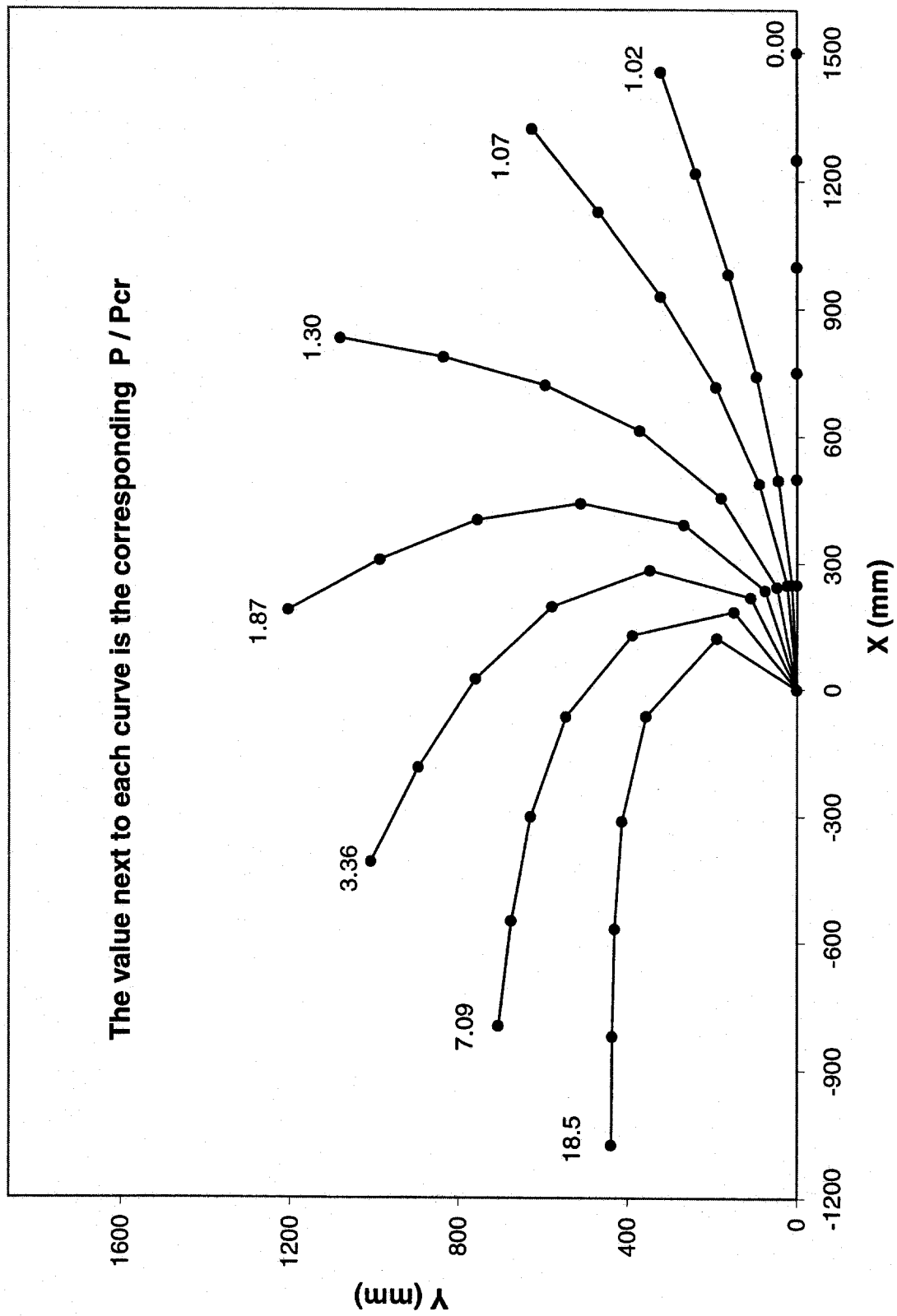
Fig. 2.15 Deformed Shapes of Cantilever Pipe of Example 2 for Different Values of P / Pcr

75

# CHAPTER 3. CONSTITUTIVE RELATIONSHIPS FOR PIPE MATERIAL

## 3.1 INTRODUCTION

This chapter describes the elastic-plastic material model developed for the finite element formulation. The plasticity formulation is presented after a discussion on the choices of stress and strain. The formulation utilizes the von Mises yield criterion which is widely used for steel. The material strain hardening is accounted for using a combination of isotropic and kinematic strain hardening. This chapter ends with a discussion on how the constitutive relationships fit into the updated Lagrangian formulation presented in the previous chapter.

## 3.2 THE CHOICE OF STRESS AND STRAIN MEASURES

The stress and strain measures employed in the elastic-plastic formulation must be work-conjugate. This means that their product can be used to evaluate the internal work in a given body. There are several work-conjugate pairs of stress and strain. The three most common pairs are the engineering stress and engineering strain, the 2nd Piola-Kirchhoff stress and Green-Lagrange strain, and Cauchy (true) stress and logarithmic (true) strain. As described in Sec. 2.3, the 2nd Piola-Kirchhoff stress and Green-Lagrange strain measures have been chosen in this study. Moreover, due to the choice of an updated Lagrangian formulation, the 2nd Piola-Kirchhoff stress and Green-Lagrange strain are measured with respect to the latest equilibrium configuration.

A formulation based on true stress and true strain is effective in large strain analysis because the stress and strain measures used are those that describe the material response in a natural way (Bathe 1982). True stress and logarithmic strain measures are commonly used for problems in metal plasticity. One motivation for this choice is that when true stress (force per current unit area) is plotted against logarithmic strain, the tension, compression, and torsion test results coincide closely with each other (Hibbit et al. 1993a). Since Cauchy (true) stress and logarithmic (true) strain measures result in a material response which is independent of the mode of loading, they are the best choice for developing the constitutive relationships. Thus, the stress and strain measures used in the following section are true stress and strain measures.

## 3.3 ELASTIC-PLASTIC FORMULATION

In the following subsections, first the fundamentals of the plasticity formulation are presented. Thereafter the necessary constitutive equations are derived and fine-tuned for the finite element formulation presented in this study.

Following the conclusion of Section 3.2, in the subsequent derivations, $\sigma_{ij}$ and $\varepsilon_{ij}$ represent Cauchy (true) stress and logarithmic (true) strain, respectively.

### 3.3.1 Fundamentals of Elastic-Plastic Formulations

The fundamentals of elasto-plasticity formulation employed in this model, and discussed below, have been mostly adapted from the book by Chen and Han (1988). These include discussions on yield function, hardening rule, plastic potential and flow rule, and consistency condition.

#### 3.3.1.1 Yield Function

The yield function determines the elastic limits of a material under a combined state of stress. The yield stress is, in general, a function of the state of stress, $\sigma_{ij}$, and can be expressed as

$$f(\sigma_{ij}, k) = 0 \tag{3.1}$$

where k is a hardening parameter. The yield function can be represented geometrically as a surface in stress space. For a perfectly plastic material, the yield function remains unchanged. Thus, the parameter k in Eq. (3.1) is a constant, and the yield surface is hence fixed in the stress space. For a work-hardening material, however, the yield surface changes as elastic-plastic deformation occurs.

#### 3.3.1.2 Hardening Rule

With the initial yield surface known, the work hardening rule defines its modification during the process of plastic flow. A number of hardening rules can be found in the literature. The most widely used are the isotropic hardening rule, the kinematic hardening rule, and a combination of both, the *mixed hardening* rule.

The isotropic hardening rule is based on the assumption that the initial yield surface expands uniformly without translation or distortion in the stress space as plastic

77

deformation occurs. The size of the yield surface is governed by the value of the parameter k, which depends upon plastic strain history.

The kinematic hardening rules assume that, during the plastic flow, the loading surface translates in stress space, maintaining the size, shape, and orientation of the initial surface. This rule is implemented by keeping k constant and replacing the stress tenor, $\sigma_{ij}$, in Eq. (3.1) with the reduced stress tensor, $\bar{\sigma}_{ij}$. Reduced stress components are measured from the center of the yield surface:

$$\bar{\sigma}_{ij} = \sigma_{ij} - \alpha_{ij} \tag{3.2}$$

where $\alpha_{ij}$ are the coordinates of the yield surface center in the stress space, and they depend on the plastic strain history.

A combination of isotropic and kinematic hardening results in the more general mixed hardening rule (Hodge, 1957). Here the yield surface undergoes a translation defined by $\alpha_{ij}$ and a uniform expansion measured by k. This establishes a more general work hardening, which contains the isotropic and kinematic hardening rules as its two bounds.

Detailed discussion on the contribution of the isotropic and kinematic strain hardening in the mixed hardening model is presented in Section 3.3.2. Further description of the kinematic hardening rule can be found in Section 3.3.3.

The kinematic and mixed-hardening rules are normally used for load reversal and cyclic loading conditions. In a monotonic loading condition, as is the main focus of this study, the isotropic hardening rule suffices. Thus, in all of the examples presented in this work, the isotropic hardening rule has been adopted.

### 3.3.1.3 Elastic and Plastic Strain Increment Tensors

A basic assumption for an elastic-plastic deformation is that the total strain increment tensor, $d\varepsilon_{ij}$, consists of the sum of the elastic and plastic strain increment tensors:

$$d\varepsilon_{ij} = d\varepsilon_{ij}^e + d\varepsilon_{ij}^p \tag{3.3}$$

where $d\varepsilon_{ij}^e$ and $d\varepsilon_{ij}^p$ are the elastic and plastic strain increment tensors, respectively.

Hooke's law is assumed to provide the necessary relationship between the incremental changes of stress and elastic strain; thus,

$$d\sigma_{ij} = C_{ijkl} \, d\varepsilon_{kl}^e \qquad (3.4)$$

where $C_{ijkl}$ is the tensor of elastic moduli. Substituting for $d\varepsilon_{kl}^e$ from Eq. (3.3) gives

$$d\sigma_{ij} = C_{ijkl}( \, d\varepsilon_{kl} - d\varepsilon_{kl}^p ) \qquad (3.5)$$

This is one of the fundamental equations for developing the nonlinear constitutive relations to be discussed in Section 3.3.4.1.

### 3.3.1.4 Plastic Potential and Flow Rule

The flow rule is a kinematic assumption postulated for plastic deformation. It provides the components of the plastic strain increment tensor, $d\varepsilon_{ij}^p$, in the directions of a gradient of a plastic potential function of the stresses, $g(\sigma_{ij})$. The plastic flow equations can be expressed as

$$d\varepsilon_{ij}^p = \frac{\partial g}{\partial \sigma_{ij}} \, d\lambda \qquad (3.6)$$

where $d\lambda$ is a positive scalar factor of proportionality. Of great practical importance is the case where the yield function and the plastic potential functions coincide, that is, f = g. This implies

$$d\varepsilon_{ij}^p = \frac{\partial f}{\partial \sigma_{ij}} \, d\lambda \qquad (3.7)$$

Consequently, the plastic flow develops along the normal to the yield surface. Equation (3.7) is called the associated flow rule and has been successfully used for metals (Chen and Han 1988). This is another fundamental equation to be used in formulating the nonlinear constitutive relations developed in Section 3.3.4.1.

### 3.3.1.5 Consistency Condition

The consistency condition requires the state of stress to remain on the yield surface during plastic flow. Thus, after a small elastic-plastic deformation, the yield condition expressed by Eq. (3.1) must still be satisfied. Hence,

$$f(\sigma_{ij} + d\sigma_{ij}, \ k + dk) = f(\sigma_{ij}, \ k) + df = 0 \qquad (3.8)$$

This, in combination with Eq. (3.1), gives

$$df = 0 \qquad (3.9)$$

The scalar $d\lambda$ can be determined from this condition, as discussed in Section 3.3.4.1.

### 3.3.2 von Mises Yield Function

One of the most commonly used yield criteria in metal plasticity is the von Mises yield criterion. In the following subsections, the von Mises yield function is generalized for a mixed-hardening material. Subsequently, the plastic moduli are defined in connection with the von Mises yield function.

#### 3.3.2.1 Generalization of Yield Function for Mixed Hardening

The von Mises yield criterion for an isotropic-hardening material can be expressed as

$$f(\sigma_{ij}, k) = \frac{3}{2} s_{ij} s_{ij} - k^2 = 0 \qquad (3.10)$$

where $s_{ij}$ is the deviatoric stress, defined as

$$s_{ij} = \sigma_{ij} - \frac{1}{3} \sigma_{kk} \delta_{ij} \qquad (3.11)$$

The hardening parameter, $k$, is generally defined as a function of either the effective plastic strain or the plastic work. Bland (1956) showed that for any yield function that is linear or quadratic (such as the von Mises yield function), using either the effective plastic strain or the plastic work as the argument for $k$ is mathematically equivalent. Here, the effective plastic strain, which is the simpler choice, is adopted as $k$ in the von Mises yield criterion. For a von Mises material, the effective strain, $\varepsilon_p$, is defined in incremental form as

$$d\varepsilon_p = \sqrt{\frac{2}{3} d\varepsilon_{ij}^p \, d\varepsilon_{ij}^p} \qquad (3.12)$$

In a mixed hardening formulation, the plastic strain increment tensor is assumed to be the sum of isotropic and kinematic portions, denoted by $d\varepsilon_{ij}^{iso}$ and $d\varepsilon_{ij}^{kin}$, respectively:

$$d\varepsilon_{ij}^p = d\varepsilon_{ij}^{iso} + d\varepsilon_{ij}^{kin} \qquad (3.13)$$

The isotropic plastic strain increment, $d\varepsilon_{ij}^{iso}$, is associated with the expansion of the yield surface, whereas the kinematic plastic strain increment, $d\varepsilon_{ij}^{kin}$, is associated with the

translation of the yield surface. These two strain components can be expressed as (Chen and Han, 1988)

$$d\varepsilon_{ij}^{iso} = Md\varepsilon_{ij}^{p} \tag{3.14}$$

$$d\varepsilon_{ij}^{kin} = (1-M)d\varepsilon_{ij}^{p} \tag{3.15}$$

in which M is the parameter of mixed hardening. It has the range $0 \le M \le 1$.

For a mixed-hardening material, the generalized form of the von Mises yield function is defined as (Chen and Han, 1988)

$$f(\overline{\sigma}_{ij}, \overline{k}) = \frac{3}{2}\overline{s}_{ij}\overline{s}_{ij} - \overline{k}^2(\overline{\varepsilon}_p) = 0 \tag{3.16}$$

where $\overline{s}_{ij}$ is the reduced deviatoric stress, defined by

$$\overline{s}_{ij} = \overline{\sigma}_{ij} - \frac{1}{3}\overline{\sigma}_{kk}\delta_{ij} \tag{3.17}$$

and $\overline{\varepsilon}_p$ is the *reduced effective strain*, which is defined in incremental form as

$$d\overline{\varepsilon}_p = \sqrt{\frac{2}{3}d\varepsilon_{ij}^{iso}d\varepsilon_{ij}^{iso}} \tag{3.18}$$

From Eqs. (3.12), (3.14), and (3.18), the relationship between the effective strain and the reduced effective strain is obtained as

$$d\overline{\varepsilon}_p = M\,d\varepsilon_p \tag{3.19}$$

The hardening parameter for an isotropic-hardening material (i.e., k in Eq.(3.10)) is called the *effective stress* because it corresponds to the yield stress in a uniaxial tension test. For a von Mises material, the effective stress, $\sigma_e$, can be expressed as (Chen and Han, 1988)

$$\sigma_e = \sqrt{\frac{3}{2}s_{ij}s_{ij}} \tag{3.20}$$

Similarly, for a mixed-hardening material, the *reduced effective stress*, $\overline{\sigma}_e$, is used as the hardening parameter (i.e., $\overline{k}$ in Eq.(3.16)). The reduced effective stress for a von Mises material can be expressed as (Chen and Han, 1988)

$$\overline{\sigma}_e = \sqrt{\frac{3}{2}\overline{s}_{ij}\overline{s}_{ij}} \tag{3.21}$$

Substituting $\overline{\sigma}_e$ for $\overline{k}$ in Eq. (3.16) gives the von Mises yield condition for mixed hardening as

$$f(\sigma_{ij}, \sigma_{ij}, \overline{\varepsilon}_p) = \frac{3}{2}\overline{s}_{ij}\overline{s}_{ij} - \overline{\sigma}_e^{\,2}(\overline{\varepsilon}_p) = 0 \qquad (3.22)$$

### 3.3.2.2 Plastic Moduli

The relationship between effective stress and effective strain, characterizing the hardening process of a material, is determined by the experimental uniaxial stress-strain relationship, which has the general form

$$\sigma_e = \sigma_e(\varepsilon_p) \qquad (3.23)$$

In the incremental form it becomes

$$d\sigma_e = H_p \, d\varepsilon_p \qquad (3.24)$$

where $H_p(\sigma_e)$ is called the *plastic modulus*. For an isotropic-hardening material, the plastic modulus is associated with the expansion of the yield surface. For a mixed-hardening material, however, it is the *reduced plastic modulus* defined by

$$\overline{H}_p = \frac{d\overline{\sigma}_e}{d\overline{\varepsilon}_p} \qquad (3.25)$$

that represents the expansion of the yield surface (Chen and Han, 1988). Nevertheless, note that the experimental relationship is always that expressed by Eq. (3.23). In a uniaxial test, $d\sigma_e$ and $d\varepsilon_p$ are equal to $d\sigma_{11}$ and $d\varepsilon_{11}^p$, respectively. (Subscript 1 represents the longitudinal direction in the uniaxial test.) The values of the reduced effective stress and strain, however, depend on the choice of the mixed hardening parameter, M. Besides, the value of $d\overline{\sigma}_e$, which is equal to $d\overline{\sigma}_{11}$, cannot be determined from the test results because the value of $d\alpha_{11}$ can be obtained only from the theory. (Note that $d\overline{\sigma}_{11} = d\sigma_{11} - d\alpha_{11}$ according to Eq. (3.2).)

### 3.3.3 Kinematic Hardening Rule

There are two classical kinematic hardening rules that can be considered in the formulation. They are the Prager and Ziegler kinematic hardening rules. The hardening rule in each case relates the increments in the coordinates of the yield surface center, $d\alpha_{ij}$, to the strain increments and the current states of stress and strain. Ziegler (1959) modified the Prager hardening rule to make it valid for subspaces. Moreover, the Ziegler

hardening rule results in less complex formulation in this study. Therefore, the Ziegler kinematic hardening rule is adopted herein.

Ziegler assumed that the translation of the yield surface occurs in the direction of the reduced stress vector as expressed by

$$d\alpha_{ij} = d\mu \, (\sigma_{ij} - \alpha_{ij}) \qquad (3.26)$$

where $d\mu$ is a positive proportionality factor, which depends on the history of the deformation. This factor is assumed to have the form

$$d\mu = a \, d\varepsilon_p \qquad (3.27)$$

in which $a$ is a positive non-dimensional constant characteristic for a given material. Thus,

$$d\alpha_{ij} = a \, d\varepsilon_p \, (\sigma_{ij} - \alpha_{ij}) \qquad (3.28)$$

For a mixed-hardening material, $d\bar{\varepsilon}_p$ replaces $d\varepsilon_p$ in Eq. (3.28) and it can be shown (Chen and Han 1988) that

$$\overline{H}_p = H_p = a \, \bar{\sigma}_e \qquad (3.29)$$

Thus, for a mixed-hardening material with the Ziegler rule, from Eqs. (3.29) and (3.15),

$$d\alpha_{ij} = \frac{H_p}{\bar{\sigma}_e}(1-M)(\sigma_{ij} - \alpha_{ij})d\varepsilon_p \qquad (3.30)$$

## 3.3.4 Derivation of Constitutive Relationships

In the following subsections, first the nonlinear constitutive relationships for a mixed-hardening material is derived. They relate the increments of stress and strain components during elastic-plastic deformation. Subsequently, the general constitutive relations are simplified for a pipe based of the assumptions made in Section 2.4. Finally, the constitutive relations are obtained for the stress and strain measures used in the pipeline-beam element formulation.

### 3.3.4.1 Derivation of Constitutive Tensor

In this section, the nonlinear constitutive relationships for a mixed-hardening material is derived. They relate the increments of stress and strain components during elastic-plastic deformation.

For the yield function expressed in Eq. (3.22), the consistency condition, i.e., Eq. (3.9) becomes

$$df = \frac{\partial f}{\partial \sigma_{ij}} d\sigma_{ij} + \frac{\partial f}{\partial \alpha_{ij}} d\alpha_{ij} + \frac{\partial f}{\partial \bar{\varepsilon}_p} d\bar{\varepsilon}_p = 0 \qquad (3.31)$$

In the following, each of the six terms in Eq. (3.31) is determined in terms of the current stress and strain states, strain increments, and the scalar $d\lambda$. After appropriate substitutions, Eq.(3.31) is solved for the scalar $d\lambda$. The constitutive relationship is then obtained by using the expression for $d\lambda$.

*i) Expression for* $\dfrac{\partial f}{\partial \sigma_{ij}}$

It can be shown (Chen and Han 1988) that

$$\frac{\partial f}{\partial \sigma_{ij}} = 3\,\bar{s}_{ij} \qquad (3.32)$$

*ii) Expression for* $d\bar{\varepsilon}_p$

In order to derive $d\bar{\varepsilon}_p$, the term $d\varepsilon_{ij}^p$ is first obtained from Eq. (3.7) (i.e., the flow rule) and Eq. (3.32) as

$$d\varepsilon_{ij}^p = 3\,\bar{s}_{ij} d\lambda \qquad (3.33)$$

Equations (3.12), (3.19), and (3.33) yield $d\bar{\varepsilon}_p$ as

$$d\bar{\varepsilon}_p = 2\,M\,\bar{\sigma}_e\,d\lambda \qquad (3.34)$$

*iii) Expression for* $\dfrac{\partial f}{\partial \bar{\varepsilon}_p}$

To determine $\dfrac{\partial f}{\partial \bar{\varepsilon}_p}$, Eq. (3.22) is differentiated with respect to $\bar{\varepsilon}_p$.

$$\frac{\partial f}{\partial \bar{\varepsilon}_p} = -2\,\bar{\sigma}_e\,\frac{\partial \bar{\sigma}_e}{\partial \bar{\varepsilon}_p} = -2\,\bar{\sigma}_e\,\overline{H}_p \qquad (3.35)$$

From Eq. (3.29) for the Ziegler kinematic hardening rule, $\overline{H}_p$ equals $H_p$. Hence,

$$\frac{\partial f}{\partial \bar{\varepsilon}_p} = -2\,\bar{\sigma}_e\,H_p \qquad (3.36)$$

*iv) Expression for* $\dfrac{\partial f}{\partial \alpha_{ij}}$

The chain rule is used to find $\dfrac{\partial f}{\partial \alpha_{ij}}$, using Eqs. (3.2) and (3.32), as

$$\frac{\partial f}{\partial \alpha_{ij}} = \frac{\partial f}{\partial \bar{\sigma}_{kl}} \frac{\partial \bar{\sigma}_{kl}}{\partial \alpha_{ij}} = 3\,\bar{s}_{kl}(-\bar{s}_{ik}\,\delta_{jl}) \tag{3.37}$$

where $\delta_{jl}$ is the Kronecker delta. Hence,

$$\frac{\partial f}{\partial \alpha_{ij}} = -3\,s_{ij} \tag{3.38}$$

### v) Expression for $d\alpha_{ij}$

The term $d\alpha_{ij}$ can be obtained from Eqs. (3.30) and (3.34) as

$$d\alpha_{ij} = 2\,H_p\,(1-M)\,\bar{\sigma}_{ij}\,d\lambda \tag{3.39}$$

### vi) Expression for $d\sigma_{ij}$

Finally, $d\sigma_{ij}$ is obtained from Eqs. (3.5) and (3.33) as

$$d\sigma_{ij} = C_{ijkl}(d\varepsilon_{kl} - 3\,\bar{s}_{kl}\,d\lambda) \tag{3.40}$$

Substituting Eqs. (3.32), (3.34), (3.36), (3.38), (3.39), and (3.40) into Eq. (3.31) and solving it for $d\lambda$ results in the following equation for a mixed-hardening material.

$$d\lambda = \frac{3\,\bar{s}_{ij}\,C_{ijkl}\,d\varepsilon_{kl}}{9\,\bar{s}_{ij}\,C_{ijkl}\,\bar{s}_{kl} + 4H_p\,\bar{\sigma}_e^{\,2}} \tag{3.41}$$

Substituting Eq. (3.41) back into Eq. (3.40) gives

$$d\sigma_{ij} = \left(C_{ijpq} - \frac{9\,C_{ijkl}\,\bar{s}_{kl}\,\bar{s}_{mn}\,C_{mnpq}}{9\,\bar{s}_{ij}\,C_{ijkl}\,\bar{s}_{kl} + 4H_p\,\bar{\sigma}_e^{\,2}}\right) d\varepsilon_{pq} \tag{3.42}$$

This is the constitutive relationship between the stress and strain increments in an elastic–plastic deformation.

By defining $C_{ijpq}^*$ as the term in the brackets in Eq. (3.42), namely,

$$C_{ijpq}^* = C_{ijpq} - \frac{9\,C_{ijkl}\,\bar{s}_{kl}\,\bar{s}_{mn}\,C_{mnpq}}{9\,\bar{s}_{ij}\,C_{ijkl}\,\bar{s}_{kl} + 4H_p\,\bar{\sigma}_e^{\,2}} \tag{3.43}$$

Equation (3.42) becomes

$$d\sigma_{ij} = C_{ijpq}^*\,d\varepsilon_{pq} \tag{3.44}$$

where, $C_{ijpq}^*$ is called the *elastic-plastic constitutive tensor*.

### 3.3.4.2 Simplified Constitutive Relations for a Pipe

In this section, the general constitutive relationships, derived in the previous section, are simplified for a pipe based of the assumptions made in Section 2.4.

In this discussion, the indices 1, 2 , and 3 refer to the longitudinal, circumferencial, and through thickness directions, respectively, for any given material point on a pipe cross-section. Since the shear stresses are assumed to be insignificant, these three directions are considered to coincide with the principal axes.

As mentioned in Section 2.4, since the pipe wall thickness is much smaller than the pipe diameter for a typical pipeline, the radial stresses are insignificant, and hence, they are ignored. Thus,

$$\sigma_3 = d\sigma_3 = 0 \tag{3.45}$$

Furthermore, as assumed in Section 2.4, the internal pressure, if any, is applied to the initial pipe configuration prior to any other loading. Moreover, it is assumed that during and at the end of pressurization, the pipe remains elastic. It is also assumed that the pressure remains constant throughout the analysis. Hence,

$$\sigma_2 = \frac{pR_i}{t} \tag{3.46a}$$

$$d\sigma_2 = 0 \tag{3.46b}$$

where p is the internal pressure, $R_i$ is the internal radius, and t is the pipe thickness.

Since $d\sigma_2 = d\sigma_3 = 0$, the term $\dfrac{\partial f}{\partial \sigma_{ij}} d\sigma_{ij}$ in Eq. (3.31) becomes

$$\frac{\partial f}{\partial \sigma_{ij}} d\sigma_{ij} = \frac{\partial f}{\partial \sigma_1} d\sigma_1 \tag{3.47}$$

which, in turn, can be expressed using Eqs. (3.5), (3.32), and (3.33) as

$$\frac{\partial f}{\partial \sigma_1} d\sigma_1 = 3\bar{s}_1 E (d\varepsilon_1 - 3\bar{s}_1 d\lambda) \tag{3.48}$$

where E is the modulus of elasticity.

Using Eq. (3.48) and some algebraic simplification, Equations (3.41) and (3.42) become

$$d\lambda = \frac{(2\bar{\sigma}_1 - \bar{\sigma}_2)E}{(2\bar{\sigma}_1 - \bar{\sigma}_2)^2 E + 4H_p \bar{\sigma}_e^2} d\varepsilon_1 \qquad (3.49)$$

and

$$d\sigma_1 = \left[ 1 - \frac{(2\bar{\sigma}_1 - \bar{\sigma}_2)^2 E}{(2\bar{\sigma}_1 - \bar{\sigma}_2)^2 E + 4H_p \bar{\sigma}_e^2} \right] E\, d\varepsilon_1 \qquad (3.50)$$

By defining $\widetilde{C}^{EP}$ as

$$\widetilde{C}^{EP} = \left[ 1 - \frac{(2\bar{\sigma}_1 - \bar{\sigma}_2)^2 E}{(2\bar{\sigma}_1 - \bar{\sigma}_2)^2 E + 4H_p \bar{\sigma}_e^2} \right] E = \frac{4H_p \bar{\sigma}_e^2 E}{(2\bar{\sigma}_1 - \bar{\sigma}_2)^2 E + 4H_p \bar{\sigma}_e^2} \qquad (3.51)$$

Equation (3.50) becomes

$$d\sigma_1 = \widetilde{C}^{EP} d\varepsilon_1 \qquad (3.52)$$

Note that in the all of the above equations, the stress and strain measures are the true (Cauchy) stress and true (logarithmic) strain measures, respectively.

### 3.3.4.3 Constitutive Relationship for Pipeline-Beam Element

In this section, the constitutive relationship derived in the previous section between the true stress and strain measures (i.e. Eq. (3.52)) is modified to obtain the constitutive relationship required for the pipeline-beam element.

In the analysis to find an equilibrium solution for time t+$\Delta$t, the pipeline-beam element formulation uses the 2nd Piola-Kirchhoff stress and Green-Lagrange strain measures with respect to the configuration at time t. In the following, first the modification of the constitutive coefficient, $\widetilde{C}^{EP}$, is considered for the 2nd Piola-Kirchhoff stress and Green-Lagrange strain measures with respect to a general configuration. Then, the implications of choosing time t as the reference configuration are discussed.

The relationship between the longitudinal Green-Lagrange strain, $E_1$, and the longitudinal engineering strain, $e_1$, assuming the longitudinal axis remains a principal axis, can be written as (Fung, 1965)

$$E_1 = e_1 + \frac{e_1^2}{2} \tag{3.53}$$

The logarithmic strain in the longitudinal direction, $\varepsilon_1$, can be expressed in terms of the engineering strain, $e_1$, as (Hill, 1950)

$$\varepsilon_1 = \ln(1 + e_1) \tag{3.54}$$

Equations (3.53) and (3.54) give the relationship between the longitudinal logarithmic strain and the longitudinal Green-Lagrange strain as

$$\varepsilon_1 = \frac{1}{2}\ln(1 + 2E_1) \tag{3.55}$$

Differentiating both sides of Eq. (3.55) yields

$$d\varepsilon_1 = \frac{dE_1}{1 + 2E_1} \tag{3.56}$$

At time t, the relationship between the Cauchy (true) stress tensor and the 2nd Piola-Kirchhoff stress tensor measured with respect to the configuration at time $\tau$ can be expressed as (Bathe, 1996)

$$^t_\tau S = \frac{^\tau\rho}{^t\rho}\ ^t_\tau F^{-1}\ ^t\sigma\ ^t_\tau F^{-T} \tag{3.57}$$

where

$^t_\tau S =$ the 2nd Piola-Kirchhoff stress tensor measured at time t with respect to the configuration at time $\tau$

$^t\sigma =$ the Cauchy (true) stress tensor measured at time t

$^t_\tau F^{-1} =$ the inverse of the deformation gradient at time t with respect to the configuration at time $\tau$ excluding all rigid-body motions

$^t_\tau F^{-T} =$ the transpose of $^t_\tau F^{-1}$

$^\tau\rho =$ mass density at time $\tau$

$^t\rho =$ mass density at time t

The ratio $\dfrac{^\tau\rho}{^t\rho}$ can be expressed as

$$\frac{^\tau\rho}{^t\rho} = \frac{^tV}{^\tau V} = (1 + {^t_\tau e_1})(1 + {^t_\tau e_2})(1 + {^t_\tau e_3}) \tag{3.58}$$

where $_\tau^t e_1$, $_\tau^t e_2$, and $_\tau^t e_3$ are the engineering strains measured at time t with respect to the configuration at time $\tau$ in the longitudinal, circumferencial, and through-thickness directions, respectively. Using Eq. (3.54), Eq. (3.58) becomes

$$\frac{^\tau\rho}{^t\rho} = \exp(_\tau^t\varepsilon_1 + _\tau^t\varepsilon_2 + _\tau^t\varepsilon_3) \tag{3.59}$$

where $_\tau^t\varepsilon_1$, $_\tau^t\varepsilon_2$, and $_\tau^t\varepsilon_3$ are the logarithmic (true) strains measured at time t with respect to the longitudinal, circumferencial, and through-thickness directions, respectively.

Assuming the longitudinal, circumferencial, and through thickness directions remain the principal axes, Equation (3.57) can be written in matrix form as

$$\begin{bmatrix} _\tau^t S_1 & 0 & 0 \\ 0 & _\tau^t S_2 & 0 \\ 0 & 0 & _\tau^t S_3 \end{bmatrix} = \frac{^\tau\rho}{^t\rho} \begin{bmatrix} \dfrac{1}{1+_\tau^t e_1} & 0 & 0 \\ 0 & \dfrac{1}{1+_\tau^t e_1} & 0 \\ 0 & 0 & \dfrac{1}{1+_\tau^t e_1} \end{bmatrix} \begin{bmatrix} ^t\sigma_1 & 0 & 0 \\ 0 & ^t\sigma_2 & 0 \\ 0 & 0 & ^t\sigma_3 \end{bmatrix} \begin{bmatrix} \dfrac{1}{1+_\tau^t e_1} & 0 & 0 \\ 0 & \dfrac{1}{1+_\tau^t e_1} & 0 \\ 0 & 0 & \dfrac{1}{1+_\tau^t e_1} \end{bmatrix} \tag{3.60}$$

Hence,

$$_\tau^t S_1 = \frac{\exp(_\tau^t\varepsilon_1 + _\tau^t\varepsilon_2 + _\tau^t\varepsilon_3)}{(1+_\tau^t e_1)^2} \, ^t\sigma_1 \tag{3.61}$$

From Eq. (3.53),

$$(1+_\tau^t e_1)^2 = 1 + 2 \, _\tau^t E_1 \tag{3.62}$$

which after substitution in Eq. (3.61) yields

$$_\tau^t S_1 = \frac{\exp(_\tau^t\varepsilon_1 + _\tau^t\varepsilon_2 + _\tau^t\varepsilon_3)}{1 + 2 \, _\tau^t E_1} \, ^t\sigma_1 \tag{3.63}$$

The differentiation of both sides in Eq. (3.63) results in the following equation after an infinitesimal deformation

$$d_\tau^t S_1 = \exp(_\tau^t\varepsilon_1 + _\tau^t\varepsilon_2 + _\tau^t\varepsilon_3)\left[ \frac{d\,^t\sigma_1}{1 + 2 \, _\tau^t E_1} - \frac{2 \, ^t\sigma_1 \, d_\tau^t E_1}{(1 + 2 \, _\tau^t E_1)^2} + (d_t\varepsilon_1 + d_t\varepsilon_2 + d_t\varepsilon_3)\frac{^t\sigma_1}{1 + 2 \, _\tau^t E_1} \right] \tag{3.64}$$

where the infinitesimal increments of stress and strain occur within times t and t+dt. Using Eq. (3.52),

$$d^t\sigma_1 =_t \tilde{C}^{EP}{}_t d\varepsilon_1 \tag{3.65}$$

Which, using Eq. (3.56), becomes

$$d^t\sigma_1 = \frac{_t\tilde{C}^{EP} d_\tau^t E_1}{1 + 2\,_\tau^t E_1} \tag{3.66}$$

The expression for the term $(d_t\varepsilon_1 + d_t\varepsilon_2 + d_t\varepsilon_3)$ in Eq. (3.64) depends on the state of the material. when the material is still in elastic state, the following equations are considered.

$$\varepsilon_1 = \frac{1}{E}(\sigma_1 - v\sigma_2) \tag{3.67a}$$

$$\varepsilon_2 = \frac{1}{E}(\sigma_2 - v\sigma_1) \tag{3.67b}$$

$$\varepsilon_3 = \frac{-v}{E}(\sigma_1 + \sigma_2) \tag{3.67c}$$

Noting that $d\sigma_2 = d\sigma_3 = 0$, the differentiation of Eqs. (3.67) gives

$$d_t\varepsilon_1 + d_t\varepsilon_2 + d_t\varepsilon_3 = \frac{1-2v}{E}d^t\sigma_1 = (1-2v)d_t\varepsilon_1 \tag{3.68}$$

When the infinitesimal deformation is elastic-plastic, using Eq. (3.3) the term $(d_t\varepsilon_1 + d_t\varepsilon_2 + d_t\varepsilon_3)$ can be expressed as

$$d_t\varepsilon_1 + d_t\varepsilon_2 + d_t\varepsilon_3 = d_t\varepsilon_1 + (d_t\varepsilon_2^e + d_t\varepsilon_2^p) + (d_t\varepsilon_3^e + d_t\varepsilon_3^p) \tag{3.69}$$

The term $d_t\varepsilon_2^e$ can be expressed by differentiating Eq. (3.67b) and using Eq. (3.3) as

$$d_t\varepsilon_2^e = \frac{-v}{E}d^t\sigma_1 = -v\,d_t\varepsilon_1^e = -v(d_t\varepsilon_1 - d_t\varepsilon_1^p) \tag{3.70}$$

Similarly,

$$d_t\varepsilon_3^e = \frac{-v}{E}d^t\sigma_1 = -v\,d_t\varepsilon_1^e = -v(d_t\varepsilon_1 - d_t\varepsilon_1^p) \tag{3.71}$$

Substituting for $d_t\varepsilon_2^e$ and $d_t\varepsilon_3^e$ from Eqs. (3.70) and (3.71) into Eq. (3.69) gives

$$d_t\varepsilon_1 + d_t\varepsilon_2 + d_t\varepsilon_3 = d_t\varepsilon_1 + (d_t\varepsilon_2^p + d_t\varepsilon_3^p) - 2v(d_t\varepsilon_1 - d_t\varepsilon_1^p) \tag{3.72}$$

From Eq. (3.33),

$$d_t\varepsilon_1^p + d_t\varepsilon_2^p + d_t\varepsilon_3^p = 3\bar{s}_{ii}\,d\lambda = 0 \qquad (3.73)$$

Thus, the term $(d_t\varepsilon_2^p + d_t\varepsilon_3^p)$ in Eq. (3.72) can be replaced with $-d_t\varepsilon_1^p$. Hence,

$$d_t\varepsilon_1 + d_t\varepsilon_2 + d_t\varepsilon_3 = (1-2\nu)(d_t\varepsilon_1 - d_t\varepsilon_1^p) \qquad (3.74)$$

The term $d_t\varepsilon_1^p$ is obtained from Eqs. (3.33) and (3.49) as

$$d_t\varepsilon_1^p = (2\,_t\bar{\sigma}_1 - _t\bar{\sigma}_2)d\lambda = \frac{(2\,_t\bar{\sigma}_1 - _t\bar{\sigma}_2)^2\,E}{(2\,_t\bar{\sigma}_1 - _t\bar{\sigma}_2)^2\,E + 4\,_tH_p\,_t\bar{\sigma}_e^2}\,d_t\varepsilon_1 \qquad (3.75)$$

Incorporating Eq. (3.75) into Eq. (3.74) gives

$$d_t\varepsilon_1 + d_t\varepsilon_2 + d_t\varepsilon_3 = \frac{4\,_tH_p\,_t\bar{\sigma}_e^2\,(1-2\nu)}{(2\,_t\bar{\sigma}_1 - _t\bar{\sigma}_2)^2\,E + 4\,_tH_p\,_t\bar{\sigma}_e^2}\,d_t\varepsilon_1 \qquad (3.76)$$

Therefore, as seen in both Eqs. (3.68) and (3.76), the term $(d_t\varepsilon_1 + d_t\varepsilon_2 + d_t\varepsilon_3)$ can be written in a general form of

$$d_t\varepsilon_1 + d_t\varepsilon_2 + d_t\varepsilon_3 = \beta\,d_t\varepsilon_1 \qquad (3.77)$$

where $\beta$ can be expressed for an elastic deformation as

$$\beta = 1 - 2\nu \qquad (3.78)$$

and for an elastic-plastic deformation as

$$\beta = \frac{4\,_tH_p\,_t\bar{\sigma}_e^2\,(1-2\nu)}{(2\,_t\bar{\sigma}_1 - _t\bar{\sigma}_2)^2\,E + 4\,_tH_p\,_t\bar{\sigma}_e^2} \qquad (3.79)$$

Incorporating Eqs. (3.56), (3.66), and (3.78) into Eq. (3.64) results in

$$d_\tau^t S_1 = \exp(-3\,_\tau^t\varepsilon_1 + _\tau^t\varepsilon_2 + _\tau^t\varepsilon_3)[_t\tilde{C}^{EP} + (\beta-2)\,^t\sigma_1]d_\tau^t E_1 \qquad (3.80)$$

Thus, the constitutive coefficient used in the finite element formulation, $_tC^{EP}$, becomes

$$_tC^{EP} = \exp(-3\,_\tau^t\varepsilon_1 + _\tau^t\varepsilon_2 + _\tau^t\varepsilon_3)[_t\tilde{C}^{EP} + (\beta-2)\,^t\sigma_1] \qquad (3.81)$$

91

For a steel pipe material, the change in volume is very small. Therefore, the ratio $\dfrac{^{\tau}\rho}{^{t}\rho}$ represented by $\exp(^{t}_{\tau}\varepsilon_1 + ^{t}_{\tau}\varepsilon_2 + ^{t}_{\tau}\varepsilon_3)$, is almost equal to one. Hence Eq. (3.81) becomes

$$_{t}C^{EP} \approx \exp(-4^{t}_{\tau}\varepsilon_1)[_{t}\widetilde{C}^{EP} + (\beta - 2)^{t}\sigma_1] \tag{3.82}$$

Moreover, at high levels of nonlinearity, where $_{t}H_p$ is much smaller than E, the factor $\beta$ given by Eq. (3.79) becomes negligible compared to 2 in Eq. (3.82). Hence, Eq. (3.82) becomes

$$_{t}C^{EP} \approx \exp(-4^{t}_{\tau}\varepsilon_1)(_{t}\widetilde{C}^{EP} - 2^{t}\sigma_1) \tag{3.83}$$

When the steel material is still elastic, the effects of both $\exp(-4^{t}_{\tau}\varepsilon_1)$ and $(\beta - 2)^{t}\sigma_1$ are negligible. Thus, Eq. (3.82) becomes

$$_{t}C^{EP} \approx _{t}\widetilde{C}^{EP} = E \tag{3.84}$$

For a *total Lagrangian* formulation, where the initial configuration is taken as the reference configuration, $\tau = 0$, and hence, Equation (3.81) becomes

$$_{t}C^{EP} = \exp(-3^{t}_{0}\varepsilon_1 + ^{t}_{0}\varepsilon_2 + ^{t}_{0}\varepsilon_3)[_{t}\widetilde{C}^{EP} + (\beta - 2)^{t}\sigma_1] \tag{3.85}$$

For an *updated Lagrangian* formulation, where the configuration at time t is taken as the reference configuration, $\tau = t$. And since $^{t}_{t}\varepsilon_1 = ^{t}_{t}\varepsilon_2 = ^{t}_{t}\varepsilon_3 = 0$, Equation (3.81) becomes

$$_{t}C^{EP} = _{t}\widetilde{C}^{EP} + (\beta - 2)^{t}\sigma_1 \tag{3.86}$$

Equation (3.86) is used in the updated Lagrangian formulation developed in this study.

## 3.4 PROCEDURE TO EVALUATE STRESS INCREMENT

The procedure to find the constitutive coefficient used in the finite element formulation, $_{t}C^{EP}$, was discussed in Section 3.3. In this section, the procedure to update the longitudinal stress for a given strain increment is presented. This procedure needs to be carried out both in evaluating the stiffness matrix and in calculating the stresses upon achieving convergence in a loading step.

92

In terms of the notation for the longitudinal stress, $\tilde{\sigma}_1$, it will be denoted by $\sigma_1$ in this section. This is to avoid confusion because the notation $\overline{\sigma}_1$ is used for reduced longitudinal stress in this section.

Assuming the equilibrium configuration at time t is known, in order to update the longitudinal stress for the configuration at time t+Δt, whether the solution has converged or not, the following general equation is utilized.

$$^{t+\Delta t}\sigma_1 = {}^t\sigma_1 + \int_t^{t+\Delta t} d\sigma_1 \tag{3.87}$$

To carry out the above integration, the total strain increment is divided into small enough strain increments. However, if there is an elastic portion to the strain increment, the integration for the elastic portion can be performed in one step, that is, no division needs to be carried out.

Equations (2.52) and (2.53) are used to calculate the linear and nonlinear portions of the strain increment for a given set of displacement increments. The summation of these two portions as per Eq. (2.45) produces the Green-Lagrange strain increment with respect to the configuration at time t, denoted by $_t\tilde{E}_1$ (note that subscripts 1 and 11 are used interchangeably in this work). This strain must be converted to the logarithmic (true) strain measure before proceeding with the constitutive relationships. Thus,

$$_t\tilde{\varepsilon}_1 = \frac{1}{2}\ln(1 + 2\,_t\tilde{E}_1) \tag{3.88}$$

where $_t\tilde{\varepsilon}_1$ is the equivalent logarithmic strain increment.

Given the longitudinal strain increment, $_t\tilde{\varepsilon}_1$, the following steps are carried out to calculate the longitudinal stress increment.

### Step 1

First, it should determined whether there will be any elastic-plastic deformation at all. To do that the von Mises yield criterion is considered for a biaxial case (note that through-thickness stress, $\overline{\sigma}_3$, is always assumed to be zero):

$$f(\overline{\sigma}_1, \overline{\sigma}_2, \overline{\sigma}_e) = \overline{\sigma}_1{}^2 + \overline{\sigma}_2{}^2 - \overline{\sigma}_1\overline{\sigma}_2 - \overline{\sigma}_e{}^2 = 0 \tag{3.89}$$

where $\bar{\sigma}_e$ remains equal to the initial yield stress, $\sigma_y$, up until the first occurrence of plastic flow. In the stress space, the yield surface represented by Eq. (3.89) is reduced to an ellipse as shown by Fig. 3.1.

Assuming a purely elastic increment, i.e.,

$$^{t+\Delta t}\bar{\sigma}_1 = {}^t\bar{\sigma}_1 + E \, _t\tilde{\varepsilon}_1 \qquad (3.90)$$

(i) if $f(^{t+\Delta t}\bar{\sigma}_1, \bar{\sigma}_2, {}^t\bar{\sigma}_e) \leq 0$, then the stress update based on Eq. (3.90) is valid. This is the end of the procedure.

(ii) if $f(^{t+\Delta t}\bar{\sigma}_1, \bar{\sigma}_2, {}^t\bar{\sigma}_e) > 0$, i.e., if the stress state falls out of the yield ellipse, then there is elastic-plastic deformation in the increment. Go to Step 2.

## *Step 2*

Here the elastic fraction of the increment, defined by Q, is determined. Thus, the elastic and elastic-plastic portions of the strain increment are $Q \, _t\tilde{\varepsilon}_1$ and $(1-Q) \, _t\tilde{\varepsilon}_1$, respectively. To that aim, first the elastic increment in the longitudinal stress required to bring the stress state to the yield ellipse, denoted by $\Delta_e\sigma_1$, should be determined. Since this is an elastic increment, the yield ellipse remains unchanged, and thus, $\Delta_e\bar{\sigma}_1 = \Delta_e\sigma_1$. The value of $\Delta_e\sigma_1$ can be obtained using Eq. (3.89) by replacing $\bar{\sigma}_1$ with $({}^t\bar{\sigma}_1 + \Delta_e\sigma_1)$:

$$({}^t\bar{\sigma}_1 + \Delta_e\sigma_1)^2 + \bar{\sigma}_2{}^2 - ({}^t\bar{\sigma}_1 + \Delta_e\sigma_1)\bar{\sigma}_2 - {}^t\bar{\sigma}_e{}^2 = 0 \qquad (3.91)$$

This leads to the following two roots

$$\Delta_e\sigma_1 = \frac{1}{2}\left[ (\bar{\sigma}_2 - 2\,{}^t\bar{\sigma}_1) \pm \sqrt{(\bar{\sigma}_2 - 2\,{}^t\bar{\sigma}_1)^2 + 4({}^t\bar{\sigma}_e{}^2 - {}^t\bar{\sigma}_1{}^2 - \bar{\sigma}_2{}^2 + {}^t\bar{\sigma}_1\bar{\sigma}_2)} \right] \qquad (3.92)$$

Assuming point A in Fig. 3.1 represents the stress state at time t, these two roots correspond to the distances on the right and left of point A to be traversed along the $\bar{\sigma}_1$ axis to get to the yield ellipse. If point A is located inside the ellipse at time t, one root is positive and the other is negative. The positive root corresponds to moving in the positive $\bar{\sigma}_1$ direction, and the negative root corresponds to moving in the negative $\bar{\sigma}_1$ direction. If, however, point A is located on the yield ellipse at time t, one of the roots is zero.

The selection of the right root depends on the sign of the longitudinal strain increment, $_t\tilde{\varepsilon}_1$. As Fig. 3.1 indicates, a positive longitudinal strain increment tends to

move the stress state in the positive $\overline{\sigma}_l$ direction, whereas a negative $_t\tilde{\varepsilon}_l$ tends to move the stress state in the negative $\overline{\sigma}_l$ direction. Therefore, the right root is the one with the same sign as that of $_t\tilde{\varepsilon}_l$. In order for the selection criterion to work in the limiting conditions, i.e., when the stress state is on the yield ellipse at time t, the criterion is defined as follows: the selected root is the one that produces a greater value for the ratio $\dfrac{\Delta_e\sigma_l}{_t\tilde{\varepsilon}_l}$.

The elastic strain increment, thus, can be expressed as

$$_t\tilde{\varepsilon}_l^{\,e} = \frac{\Delta_e\sigma_l}{E} \qquad (3.93)$$

Hence, the fraction Q is obtained as

$$Q = \frac{_t\tilde{\varepsilon}_l^{\,e}}{_t\tilde{\varepsilon}_l} = \frac{\Delta_e\sigma_l}{E\,_t\tilde{\varepsilon}_l} \qquad (3.94)$$

The stress can be updated for the elastic fraction of the strain increment as

$$^{t+\Delta t}\sigma_l^{\,e} = {}^t\sigma_l + \Delta_e\sigma_l = {}^t\sigma_l + QE\,_t\tilde{\varepsilon}_l \qquad (3.95)$$

where $^{t+\Delta t}\sigma_l^{\,e}$ is the updated stress for the elastic portion of the increment. Go to Step 3 to update the stress for the inelastic portion of the strain increment, $(1-Q)\,_t\tilde{\varepsilon}_l$.


### Step 3

To carry out the integration of Eq. (3.87), the inelastic portion of the strain increment, $(1-Q)\,_t\tilde{\varepsilon}_l$, is divided into NSUB sub-increments. The value of NSUB should be large enough to obtain the required precision. Assuming the acceptable size of strain sub-increments as 10 microstrain, the number NSUB can be estimated as

$$NSUB = \frac{(1-Q)\,_t\tilde{\varepsilon}_l}{0.00001} \qquad (3.96)$$

Hence, the magnitude of the strain sub-increments, $d_t\tilde{\varepsilon}_l$, can be obtained as

$$d_t\tilde{\varepsilon}_l = \frac{(1-Q)\,_t\tilde{\varepsilon}_l}{NSUB} \qquad (3.97)$$

For each strain sub-increment, the stress sub-increment, $d\sigma_l$, is obtained from Eq. (3.52) and it is added to the total longitudinal stress from the last sub-increment:

$$\sigma_l^{(i)} = \sigma_l^{(i-1)} + d\sigma_l = \sigma_l^{(i-1)} + \tilde{C}^{EP(i-1)} d_t\tilde{\varepsilon}_l \qquad (3.98)$$

where i refers to the number of sub-increment for which the stress sub-increment is being calculated. And $\widetilde{C}^{EP^{(i-1)}}$ is calculated from Eq. (3.51) as

$$\widetilde{C}^{EP^{(i-1)}} = \frac{4H_p^{(i-1)}\bar{\sigma}_e^{(i-1)^2} E}{(2\bar{\sigma}_1^{(i-1)}-\bar{\sigma}_2)^2 E + 4H_p^{(i-1)}\bar{\sigma}_e^{(i-1)^2}} \tag{3.99}$$

where $H_p^{(i-1)}$ is the value of $\dfrac{d\sigma_e}{d\varepsilon_p}$ obtained from the input stress-strain curve at the end of the previous sub-increment.

Before going to the next sub-increment, the values of the effective plastic strain, reduced effective stress, and the position of the center of the yield ellipse must be updated as well. The reduced effective stress is updated using Eq. (3.89):

$$\bar{\sigma}_e^{(i)} = \sqrt{\bar{\sigma}_1^{(i)^2}+\bar{\sigma}_2^2-\bar{\sigma}_1^{(i)}\bar{\sigma}_2} \tag{3.100}$$

From Eqs. (3.12) and (3.21), the effective plastic strain can be updated as

$$\varepsilon_p^{(i)} = \varepsilon_p^{(i-1)} + d\varepsilon_p = \varepsilon_p^{(i-1)} + 2\,\bar{\sigma}_e^{(i)}\,d\lambda \tag{3.101}$$

where $d\lambda$ is obtained from Eq. (3.49) as

$$d\lambda = \frac{(2\bar{\sigma}_1^{(i-1)}-\bar{\sigma}_2)\,E}{(2\bar{\sigma}_1^{(i-1)}-\bar{\sigma}_2)^2 E + 4H_p^{(i-1)}\bar{\sigma}_e^{(i-1)^2}}\,d_t\tilde{\varepsilon}_1 \tag{3.102}$$

Finally, the position of the center of the yield ellipse is updated using Eq. (3.39) as

$$\alpha_1^{(i)} = \alpha_1^{(i-1)} + d\alpha_1 = \alpha_1^{(i-1)} + 2H_p^{(i-1)}(1-M)\,\bar{\sigma}_1\,d\lambda \tag{3.103a}$$

$$\alpha_2^{(i)} = \alpha_2^{(i-1)} + d\alpha_2 = \alpha_2^{(i-1)} + 2H_p^{(i-1)}(1-M)\,\bar{\sigma}_2\,d\lambda \tag{3.103b}$$

These values are required for calculating the reduced values of stresses using Eq. (3.2)

The integrations over the cross-sectional area, as expressed by Eqs. 2.77, 2.78, and 2.80, are carried out over the actual area at the latest converged configuration. This involves a correction of the tributary area of the sampling points around the cross-section

based on the axial strain at the sampling point (Yoosef-Ghodsi et al., 1994). Thus, the modified tributary area, $\Delta^t A$, used in solving for the time step $t+\Delta t$, can be expressed as

$$\Delta^t A = \frac{\Delta^0 A}{1 + {}^t \tilde{e}_1} \tag{3.104}$$

where $\Delta^0 A$ is the initial value of the tributary area (i.e., in a stress-free configuration), and ${}^t \tilde{e}_1$ is the engineering axial strain at the sampling point. Using Eq. (3.54), the engineering axial strain at the sampling point, ${}^t \tilde{e}_1$, can be obtained as

$$^t \tilde{e}_1 = \exp({}^t \tilde{\varepsilon}_1) - 1 \tag{3.105}$$

where ${}^t \tilde{\varepsilon}_1$ is true strain value at the sampling point.
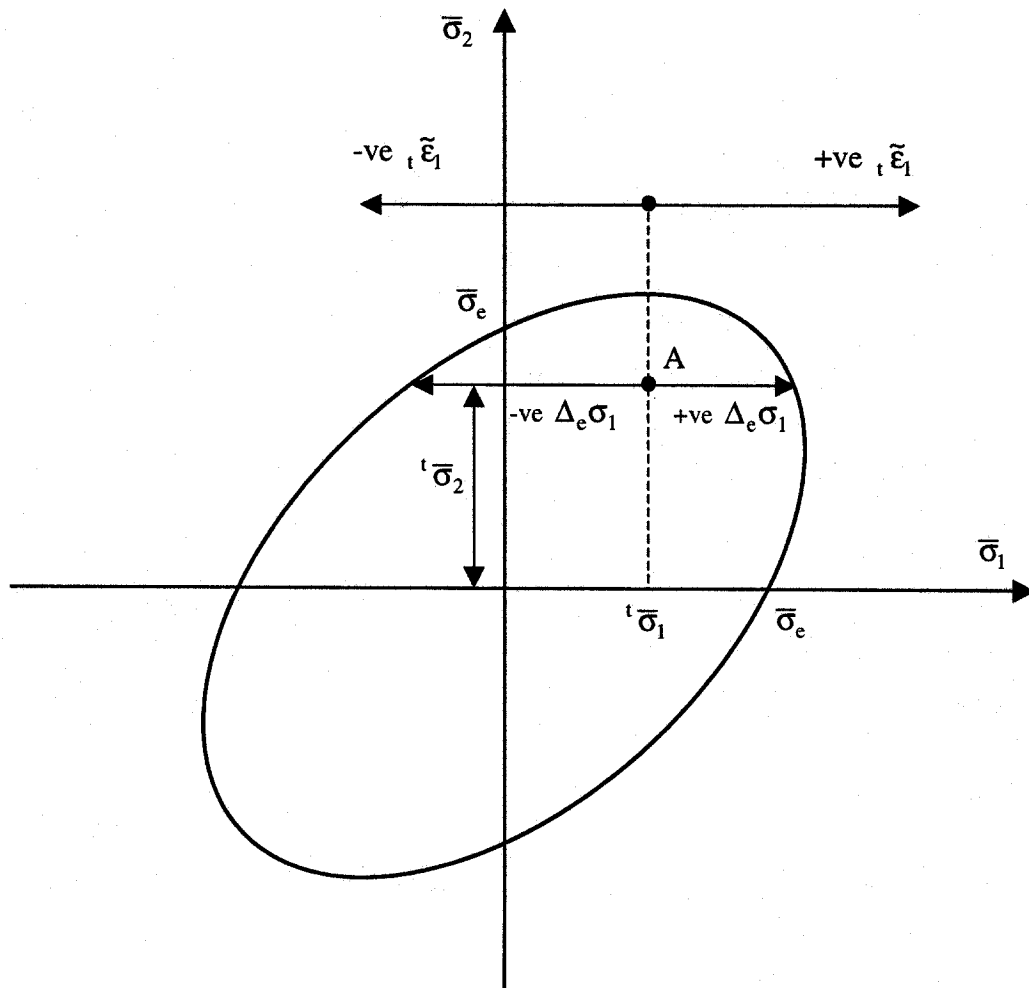
Fig. 3.1 von Mises Yield Ellipse for Biaxial State of Stress

# CHAPTER 4. PIPELINE-SOIL INTERACTION MODEL

## 4.1 INTRODUCTION

This chapter describes the pipeline-soil interaction model developed for the finite element formulation. Pipeline-soil interaction plays an important role in the response of buried pipelines under a variety of loading conditions. This role is particularly important when the pipe is subjected to ground movement or where there is potential for thermal upheaval buckling.

In the case of ground settlement, all of the loading is imposed through pipeline-soil interaction. Thus, after describing the soil springs and pipe-soil interaction model, the ground settlement models developed in this study are presented. This includes a description of the solution method utilized in the ground settlement analysis. At the end, a numerical example is presented on the analysis of a pipeline subjected to ground settlement.

## 4.2 SOIL SPRINGS

As described in Section 2.8.2, the soil springs are considered to be oriented in the local coordinate system as continuous entities. As Fig. 2.5 shows, there are three types of springs modeling the reaction from soil surrounding the pipeline. The transverse support from the soil beneath and above the pipe are modeled by bearing and uplift springs, respectively. The frictional interaction along the pipeline is modeled using longitudinal springs.

The continuous effects of soil springs are evaluated at the Gauss integration points along the each element. Thus, in practice, the soil support is modeled by discrete soil springs. In terms of transverse pipe-soil interaction, this implies that the surrounding soil can be divided into slices, each represented by soil springs, such that interaction between slices can be ignored. As mentioned in Section 2.4, this corresponds to the main assumption for the classical Winkler foundation. This might introduce some inaccuracy since the interaction between slices can sometimes be important, such as for dense soil and soil at yield. However, given the low accuracy of the available soil properties in practice and the fact that the pipeline behavior is the focus of this study, this assumption is appropriate.

The basic assumptions and the constitutive relations for the soil springs are discussed in the following subsections. The constitutive relations for soil springs are defined in terms of force-deformation relations. For each type of soil spring, formulas are suggested from "Guidelines for the Seismic Design of Oil and Gas Pipeline Systems" (CGL, 1984) for calculating the spring constants given the basic soil properties. These formulas, presented for sand and clay only, should be viewed as a general guide to be used in lieu of site-specific data on the spring constants.

## 4.2.1 Bearing Springs

The bearing springs are assumed to work only in compression and to have an elastic-perfectly plastic force-deformation constitutive relationship as shown in Fig. 4.1. For downward motion, the pipeline is assumed to act as a cylindrically-shaped strip footing and the ultimate soil resistance is obtained by the conventional bearing capacity theory as (CGL, 1984)

$$F_{By} = c N_c D + \bar{\gamma} H N_q D + \frac{1}{2} \gamma D^2 N_\gamma \qquad (4.1)$$

where

   c = soil cohesion or undrained shear strength, $S_u$

   $\gamma$ = total soil unit weight

   $\bar{\gamma}$ = effective soil unit weight

   D = pipe outside diameter

   H = the depth of pipe center

   $N_c$, $N_q$, and $N_\gamma$ = bearing capacity factors for horizontal strip footing given by

$$N_q = \exp(\pi \tan \phi) \tan^2 (\frac{\pi}{4} + \frac{\phi}{2}) \qquad (4.2a)$$

$$N_c = (N_q - 1) \cot \phi \qquad (4.2b)$$

$$N_\gamma = (N_q - 1) \tan(1.4\phi) \qquad (4.2c)$$

where $\phi$ is the angle of internal friction.

For the case of undrained loading in clays, where $\phi = 0$, Equation (4.1) becomes

$$F_{By} = c N_c D = S_u N_c D \qquad (4.3)$$

where $S_u$ is the undrained shear strength of the clay soil.

100

The yield displacement, $\Delta_{By}$ (as shown in Fig. 4.1), can be considered to be on the order of 10% to 15% of the pipe outside diameter for both sand and clay (CGL, 1984). Thus,

$$\Delta_{By} = 0.10D \text{ to } 0.15D \tag{4.4}$$

## 4.2.2 Uplift Springs

Similarly to the bearing springs, the uplift springs are also assumed to work only in compression. Two types of constitutive relationship are available for the uplift springs. The first one is an elastic-perfectly plastic force-deformation constitutive relationship as shown in Fig. 4.2. This constitutive relationship, which is identical to that employed for the bearing springs, is adequate in most cases. The second type of constitutive relationship takes into account the loss of the uplift spring force as the pipe moves drastically upwards. This is particularly important in upheaval buckling of the pipe due to thermal action. Thus, the piecewise linear force-deformation relation ends with a descending branch that reaches a zero force value by the time the pipe emerges from the soil. A sample of such constitutive relationship is shown in Fig. 4.3.

For sands and other non-cohesive materials, the uplift resistance per unit length of pipeline, $F_{Uy}$ (as shown in Figs. 4.2 and 4.3), can be expressed as (CGL, 1984)

$$F_{Uy} = \bar{\gamma} H N_{qv} D \tag{4.5}$$

where $N_{qv}$ is the vertical uplift factor which can be obtained from Fig. 4.4 for different $H/D$ and $\phi$ values. The curves in Fig. 4.4 are based on test results reported by Trautmann and O'Rourke (1983). The yield displacement, $\Delta_{By}$ (as shown in Figs. 4.2 and 4.3), can be considered to range from 0.01H to 0.015H for dense to loose sand (CGL, 1984). Thus,

$$\Delta_{Uy} = 0.01H \text{ to } 0.015H \quad \text{for dense to loose sand} \tag{4.6}$$

For clays, the uplift resistance per unit length of pipeline, $F_{Uy}$, can be expressed as (CGL, 1984)

$$F_{Uy} = S_u N_{cv} D \tag{4.7}$$

where $N_{cv}$ is the vertical uplift factor which can be obtained from the theoretical solutions of Vesic (1969) as

$$N_{cv} = 1.641 \left( \frac{H}{D} \right) \tag{4.8}$$

101

The yield displacement, $\Delta_{By}$, can be considered to range from 0.1H to 0.2H for stiff to soft clay (CGL, 1984). Thus,

$$\Delta_{Uy} = 0.1H \text{ to } 0.2H \quad \text{for stiff to soft clay} \tag{4.9}$$

## 4.2.3 Longitudinal Springs

The longitudinal springs, which represent the sliding resistance along the pipeline, are assumed to have an elastic-perfectly plastic force-deformation constitutive relationship as shown in Fig. 4.5. The axial load per unit length of the pipeline is obtained by integrating the frictional stress along the length of contact between the soil and pipeline.

For sands and other non-cohesive materials, the longitudinal resistance per unit length of pipeline, $F_{Ly}$ (as shown in Fig. 4.5), can be expressed as (CGL, 1984)

$$F_{Ly} = \frac{\pi D}{2} \bar{\gamma} H (1 + K_0) \tan \delta \tag{4.10}$$

where

$K_0$ = coefficient of soil pressure at rest, approximated as $(1 - \sin \phi)$

$\delta$ = interface angle of friction between soil and pipeline

The yield displacement, $\Delta_{Ly}$ (as shown in Fig. 4.5), for sand can be considered to be on the order of 0.1 to 0.2 inches (2.5 to 5 mm) for dense to loose sand (CGL, 1984).

For clays, the longitudinal resistance per unit length of pipeline, $F_{Ly}$, can be expressed as (CGL, 1984)

$$F_{Ly} = \pi D \alpha S_u \tag{4.11}$$

where $\alpha$ is an empirical coefficient, called the 'adhesion factor'. Figure 4.6 gives the value of the adhesion factor as functions of the undrained shear strength of the clay soil, $S_u$ based on studies by Woodward et al (1961) and Trigg and Rizkalla (1994). The following polynomial fit closely approximates the curve proposed by Woodward et al (1961):

$$\alpha = (-1.2435e-9) S_u^4 + (4.2884e-7) S_u^3 - (1.6562e-6) S_u^2 - (0.012399) S_u + 1.4504 \tag{4.12}$$

102

Trigg and Rizkalla (1994), came up with a totally different curve based on NOVA's full scale field longitudinal pipe pull-out tests in cohesive Alberta soils. This curve can be approximated by the following equations as plotted in Fig. 4.6.

For $S_u \leq 20$; $\qquad$ $\alpha = 0.5$ $\qquad$ (4.13a)

For $20 < S_u \leq 65$; $\qquad$ $\alpha = 0.25 + \dfrac{0.25}{45}(65 - S_u)$ $\qquad$ (4.13b)

For $65 < S_u \leq 100$; $\qquad$ $\alpha = 0.2 + \dfrac{0.05}{35}(100 - S_u)$ $\qquad$ (4.13c)

For $S_u > 100$; $\qquad$ $\alpha = 0.2$ $\qquad$ (4.13b)

The considerable difference between the two curves in Fig. 4.6 suggests that there might be other factors affecting the cohesion factor besides the undrained shear strength. Until further studies determine these factors, it is recommended that field tests be carried out to obtain a reliable adhesion factor value or curve for a specific location.

The yield displacement, $\Delta_{Ly}$, for clay can be taken to be on the order of 0.2 to 0.4 inches (5 to 10 mm) for stiff to soft clay (CGL, 1984). Thus,

$$\Delta_{Ly} = 0.2 \text{in. to } 0.4 \text{in.} (5 \text{mm to } 10 \text{mm}) \quad \text{for stiff to soft clay} \qquad (4.14)$$

### 4.2.4 Transverse Horizontal Springs

In a special case where the pipe is analyzed in a horizontal plane, the bearing and uplift springs should be replaced with horizontal springs. Assuming the ground surface is horizontal too, there will be no distinction between the two sets of transverse horizontal springs on either side of the pipeline. As a result of the symmetry, identical horizontal springs replace both the bearing and uplift springs. The transverse horizontal springs are assumed to work only in compression and to have an elastic-perfectly plastic force-deformation constitutive relationship as shown in Fig. 4.7. The ultimate soil resistance in transverse horizontal motion, $F_{Hy}$, is obtained by a model originally developed for vertical piles subjected to horizontal loading (Audibert and Nyman, 1977):

$$F_{Hy} = \bar{\gamma} H N_{qh} D \qquad (4.15)$$

where $N_{qh}$ is the horizontal bearing capacity factor. For sands and other non-cohesive materials, $N_{qh}$ can be expressed as (Hansen, 1961)

$$N_{qh} = \frac{k_{0q} + k_{iq} a_q \left( \dfrac{H}{D} \right)}{1 + a_q \left( \dfrac{H}{D} \right)}$$

(4.16)

where

$$a_q = \frac{k_{0q} k_0 \sin \phi}{\left( k_{iq} - k_{0q} \right) \sin(\dfrac{\pi}{4} + \dfrac{\phi}{2})}$$

(4.17a)

$$k_{iq} = N_c d_{ic} k_0 \tan \phi$$

(4.17b)

$$k_{0q} = \exp\left[ (\dfrac{\pi}{2} + \phi) \tan \phi \right] \cos \phi \tan(\dfrac{\pi}{4} + \dfrac{\phi}{2}) - \exp\left[ -(\dfrac{\pi}{2} - \phi) \tan \phi \right] \cos \phi \tan(\dfrac{\pi}{4} - \dfrac{\phi}{2})$$

(4.17c)

$$k_0 = 1 - \sin \phi$$

(4.17d)

$$N_c = \frac{1}{\tan \phi} \left[ \exp(\pi \tan \phi) \tan^2(\dfrac{\pi}{4} + \dfrac{\phi}{2}) - 1 \right]$$

(4.17e)

$$d_{ic} = 1 + 0.5833 \left( 7 \tan^4 \phi + 1 \right)$$

(4.17f)

For cohesive soils, $N_{qh}$ can be expressed as (Hansen, 1961)

$$N_{qh} = \frac{k_{0c} + k_{ic} a_c \left( \dfrac{H}{D} \right)}{1 + a_c \left( \dfrac{H}{D} \right)}$$

(4.18)

where

$$a_c = \frac{k_{0c} \sqrt{2}}{k_{ic} - k_{0c}}$$

(4.19a)

$$k_{ic} = 1.5833(\pi + 2)$$

(4.19b)

$$k_{0c} = \frac{\pi}{2} + 1$$

(4.19c)

The following values of yield displacement, $\Delta_{Hy}$, are recommended for different sand types (CGL, 1984):

$$\Delta_{Hy} = 0.07 \text{ to } 0.10 \left( H + \frac{D}{2} \right) \text{ for loose sand} \qquad (4.20a)$$

$$\Delta_{Hy} = 0.03 \text{ to } 0.05 \left( H + \frac{D}{2} \right) \text{ for medium sand} \qquad (4.20b)$$

$$\Delta_{Hy} = 0.02 \text{ to } 0.03 \left( H + \frac{D}{2} \right) \text{ for dense sand} \qquad (4.20c)$$

For clays, $\Delta_{Hy}$, can be taken as (CGL, 1984)

$$\Delta_{Hy} = 0.03 \text{ to } 0.05 \left( H + \frac{D}{2} \right) \qquad (4.21)$$

## 4.3 PIPE-SOIL INTERACTION MODEL

The pipe-soil interaction model is based on the assumptions for the pipe-soil interface springs and the procedures to obtain the deformation of the soil springs. These are discussed in the following subsections.

### 4.3.1 Ground Profile

The ground profile is defined as the profile of the soil interfacing the pipeline in the initial configuration of the pipeline. Geometrically, this profile corresponds to the pipeline axis and is approximated by straight lines connecting the nodal points. In a non-settlement analysis, this profile remains constant, whereas in a settlement analysis, the profile changes as settlement increases.

There are a number of environmental phenomena that result in ground settlement. They include differential thaw settlement, frost heave, fault movement, and earthquake-induced ground movement. Thus in order to accommodate a variety of settlement types, three types of settlement templates have been implemented in this work. These are *stepwise, smooth,* and *piecewise linear* ground settlement as shown in Fig. 4.8a (Zhou and Murray, 1993).

For a given settlement, a part of the ground that fully settles is called the *stable zone* and the part of the ground that does not settle and hence remains stationary is called the

*unstable zone* (see Fig. 4.8). In an actual settlement, there is a region of ground between the stable and unstable zones which is subjected to partial settlement varying from zero at its boundary with stable zone to full settlement at its boundary with the unstable zone. This region of the ground is called the *transition zone*.

The stepwise settlement profile is the most simplistic representation of the ground settlement profile. In this model, the transition zone between the stable and unstable zones is reduced to zero. However since the pipeline separates from the supporting soil in the transition zone, the simplification is acceptable. Moreover, a stepwise profile results in more severe pipe stresses than does a settlement profile including a transition zone. Therefore, from a design point of view, a stepwise settlement profile is the most conservative of all profiles. Only one parameter, the differential settlement $^t\delta$, is required to define a step-wise settlement profile.

The smooth settlement profile represents the transition zone by a smooth curve. This curve consists of two parts that are symmetric about a center origin. The center is located at the middle of the transition zone and at half the differential settlement. According to the coordinate system of Fig. 4.8b, the smooth curve can be defined by the following equations:

$$^t\Delta y_G = 0 \qquad\qquad \hat{x} < -L_{TR} \qquad (4.22a)$$

$$^t\Delta y_G = -\frac{^t\delta}{2L_{TR}^3}\left(2(L_{TR} + \hat{x})^3 - \frac{(L_{TR} + \hat{x})^4}{L_{TR}}\right) \qquad -L_{TR} \leq \hat{x} \leq 0 \qquad (4.22b)$$

$$^t\Delta y_G = \frac{^t\delta}{2L_{TR}^3}\left(2(L_{TR} - \hat{x})^3 - \frac{(L_{TR} - \hat{x})^4}{L_{TR}}\right) - {}^t\delta \qquad 0 \leq \hat{x} \leq L_{TR} \qquad (4.22c)$$

$$^t\Delta y_G = -{}^t\delta \qquad\qquad \hat{x} > L_{TR} \qquad (4.22d)$$

Where

$^t\Delta y_G$ = ground settlement at time t

$\hat{x} = x - x_{TR}$

$x$ = the global x coordinate of the ground

$x_{TR}$ = the global x coordinate of the mid-point of transition zone

$^t\delta$ = the differential settlement

$L_{TR}$ = the half-length of the transition zone.

Equations (4.22) provide a settlement profile that is continuous up to the second-order derivative at both ends and at the center of the transition zone. The smooth profile allows the shape of the transition zone to be considered in an approximate way.

The piecewise linear settlement profile is composed of piecewise straight lines connecting the settlement ordinates at certain points (see Fig. 4.8c). When the differential settlement is increased, settlements at those points are proportionally increased. This provides a simple yet powerful tool for modeling a variety of settlement shapes. This allows for zone settlement analysis, where a relatively short length of pipe is subjected to a local settlement.

Unlike the step-wise and smooth settlement profiles, the piecewise linear settlement profile allows for application of non-vertical settlements. As Fig. 4.9 shows, this is particularly useful for settlement analysis of pipes embedded in slopes. In order to utilize a piecewise linear settlement profile, the user needs to provide the pattern and angle of settlement.

Based on the above discussion, in a non-settlement analysis, such as a thermal analysis, the ground profile is always a piecewise linear profile. This is true for settlement problems with the exception of the transition zone in the smooth settlement profile, which are defined by cubic curves of Eqs. (4.22b) and (4.22c).

## 4.3.2 Deformation of Soil Springs

The deformation of the three types of springs, described in Section 4.2, is determined from the relative position of the pipeline and the soil. The constitutive relations for these springs are then utilized to calculate the resultant lateral and longitudinal stiffness and force values used in the formulation. This process and the assumptions involved are described in the following subsections.

### 4.3.2.1 Lateral Springs

There are two major assumptions associated with vertical displacement of the pipe. They are
i.  As the pipe moves downward the top soil is assumed to start moving down with the pipe after the force in the uplift spring has vanished. Thus, due to downward motion of the pipe, the force in the uplift spring, if any, starts to decrease

according to the *unloading* path shown in Fig. 4.2. Once the unloading is completed, the top soil is assumed to move downward as the downward motion of the pipe continues.

ii.  As the pipe moves upward, since the bottom soil is assumed to be stationary, a gap starts to form between the pipe and the bottom soil once the force in the bearing spring vanishes. Thus, due to upward motion of the pipe, the force in the bearing spring, if any, starts to decrease according to the *unloading* path shown in Fig. 4.1. Once the unloading is completed, a gap starts to form and grow as the upward motion of the pipe continues.

As a result of these assumptions, in most cases, for a pair of bearing and uplift springs acting on a given cross-section of a pipe, only one of them is active at any time.

The *gap width* for a cross-section is defined as the separation distance between the pipe and the ground profile in the direction normal to the current pipe configuration. As Fig. 4.10 shows, a negative gap width indicates that the pipe profile is below the ground profile at the sampling point.

As discussed in Section 2.8.2, in assembling the stiffness matrix and load vector, the soil stiffness and force values are calculated at Gaussian integration points. The gap width for an arbitrary integration point, located at global coordinates ${}^t x_{GI}$ and ${}^t y_{GI}$, is calculated using the equation of the line normal to the current pipe profile (see Fig. 4.10). The equation of the normal can be expressed as

$$(\cos{}^t\theta)(x - {}^t x_{GI}) + (\sin{}^t\theta)(y - {}^t y_{GI}) = 0 \qquad (4.23)$$

Where, as shown in Fig. 4.10, ${}^t\theta$ is the pipe slope at time t, and $\cos{}^t\theta$ and $\sin{}^t\theta$ are expressed by Eqs. (2.38a) and (2.38b), respectively.

The normal line defined by Eq. (4.23) is then intercepted with the ground profile, which is, in most cases, a piecewise linear profile. In this case, the interception point of the two straight lines are found simply by solving a system of two equations and two unknowns. However, for the transition zone in the smooth settlement profile, which are defined by cubic curves, the bisection method is used to find the x-coordinate of the intersection point. And hence, using the normal equation, the y-coordinate of the interception point is obtained. The gap width at time t, ${}^t G$ is then calculated as

$$^tG = \sqrt{(^tx_{GI} - ^tx_{int})^2 - (^ty_{GI} - ^ty_{int})^2} \qquad (4.24)$$

Where $^tx_{int}$ and $^ty_{int}$ are the x- and y-coordinates of the interception point at time t, respectively.

Since the response of the lateral springs is path-dependent, the force and stiffness values are updated from the last equilibrium configuration. Thus, the increment of upward displacement of the pipe with respect to the ground at time t+$\Delta$t, $^{t+\Delta t}\Delta_u$, is calculated as

$$^{t+\Delta t}\Delta_u = ^{t+\Delta t}G - ^tG \qquad (4.25)$$

A negative $^{t+\Delta t}\Delta_u$ signifies a downward motion of the pipe with respect to the ground profile from time t to time t+$\Delta$t. The value of $^{t+\Delta t}\Delta_u$ is then used in association with the constitutive relationships for the bearing and uplift springs, as described in Sections 4.2.1 and 4.2.2, to update the force and stiffness values for each spring.

If a spring has yielded or has been disengaged due to a gap formation, the corresponding stiffness is set to zero. The resultant stiffness and force values are obtained by summing the corresponding values for the bearing and uplift springs.

### 4.3.2.2 Longitudinal Spring

It is assumed that the longitudinal springs operate independently from the bearing and uplift springs. In other words, the force level in the lateral springs is not accounted for in determining the longitudinal spring force. As a result, the stiffness of the longitudinal springs will not change due to the variation of lateral spring forces. Therefore, only the history of relative longitudinal displacement of the pipe with respect to the ground determines the longitudinal spring force and stiffness values.

Figure 4.11 shows the configuration of a pipe at time t, which, in the course the next time step, is subjected to a ground settlement increment of d$\Delta$ and displacement increments of u and v in the global coordinate system. The settlement increment is applied along an arbitrary direction, designated by the angle $\beta$ as shown in Fig. 4.11. Note that for a vertical settlement analysis $\beta$ is zero, and for a non-settlement analysis, d$\Delta$ is zero.

The relative longitudinal displacement increment of the pipe with respect to the ground, $d\hat{u}$, at a given integration point from time t to time $t+\Delta t$ can be expressed as

$$d\hat{u} = \tilde{u} + d\Delta\cos{}^t\gamma \qquad (4.26)$$

where the angle ${}^t\gamma$ is the angle between the settlement direction and the tangential direction at the integration point at time t. The term $\tilde{u}$ is the increment of the pipe displacement in tangential direction at the integration point. This displacement increment can be obtained in terms of the global displacement increments as

$$\tilde{u} = (\cos{}^t\theta)u + (\sin{}^t\theta)v \qquad (4.27)$$

The angle ${}^t\gamma$ can be expressed in terms of the angles ${}^t\theta$ and $\beta$ as

$$ {}^t\gamma = 90° - ({}^t\theta + \beta) \qquad (4.28)$$

Substituting for ${}^t\gamma$ from Eq. (4.28) into Eq. (4.26) gives

$$d\hat{u} = \tilde{u} + d\Delta\sin({}^t\theta + \beta) \qquad (4.29)$$

The value of $d\hat{u}$, obtained from Eq. (4.29) is used in association with the constitutive relationships for the bearing and uplift springs, as described in Section 4.2.3, to update the force and stiffness value for the longitudinal spring.

## 4.4 SOLUTION PROCEDURE FOR SETTLEMENT ANALYSIS

The solution technique for settlement analysis was adapted from a constrained displacement technique proposed by Zhou and Murray (1993) for solving settlement problems. This scheme is a full Newton-Raphson iterative method with a constraint to limit the magnitude of the displacement increments in each iteration. The reason for implementing the constraint is that the displacement increments can be very large as the pipe loses its transverse support due to a settlement increment.

In a settlement analysis, using any of the settlement profiles described in Section 4.3.1, the settlement is applied gradually by proportionally increasing a settlement pattern. Thus the total settlement at any given load step can be represented by a settlement factor, $F_s$, which multiplies by the settlement pattern to give the total settlement along the pipeline for that time step (time t). At the beginning of the next time step the settlement factor is increased by a prescribed value, $\Delta F_s$, which takes the pipe to the time step $t+\Delta t$. This will change both the stiffness matrix and the unbalanced load vector due to the soil

spring modifications. The full Newton-Raphson procedure starts with the following system of equations:

$$\Delta \mathbf{u}_1 = {}^{t+\Delta t}\mathbf{K}_0^{-1}\left({}^{t+\Delta t}\mathbf{P}_0 - {}^{t}\mathbf{Q}_0\right)$$  (4.30)

where

$\Delta \mathbf{u}_1$ = vector of displacement increments for Iteration 1

${}^{t+\Delta t}\mathbf{K}_0$ = stiffness matrix for the pipe configuration at Iteration 1 and incremented settlement (i.e., $F_s + \Delta F_s$)

${}^{t}\mathbf{Q}_0$ = equilibrating force vector for the pipe configuration at Iteration 1

${}^{t+\Delta t}\mathbf{P}_0$ = External load vector including modified soil springs due to the settlement increment

From the second iteration onward, the equilibrium equations can be written as

$$\Delta \mathbf{u}_{j+1} = {}^{t+\Delta t}\mathbf{K}_j^{-1}\left({}^{t+\Delta t}\mathbf{P}_j - {}^{t+\Delta t}\mathbf{Q}_j\right)$$  (4.31)

where

$\Delta \mathbf{u}_{j+1}$ = vector of displacement corrections for Iteration j+1

${}^{t+\Delta t}\mathbf{K}_j$ = stiffness matrix for the pipe configuration at Iteration j and latest ground configuration

${}^{t+\Delta t}\mathbf{Q}_j$ = equilibrating force vector for the pipe configuration at Iteration j

${}^{t+\Delta t}\mathbf{P}_j$ = External load vector matrix for the pipe configuration at Iteration j and latest ground configuration

The total displacement increment for the time step is then updated as

$$\Delta \mathbf{u}_{j+1}^{\text{Total}} = \Delta \mathbf{u}_j^{\text{Total}} + \Delta \mathbf{u}_{j+1}$$  (4.32)

When the norm of displacement increments obtained from Eqs. (4.30) and (4.31), $\left\|\Delta \mathbf{u}_j\right\|$, exceeds a prescribed limit, $\Delta_0$ (called *displacement limit*), the displacement increments are modified as

$$\Delta \mathbf{u}_i^{\text{mod}} = \frac{\Delta_0}{\left\|\Delta \mathbf{u}_j\right\|}\Delta \mathbf{u}_i$$  (4.33)

Where $\Delta u_i^{mod}$ is the modified displacement increment vector. An appropriate value for the displacement limit, $\Delta_0$, can be obtained by numerical experimentation.

## 4.5 EXAMPLE AND VERIFICATION OF SETTLEMENT ANALYSIS

The solution for settlement analysis is verified by comparing the results of ABP to those of PIPLIN and ABP using the pipe element of Zhou and Murray (1993). The pipe element developed by Zhou and Murray, as the first pipe element employed in ABP, will be called *old element*, as opposed to *new element* referring to the $C^1$ pipe element developed in this study.

The computer program PIPLIN has been commonly used and accepted in the pipeline industry for many years. Both ABP and PIPLIN use stress-strain constitutive relations and the plasticity theory based on von Mises yield condition. However, there are three main differences between the two programs in terms of the basic assumptions in the formulation:

- **Soil springs orientation**: In ABP the springs directions remain constant with respect to the local coordinate system at any given integration point. Thus the directions of the soil springs rotate as the pipe rotates at a given point. Whereas in PIPLIN, the springs directions remain constant with respect to the global coordinate system, and hence they remain unchanged as the pipe rotates.

- **Hardening rules**: In ABP a mixed hardening rule is used that can range from a fully isotropic hardening rule to a fully kinematic hardening rule. In PIPLIN, however, a special kind of kinematic hardening rule is used, which is based on Mroz (1967) theory. This is a different kind of kinematic hardening than ABP utilizes.

- **Integration over the cross-sectional area**: Since ABP uses true stress and strain measure in its formulation, the integration of all quantities, such as stress, over the cross-sectional area utilizes the actual area in the latest converged configuration. This involves a correction of the tributary area of the sampling points around the cross-section using the axial strain at the sampling point (see Eq. (3.104)). In PIPLIN, however, the types of stress and strain measures used are not specified. Moreover, the cross-sectional integrations use the original area rather than the actual area.

The above differences are not considered to cause significant disparity between the responses from the two programs. Therefore, a relatively close agreement between the results of the two programs is still required to verify ABP. Moreover, since the ABP

program using the old element has already been validated by Zhou and Murray (1993), a close agreement between the responses of the old and new elements should be expected. The following example demonstrates the above corroborations.

In this example, a pipeline of 550 feet (167.6 m) in length is subjected to differential settlement. The pipe has an outside diameter of 12.75 inches (324 mm), a thickness of 0.247 inches (6.27 mm) and an internal pressure of 1 ksi (6.895 MPa). As Figure 4.12 shows, a stepwise settlement zone of 600 inches (50 m) in length is assumed to occur in the middle of the pipe. Such a settlement is typically a consequence of non-uniform thaw settlement due to various environmental causes. The pipe is also assumed to be subjected to a uniformly distributed overburden load of 0.0656 kips/in.

The pipe material is assumed to be of grade X52 (SMYS = 52 ksi) steel with kinematic elastic-plastic hardening. The true stress-strain plot for the pipe material is shown in Fig. 4.13. The analytical results from ABP and PIPLIN are presented in the following.

The results presented here correspond to a ground settlement of 40 inches. Figure 4.14 shows the deformed configuration obtained from ABP (both old and new elements) and PIPLIN solutions. Figures 4.15 to 4.18 show the distribution of curvature, moment, bottom-fiber strain, and top-fiber strain along the pipe for the three solutions, respectively. Close agreement is observed between the ABP results of the old and new elements. A weaker agreement is seen between the ABP responses on one hand and the PIPLIN responses on the other hand. However, considering the above-mentioned differences between the fundamental assumptions for ABP and PIPLIN, the agreement between their responses is deemed satisfactory. These observations establish the credibility of the solution procedure implemented in ABP using the $C^1$ pipe element for settlement analysis.

The superiority of the new element over the old element can be noted from the moment diagram in Fig. 4.16. In order to examine the differences more closely, the moment responses for only 600 inches of the pipe is shown in Figure 4.19. The undesired oscillatory nature of the moment response is diminished by switching from the old element to the new element. Similar observation can be made from the axial force responses of the two elements as shown in Fig. 4.20.
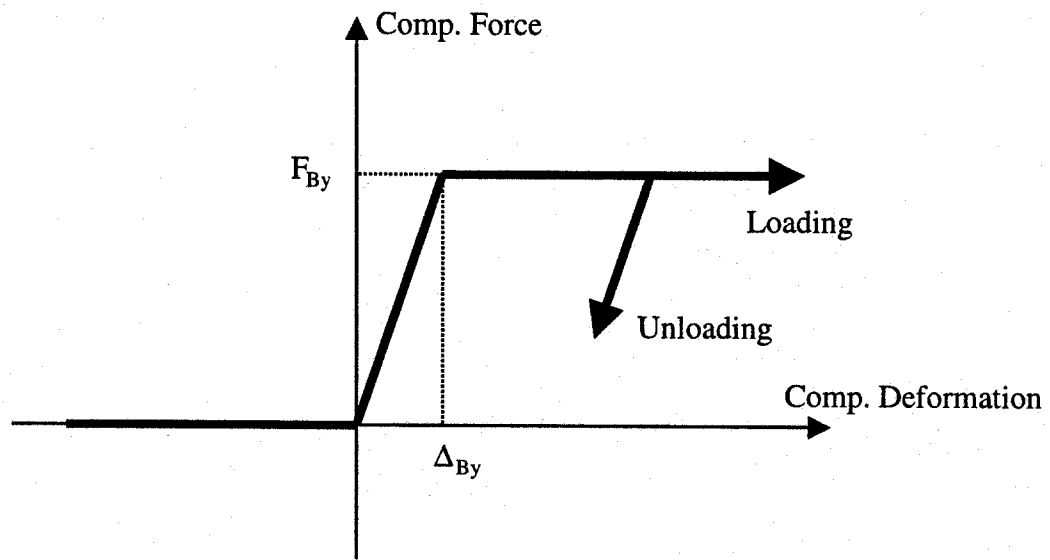
Fig. 4.1 Typical Constitutive Relation for Bearing Springs
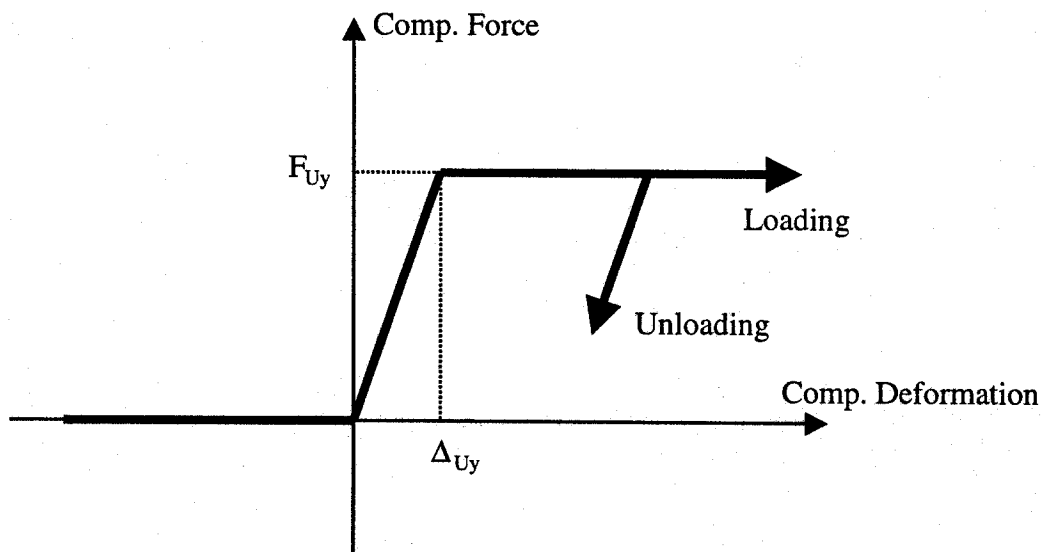


Fig. 4.2 Type 1 Constitutive Relation for Uplift Springs

114
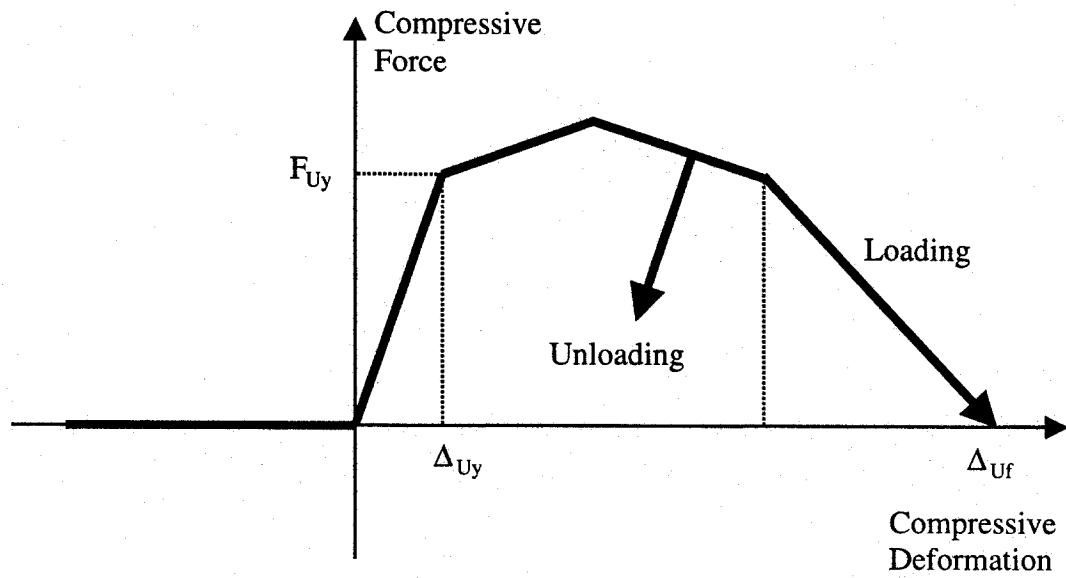
Fig. 4.3 Type 2 Constitutive Relation for Uplift Springs
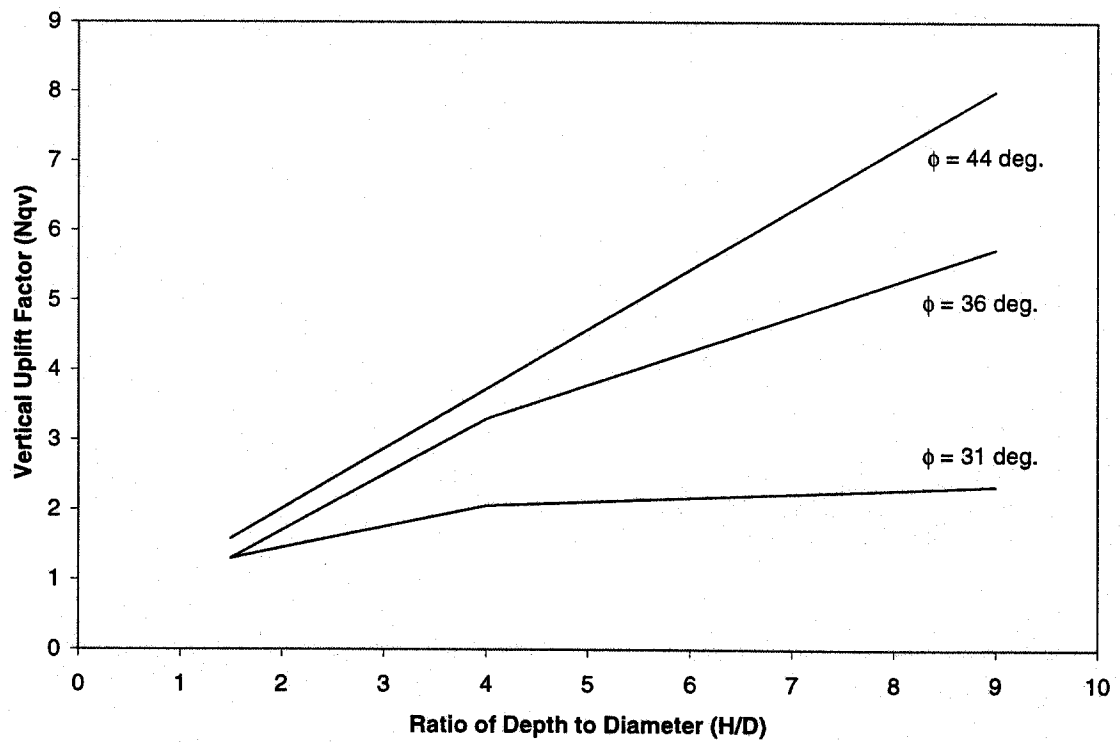


Fig. 4.4 Vertical Uplift Factor for Sand as a Function of Depth to Diameter Ratio of
Buried Pipelines
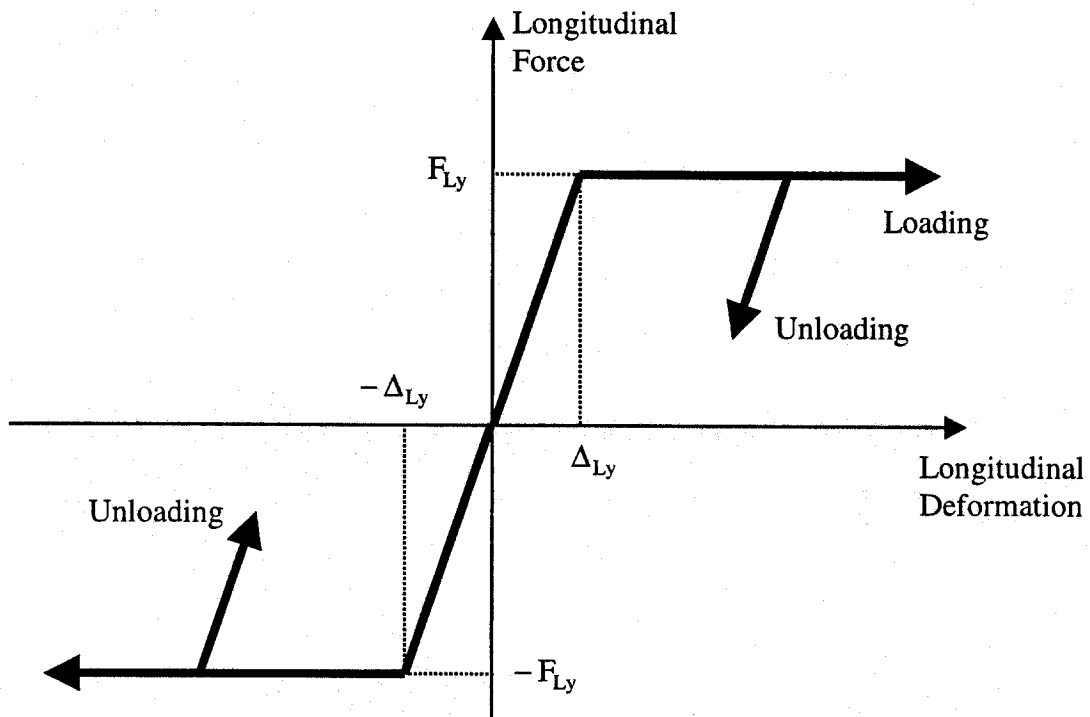
Fig. 4.5  Typical Constitutive Relation for Longitudinal Springs
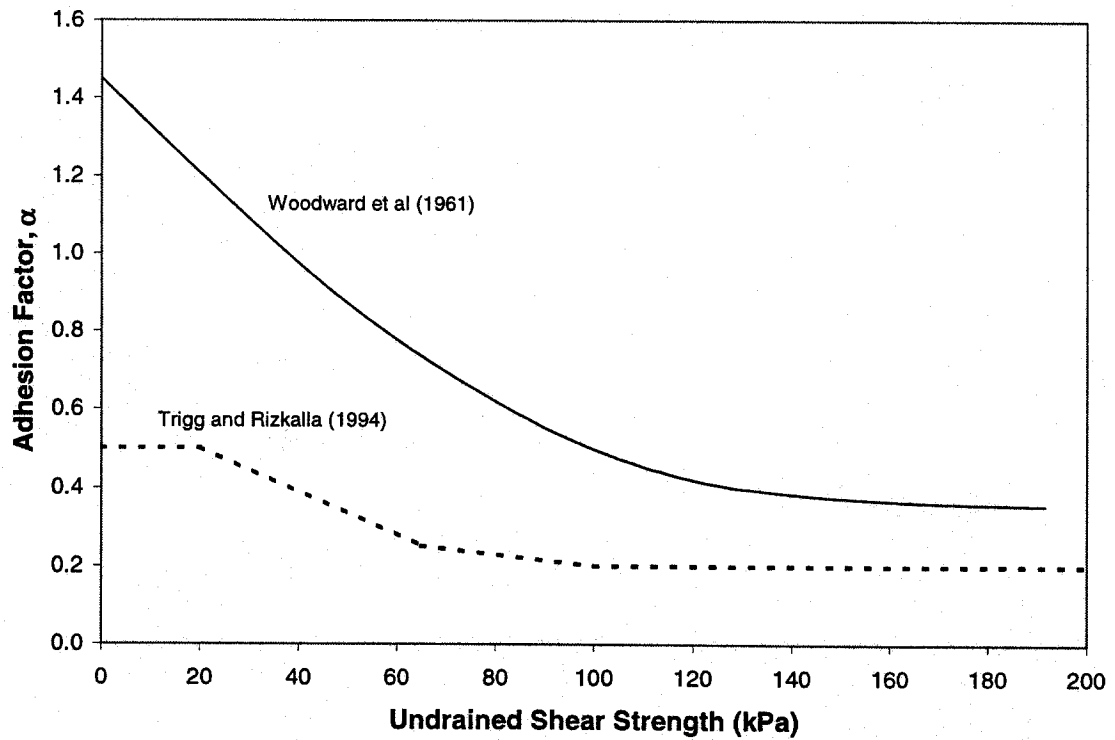


Fig. 4.6  Adhesion Factor Plotted as a Function of Undrained Shear Strength

116
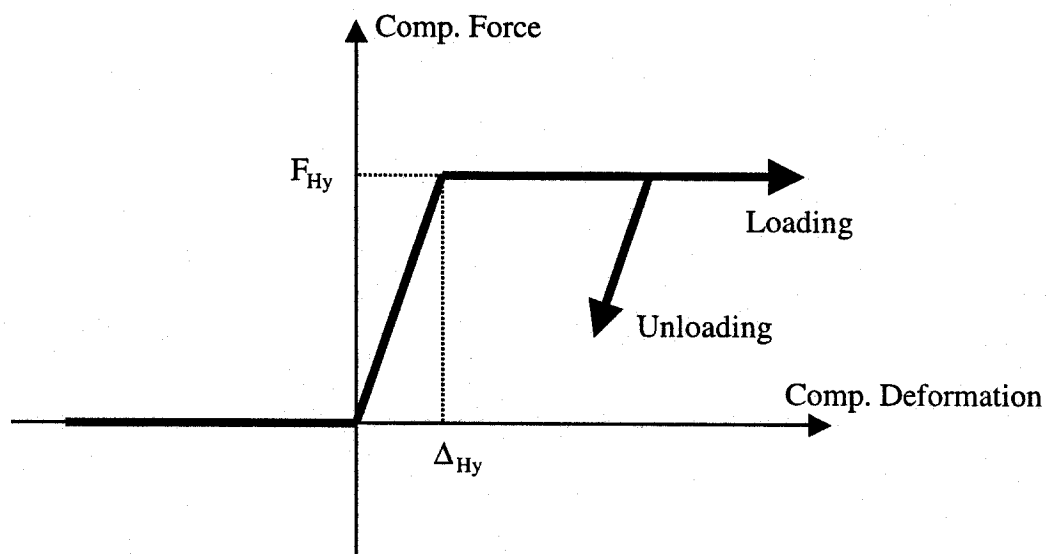
Fig. 4.7 Typical Constitutive Relation for Horizontal Springs

a. Stepwise Settlement Profile



b. Smooth Settlement Profile



c. Piecewise Linear Settlement Profile
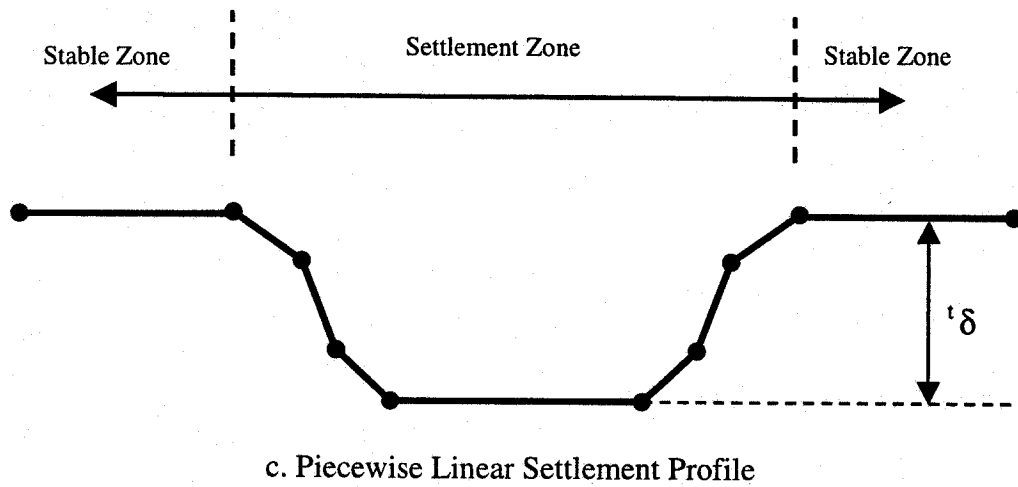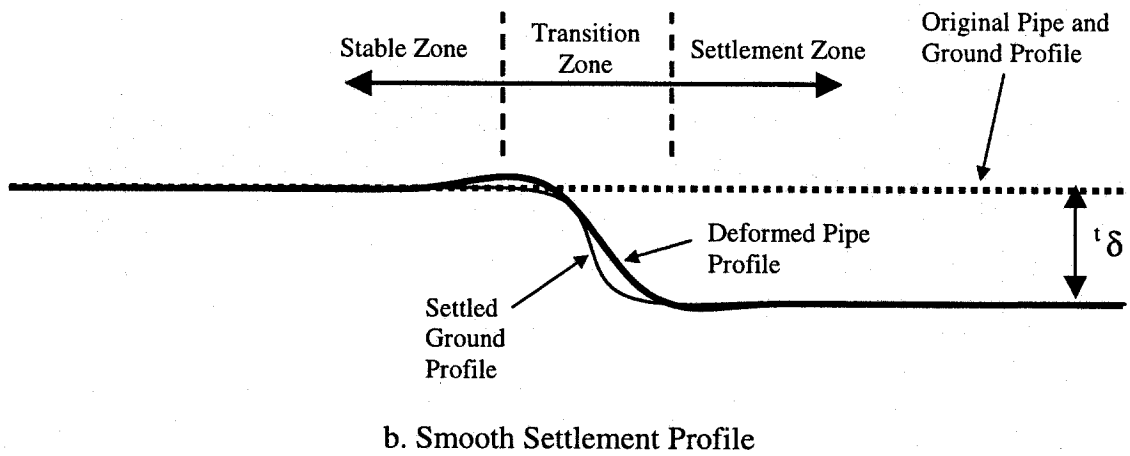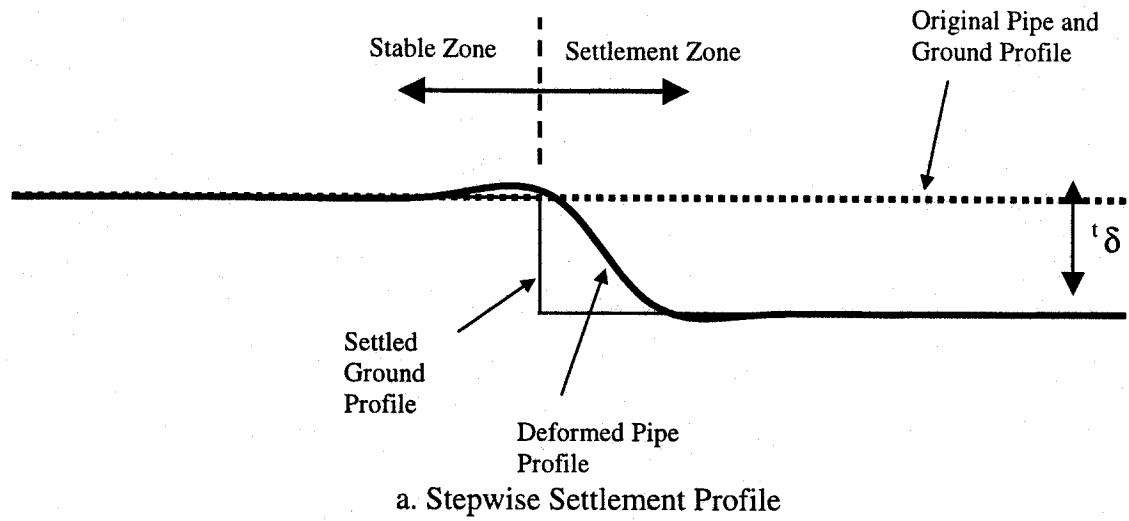
Fig. 4.8  Settlement Profiles in ABP

118

Arrows show the size and direction of settlement (same direction throughout).
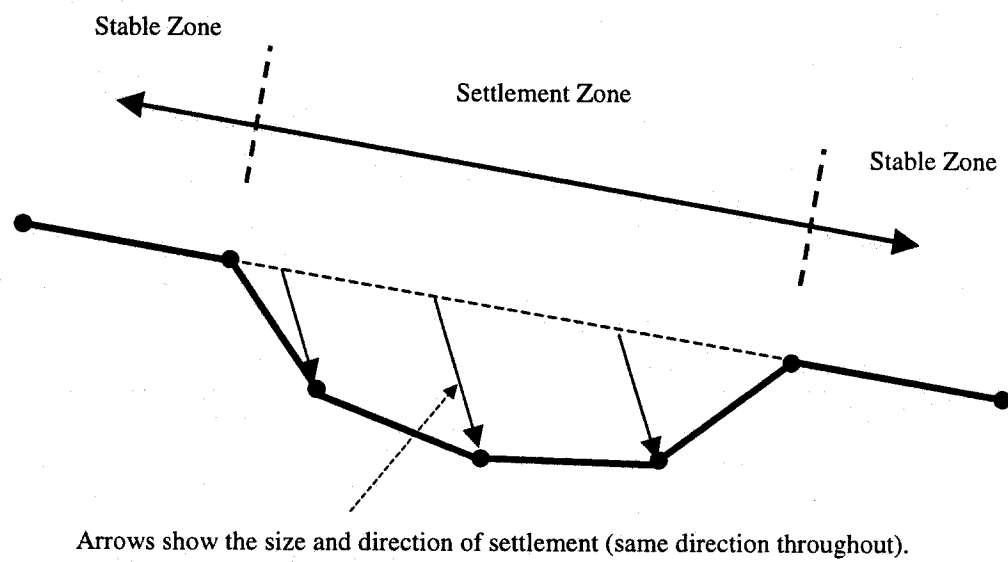
Fig. 4.9  Generalized Piecewise Linear Settlement Profile

119

Pipe Profile          Gaussian Integration Point
$(x_{GI}, y_{GI})$

$\theta$

G = Gap Width

Ground Profile          Interception
Point $(x_{int}, y_{int})$
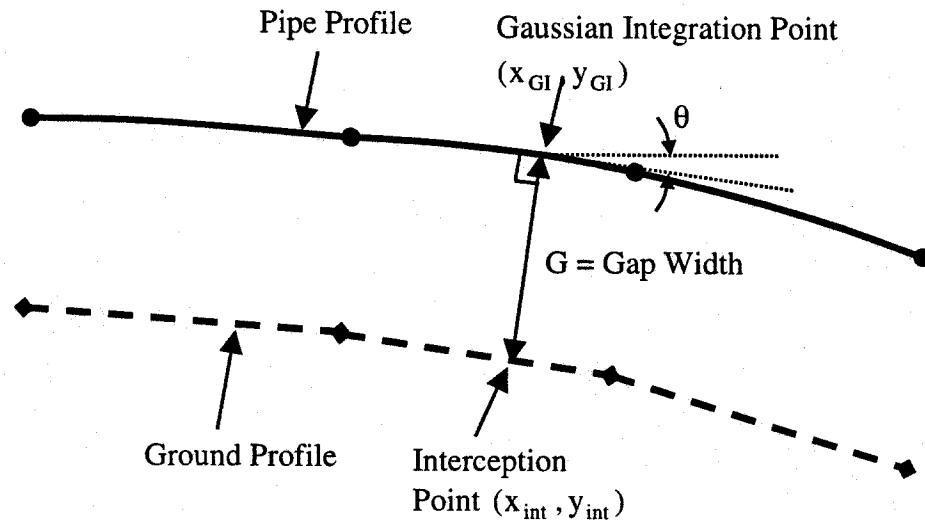
a. Positive Gap Width for Base Springs

Ground Profile          Interception
Point $(x_{int}, y_{int})$

G = Gap Width

$\theta$

Gaussian
Integration Point
$(x_{GI}, y_{GI})$
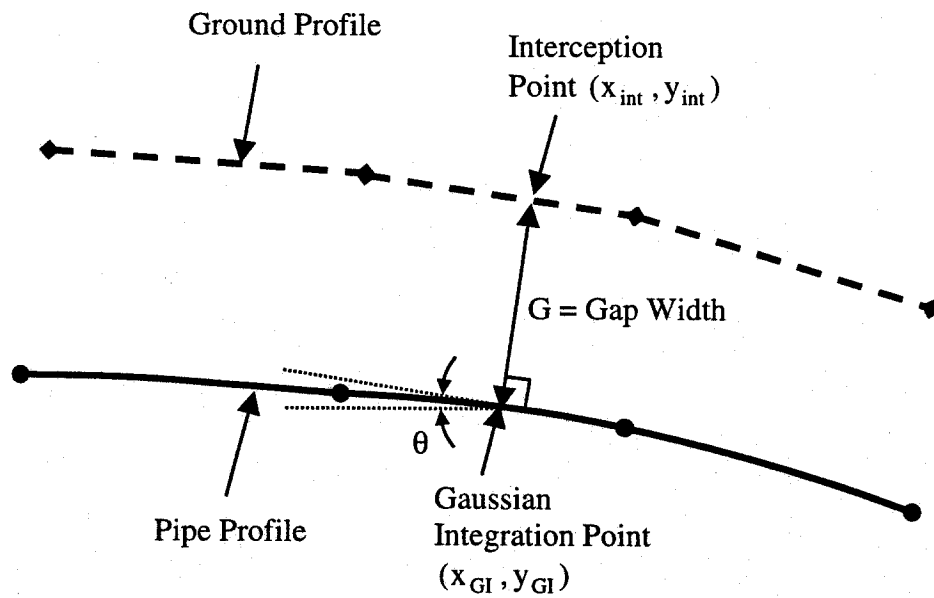
Pipe Profile

b. Negative Gap Width for Base Spring

Fig. 4.10  Gap Width Definition

120
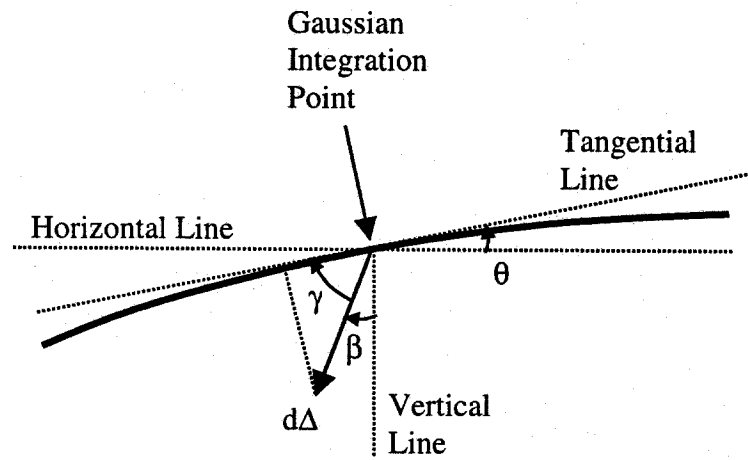
Fig. 4.11 Pipe Subjected to Inclined Settlement of dΔ at Arbitrary Integration Point
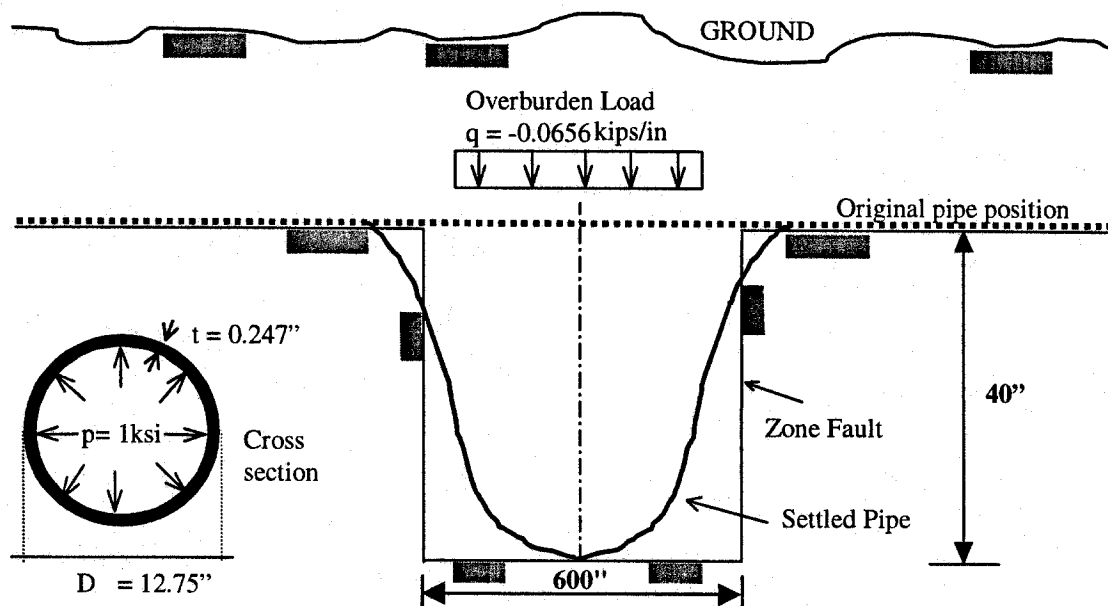
a) Loading and Settlement Profile
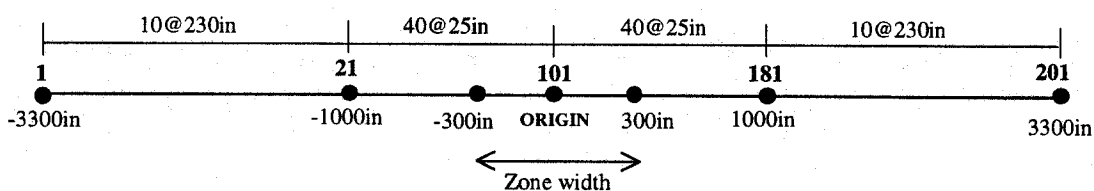


b) Model Discretization
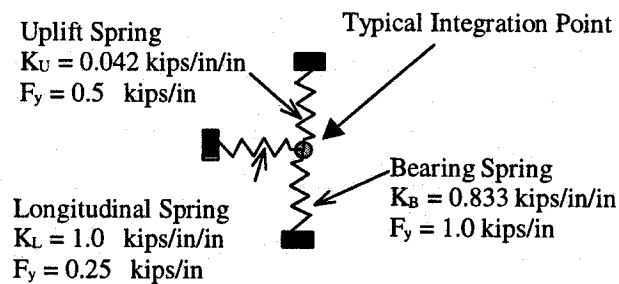


c) Soil Spring Properties

Fig. 4.12 Layout of Example for Ground Settlement Analysis

122
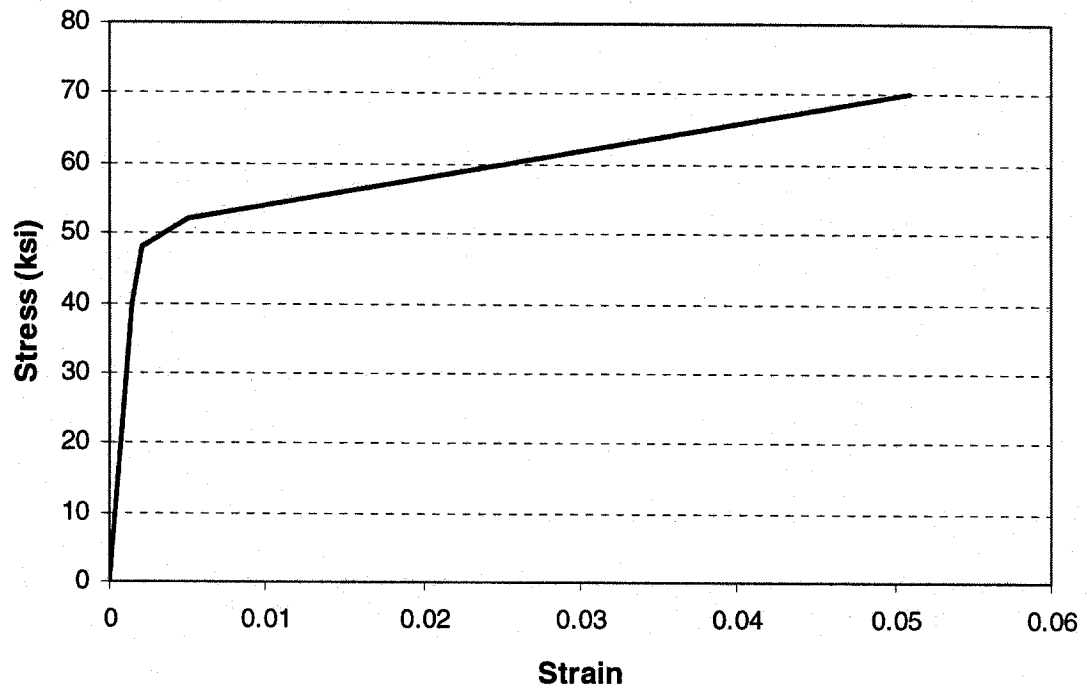
Fig. 4.13 True Stress-Strain Relationship for X52 Steel Pipe Material
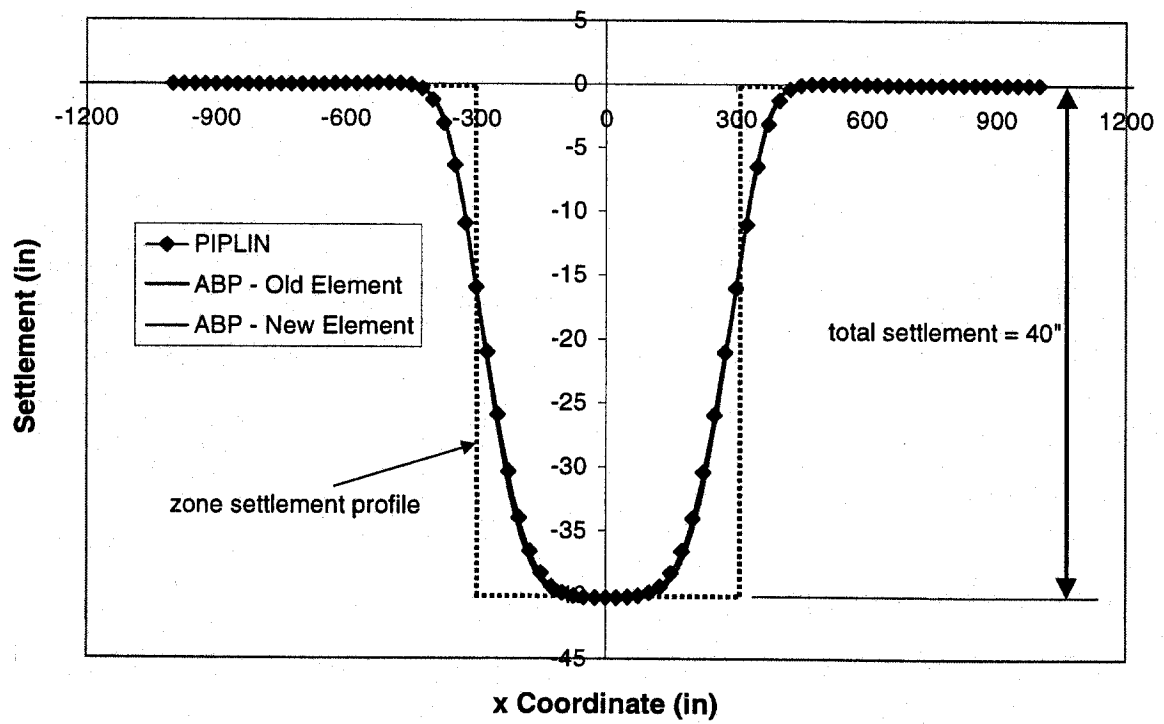


Fig. 4.14 Pipe Profile at 40" of Settlement for Different Solutions
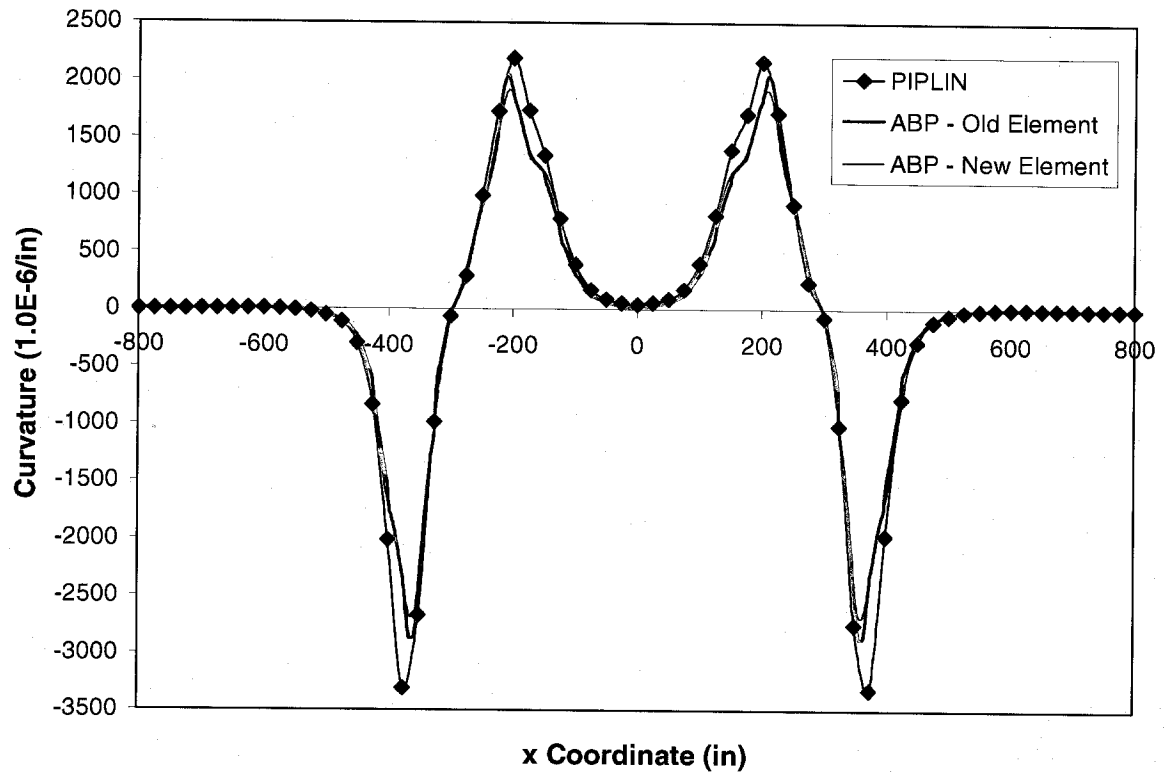
Fig. 4.15  Pipe Curvature at 40" of Settlement for Different Solutions
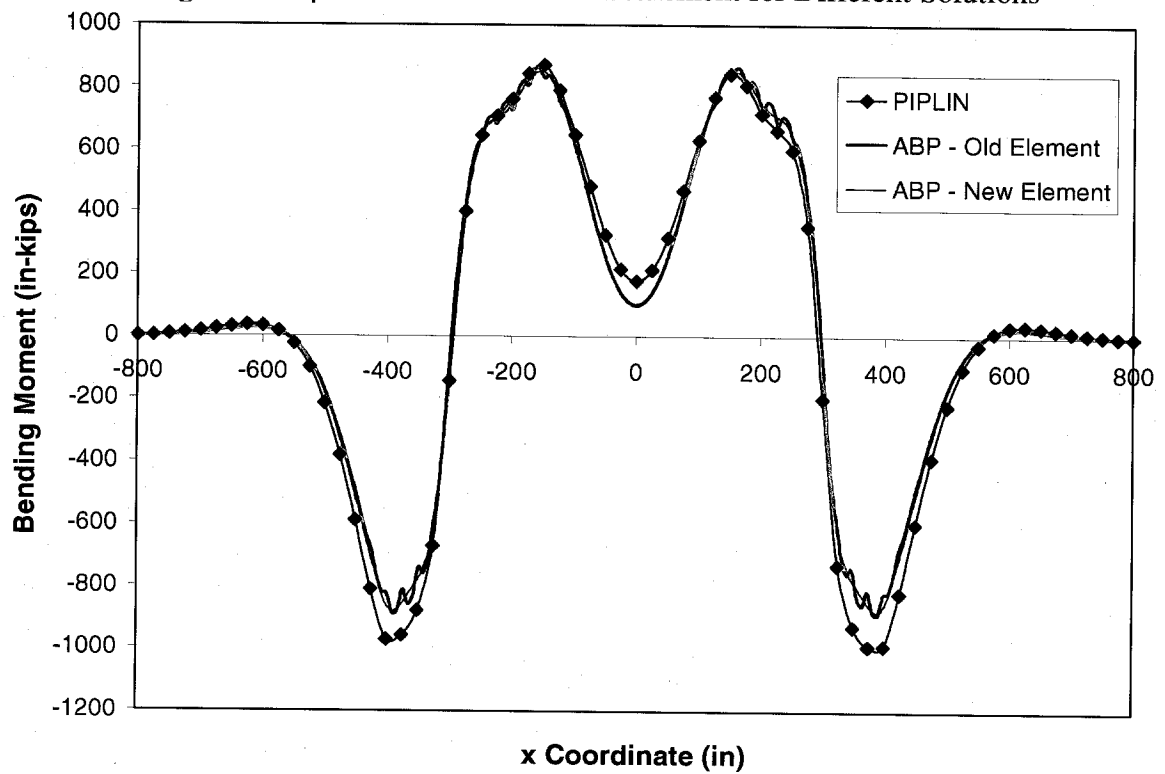


Fig. 4.16  Pipe Bending Moment at 40" of Settlement for Different Solutions

124
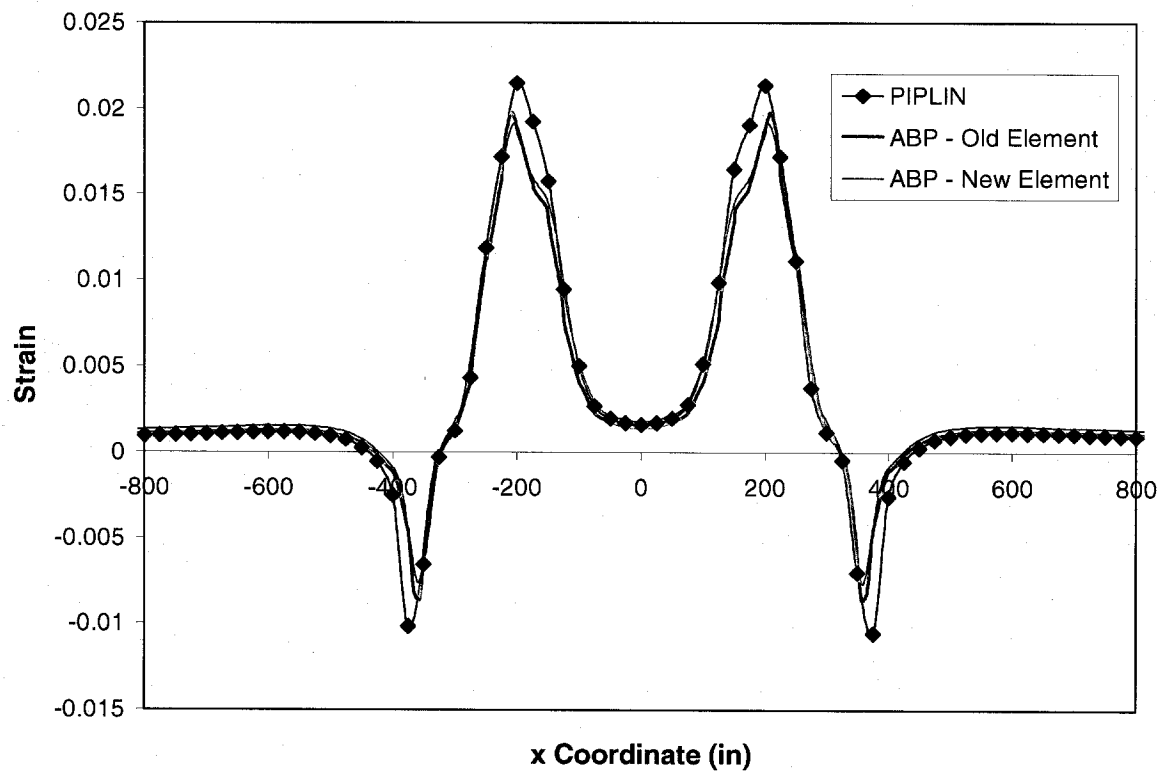
Fig. 4.17 Bottom Strain Distribution at 40" of Settlement for Different Solutions
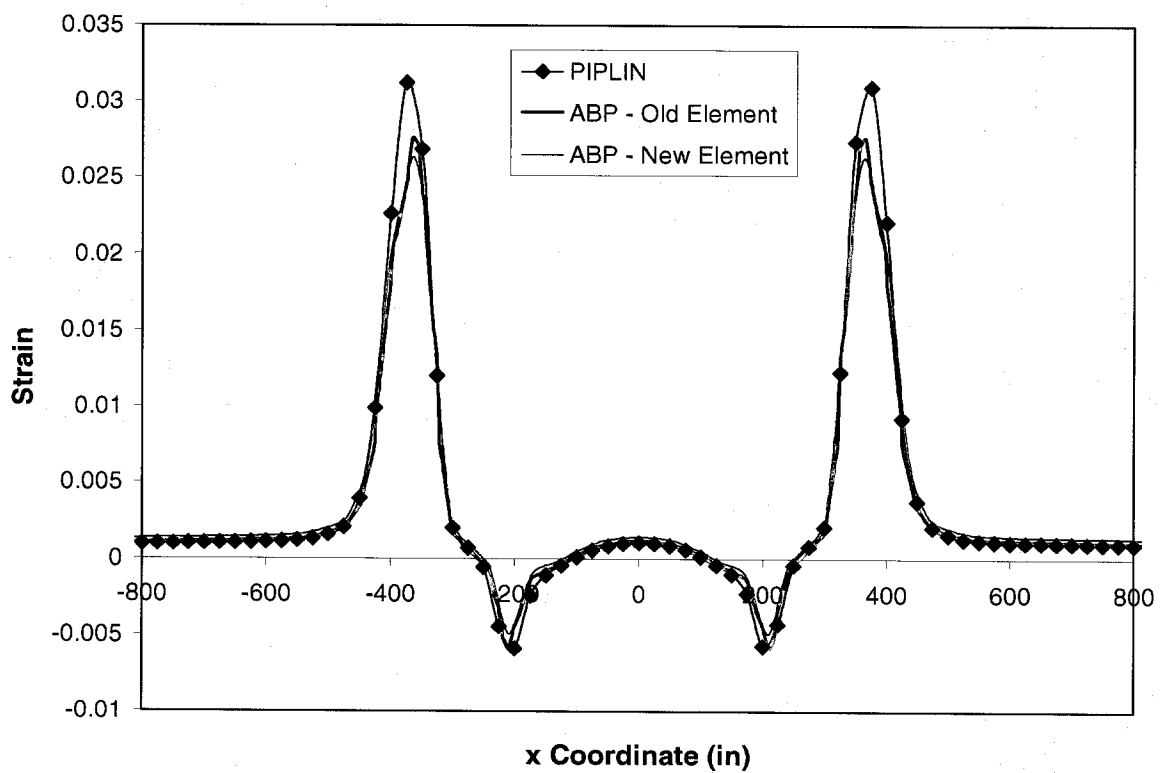


Fig. 4.18 Top Strain Distribution at 40" of Settlement for Different Solutions

125
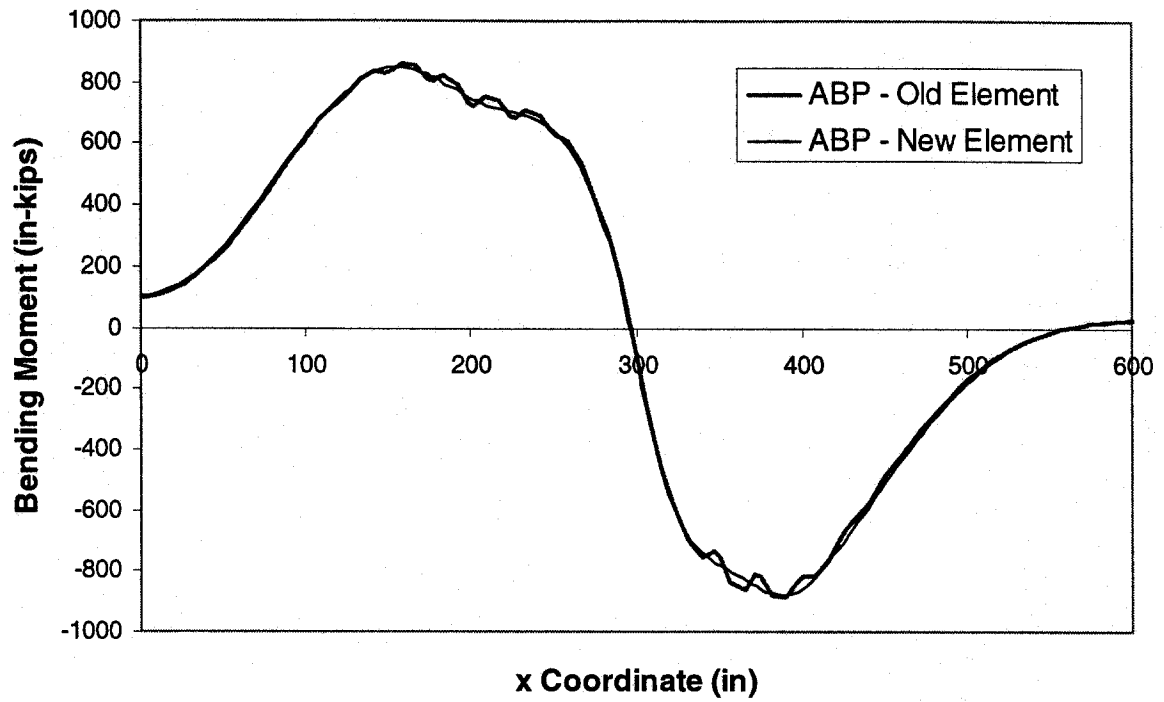
Fig. 4.19 Bending Moment Response at 40" of Settlement for ABP Old and New Elements
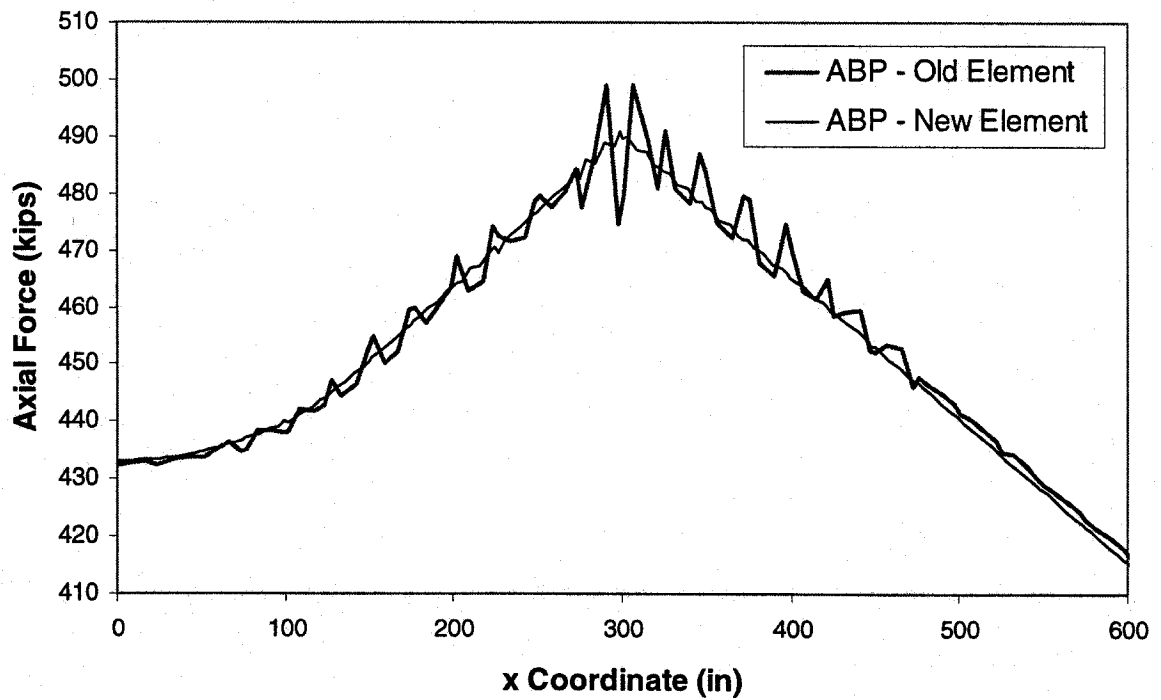


Fig. 4.20 Axial Force Response at 40" of Settlement for ABP Old and New Elements

# CHAPTER 5. THERMAL BUCKLING ANALYSIS

## 5.1 INTRODUCTION

This chapter describes the thermal buckling formulation implemented in the finite element formulation. The significance of thermal buckling analysis is in situations where the pipe undergoes relatively large temperature changes. This is usually due to the large difference between the pipe temperature upon the completion of the pipeline construction and the temperature of the pipe in service. This is of particular importance for pipelines in arctic and sub-arctic areas, which are normally constructed in winter months and, depending on the fluid temperature, can experience high temperatures in service. In this case, the thermal buckling could occur in the summer, when the ground is not frozen , and thus, provides much less resistance to the upheaval than does the frozen ground in the winter months. In particular, when the pipe passes through muskeg areas or regions that can turn into marshland in the summer time, the chance of thermal buckling increases. This is because, in this case, the ground can provide little resistance against large pipe deformation.

Submarine pipelines that carry fluids at high temperature, such as the oil lines of North Sea, are also susceptible to thermal buckling. The main cause of the thermal buckling is the fact that the fluid in the pipe is much hotter than the surrounding sea water. In the past two decades, such pipelines have suffered some well-publicized thermal buckling failures resulting in substantial financial losses in terms of repair and replacement costs in addition to lost production. These pipelines have undergone two different types of thermal buckling. First is upheaval buckling, which occurs in a vertical plane and normally results in emerging of the pipe out of the ground or sea bed. Second is the snaking phenomenon, which causes the pipe to buckle in a horizontal plane leading to an S-shape pipe configuration.

This chapter first describes the physical phenomenon of thermal buckling. Then the formulation of thermal analysis is presented. This chapter ends with three examples verifying the thermal analysis formulation.

## 5.2 THERMAL BUCKLING PHENOMENON

When a pipeline operated at a higher temperature than the ambient temperature at the time of installation, it tends to expand. However, if the line is restrained from expansion,

127

for example by soil friction, the pipe is subjected to an axial compressive load. For a buried (i.e., trenched or covered) pipeline, the lateral (horizontal) soil resistance normally exceeds the vertical uplift resistance, provided by the pipe's weight (or submerged weight) and the soil cover. In this case, as Fig. 5.1 shows, the buried pipe moves up in the vertical plane, which in favorable circumstances, leads to emerging of the pipe out of the ground.

Ju and Kyriakides (1988) summarized the results of pervious studies on upheaval buckling phenomenon. They conclude, as shown in Figs. 5.2 and 5.3, that for both fictional and frictionless soils, the perfect geometry (i.e., zero out-of-straightness) does not possess a bifurcation load. In other words, the stable pre-buckling response and the unstable post-buckling response intersect only at an infinite value of axial load. Moreover, in a frictionless case, as shown in Fig. 5.2, the post-buckling response is totally unstable (Ju and Kyriakides, 1988). However, in a frictional case, as shown in Fig. 5.3, the post-buckling response is characterized by a minimum temperature rise, $\Delta T_m$, after which the post-buckling response becomes stable.

As both Figs. 5.3 and 5.3 show, in the presence of an initial out-of-straightness (i.e., imperfect geometry), the uplift response in characterized by a limit temperature rise, $\Delta T_{cr}$. Moreover, an initial temperature rise, $\Delta T_i$, is required to initially lift the pipe off the ground. Then upon reaching the critical temperature rise, $\Delta T_{cr}$, the pipe buckles. To follow the downward static equilibrium path requires a drop in temperature upon reaching $\Delta T_{cr}$, which does not normally occur for an actual pipeline. Thus, in reality, once the temperature reaches $\Delta T_{cr}$, the pipe snaps through dynamically to reach the upward, stable post-buckling curve (see Fig. 5.3).

## 5.3 THERMAL ANALYSIS SOLUTION

### 5.3.1 Introduction

The thermal analysis is formulated based on the isoparametric $C^1$ beam element introduced in Chapter 2, the elastic-plastic constitutive relationships outlined in Chapter 3, and the pipe-soil interaction model described in Chapter 4. The arc-length solution technique for *applied loads*, as discussed in Section 2.10.3, has been modified to be employed in the thermal solution. The details of the formulation are presented in the following sections.

128

## 5.3.2 Thermal Load Vector

Temperature change, as loading condition, occurs independently from any other load, such as applied loads and ground settlement. Thus in this formulation, temperature is the only loading agent subject to variation. Moreover, the arc-length technique, introduced later in this chapter, also requires the temperature to be the only varying load. The temperature change is assumed to be uniform along the pipeline.

The contributions of the temperature change in the stiffness matrix and load vector are determined using the resulting thermal strain, $E_{ij}^T$:

$$^t E_{ij}^T = \alpha \; ^t\Delta T \; \delta_{ij} \tag{5.1}$$

where $^t E_{ij}^T$ = The ij component of the thermal strain at time t

$\quad \alpha$ = Thermal expansion coefficient of the pipe material

$\quad ^t\Delta T$ = The Temperature rise at time t

$\quad \delta_{ij}$ = Kronecker delta = $\begin{cases} 0 & \text{when } i \neq j \\ 1 & \text{when } i = j \end{cases}$

Assuming the equilibrium configuration has been obtained at time t corresponding to a temperature rise of $^t\Delta T$, the objective here is to find the equilibrium configuration at time t+$\Delta$t corresponding to an incremented temperature rise of $^{t+\Delta t}\Delta T$:

$$^{t+\Delta t}\Delta T = {}^t\Delta T + \Delta T \tag{5.2}$$

where $\Delta T$ is the increment of the temperature rise. Considering the virtual work equation expressed by Eq. (2.5), the incremental stress, $_t S_{ij}$ becomes

$$_t S_{ij} = {}_t C_{ijrs}^{EP} \left( {}_t E_{rs} - {}_t E_{rs}^T \right) \tag{5.3}$$

This will add a thermal term, $I_T$, to the equation of virtual work:

$$I_T = -\int_{{}^tV} {}_t C_{ijrs}^{EP} \; {}_t E_{rs}^T \; \delta_t E_{ij} \; d^t V \tag{5.4}$$

Whereby Equation (2.6) becomes

$$I_T + \int_{{}^tV} {}_t C_{ijrs}^{EP} \; {}_t e_{rs} \; \delta_t e_{ij} \; d^t V + \int_{{}^tV} {}^t\sigma_{ij} \; \delta_t \eta_{ij} \; d^t V = \delta^{t+\Delta t} W_{ext} - \int_{{}^tV} {}^t\sigma_{ij} \; \delta_t e_{ij} \; d^t V \tag{5.5}$$

129

However, the term $I_T$ needs to be linearized and the stiffness and load contributions extracted.

As concluded in Section 2.6, only the longitudinal stress and strain need to be considered in the virtual work equation of the finite element formulation employed in this study. Therefore, also incorporating Eqs. (2.4b) and (5.2), thermal term, $I_T$, can be written as

$$I_T = -\alpha\ {}^t\Delta T \left( \int_{{}^t V} {}_t C^{EP}\ \delta_t e_{11}\ d\ {}^t V \right) - \alpha\ {}^t\Delta T \left( \int_{{}^t V} {}_t C^{EP}\ \delta_t \eta_{11}\ d\ {}^t V \right) \qquad (5.6)$$

Since $\Delta T$ itself is an unknown to be determined in the iteration procedure, the second term in Eq. (5.6) is of the second order, and therefore, is dropped from the linearized equilibrium equation. Thus, retaining only its first term, Equation (5.6) reduces to

$$I_T = -\alpha\ {}^t\Delta T \left( \int_{{}^t V} {}_t C^{EP}\ \delta_t e_{11}\ d\ {}^t V \right) \qquad (5.7)$$

Substituting for ${}_t \tilde{e}_{11}$ in Eq. (5.7) using Eqs. (2.64) and (2.68) yields $I_T$ as

$$I_T = -\alpha\ {}^t\Delta T \sum_e \langle \delta u \rangle \left( \int_{{}^t L_e} ({}^t D_1 \{{}^t B_1^L\} + {}^t D_2 \{{}^t B_2^L\}) d\ {}^t s \right) \qquad (5.8)$$

Thus, after linearization, $I_T$ contributes only to the load vector and not the stiffness matrix. Moreover, Equation (5.8) indicates that the thermal load vector depends on the most recent geometry (through $\{{}^t B_1^L\}$ and $\{{}^t B_2^L\}$) and the state of stress around the cross-section (through ${}^t D_1$ and ${}^t D_2$). Therefore, unlike the reference load in an *applied load* analysis, the thermal reference load varies as the pipe deforms and/or plastifies. Consequently, the thermal reference load is updated for each iteration within a load step.

### 5.3.3 Far-field Condition

In many cases of pipeline analysis, a characteristic length of an infinitely long pipe undergoes most of the transverse displacements and/or buckling. In these situations, it is computationally economical if only the characteristic length of the pipeline can be modeled by applying appropriate end boundary conditions. *Far-field condition* (Andrew

Palmer and Associates, 1993) is the term referring to this end boundary condition that obviates the modeling of a very long length of pipeline.

The essence of far-field condition is to apply appropriate end axial forces given certain values of end axial displacements. It is assumed that the original pipe is infinitely long. However, since the axial friction dies down rapidly with increasing distance from the characteristic segment of the pipe, a long enough pipe can effectively be considered of infinite length for the far-field condition. Furthermore, it is assumed that the infinite lengths of pipe curtailed from the model are effectively straight and remain elastic throughout the analysis.

In the following derivation, the pipe is assumed to have an initial lay tension force of $N_0$, an internal pressure of p, and a temperature rise of $\Delta T$. Moreover, as Fig. 5.4 shows, the left and right ends of the model are assumed to have axial displacements of $u_0$ and $u_L$ (subscript L referring to the model length), respectively. In a typical analysis, the two ends of the model move inwards (towards each other). Therefore $u_0$ and $u_L$ normally have positive and negative values, respectively. By the same token, $F_0$ and $F_L$ are normally positive and negative, respectively. In the analysis, each of these end forces is considered to be tangent to the pipe axis in the initial configuration. Thus the directions of the end forces remain constant throughout the analysis. The choice of the direction for the end forces as tangent to the pipe axis in the most recent configuration would constitute the end forces as follower forces, which are prone to cause solution instabilities.

Focusing on the infinitely long pipe segment to the right of the model, the axial equilibrium equation for the free body diagram in Fig. 5.4d can be written as

$$N + dN = N + f\,dx \tag{5.9}$$

Hence,

$$\frac{dN}{dx} = f \tag{5.10}$$

For the infinitely long pipe segments to the left and right of the model, which are assumed to remain elastic, the total axial force at a given cross-section can be obtained by summing all of the individual effects:

$$N = N_0 + EA\left(\frac{du}{dx} - \varepsilon_0\right) \tag{5.11}$$

131

where u is axial displacement along the pipe and $\varepsilon_0$ is the sum of the strains due to the temperature change, $\Delta T$, and the internal pressure, p, if the pipe was free to deform axially (Yoosef-Ghodsi et al, 1994):

$$\varepsilon_0 = \alpha \Delta T - \frac{\nu}{E} \sigma_\theta \qquad (5.12)$$

Substituting for N from Eq. (5.11) into Eq. (5.10) yields

$$f = EA \frac{d^2 u}{dx^2} \qquad (5.13)$$

The solution from this point onward depends on whether or not the soil friction remains elastic all along the infinitely long segment. These cases are treated separately as follows.

**(a) Elastic soil friction**

When soil friction remains elastic all along the infinitely long segment, the friction at any point can be expressed as

$$f = k_L u \qquad (5.14)$$

Substituting for f from Eq. (5.14) into Eq. (5.13) yields

$$EA \frac{d^2 u}{dx^2} - \psi^2 u = 0 \qquad (5.15)$$

where

$$\psi = \sqrt{\frac{k_L}{EA}} \qquad (5.16)$$

The general solution for the differential equation (Eq. (5.15)) is

$$u = C_1 e^{-\psi x} + C_2 e^{\psi x} \qquad (5.17)$$

By applying the following boundary conditions

$$u(0) = u_L \qquad (5.18a)$$

$$u(\infty) = 0 \qquad (5.18b)$$

the solution turns into

$$u = u_L e^{-\psi x} \qquad (5.19)$$

Substituting for u from Eq. (5.19) into Eq. (5.11) yields

$$N(x) = N_0 + EA\left(-\psi u_L e^{-\psi x} - \varepsilon_0\right) \tag{5.20}$$

Hence, the axial force at the right end of the model becomes

$$F_L = N(0) = N_0 - EA\left(\psi u_L + \varepsilon_0\right) \tag{5.21}$$

Similarly, the axial force at the left end of the model can be shown to be

$$F_0 = -N_0 - EA\left(\psi u_0 - \varepsilon_0\right) \tag{5.22}$$

### (b) Elastic-plastic soil friction

The pipe axial displacement along the infinitely long segments, u, continually decreases with distance from the model ends. Thus, when the axial displacement at a model end exceeds the soil longitudinal yield displacement, $\Delta_{Ly}$, a portion of the infinitely long segment adjacent to the model end will have a plastified soil friction. Therefore, over the length with plastic soil friction, specified by $x_0$ as per Fig. 5.4c, the soil friction is constant, at the yield value for the soil friction, $F_{Ly}$:

$$f = \text{sign}(u_L)F_{Ly} \quad \text{for } x \leq x_0 \tag{5.23}$$

Substituting for f from Eq. (5.23) into Eq. (5.13) yields

$$\frac{d^2 u}{dx^2} = \beta \quad \text{where } \beta = \text{sign}(u_L)\frac{F_{Ly}}{EA} \tag{5.24}$$

The solution to the above differential equation is

$$u = \frac{\beta x^2}{2} + C_3 x + C_4 \tag{5.25}$$

By applying the following boundary conditions

$$u(0) = u_L \tag{5.26a}$$

$$u(x_0) = \text{sign}(u_L)\Delta_{Ly} \tag{5.26b}$$

the constants, $C_3$ and $C_4$ become

$$C_4 = u_L \tag{5.27a}$$

$$C_3 = \frac{1}{x_0}\left(\text{sign}(u_L)\Delta_{Ly} - u_L - \frac{\beta x_0^2}{2}\right) \tag{5.27b}$$

For $x \geq x_0$ the soil friction is elastic. Thus, similarly to the elastic soil friction case, the governing differential equation is Eq. (5.15) with the solution:

$$u = C_5 e^{-\psi x} + C_6 e^{\psi x} \tag{5.28}$$

133

By applying the following boundary conditions

$$u(x_0) = \text{sign}(u_L)\Delta_{Ly} \tag{5.29a}$$

$$u(\infty) = 0 \tag{5.29b}$$

the solution turns into

$$u = \text{sign}(u_L)\Delta_{Ly}\, e^{\psi(x_0 - x)} \tag{5.30}$$

The unknown $x_0$ is determined from the condition that the axial force, N, approaching from either side at $x = x_0$ should match up. Considering Eq. (5.11), this condition require that $\dfrac{du}{dx}$ have the same value at $x = x_0$ approaching from either side. Incorporating u from Eqs. (5.25) and (5.30) into this condition results in

$$\beta x_0 + C_3 = -\psi\,\text{sign}(u_L)\Delta_{Ly} \tag{5.31}$$

Substituting for $C_3$ from Eq. (5.27b) into Eq. (5.31) yields

$$\beta x_0 + \frac{1}{x_0}\left(\text{sign}(u_L)\Delta_{Ly} - u_L - \frac{\beta x_0^2}{2}\right) = -\psi\,\text{sign}(u_L)\Delta_{Ly} \tag{5.32}$$

Choosing the positive root of the equation, $x_0$ can be expressed as

$$x_0 = \frac{\text{sign}(u_L)}{\beta}\left(\sqrt{\psi^2 \Delta_{Ly}^2 + 2\beta(u_L - \text{sign}(u_L)\Delta_{Ly})} - \psi\Delta_{Ly}\right) \tag{5.33}$$

which can be simplified to

$$x_0 = \frac{\text{sign}(u_L)}{\beta}\left(\sqrt{|\beta|(2|u_L| - \Delta_{Ly})} - \psi\Delta_{Ly}\right) \tag{5.34}$$

Using Eq. (5.11), the axial force at the right end of the model becomes

$$F_L = N(0) = N_0 + EA\left(\frac{du}{dx}(0) - \varepsilon_0\right) \tag{5.35}$$

Substituting for u from Eq. (5.25) into Eq. (5.35) gives

$$F_L = N(0) = N_0 + EA(C_3 - \varepsilon_0) \tag{5.36}$$

The constant $C_3$ can be obtained using Eqs. (5.31) and (5.34) as

$$C_3 = -\text{sign}(u_L)\sqrt{|\beta|(2|u_L| - \Delta_{Ly})} \tag{5.37}$$

Substituting for $C_3$ from Eq. (5.37) into Eq. (5.36) yields

$$F_L = N(0) = N_0 - EA\varepsilon_0 - \text{sign}(u_L)\left(\sqrt{EAF_{Ly}\left(2|u_L| - \Delta_{Ly}\right)}\right) \qquad (5.38)$$

Similarly, the axial force at the left end of the model can be shown to be

$$F_0 = -N_0 + EA\varepsilon_0 - \text{sign}(u_0)\left(\sqrt{EAF_{Ly}\left(2|u_0| - \Delta_{Ly}\right)}\right) \qquad (5.39)$$

## 5.3.4 Solution Techniques

Three solution techniques were implemented for the thermal analysis. They are:

    a)   modified arc-length method

    b)   linearized arc-length method

    c)   displacement control method

These methods are described in the following subsections.

### 5.3.4.1 Modified Arc-Length Method

The modified arc-length method utilized in the thermal analysis has been devised based on the modified arc-length method used in the applied load analysis (as outlined in Section 2.10.3) with some enhancements. There are also differences due to the varying nature of the thermal reference load.

The temperature change at any time, $\Delta T$, is assumed to be a multiple of a reference temperature change, $\theta$. Thus at time t:

$$^t\Delta T = {}^t\Delta\lambda\,\theta \qquad (5.40)$$

where $^t\Delta\lambda$ is the thermal load vector at time t. Hence the thermal reference load, $\hat{P}^{th}$, is obtained from Eq. (5.8) by substituting $\theta$ for $^t\Delta T$ and a sign change:

$$^t\hat{P}^{th} = \alpha\,\theta \sum_e \left( \int_{{}^tL_e} \left( {}^tD_1\{{}^tB_1^L\} + {}^tD_2\{{}^tB_2^L\} \right) d\,^ts \right) \qquad (5.41)$$

The sign change is because the thermal integral, $I_T$, which contributes to the load vector only, is moved to the other side of the virtual work equation. Note that the above sum over all of the elements arranges the 12x1 vectors for the elements into a much larger-dimension vector for the whole pipeline. In this process, only the items relevant to the same degrees of freedom (at the junction nodes of adjacent elements) are added together.

135

If the option of far-field condition is applied at a pipe end, an axial force of magnitude $EA\alpha\theta$ (in the same direction as the end axial force due to far-field condition) needs to be added to the thermal reference load vector. This would account for the thermal effect of the infinitely long continuation of pipe not included in the model.

As an enhancement to the modified arc-length method of Section 2.10.3, an attempt is made to add the option of a non-dimensionalized constraint equation. The non-dimensionalizing process uses the norm of displacements and the load factor at the end of the first load step. Therefore, in practice, the non-dimensionalizing option can start from the second load step.

The non-dimensionalized constraint equation is built on the basis of the constraint equation expressed by Eq. (2.122) as

$$\frac{{}^{t}\Delta\mathbf{u}_{j+1}^{T}\ {}^{t}\Delta\mathbf{u}_{j+1}}{{}^{1}\Delta\mathbf{u}^{T}\ {}^{1}\Delta\mathbf{u}} + \frac{\zeta}{R^2}\frac{{}^{t}\Delta\lambda_{j+1}^2}{{}^{1}\Delta\lambda^2} = \Delta l_0{}^2 \tag{5.42}$$

where ${}^{1}\Delta\mathbf{u}$ and ${}^{1}\Delta\lambda$ are the vector of displacements and load factor at the end of the first load step, respectively, $\Delta l_0$ is the arc length, and R is a normalizing factor for the ratio $\dfrac{{}^{1}\Delta\lambda^2}{{}^{1}\Delta\mathbf{u}^{T}\ {}^{1}\Delta\mathbf{u}}$. For the first load step, the ratio $\dfrac{{}^{1}\Delta\lambda^2}{{}^{1}\Delta\mathbf{u}^{T}\ {}^{1}\Delta\mathbf{u}}$ tends to be typically higher than the rest of the load steps. Thus by choosing a value for R between zero and one, the ratio $\dfrac{R^2\ {}^{1}\Delta\lambda^2}{{}^{1}\Delta\mathbf{u}^{T}\ {}^{1}\Delta\mathbf{u}}$ can be made to be more representative of a typical load step.

In order to use the same procedures and formulas as used for the modified arc-length method (see Section 2.10.3) for the non-dimensionalized option, the constraint equation expressed by Eq. (5.42) needs to be converted to a form similar to Eq. (2.122). Equation (5.42) can be rewritten as

$$ {}^{t}\Delta\mathbf{u}_{j+1}^{T}\ {}^{t}\Delta\mathbf{u}_{j+1} + \zeta\frac{{}^{1}\Delta\mathbf{u}^{T}\ {}^{1}\Delta\mathbf{u}}{R^2\ {}^{1}\Delta\lambda^2}{}^{t}\Delta\lambda_{j+1}^2 = \left({}^{1}\Delta\mathbf{u}^{T}\ {}^{1}\Delta\mathbf{u}\right)\Delta l_0{}^2 \tag{5.43}$$

This results in the following scaling of the load factor and arc length:

$$\prescript{t}{}{\Delta\mu}_{j+1}^2 = \frac{\prescript{1}{}{\Delta u}^T \, \prescript{1}{}{\Delta u}}{R^2 \, \prescript{1}{}{\Delta\lambda}^2} \prescript{t}{}{\Delta\lambda}_{j+1}^2 \qquad (5.44)$$

$$\Delta l^2 = \left(\prescript{1}{}{\Delta u}^T \, \prescript{1}{}{\Delta u}\right)\Delta l_0^2 \qquad (5.45)$$

where $\prescript{t}{}{\Delta\mu}_{j+1}$ and $\Delta l$ are the new, scaled load factor and arc lengths, respectively.

In order to keep the temperature change constant while scaling the load factor, the reference temperature change, $\theta$, needs to be scaled inversely:

$$\theta_F = \frac{R \, \prescript{1}{}{\Delta\lambda}}{\sqrt{\prescript{1}{}{\Delta u}^T \, \prescript{1}{}{\Delta u}}} \theta \qquad (5.46)$$

where $\theta_F$ is the final value of the reference temperature change.

The new arc length value, $\Delta l$, is determined by substituting $\prescript{1}{}{\Delta u}$ and $\prescript{1}{}{\Delta\lambda}$ for $\prescript{t}{}{\Delta u}_{j+1}$ and $\prescript{t}{}{\Delta\lambda}_{j+1}$, respectively (note that $\Delta l$ cannot be obtained from Eq. (5.45) since $\Delta l_0$ is unknown itself):

$$\Delta l = \sqrt{\prescript{1}{}{\Delta u}^T \, \prescript{1}{}{\Delta u}\left(1 + \frac{\zeta}{R^2}\right)} \qquad (5.47)$$

Another feature implemented in the modified arc-length technique is the self-adaptive relaxation and tightening of the convergence tolerances. As convergence becomes more difficult (i.e., reaching a maximum number of iterations with no convergence), the first measure taken is to reduce the arc length. If convergence is not achieved before reaching the minimum arc length value, the tolerances are relaxed until convergence is obtained. The analyst can prescribe a limit to the extent the tolerances can be relaxed. The reverse is done when the solution seems to be carried on more easily. In other words, when the convergence criteria are met by a large margin, the tolerances are reduced accordingly.

### 5.3.4.2 Linearized Arc-Length Method

The basic difference between the linearized arc-length method and the modified arc-length method, described in the previous section, is that the constraint equation is linearized in the former to avoid solving a quadratic equation. This eliminates problems

137

associated with choosing the right root or dealing with the complex roots of a quadratic equation (such as Eq. (2.124), as discussed in Section 2.10.3).

Following Schweizerhof et al. (1986), the constraint equation can be expressed as

$$f_{j+1}\left(\Delta u_{j+1}, \Delta\lambda_{j+1}\right) = \Delta u_{j+1}^T \, \Delta u_{j+1} + \zeta\Delta\lambda_{j+1}^2 - \Delta l^2 = 0 \tag{5.48}$$

Note that, since the constraint equation is being linearized here, the original constraint equation will not exactly hold during the iterations and upon convergence. Thus, Equation (5.48) only signifies a relationship that will be enforced as closely as possible in a Newton iterative scheme. Hence, the function f will not be neglected in the following derivation. Considering Eqs. (2.114) and (2.115), the function f in Eq. (5.48) can be expanded in linear terms as

$$f_{j+1}\left(\Delta u_{j+1}, \Delta\lambda_{j+1}\right) = f_j\left(\Delta u_j, \Delta\lambda_j\right) + \frac{\partial f_j}{\partial \Delta u_j} du_{j+1} + \frac{\partial f_j}{\partial \Delta\lambda_j} d\lambda_{j+1} = 0 \tag{5.49}$$

This results in the linear equation:

$$2\Delta u_j^T \, du_{j+1} + 2\zeta\Delta\lambda_j \, d\lambda_{j+1} = -f_j \tag{5.50}$$

Substituting for $du_{j+1}$ from Eq. (2.118) into Eq. (5.50) gives the increment of the load factor, $d\lambda_{j+1}$ as

$$d\lambda_{j+1} = -\frac{\dfrac{f_j}{2} + \Delta u_j^T \, du_{j+1}^{II}}{\Delta u_j^T \, du_{j+1}^I + \zeta\Delta\lambda_j} \tag{5.51}$$

The rest of the equations used in the linearized arc-length method are identical to those used in the modified arc-length method.

### 5.3.4.3 Displacement Control Method

The basic difference between the displacement control method and the arc-length methods is in the constraint equation they use (Ramm, 1980). The displacement control method is similar to the arc-length methods in other respects. The constraint equation for the displacement control method can be expressed as

138

$$\mathbf{w}^T \Delta \mathbf{u}_{j+1} = \Delta d \qquad (5.52)$$

where $\Delta d$ is a prescribed value determining the size of the load step taken and $\mathbf{w}^T$ is a vector of carefully chosen weight factors. The weight vector can have zero members corresponding to the degrees of freedom that are intended to be excluded from the constraint equation. For example, in an upheaval buckling analysis, the analyst might choose to use only the transverse displacement of one node, which results in $\mathbf{w}^T$ having only one nonzero member associated with that displacement. If both displacements and rotation DOFs are to be included in the constraint equation, the weight factors can be chosen so as to compensate for the dimensional differences.

For the first iteration in a load step, incorporating Eq. (2.118) into Eq. (5.52) results in

$$\Delta \lambda_1 \, \mathbf{w}^T \, \Delta \mathbf{u}_1^I + \mathbf{w}^T \, \Delta \mathbf{u}_1^{II} = \Delta d \qquad (5.53)$$

This gives the initial value of the load factor change in the loading step as

$$\Delta \lambda_1 = \frac{\Delta d - \mathbf{w}^T \, \Delta \mathbf{u}_1^{II}}{\mathbf{w}^T \, \Delta \mathbf{u}_1^I} \qquad (5.54)$$

Thus, the iterations start with satisfying the constraint equation exactly. Having completed j iterations, the constraint equation for the $j+1^{st}$ iteration the can be written by expanding Eq. (5.52) as

$$\mathbf{w}^T \, \Delta \mathbf{u}_j + \mathbf{w}^T \, d\mathbf{u}_{j+1} = \Delta d \qquad (5.55)$$

Since the constraint equation has been exactly satisfied to his point, Equation (5.55) becomes

$$\mathbf{w}^T \, d\mathbf{u}_{j+1} = 0 \qquad (5.56)$$

Substituting for $d\mathbf{u}_{j+1}$ from Eq. (2.118) yields

$$d\lambda_{j+1} \, \mathbf{w}^T \, d\mathbf{u}_{j+1}^I + \mathbf{w}^T \, d\mathbf{u}_{j+1}^{II} = 0 \qquad (5.57)$$

This renders the increment of the load factor as

$$dλ_{j+1} = -\frac{\mathbf{w}^T d\mathbf{u}_{j+1}^{II}}{\mathbf{w}^T d\mathbf{u}_{j+1}^{I}} \quad (5.58)$$

The rest of the equations used in the displacement control method are identical to those used in the preceding arc-length methods.

## 5.4 VERIFICATION EXAMPLES

Three examples are presented in the following subsections to verify various aspects of the thermal analysis formulation.

### 5.4.1 Example 1: Elastic Buckling of Pressurized Pipe

In order to compare the ABP response with the theoretical buckling temperature, first the theoretical elastic buckling temperature for a pressurized pipe needs to be established. Internal pressure, by itself, is a destabilizing factor because, as discussed in Section 2.8.3, the internal pressure applies a lateral load, $q_p$, onto a bent pipe (see Eq. (2.87)).

Figure 5.5 shows an initially-straight pipe of length L and pinned-end supports subjected to an internal pressure of p. The goal here is to determine the critical value for p (i.e., the internal pressure causing buckling of the pipe). The bent pipe in Fig. 5.5 shows the buckled shape of the pipe, for which the equilibrium equation is expressed by equating the internal and external work values:

$$\underbrace{\frac{1}{2}\int_0^L q_p\, y\, dx}_{\text{External Work}} = \underbrace{\frac{1}{2}\int_0^L EI(y'')^2\, dx}_{\text{Internal Work}} \quad (5.59)$$

where from Eq. (2.87), $q_p$ can be expressed as

$$q_p = P_0\, y'' \quad (5.60)$$

Note that at the initiation of buckling the deformations are small, and hence, the pipe curvature, $\phi$, has been replaced with $y''$ (where y is the pipe deflection). Also it is reminded that $P_0 = \pi R_i^2 p$, in which $R_i$ is the pipe internal radius.

A close approximation for the buckled shape of the pipe can be expressed as

$$y = y_0 \sin\frac{\pi x}{L} \quad (5.61)$$

Substituting for $q_p$ and y from Eqs. (5.60) and (5.61), respectively, into Eq. (5.59) yields

140

$$(P_0)_{cr} \left( \frac{\pi}{L} \right)^2 y_0^2 \frac{L}{2} = EI \left( \frac{\pi}{L} \right)^4 y_0^2 \frac{L}{2} \qquad (5.62)$$

Hence,

$$(P_0)_{cr} = \underbrace{EI \left( \frac{\pi}{L} \right)^2}_{\text{Euler Buckling Load}} \qquad (5.63)$$

from which, the critical pressure is obtained as

$$p_{cr} = \frac{(P_0)_{cr}}{\pi R_i^2} = \frac{\pi EI}{(R_i L)^2} \qquad (5.64)$$

Equation (5.63) implies that, for a simply supported pipe, the buckling occurs when $P_0$ ($= \pi R_i^2 p$) reaches the Euler buckling load. It is also noted that, when a portion of a very long pipe is being considered (i.e., plane strain condition), the Poisson effect of the hoop stress due to the internal pressure partially relieves the destabilizing effect described above.

Figure 5.6 shows the layout of the pipe considered in this example. The pipe is 324.43 mm in outside diameter, 6.477 mm in wall thickness and 20 m in length. The model consists of six elements of equal length and 13 nodes. The simply-supported pipe is assumed to have far-field condition at the right end. This means that as the temperature rises, an axial load is applied at the right end of the model, simulating the effect of an infinitely long pipe segment. The pipe is assumed to be elastic with an elastic modulus of 200,000 MPa and a thermal expansion coefficient of 0.00001 per °C. Since this is a buckling problem being analyzed by a finite-element procedure, an initial imperfection needs to be applied to the model. To that purpose, the pipe is given an out-of-straightness rising linearly from zero at each end to 0.02 mm at the midspan of the model.

The critical temperature change for the elastic pipe is determined by superimposing the contributions of the temperature change, the destabilizing effect of internal pressure, and the Poisson effect. Thus,

$$\underbrace{EI \left( \frac{\pi}{L} \right)^2}_{\text{Euler Buckling Load}} = \underbrace{AE\alpha\Delta T}_{\text{Temperature Effect}} + \underbrace{\pi R_i^2 p}_{\substack{\text{Destabalizing Pressure} \\ \text{Effect}}} - \underbrace{A\nu \left( \frac{pR_i}{t} \right)}_{\text{Poisson Effect}} \qquad (5.65)$$

Hence, the critical temperature change is obtained as

141

$$\Delta T_{cr} = \frac{1}{AE\alpha}\left[EI\left(\frac{\pi}{L}\right)^2 - \pi R_i^2 p + A\nu\left(\frac{pR_i}{t}\right)\right] \qquad (5.66)$$

Two values of internal pressure are used in this example: 5 and 10 MPa. Equation (5.66) gives the critical temperature rise for these pressure values (5 and 10 MPa) as 19.783 °C and 8.374 °C, respectively.

Figure 5.7 shows the temperature change vs. midspan deflection response for the two pressure values in comparison with the theoretical values of critical temperature change. It can be seen that, using far-field condition, the finite element solution captures the critical temperature change precisely.

## 5.4.2 Example 2: Raoof and Maschner (1993) Test

Example 2 is an attempt to reproduce the results of an upheaval buckling experiment carried out by Raoof and Maschner (1993 and 1994). They tested a 90/10 Copper-Nickel-Iron (Kunifer 10) annealed pipe, 16 mm in outside diameter, and 1.05 mm in wall thickness. The pipe had a modulus of elasticity of 131,000 MPa and a thermal expansion coefficient of 0.000017 per °C. As Figure 5.8 shows, the specimen was 7 meters long and had a 'point' or 'prop' imperfection of 2 mm at the midspan. The overburden load (including the pipe and fluid weight) amounted to 0.009 N/mm. The specimen was heated gradually by pumping heated oil through it.

Since the buckling is expected to be elastic, the pipe is assumed to be elastic in the analysis. Moreover, since the relative pipe-soil displacements are expected to be small, the soil springs are assumed to be elastic. Based on the pipe embedment conditions in the experiment, the following stiffness values for the soil springs are considered:

♦ Bearing spring stiffness = 100 N/mm/mm (almost rigid)
♦ Longitudinal spring stiffness = 0.003 N/mm/mm
♦ Uplift spring stiffness = 0 (virtually no spring)

Figure 5.9 shows the temperature change vs. midspan deflection response for the above model in comparison with the experimental response obtained by Raoof and Maschner (1993 and 1994). These authors also developed a closed-form theoretical response based on the works by Hobbs and Liang (1989) and Ballet and Hobbs (1992) as shown in Fig. 5.9. In the ABP model, the prop imperfection was generated by an initial

settlement analysis so as to account for the pipe residual stresses in the propped configuration. The pipe was discretized by 28 elements in the ABP model.

Figure 5.9 indicates that the specimen snaps dynamically upon reaching the critical temperature, settling back onto a post-buckling equilibrium path.    Both the ABP response and the closed-form theoretical response closely approximate the critical temperature change.  Beyond buckling, the specimen, as expected, snaps through rather than following the static equilibrium paths of theoretical solutions.  Nevertheless, the two theoretical solutions agree very well on the descending branch down to the minimum point.  The parting of the two solutions beyond the minimum point may be due to the fact that the closed-form solution is based on small deformations – an assumption becoming less valid as one proceeds up the ascending branch.  However, a close agreement is observed between the ABP and experimental responses along the ascending post-buckling branch above the critical buckling temperature change.

### 5.4.3 Example 3: Validation by Beams on Elastic Foundation Theory

In order to compare the ABP response with the theoretical buckling temperature for an embedded pipe, first the theoretical buckling temperature for a beam on elastic foundation needs to be established. The critical value of the axial compressive force for a simply-supported beam on elastic foundation, as show in Fig. 5.10, can be expressed as (Hetenyi, 1974)

$$N_{cr} = EI\left(\frac{n\pi}{L}\right)^2 + k\left(\frac{L}{n\pi}\right)^2 \qquad (5.67)$$

where k is modulus of the foundation and n is the number of half-waves that form after buckling.  For given values of k, L, and EI, the value of n is determined in such a way as to make the above expression for $N_{cr}$ a minimum.

Figures 5.11 and 5.12 show the layout of the models considered in this example (Models A and B).  Both pipes are 324.43 mm in outside diameter and 6.477 mm in wall thickness.  The pipes are assumed to be elastic with an elastic modulus of 200,000 MPa and a thermal expansion coefficient of 0.0000116 per °C.  Models A and B are 10 and 18 meters long, and discretized into 6 and 9 elements, respectively.

The critical load of Eq. (5.67) is based on the assumption that the foundation reacts in both bearing and uplift directions (i.e., both lateral directions).  Thus, in order to model

143

a foundation modulus of 1 N/mm/mm, both bearing and uplift springs are given the stiffness value of 1 N/mm/mm. Moreover, following the assumptions of the theory of beams on elastic foundation leading to Eq. (5.67), the lateral springs are considered elastic and no longitudinal springs are included in the ABP models.

For a buckling problem to be analyzed by a finite-element procedure, an initial imperfection needs to be applied to the model. Figures 5.11 and 5.12 show the out-of-straightness patterns applied to Models A and B, respectively.

The simply-supported pipe is assumed to have far-field condition at the right end. This means that as the temperature rises, a compressive axial load proportional to the temperature change is applied at the right end of the model:

$$N = AE\alpha\Delta T \tag{5.68}$$

Hence, The critical (i.e., buckling) temperature is obtained by substituting N from Eq. (5.68) into Eq. (5.67) as

$$\Delta T_{cr} = \frac{I}{A\alpha}\left(\frac{n\pi}{L}\right)^2 + \frac{k}{EA\alpha}\left(\frac{L}{n\pi}\right)^2 \tag{5.69}$$

Based on Eq. (5.69), $\Delta T_{cr}$ is minimum at $n = 2$ (i.e., 2 half-waves) for Model A, resulting in $\Delta T_{cr} = 599.0\,^\circ C$. For Model B, $\Delta T_{cr}$ is minimum at $n = 3$ (i.e., 3 half-waves), which results in $\Delta T_{cr} = 541.8\,^\circ C$.

Figures 5.13 and 5.14 show the temperature change vs. maximum deflection response for the Models A and B, respectively, in comparison with the theoretical values of critical temperature change. It can be seen that the finite element solution captures the critical temperature change in accordance to the beams on elastic foundation theory. Figures 5.15 and 5.16 show the final deformed configurations of the pipe in Models A and B, respectively. The number of half-waves for Models A and B is two and three, respectively. These match the numbers of half-waves predicted for the two models by the beams on elastic foundation theory.

**IOS** (Initial Out of Straightness)
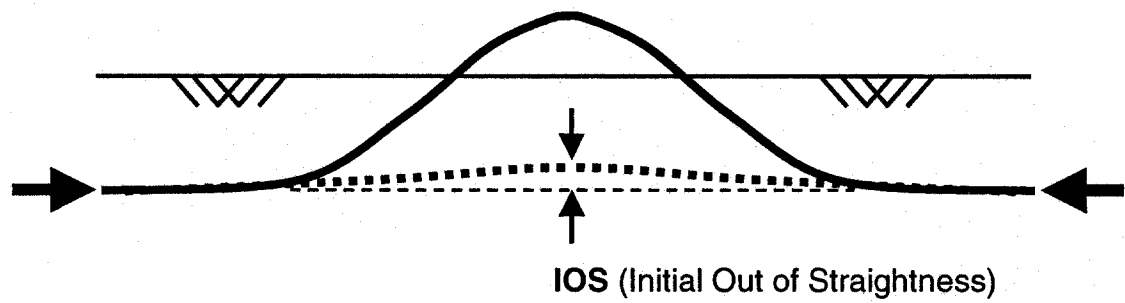
Fig. 5.1  Upheaval Buckling Mechanism
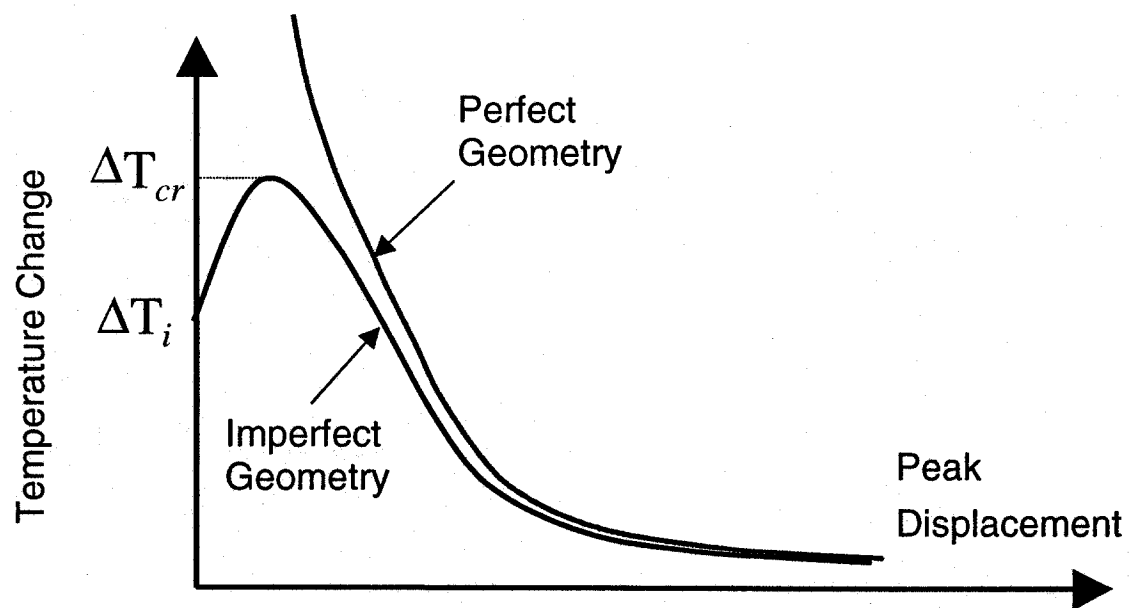


Fig. 5.2  Typical Temperature-Displacement Relationship for Frictionless Trench

145
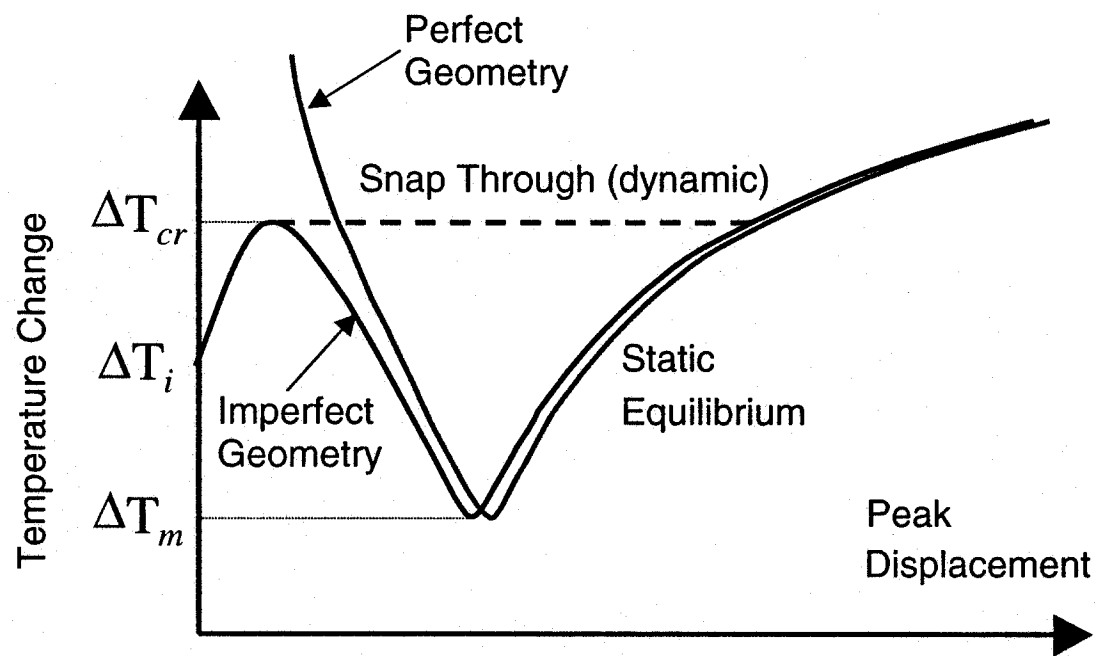
Fig. 5.3 Typical Temperature-Displacement Relationship for Frictional Trench
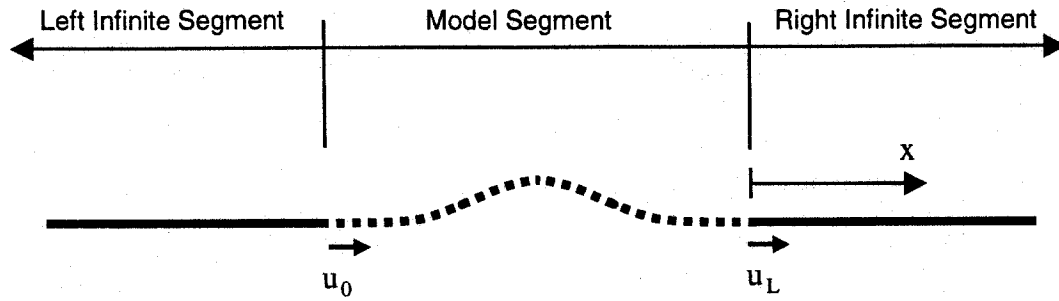
(a) Infinite Pipeline
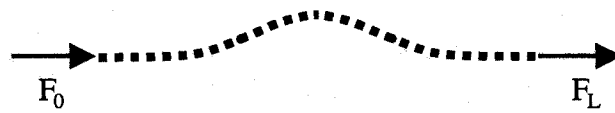


(b) Model Segment
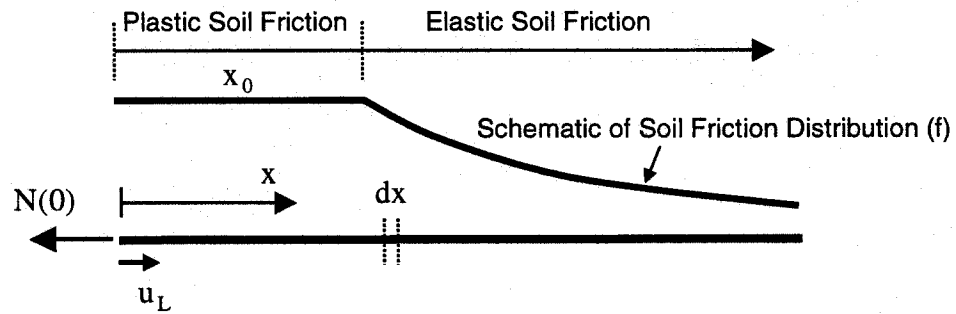


(c) Right Infinite Segment
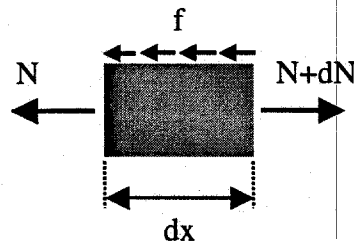


(d) Free Body diagram of an Infinitesimal Length of Right Infinite Segment

Fig. 5.4 Far-field Condition for an Infinitely Long Pipe

$$q_p = P_0 \, y''$$

(Lateral load due to internal pressure, p)

Fig. 5.5 Destabilizing Effect of Internal Pressure



20 m

Far-field
Condition

0.02 mm

Pipe Specs:

D = 324.43 mm
t = 6.477 mm
E = 200,000 MPa
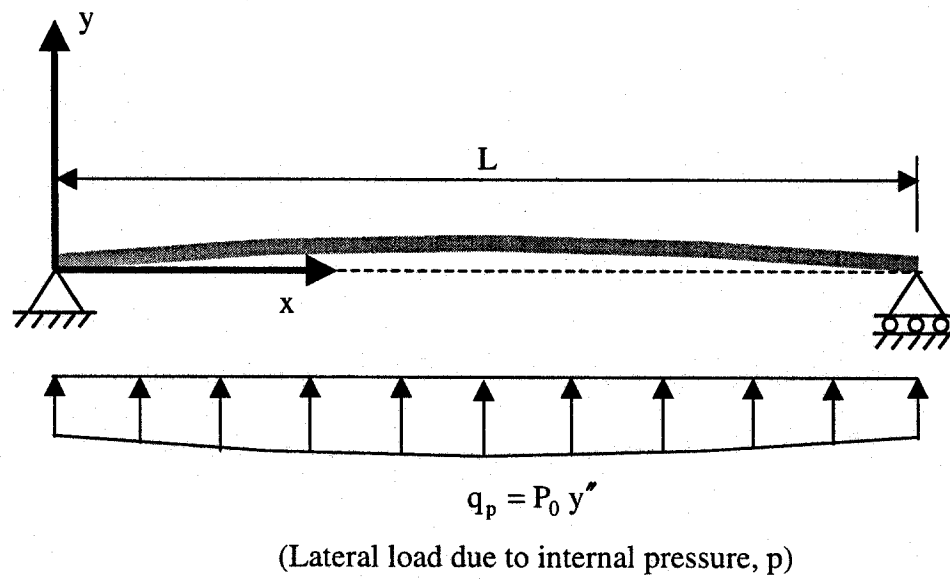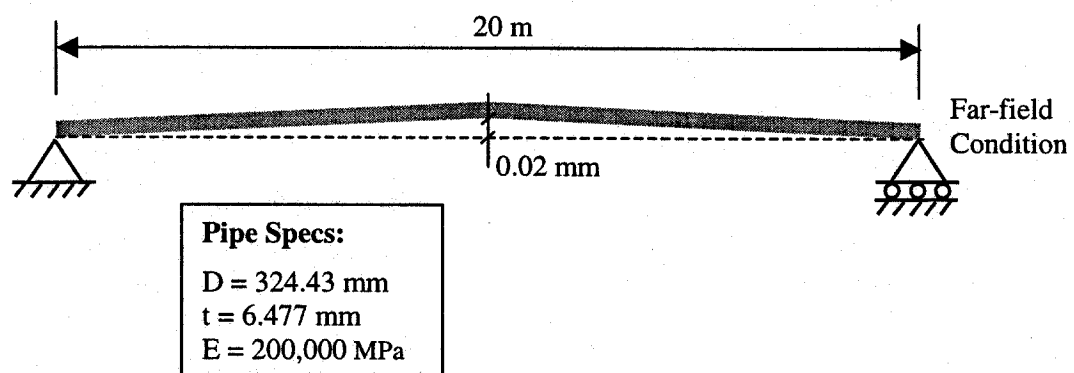
Fig. 5.6 Example 1: Elastic Buckling of Pressurized Pipe
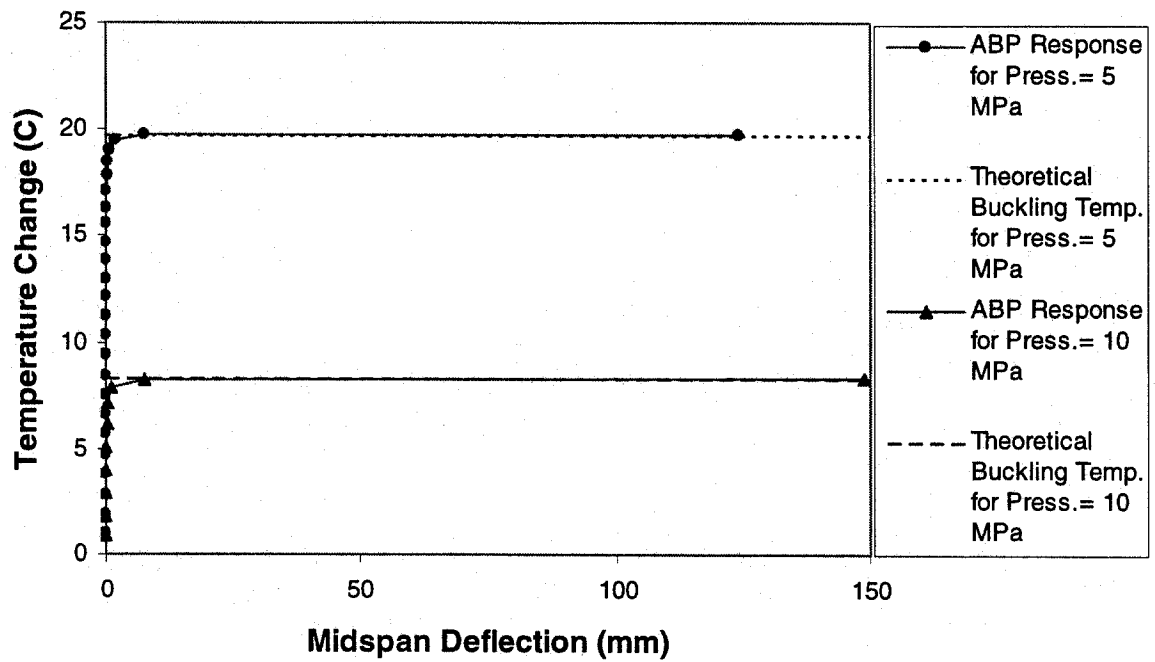
Fig. 5.7  Example 1: Comparison of ABP Responses to Theoretical Buckling
Temperature Changes
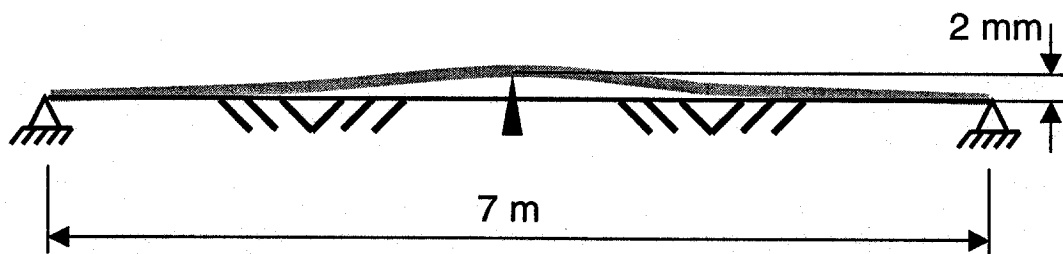


Fig. 5.8  Example 2: Raoof and Maschner Upheaval Buckling Test Layout
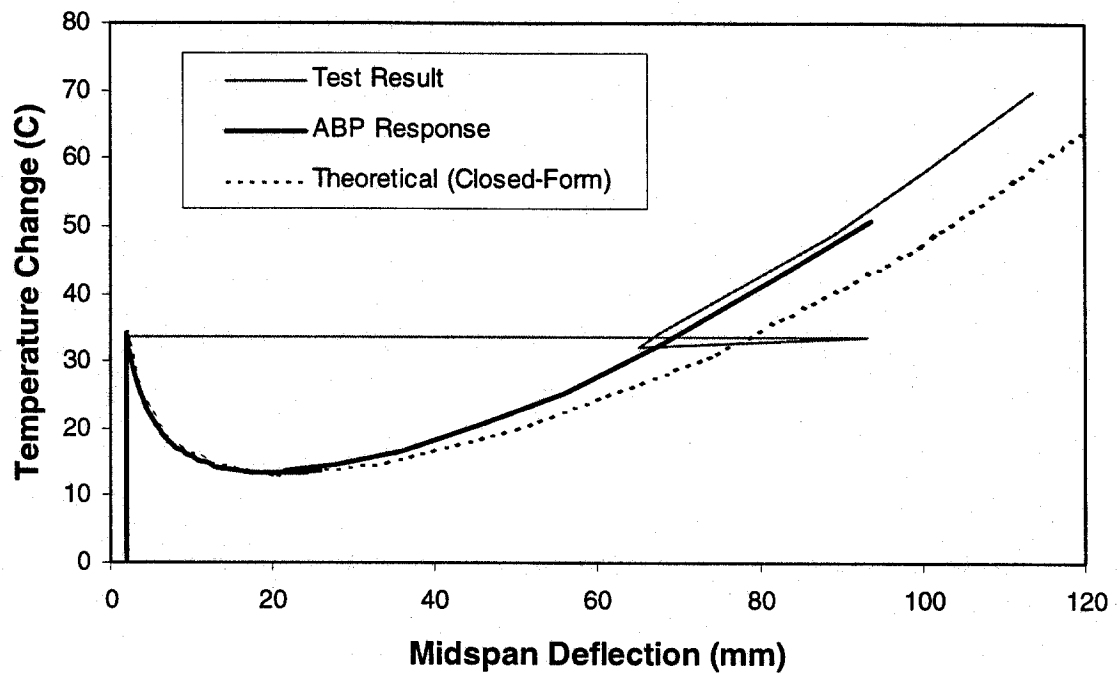
Fig. 5.9  Example 2: Comparison of ABP Response of Temperature Change vs. Midspan
Deflection to Theoretical and Test Results
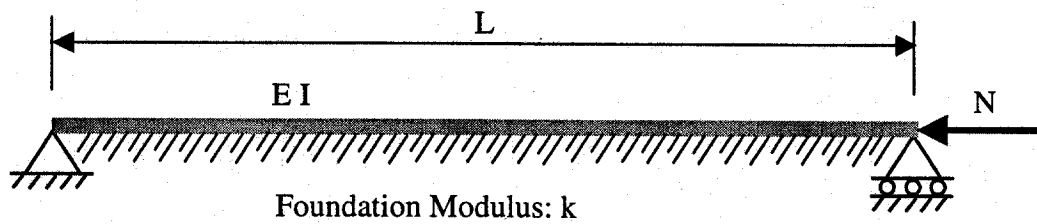


Fig. 5.10  Simply-Supported Beam on Elastic Foundation under Axial Compression
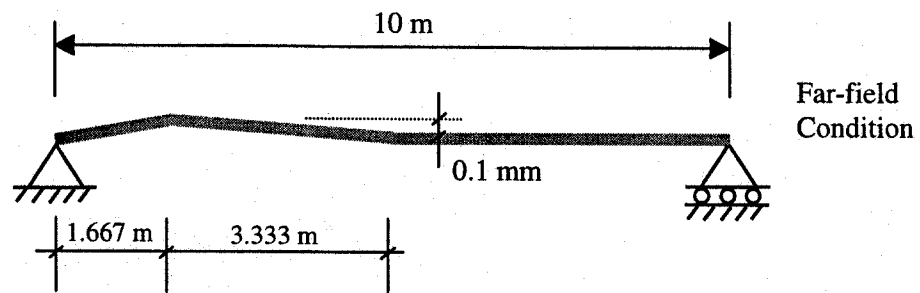
Fig. 5.11 Example 3: Layout for Model A
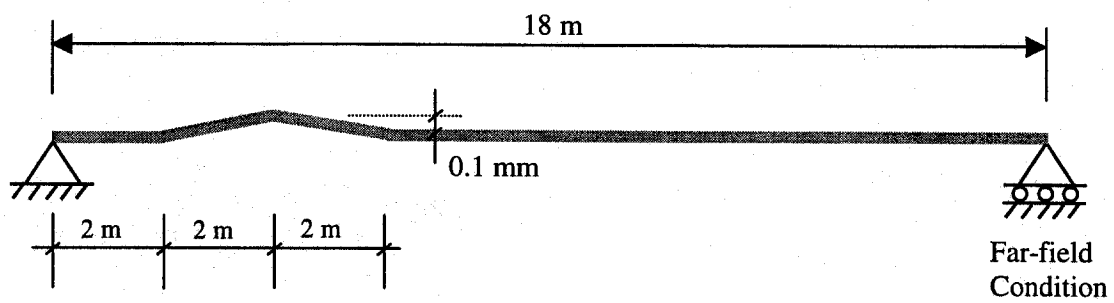


Fig. 5.12 Example 3: Layout for Model B
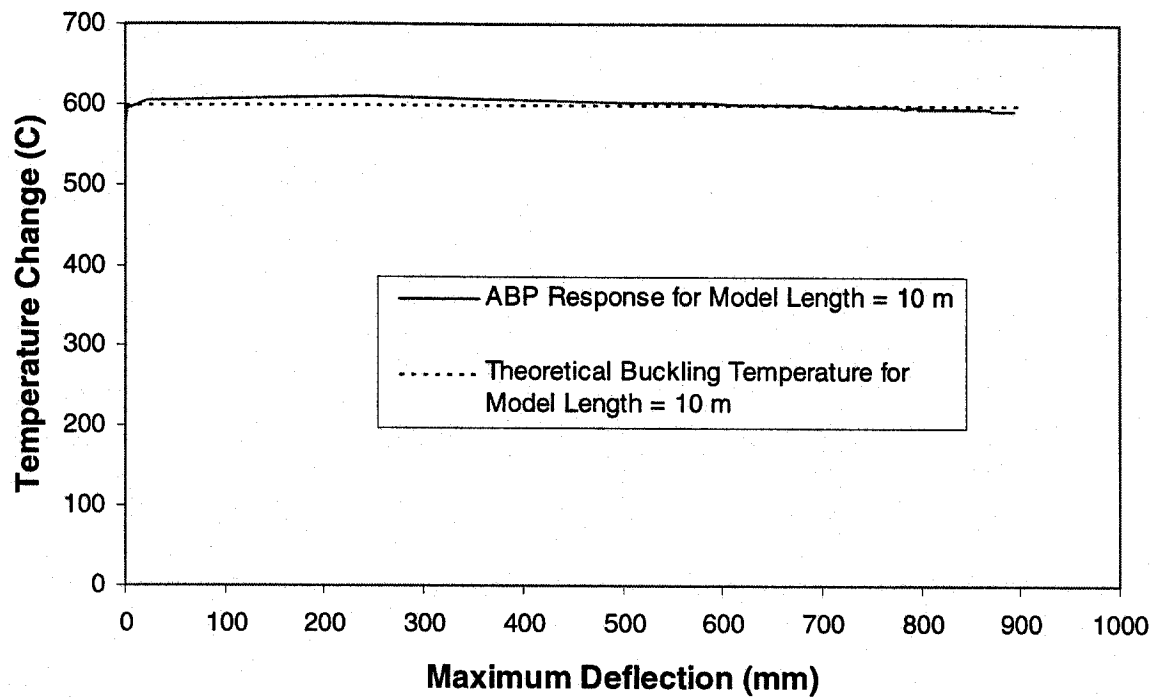
Fig. 5.13 Example 3: Comparison of ABP Response to Theoretical Buckling
Temperature Change (Beams on Elastic Foundation Theory) for Model A
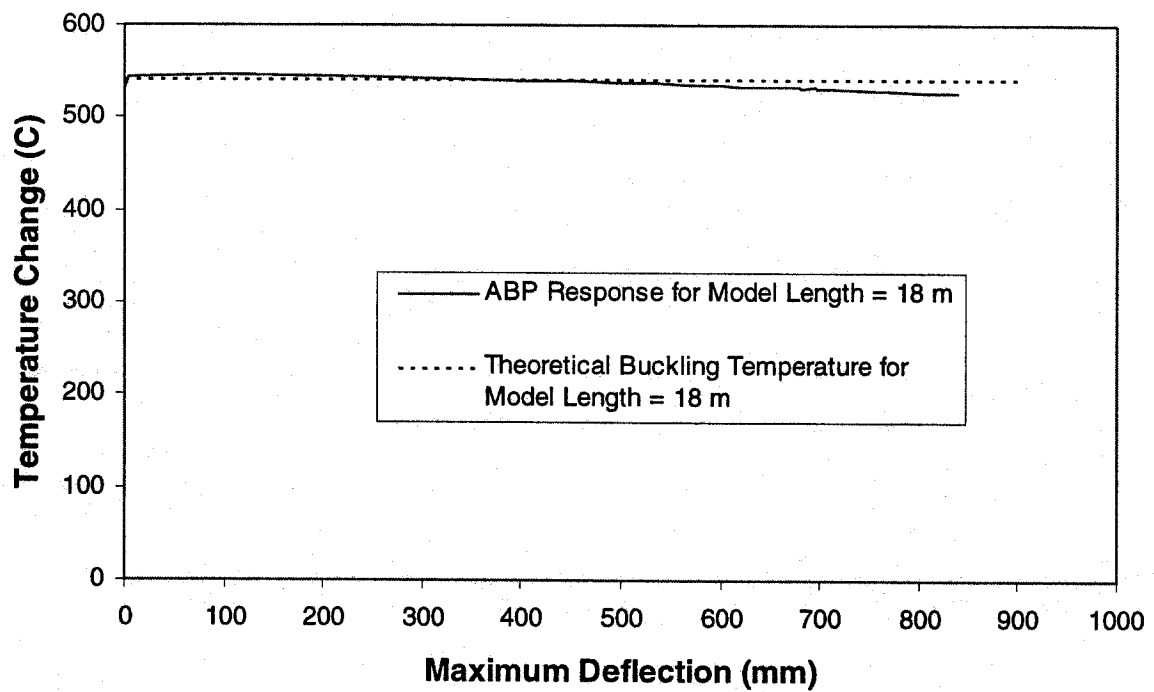


Fig. 5.14 Example 3: Comparison of ABP Response to Theoretical Buckling
Temperature Change (Beams on Elastic Foundation Theory) for Model B

152
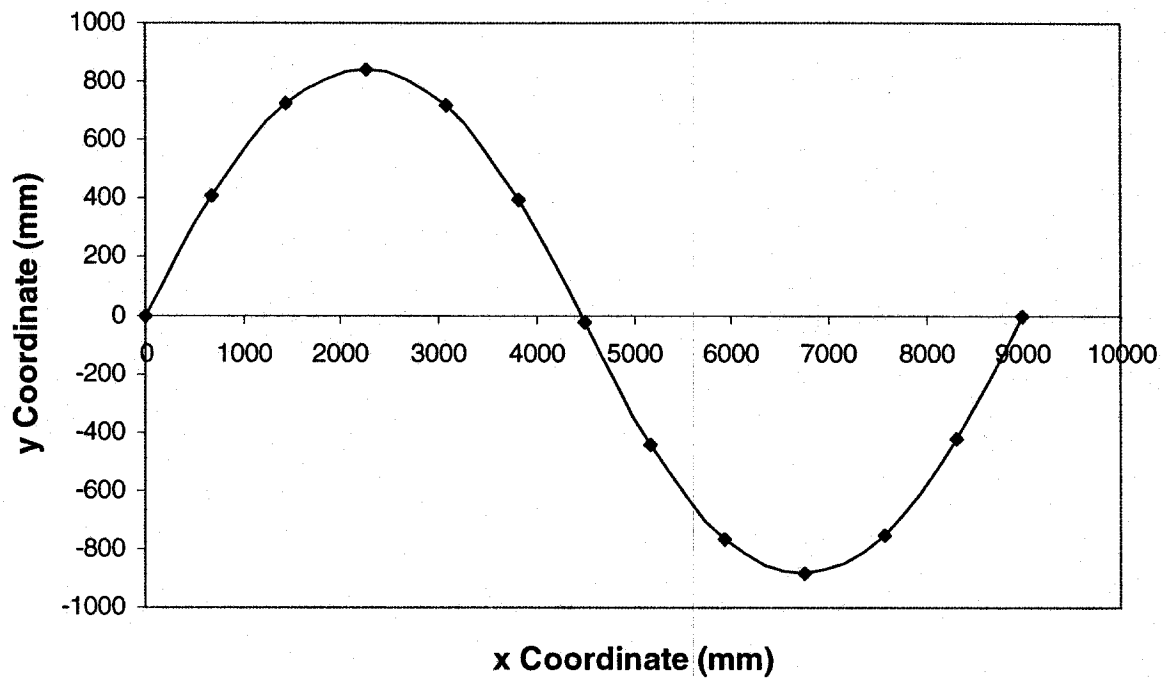
Fig. 5.15 Example 3: Final Deformed Configuration of Model A
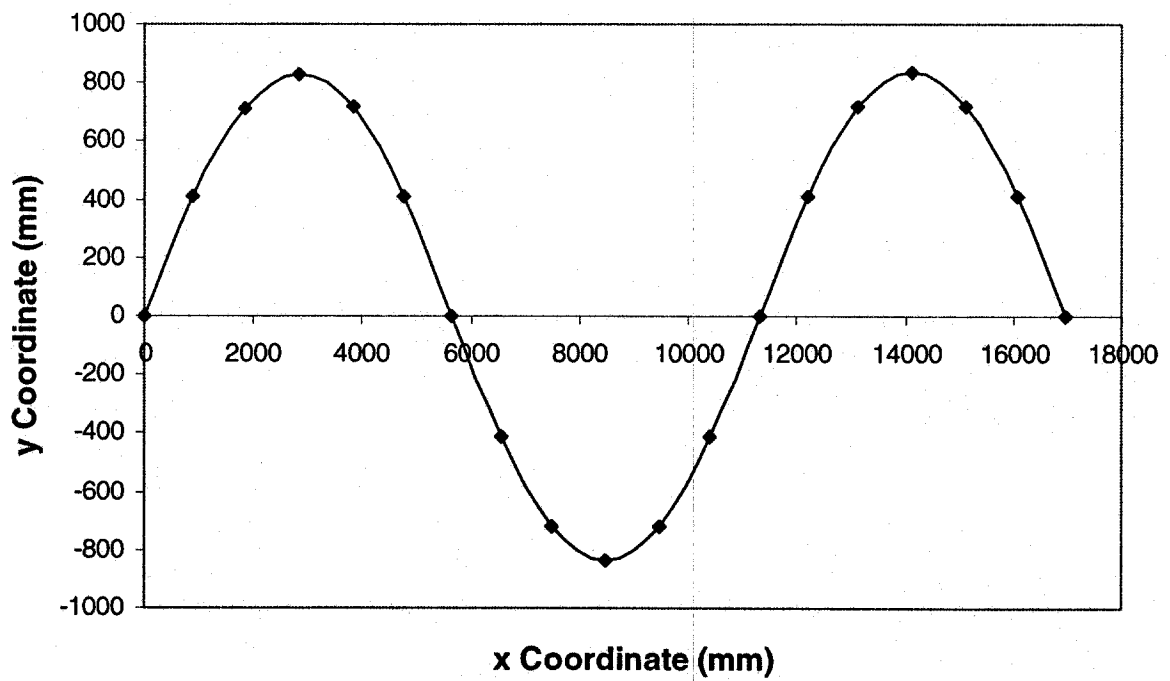


Fig. 5.16 Example 3: Final Deformed Configuration of Model B

153

# CHAPTER 6. CASE STUDIES FOR THERMAL BUCKLING ANALYSIS

## 6.1 INTRODUCTION

This chapter presents three case studies as examples demonstrating the application of thermal analysis. The first case study is a parametric study, whereby a single parameter is varied in order to study the effect of that variation. The second and third case studies stem from the investigations carried out on actual pipelines having undergone thermal buckling. The pipelines investigated in the second and third case studies are onshore and offshore pipelines, respectively.

## 6.2 CASE STUDY 1: A PARAMETRIC STUDY

Case Study 1 is a parametric study on the variation of the initial out-of-straightness (IOS) for a pipeline whose layout is show in Fig. 6.1. The pipe is 900 m long and has pinned ends. The out-of-straightness is applied over the middle 100-m length of the model in the shape of a cosine curve:

$$y_0 = \frac{IOS}{2}\left(1+\cos\frac{2\pi x}{L_i}\right) \tag{6.1}$$

where $y_0$ is the initial y coordinate of an arbitrary point located at coordinate x along the humped segment, and $L_i$ is the length of the humped segment (100 m here).

The pipe and ground specifications are as follows:
- OD = 762 mm, Wall Thickness = 8.3 mm
- Elastic-plastic pipe material, SMYS = 483 MPa, E = 205,000 MPa, $v$ = 0.3
- Thermal expansion coefficient = 0.0000116 per °C
- Pipe self-weight = 1.51 N/mm
- Internal Pressure = 7.6 MPa
- Depth of cover = 0.8 m
- Effective Soil Density = 7 kN/m³ (Saturated Soil Condition)
- Bearing spring stiffness = 0.26 N/mm/m
- Bearing spring yield Longitudinal = 20.0 N/mm
- Longitudinal spring stiffness = 0. 8 N/mm/mm
- Longitudinal spring yield Longitudinal = 8.0 N/mm

The input true stress-strain curve, as shown in Fig. 6.2, is obtained from the Ramberg-Osgood equation:

$$\varepsilon = \frac{\sigma}{E} + \varepsilon_{py} \left( \frac{\sigma}{\sigma_y} \right)^n \tag{6.2}$$

where

$\varepsilon$ = logarithmic (true) strain

$\sigma$ = Cauchy (true) stress

$\sigma_y$ = SMYS (= 483 MPa)

$\varepsilon_{py}$ = true plastic strain at SMYS, obtained from

$$\varepsilon_{py} = 0.005 - \frac{\sigma_y}{E} \tag{6.3}$$

n = Ramberg-Osgood exponent, obtained from

$$n = \frac{20.9}{\left( \dfrac{E}{200\sigma_y} - 1 \right)} \tag{6.4}$$

The constant 20.9 in Eq. (6.4) has been obtained through fitting the Ramberg-Osgood equation to a large number of stress-strain curves obtained from the tension coupons at the University of Alberta.

The uplift spring is characterized by the force-displacement curve shown in Fig. 6.3. The curve has a descending branch to account for the loss of the uplift spring force as the pipe moves drastically upwards.

Figure 6.4 shows the temperature change vs. maximum deflection response of the above model for different IOS values, ranging from 0.2 m to 6 m. As expected, the critical temperature change drops as the IOS increases. The minimum point in the post-buckling response occurs at a maximum deflection of around 770 mm for all of the IOS values. Thus, the maximum deflection corresponding to the minimum point seems to be independent of the IOS. However, the temperature change associated with the minimum point, $\Delta T_m$, seems to be of small variation only for the IOS values under 1 m. For the IOS values over 0.7 m, the value of $\Delta T_m$ increases rapidly with increasing IOS. This increase in $\Delta T_m$ in combination with the decrease in the critical temperature, $\Delta T_{cr}$, as IOS increases, results in practically disappearing the maximum point associated with the critical temperature. This can be seen in Fig. 6.4 for the IOS values above 3 m.

The ascending branches of the post-buckling responses seem to be clustered together only for the IOS values up to 1.5 m. For the IOS values above 1.5 m, the post-buckling ascending branch moves higher (i.e., higher temperature change values) as IOS increases. It can also be observed that the post-buckling ascending branches for the IOS values up to 4 m are by and large parallel to each other.

The deformed shape of the pipeline in all cases follows the same pattern: the initial imperfection grows over the initial imperfection length as the solution progresses. An example for this is presented in Fig. 6.5, where the final deformed configuration of the pipe is displayed for the IOS values of 0.2 and 1 m.

## 6.3 CASE STUDY 2: AN ONSHORE PIPELINE

### 6.3.1 Introduction and Objectives

Case Study 2 summarizes the results of an investigation carried out on an onshore gas pipeline in Northern Alberta after it had undergone thermal upheaval buckling. The original configuration of the pipe was not exactly known, however it was assumed to be essentially straight. Although no site-specific soil data was provided, the pipeline segment containing the buckle was known to be mostly buried within muskeg areas, which turn into marshlands in the summer. Figure 6.6 shows the profile of the buckled segment. It can be seen that the pipe lifted over a length of about 100 m, with 40 meters of it emerging out of the ground. The depth of the soil cover to the top of the pipe is estimated to be on average 0.9 m.

The pipe was a 30-inch line (OD = 762 mm) with a wall thickness of 8.3 mm. The installation temperature (in the winter time) was estimated at about –30 °C, and the product temperature (and hence, the pipe temperature) in the buckled segment was estimated at about 5 °C. Therefore, the buckling was assumed to have occurred at a temperature change value of about 35 °C. The average operational pressure for the pipeline was given as 7.6 MPa.

The objectives of this study are outlined as follows:
- To reproduce the buckle formation numerically by trying a variety of soil properties, in order to shed light on the circumstances under which the buckle might have formed

156

- To determine the maximum tensile and compressive strains in the buckled pipe (current configuration)
- To determine the maximum tensile and compressive strains in the pipe as the temperature change reaches the design value (75 °C)
- To determine the effects of placing a berm over the buckled segment

## 6.3.2 Analytical Model

The layout of the model used in the analysis is shown in Fig. 6.7. An IOS value of 0.3 m over 100 m (the buckle length) was assumed to be reasonable. The pipe material properties, self-weight, and thermal expansion coefficient are the same as those for the pipe in Case Study 1. Since the mechanical properties of muskeg soils are not well defined, as a starting point, the soil was assumed to be a saturated cohesive soil with an effective density of $6 \, kN/m^3$ and an undrained shear strength of 3.5 kPa. The corresponding soil spring values are obtained using the equations presented in Sections 4.2.1, 4.2.2, and 4.2.3 as given in Table 6.1.

| Bearing Spring | Stiffness (N/mm/mm) | 0.26 |
|---|---|---|
| | Yield Force (N/mm) | 19.7 |
| Longitudinal Spring | Stiffness (N/mm/mm) | 2.36 |
| | Yield Force (N/mm) | 11.8 |
| Uplift Spring | Stiffness (N/mm/mm) | 0.025 |
| | Yield Force (N/mm) | 3.24 |

Table 6.1 Initial Properties of Soil Springs

Since this work was done as the far-field boundary condition was being developed, it was decided not to use the far-field option. Thus a very long length (900 m) was considered for the model to represent an infinitely long pipeline. The subsequent examination of the axial strains at the ends of the model upon completion of the analyses confirmed the adequacy of the model length (the axial strain values should be close to $\varepsilon_0$ as given by Eq. (5.12)).

The soil properties are varied within reasonable ranges until a solution (called the *target* solution) meets both following criteria:

1) The buckling must occur at a temperature rise of about 35 °C.

157

2) The deformed model configuration after snap-through must match the current
   buckled pipe configuration (as shown in Fig. 6.6).

The model employed for the target solution is then used for the rest of the tasks as
outlined above in the objectives.

## 6.3.3 Analytical Results

Over 30 analyses were carried out for different values of soil density and longitudinal
and uplift spring properties. As an example for the soil property variations in search of
the target solution, the final fine-tuning is presented herein. The final parametric
variation involves three different values of uplift spring yield force resulting in the three
different force-displacement relationships as shown in Fig. 6.8. The other soil properties,
which are identical for the three solutions, have updated values as follows: the effective
soil density is 7 $kN/m^3$, the longitudinal springs stiffness and yield force are 0.8 N/mm
and 8 N/mm, respectively, and the bearing springs properties remain unchanged (the same
as those in Table 6.1). Figure 6.9 shows the temperature change vs. maximum deflection
response for the three solutions corresponding to the three different uplift spring
properties.

As Figure 6.9 shows, the critical temperature change increases as the uplift spring
yield force, $F_{Uy}$, increases. Moreover, the descending post-buckling branches for the
three solutions are parallel to each other, ending at minimum points, all occurring at
almost the same midspan deflection value of 0.6 m. Starting off from the minimum
points, the ascending post-buckling branches for the three solutions seem to be
proceeding closely to each other. Thus, all the three solutions satisfy the second criterion
for the target solution to the same degree. However, only the solution with $F_{Uy} = 0.017$
N/mm seems to meet the first criterion, and therefore, chosen as the target solution.

As Figure 6.10 shows, the target solution closely approximates the actual buckle
configuration at the temperature change of around 35 °C. Note that, since the solution did
not produce an output point close enough to the temperature change of 35 °C, the
deformed configurations corresponding to the data points immediately before and after
the temperature change of 35 °C are shown in Fig. 10. The maximum tensile and
compressive strain values at 37.4 °C are 0.18% and −0.12%, respectively, both
occurring at the crest of the buckle. Furthermore, both strain values remain well below
critical values (typically around 0.5%).

158

Although the axial strains at the ends of the model were close to the $\varepsilon_0$ as obtained from Eq. (5.12) for temperature changes up to 37.4 °C, the agreement seemed weaker for the temperature changes around 75 °C: axial strain values of about $-0.02\%$ vs. an $\varepsilon_0$ value of about $-0.04\%$. Since the far-field option was operational by the time these results were obtained, it was decided to reanalyze the same target model with the only change being the use of far-field condition at the ends instead of pinned ends. Figure 6.11 shows the temperature change vs. maximum deflection response of the target model for the two end boundary condition options. It can be seen that the response for the far-field option closely follows the response for the pinned-pinned option well past 75 °C (the design temperature change).

The two solutions are also compared in terms of their strain response for the top and bottom fibers of the pipe at temperature changes of about 35 °C and 75 °C in Figs. 6.12 to 6.15. The respective strain responses for the two boundary conditions accord well, especially in the case of the strain responses at the temperature change of about 75 °C. The larger difference between the strain responses at the temperature change of about 35 °C is mainly due to the fact that the response for the pinned-pinned option corresponds to a slightly higher temperature change value than does the response for the far-field option (37.4 °C vs. 36.1 °C). For the solution using the far-field option, the maximum tensile and compressive strain values along the pipe at the temperature change of 36.1 °C are 0.18% and $-0.11\%$, respectively (as compared to 0.18% and $-0.12\%$, respectively, for the pinned-pinned option, as mentioned above).

For the model with pinned ends, the maximum tensile and compressive strain values at 75.1 °C are 0.41% and $-0.38\%$, respectively, both occurring at the crest of the buckle. For the model using the far-field option, the corresponding strain values at 74.5 °C are 0.41% and $-0.37\%$, respectively, also occurring at the crest of the buckle. Thus, even at the design temperature of 75 °C the strains remain under 0.5%.

To remedy to the buckle, it was assumed that placing a proper berm over the buckled section would straighten the buckled segment. The berm was assumed to be placed over a 200-m length of pipe centering on the crest of the buckle. The berm was considered to be 1.4 m high and have a density of 17.5 kN/m$^3$. The analysis was carried out using the target model with pinned ends up to a temperature change of 37.4 °C (current condition). Then the berm was included as an added weight over the middle 200-m length of the

model in a restart analysis. The results showed that, upon placing the berm, the buckle would snap down and straighten out. The maximum tensile and compressive strain values at 37.4 °C after straightening of the pipe were 0.002% and −0.037%, respectively. Then the temperature was raised to about the design value. At a temperature change of 77.9 °C, the pipe remained essentially straight with the tensile strains all diminished. However, the maximum compressive strain increased to a value of −0.091%, still well below any critical value for the pipe.

## 6.4 CASE STUDY 3: AN OFFSHORE PIPELINE

### 6.4.1. Introduction

Following the failure of an offshore oil pipeline near the coast of Guanabara Bay in January of 2000, a study was carried out in order to investigate the circumstances that led to the failure. As part of the study, some thermal analyses were carried out using the computer program ABP in order to simulate the snaking phenomenon that the pipe experienced prior to the leak. The buckles with an amplitude of about 4 m are considered to have formed at a temperature change value of around 75 °C.

This investigation will shed some light on the circumstances under which the deformation took place. Most importantly, it will determine the strength provided by the surrounding soil. In addition, the strains obtained from the numerical solutions will be compared to the wrinkling strains expected for the pipe based on the University of Alberta's research results. Moreover, the analysis will yield the approximate value of the temperature differential at which the wrinkle started to form. The numerical model for the thermal analysis and the results are presented in the following sections.

The study of the fracture caused by the cyclic thermal loading is outside the scope of this work. There is an ongoing study at the University of Alberta on the topic of pipeline fracture under cyclic loading. Some insight to the failure phenomenon at Guanabara Bay should be gained from the results of that research.

### 6.4.2 Analytical Model

Figure 6.16 shows the layout of the numerical model. The initial out-of-straightness is chosen such that the S-shape buckling mode, similar to that of the actual pipe, is triggered. As Fig. 6.16 shows, the imperfections are assigned in triangular shapes, with a peak of 50 mm over a length of 20 m. Note that the vertical scale has been exaggerated

in order for the initial imperfections to be visible. In Fig. 6.16, the letter F at the supports signifies the usage of far-field condition at the ends of the model. This means that at any configuration of the pipe during the solution, an axial force will be applied at the ends of the model to mimic the effect of infinitely long stretches of elastic pipe beyond the ends.

In the finite element model, the pipe is discretized into 54 elements, each two meters long. The pipe size and operating pressure were given as follows:

- D = 406 mm
- t = 7.9 mm
- Operating Pressure = 3.4 MPa

The engineering stress and strain values provided for the pipe material were converted to true stress and logarithmic (true) strain measures to be used in the input for the analysis. The resulting stress-strain curve is plotted in Fig. 6.17.

The main variants in different solutions are the soil spring values. The objective here is to change the soil properties until an acceptable solution is achieved. An acceptable solution is one that produces an amplitude buckle of about 4 m at a temperature change value of around 75 °C. The results of four of the total 14 solutions are presented here. The selected solutions and their respective soil spring values are listed Table 6.2.

| Selected Solution | Transverse Springs | | Longitudinal Springs | |
|---|---|---|---|---|
| | Stiffness [N/mm/mm] | Yield [N/mm] | Stiffness [N/mm/mm] | Yield [N/mm] |
| b5 | 0.02 | 1 | 0.2 | 2 |
| b6 | 0.02 | 1 | 0.13 | 1.3 |
| b8 | 0.02 | 1 | 0.1 | 1 |
| b9 | 0.01 | 0.5 | 0.1 | 1 |

Table 6.2 Soil Properties for Selected Solutions

### 6.4.3 Analytical Results

The results of the analyses are presented in the following subsections. They include the characteristic curves for the solutions, the longitudinal strains and how they compare to the wrinkling strain, and finally some plots of the results for the best solution.

#### 6.4.3.1 Characteristic Curves

Figure 6.18 shows the temperature change vs. buckle amplitude for different solutions. These are called *characteristic curves* because they characterize the response of each solution. For all of the solutions, there is an early peak in temperature change, which corresponds to the overall buckling of the pipe into an 'S' shape.

Similarly to the previous examples and case studies, the analytical model used in this investigation traces the path of static equilibrium. To follow the descending portion of the static post-buckling response, the temperature needs to drop in a controlled manner upon buckling, which normally do not materialize in the field. Thus, in reality, upon arriving at the critical temperature change, the pipe undergoes a dynamic deformation until it ends up on the ascending part of the post-buckling response. The snap-through phenomenon is shown by the horizontal black arrows in Fig. 6.18. Thus, the pipe is expected to gain its static equilibrium on the stable post-buckling path at the same value of temperature change as the peak point. Any further temperature increase results in tracking along the ascending branch of the characteristic curve.

Since the maximum temperature differential for the buckled pipe has been specified as 75 °C, an acceptable solution must have a peak temperature change of less than 75 °C. As Fig. 6.18 shows, for all of the selected solutions, the buckling temperature is below 75 °C.

According to Table 6.2, Solutions b5, b6, and b8 all have the same transverse spring properties, but different longitudinal spring properties. Solution b9, on the other hand, has a weaker transverse spring than do the other three solutions, but the same longitudinal spring properties as for Solution b8. Thus, the following observation can be made from the curves of Fig. 6.18:

i.   The same transverse spring properties for Solutions b5, b6, and b8 result in the same buckling temperature of 61 °C for all these solutions. The weaker transverse spring for Solution b9, however, results in a lower buckling temperature of 42 °C for Solution b9.

ii.  The same longitudinal spring properties for Solutions b8 and b9 result in closeness of their ascending post-buckling response, despite their different transverse spring properties.

iii. Out of the four solutions, only Solutions b8 and b9 yield an amplitude buckle of about 4 m at a temperature change value of around 75 °C. Therefore, considering the above observations, the longitudinal springs must have a yield value of about 1 N/mm, and the transverse springs must have a yield value of about 1 N/mm or lower. Note that, in contrast to the yield values of the soil springs, the stiffness values of the soil springs have little effect in the post-buckling response of the pipe.

Figure 6.19 shows the deformed shape of the pipe for all of the solutions at configurations similar to the actual configuration of the failed pipe (i.e., amplitude buckle of 4m). Obviously, each solution produces that configuration at a different temperature value. As shown in Fig. 6.19, Solutions b5, b6, b8, and b9 reach that configuration at temperature increases of 108.4 °C, 88.3 °C, 77.8 °C, and 75.2 °C, respectively. Since only Solutions b8 and b9 can successfully simulate the field conditions, they will be the focus of the following sections for presenting the rest of analytical results.

### 6.4.3.2 Longitudinal Strain Values

Figure 6.20 shows the maximum and minimum values of the top and bottom fiber strains for Solutions b8 and b9. The maximum and minimum strain values always occur near the crests of the deformed S-shape where plastic hinges form at large deformations (see Fig. 6.19).

As Fig. 6.20 shows, at a given value of temperature change, Solution b8 produces slightly larger strains. However, the similar strain quantities for the two solutions are not far apart. At the temperature increase of 75 °C, the Solutions b8 and b9 produce compressive strains of 1.9% and 2.3%, respectively.

Extensive research has been carried out on the topic of *wrinkling strains in pipelines* at the University of Alberta for the past 10 years. Based on the results of this research, the wrinkling strain for this pipe, given its size and internal pressure, is estimated to be

around 1%. This puts the current strain (about 2%) well above the wrinkling strain. Thus, extensive wrinkling is expected in the real pipe.

As for the initiation of the wrinkles, Solution b8 is expected to wrinkle during the snap-through at a temperature increase of about 61°C, where the maximum compressive strain jumps from 0.13% to 1.5% (i.e., past the wrinkling strain). For Solution b9, however, the maximum compressive strain jumps from 0.09% to only 0.23% in the snap-through. Here the wrinkling starts at a temperature increase of about 59 °C as the solution tracks along the stable post-buckling path. Ironically, the temperature differentials associated with the initiation of wrinkling for two solutions are very close to each other (61 °C vs. 59 °C).

### 6.4.3.3 More Results for Solution b8

Since Solution b8 produces slightly larger strains, it poses a more critical scenario. Thus, the rest of the results presented herein belong to Solution b8.

Figure 6.21 shows the deformed shape of the pipe for a few equilibrium configurations along the path of static equilibrium for Solution b8 (as depicted in Fig. 6.18). The first curve corresponds to the peak point in the characteristic curve (i.e., the point of overall buckling). The second curve in Fig. 6.21 corresponds to the subsequent minimum point. The next three curves correspond to three points along the ascending part of the post-buckling response ending with a configuration comparable to the actual pipe deformed shape (i.e., a buckle amplitude of 4 m at a temperature change of 77.8°C). These curves show the development of the plastic hinges at the crests of the S-shape pipe configuration.

Figure 6.22 shows the variation of curvature along the pipe for the configuration at the temperature change of 77.8°C (which has a buckle amplitude of 4 m). Figure 6.23 shows the variation of top and bottom strain for the same configuration. As expected, both figures display spikes at the plastic hinges developing at the crests of the S-shape pipe configuration.

### 6.4.4 Conclusion and Summary

The analytical model developed in this study successfully simulated the snaking phenomenon that the failed pipeline at Guanabara Bay experienced. The soil spring

values were varied until acceptable solutions were obtained. Acceptable solution is defined as a solution that produces an amplitude buckle of about 4 m at a temperature change value of around 75°C (i.e., matching the field conditions). It was concluded that the longitudinal springs probably had a yield value of about 1 N/mm, and the transverse springs probably had a yield value of about 1 N/mm or less.

Based on the research on the wrinkling strains carried out at the University of Alberta, the wrinkling strain for the pipe is estimated to be around 1%. This puts the current analytical strain (about 2%) well above the wrinkling strain. Thus, extensive wrinkling is expected to be seen in the pipe, as is the case in the field. In addition, the temperature differential associated with the initiation of wrinkling is expected to have been around 60°C.

The study of fracture caused by the cyclic thermal loading is outside the scope of this work. The ongoing study at the University of Alberta on this topic might shed some light on the fracture phenomenon at Guanabara Bay.
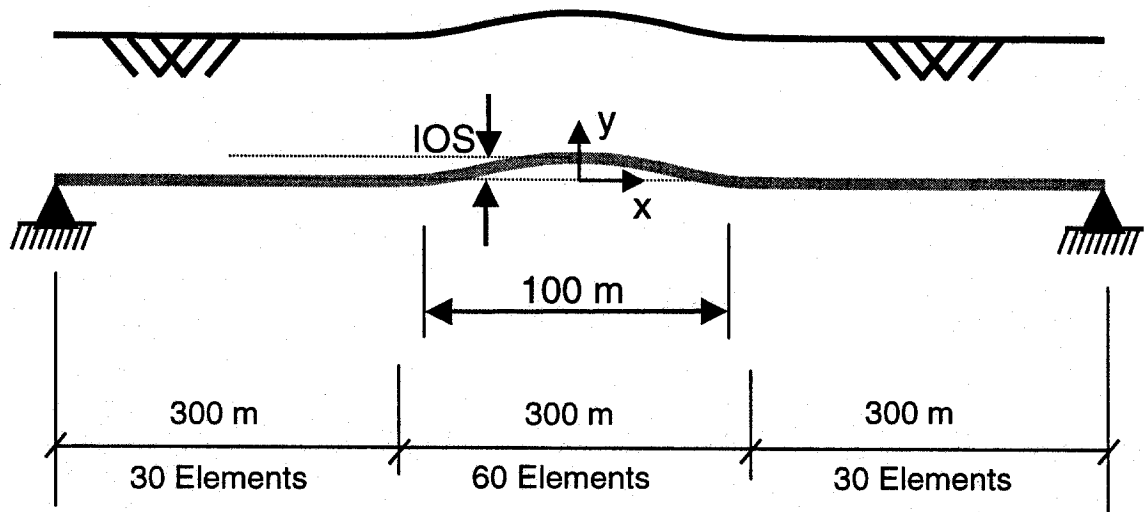
Fig. 6.1  General Layout for Pipeline in Case Study 1 (Not to Scale)
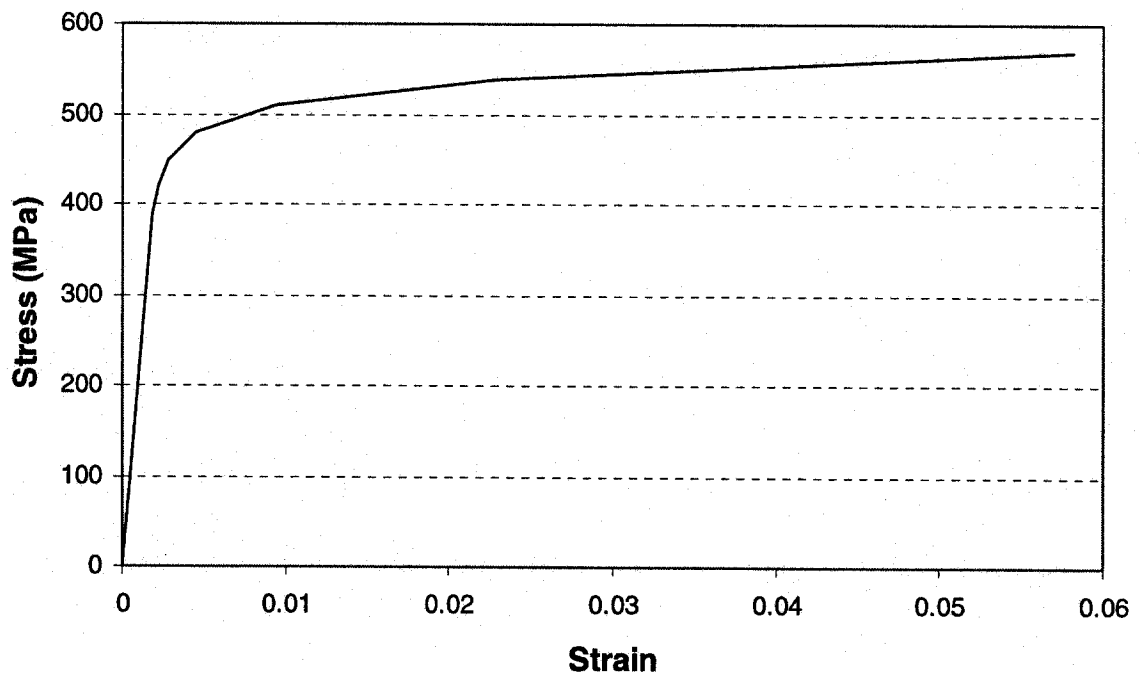


Fig. 6.2  True Stress-Strain Relationship for Pipe Material in Case Study 1
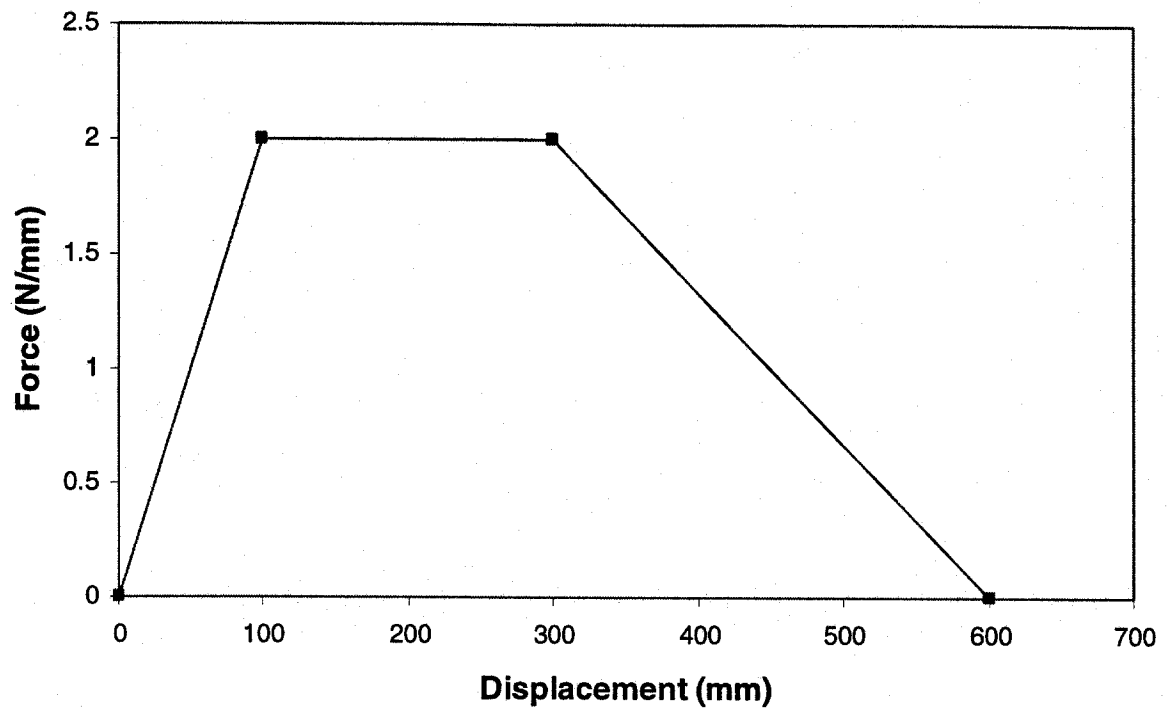
Fig. 6.3  Uplift Spring Force-Displacement Relationship in Case Study 1
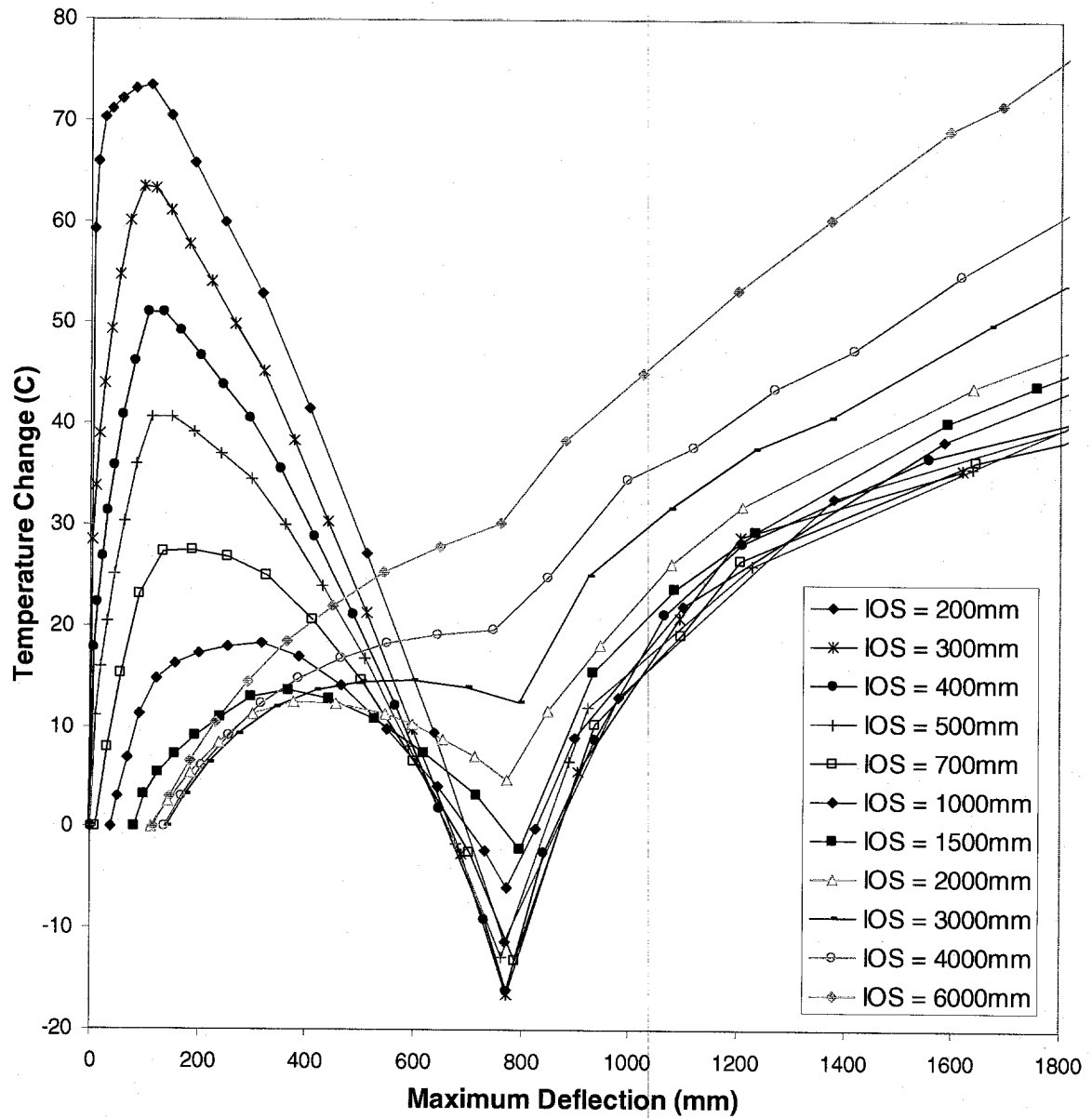
Fig. 6.4 Case Study 1: Temperature Change vs. Buckle Amplitude for Different Values of Initial Out-of-Straightness (IOS)
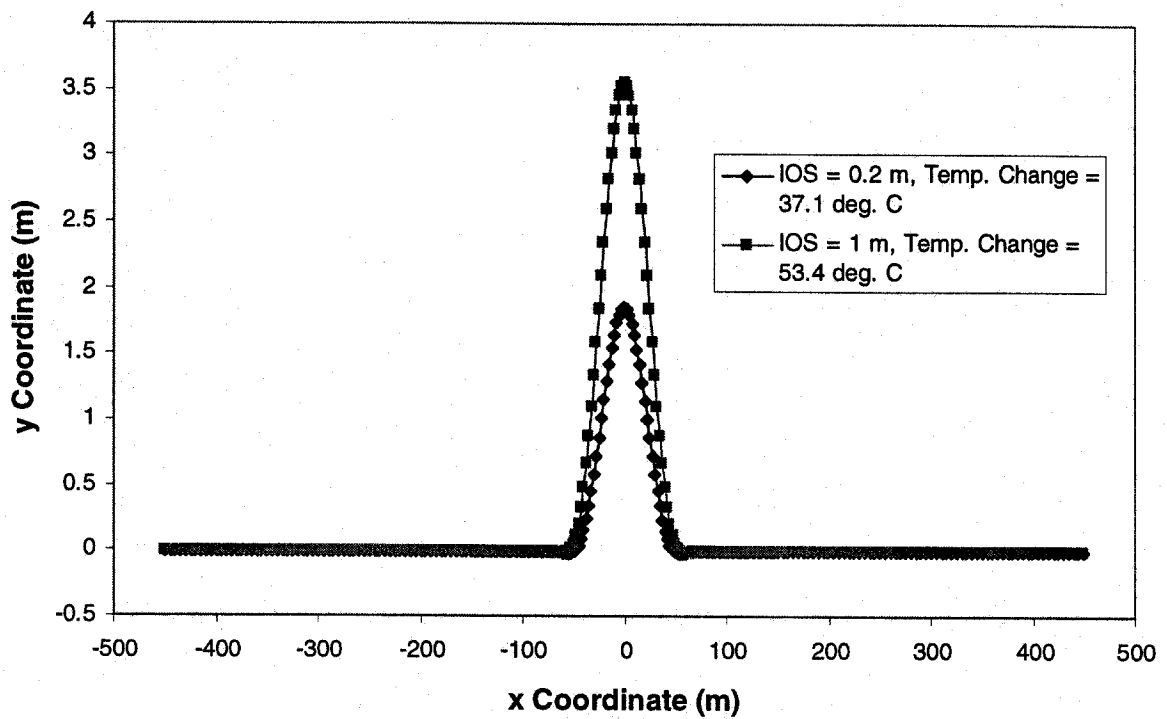
Fig. 6.5 Final Deformed Configuration for IOS Values of 0.2 and 1 m
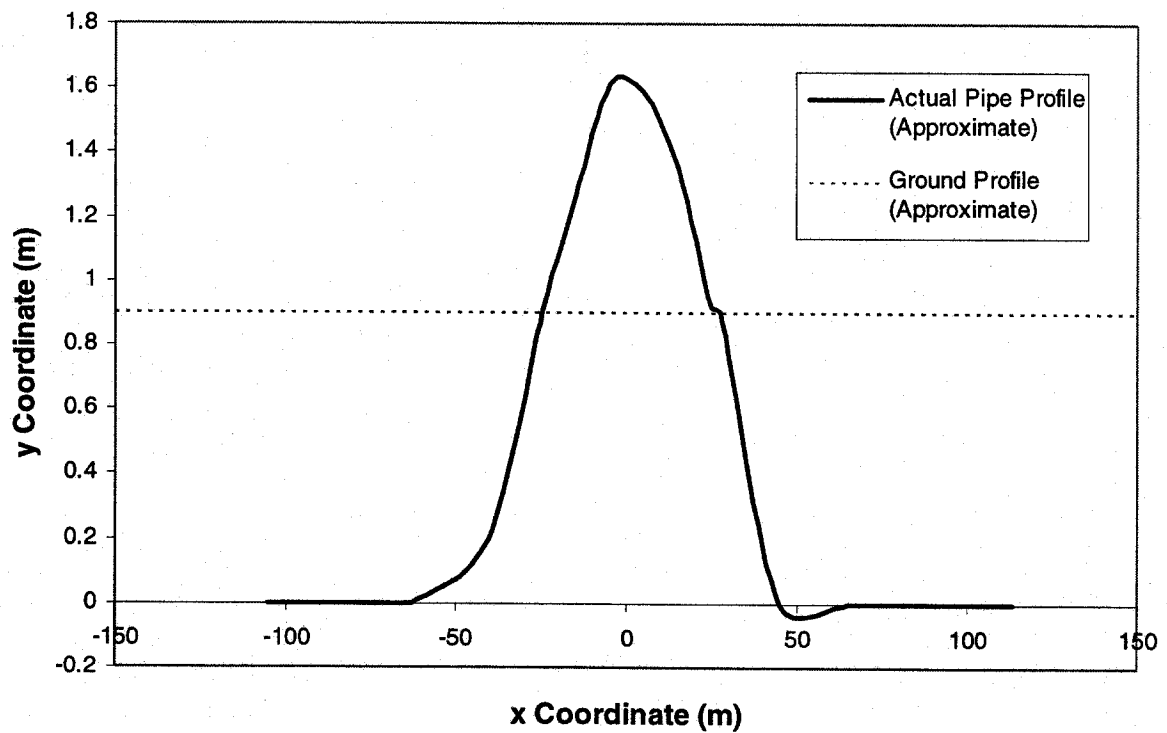


Fig. 6.6 Actual Buckle Profile in Case Study 2

169
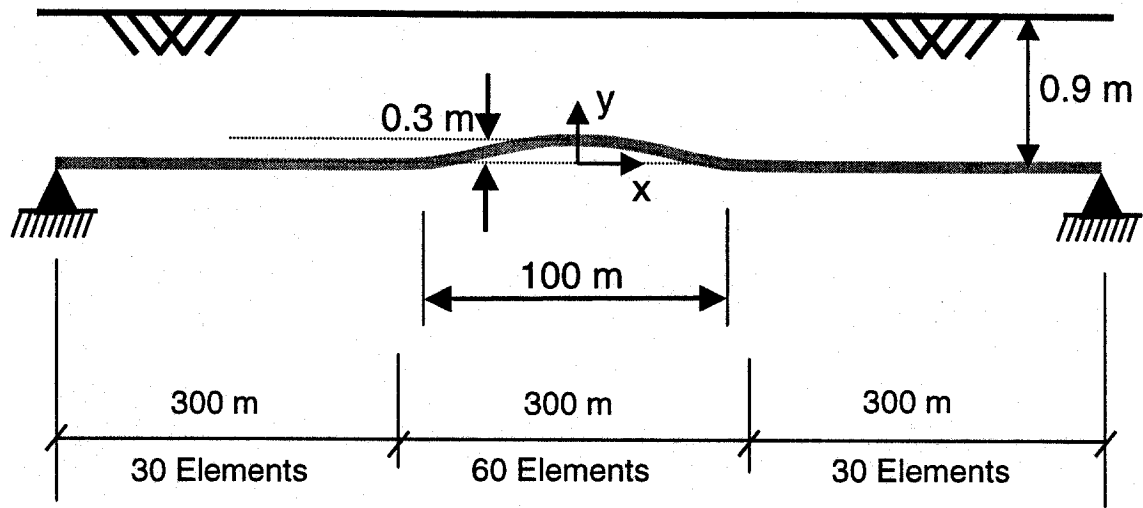
Fig. 6.7 Model Layout for Case Study 2 (Not to Scale)
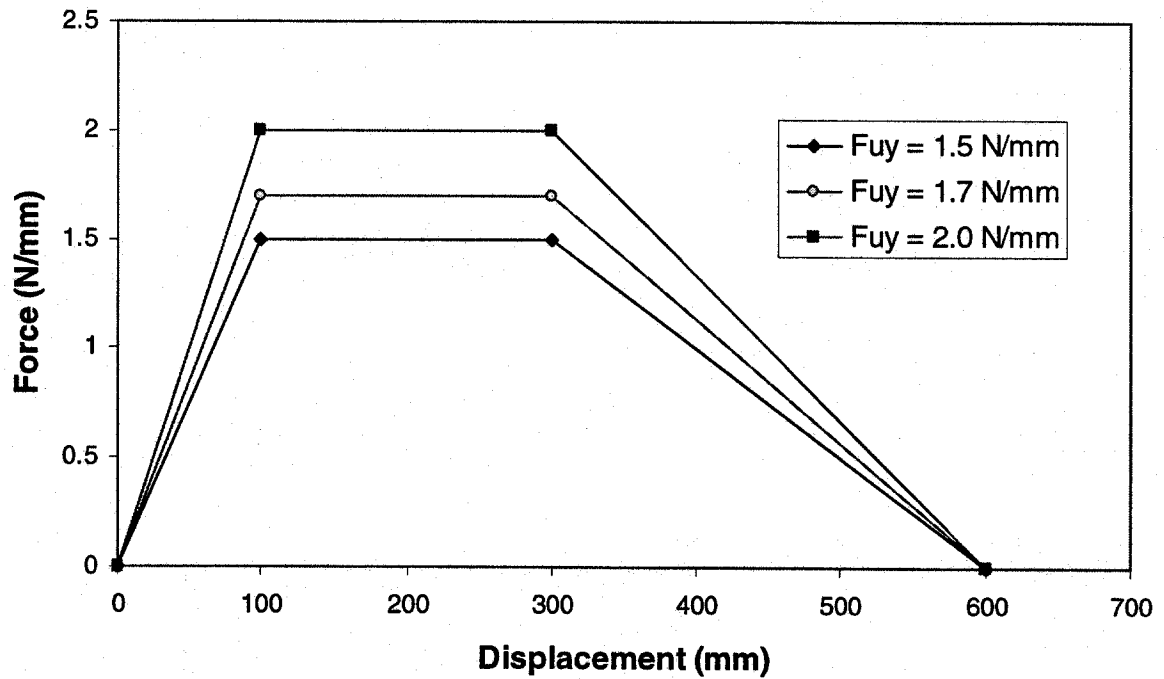


Fig. 6.8 Uplift Spring Force-Displacement Relationships Used in Final Fine-tuning in
Case Study 2
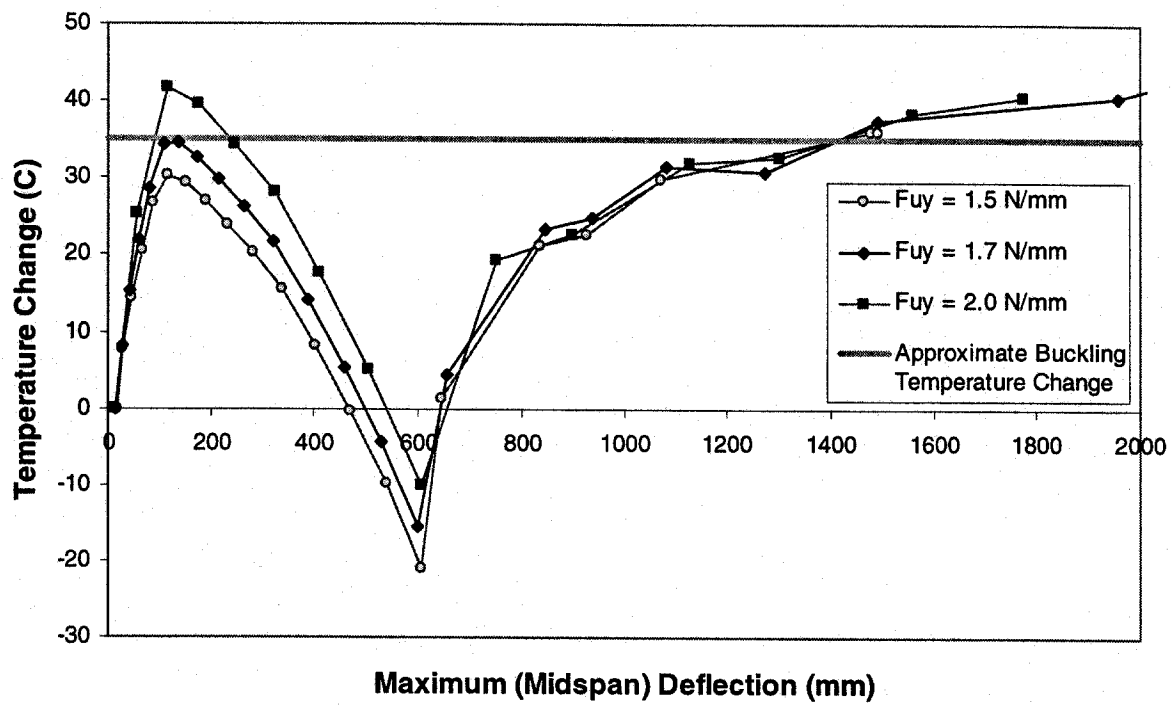
Fig. 6.9  Case Study 2: Temperature Change vs. Maximum Deflection for Different
Values of Uplift Spring Yield Force
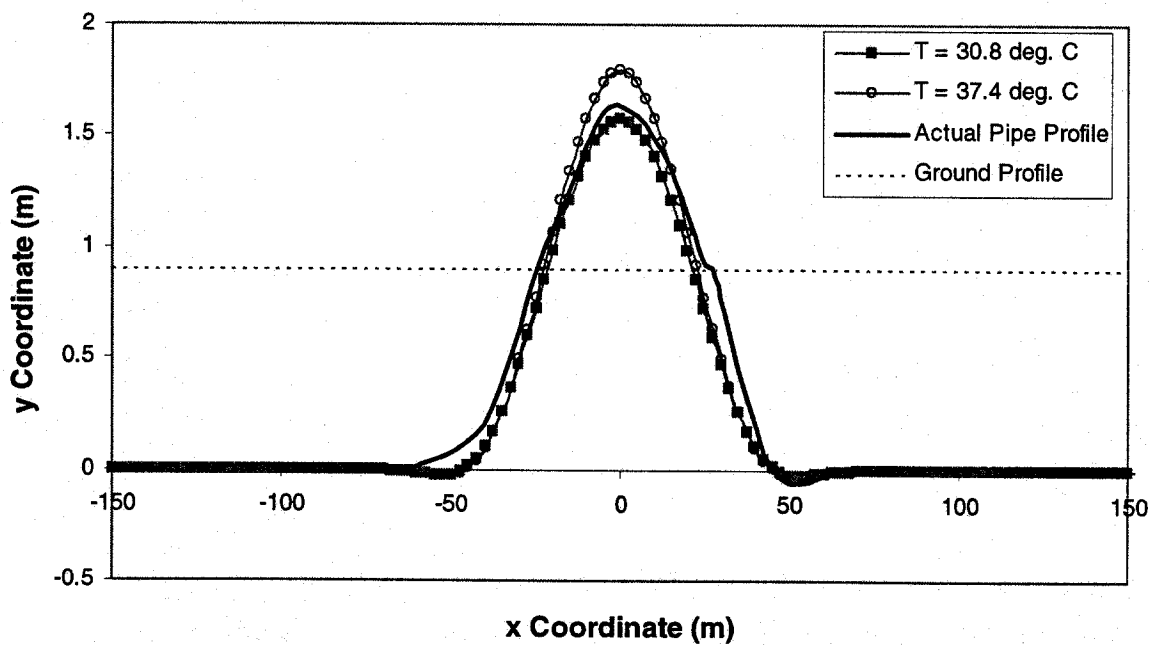


Fig. 6.10  Deformed Configurations from Target Solution Compared with Actual Buckle
Profile in Case Study 2
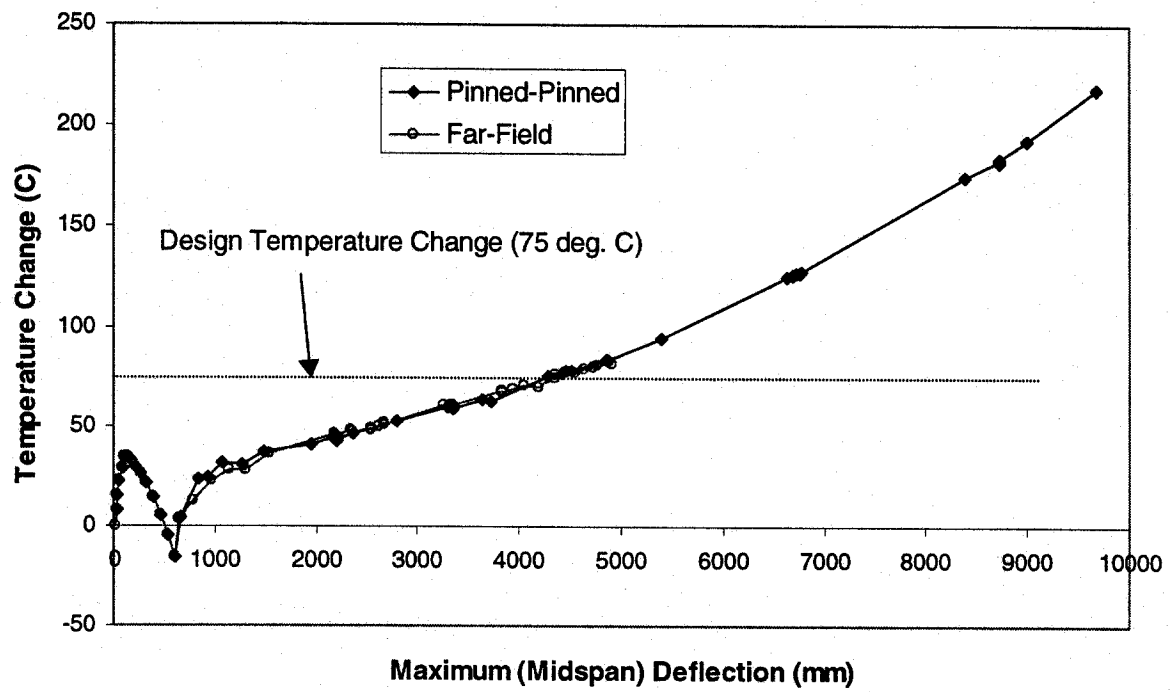
Fig. 6.11 Case Study 2: Temperature Change vs. Maximum Deflection for Different End
Boundary Conditions
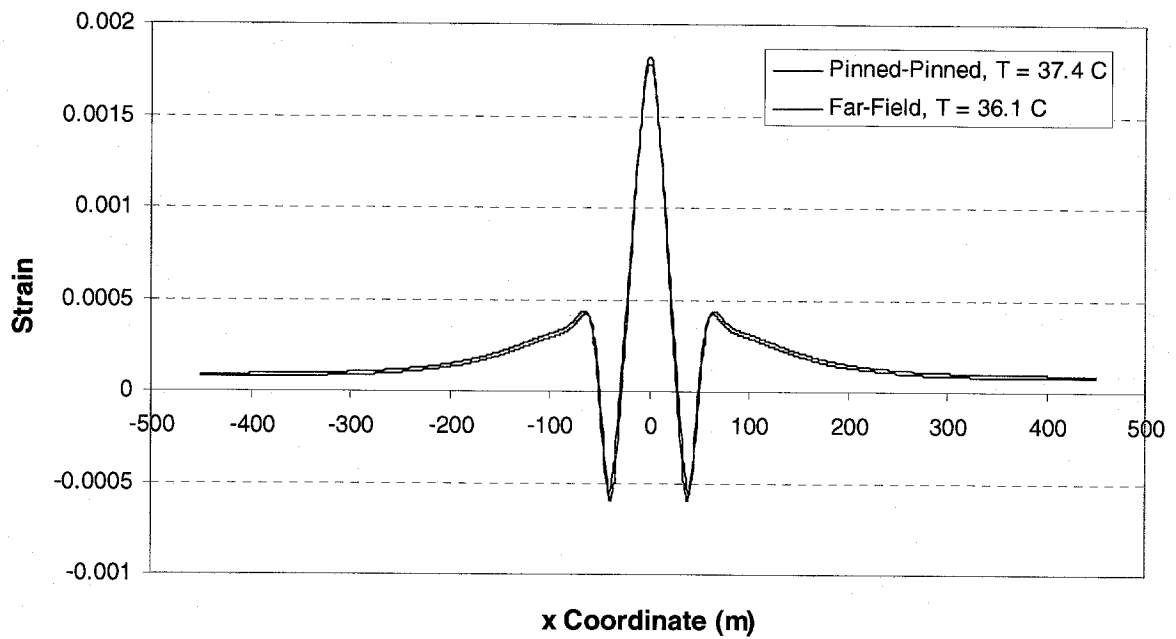
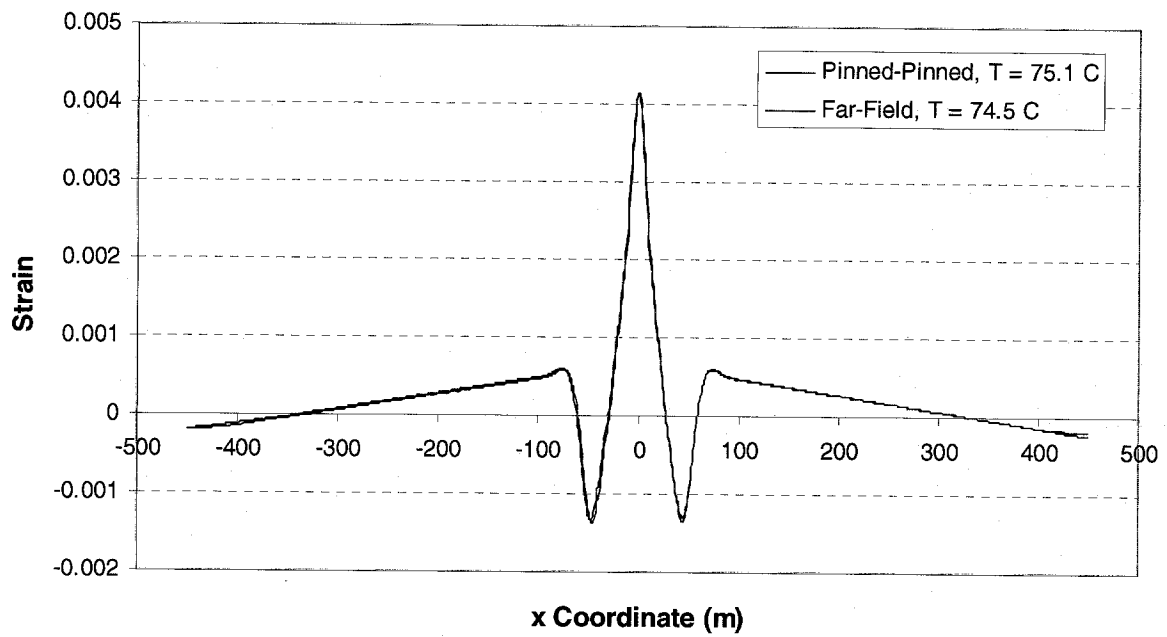Fig. 6.12 Case Study 2: Top Strain Response at about 35 °C for Different End Boundary Conditions
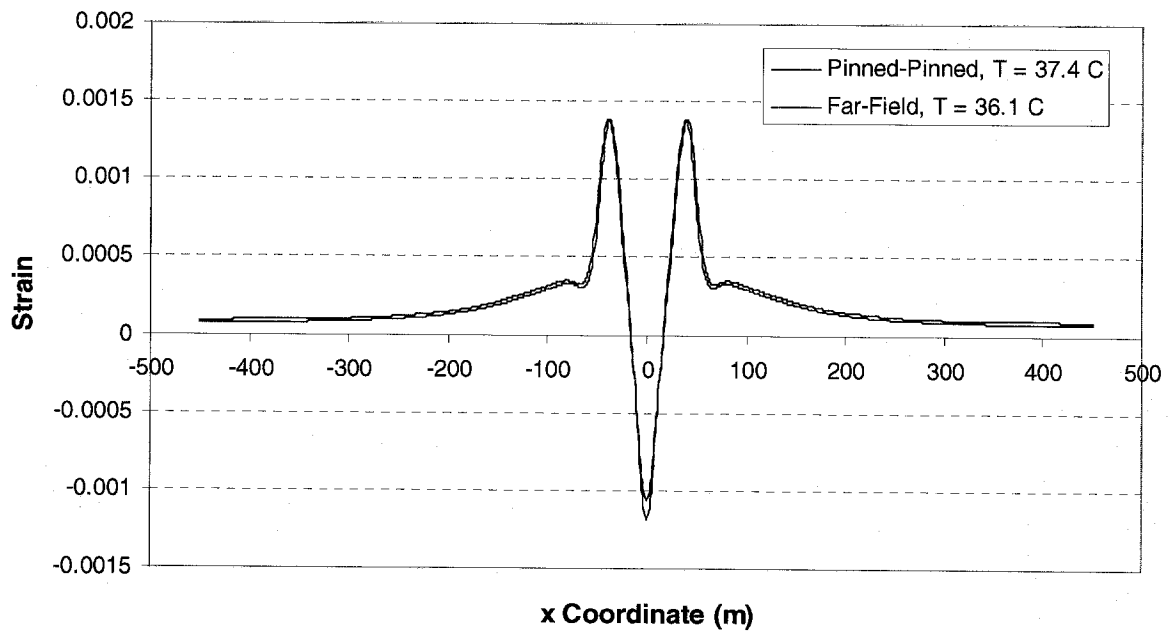


Fig. 6.13 Case Study 2: Bottom Strain Response at about 35 °C for Different End Boundary Conditions

173

Fig. 6.14  Case Study 2: Top Strain Response at about 75 °C  for Different End Boundary Conditions
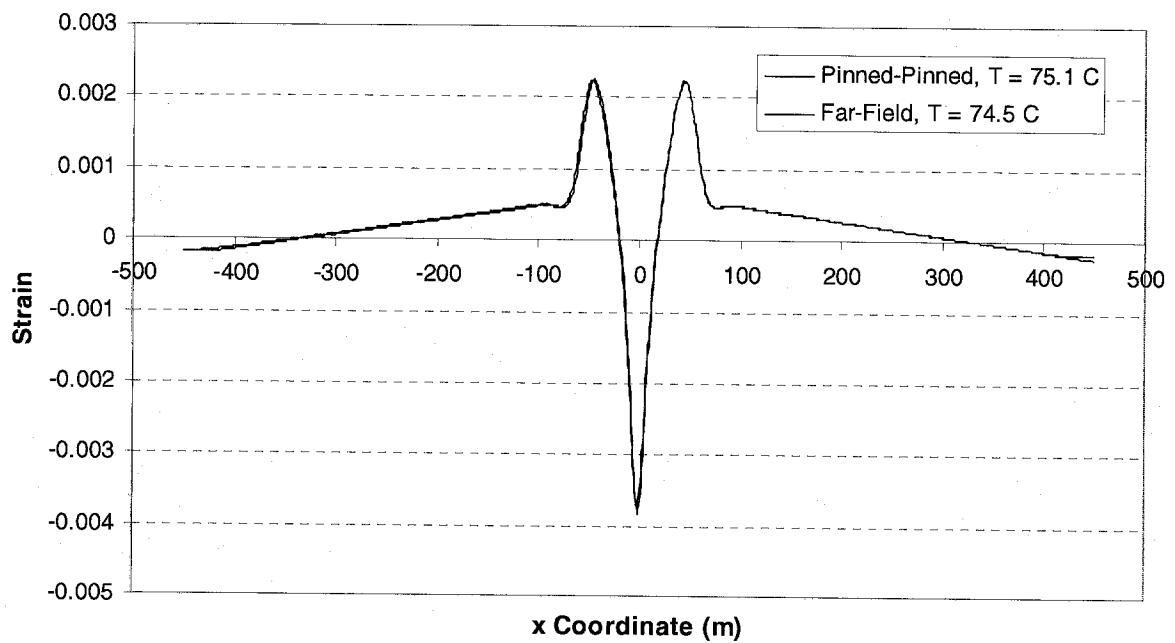


Fig. 6.15  Case Study 2: Bottom Strain Response at about 75 °C  for Different End Boundary Conditions
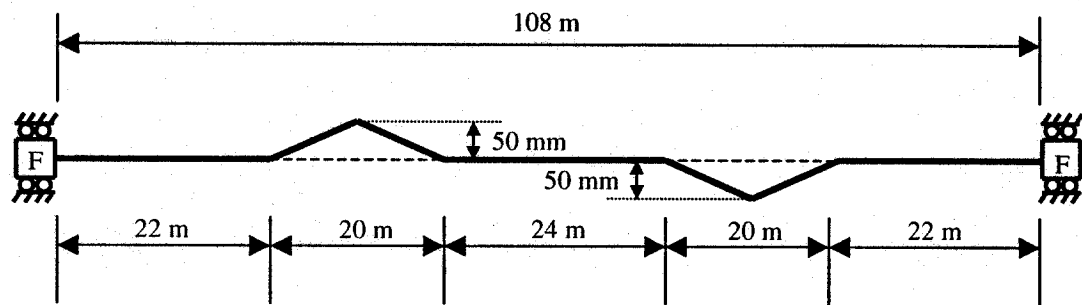
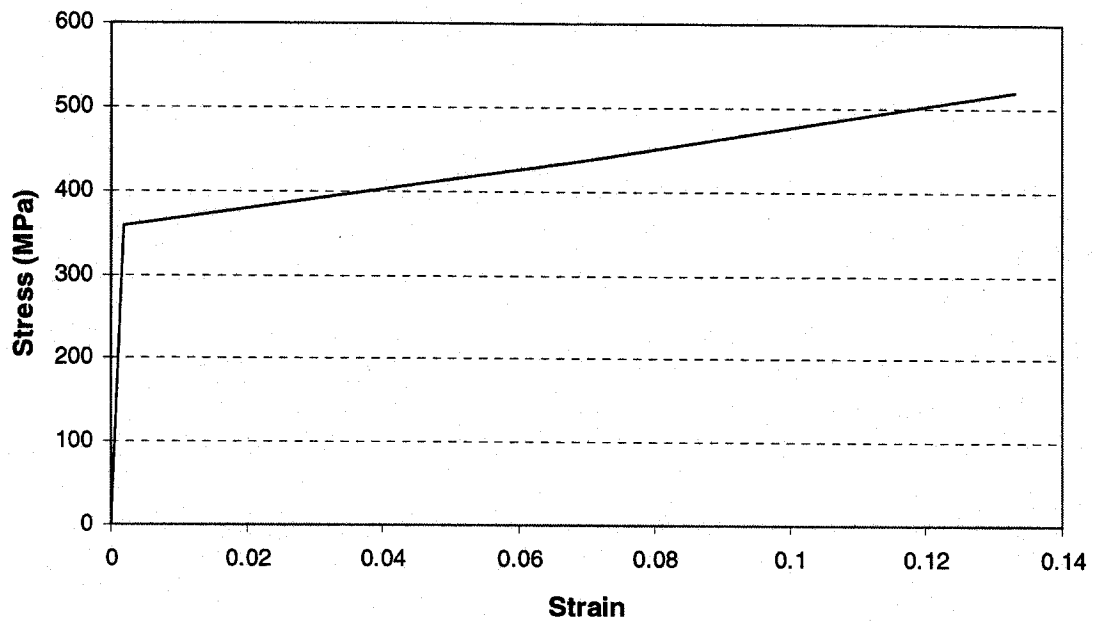Fig. 6.16 Model Layout for Case Study 3 (Not to Scale)

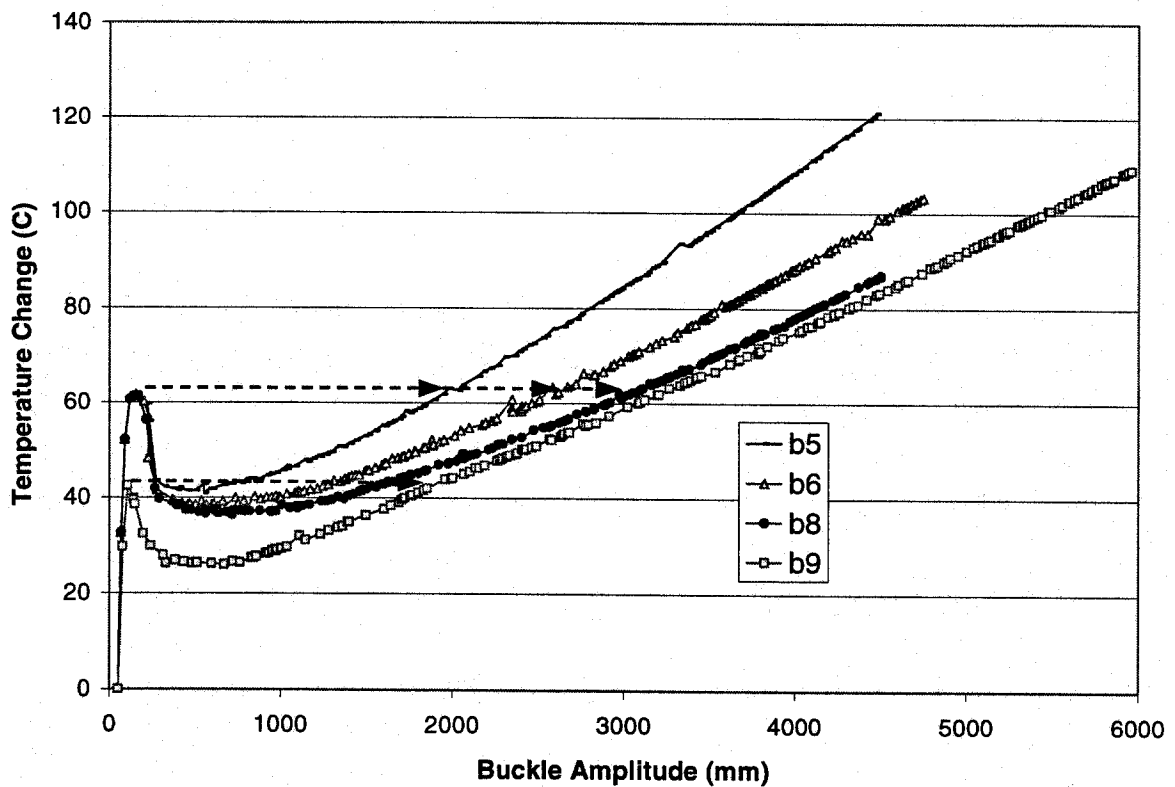Fig. 6.17 True Stress-Strain Relationship for Pipe Material in Case Study 3



Fig. 6.18 Case Study 3: Temperature Change vs. Buckle Amplitude Response for Different Solutions
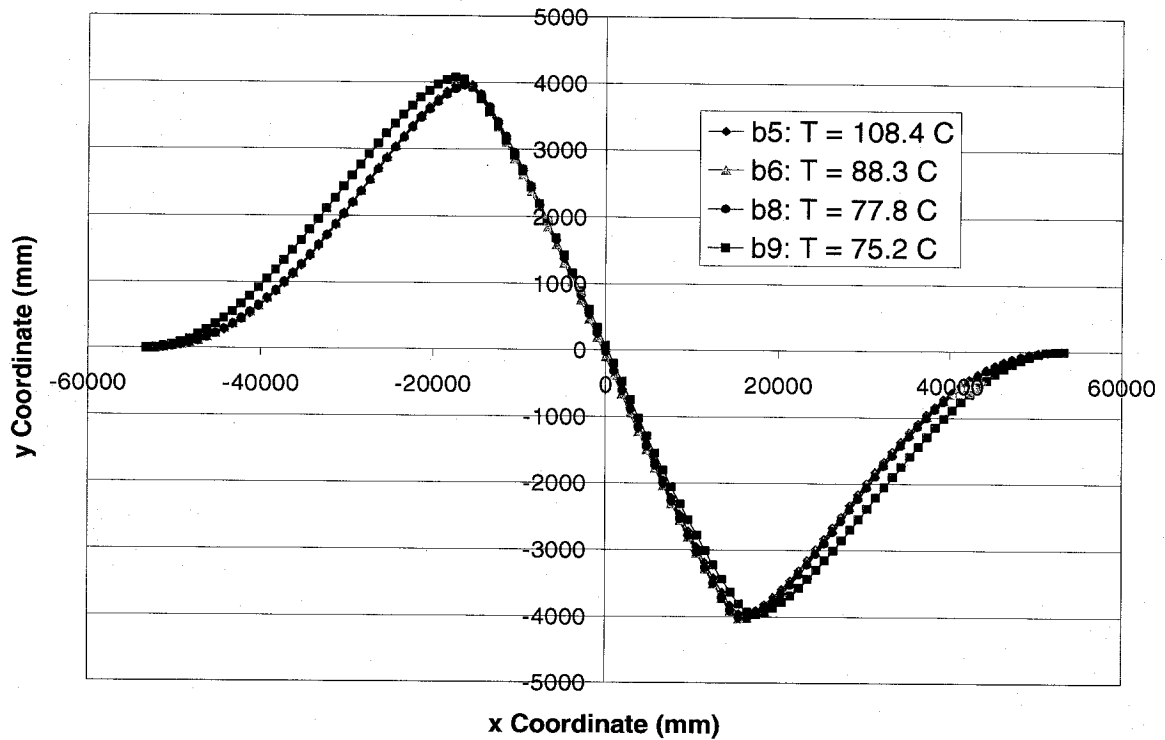
176

Fig. 6.19  Case Study 3: Pipe Deformed Shape at Buckle Amplitude of 4 m for Different Solutions
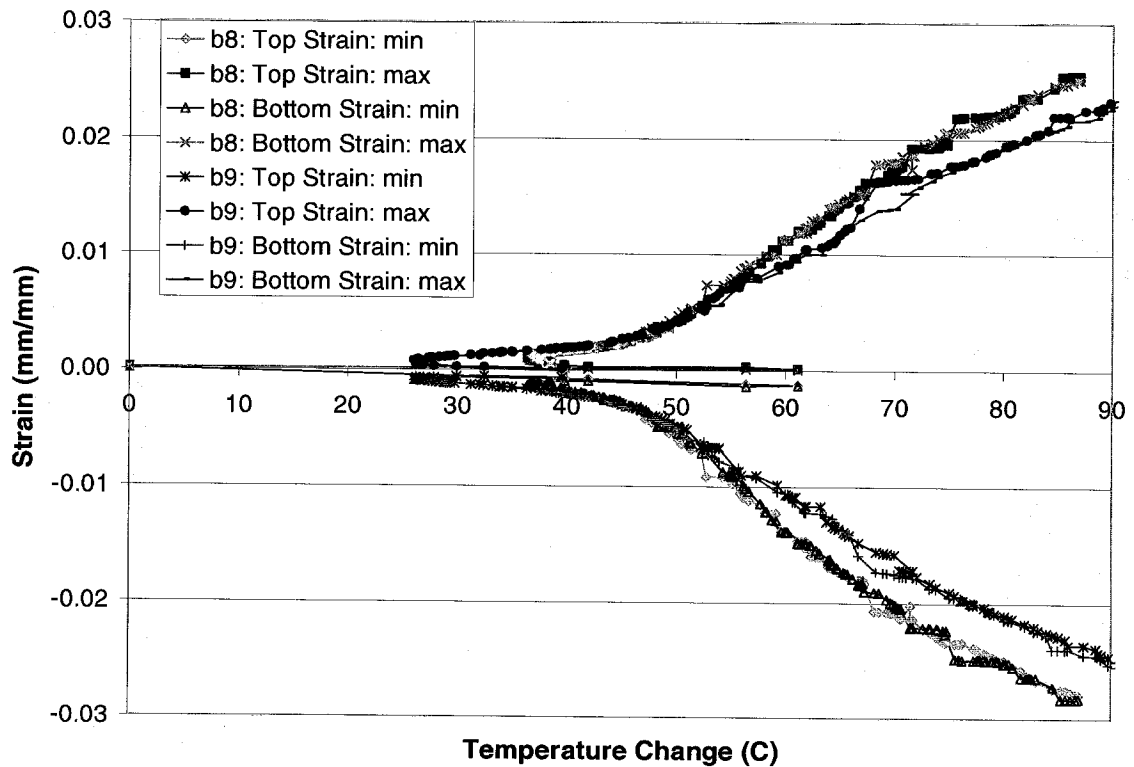


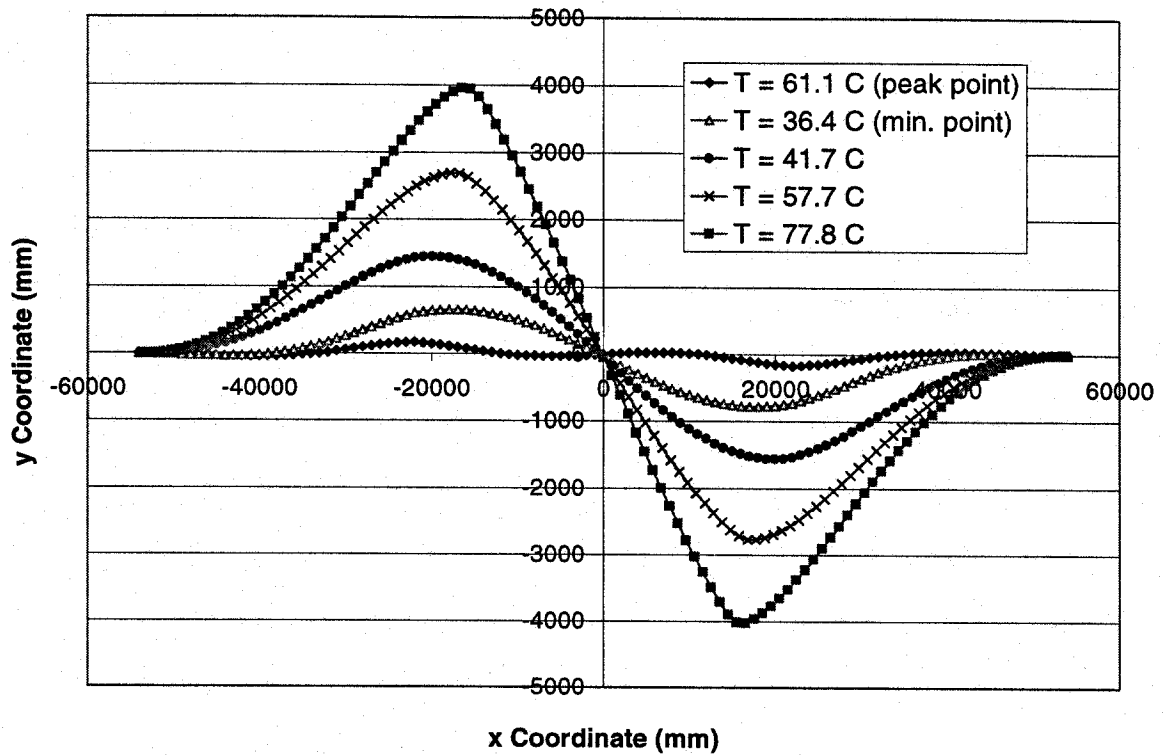Fig. 6.20  Variation of Max and Min Values of Top and Bottom Strain with Temperature

177

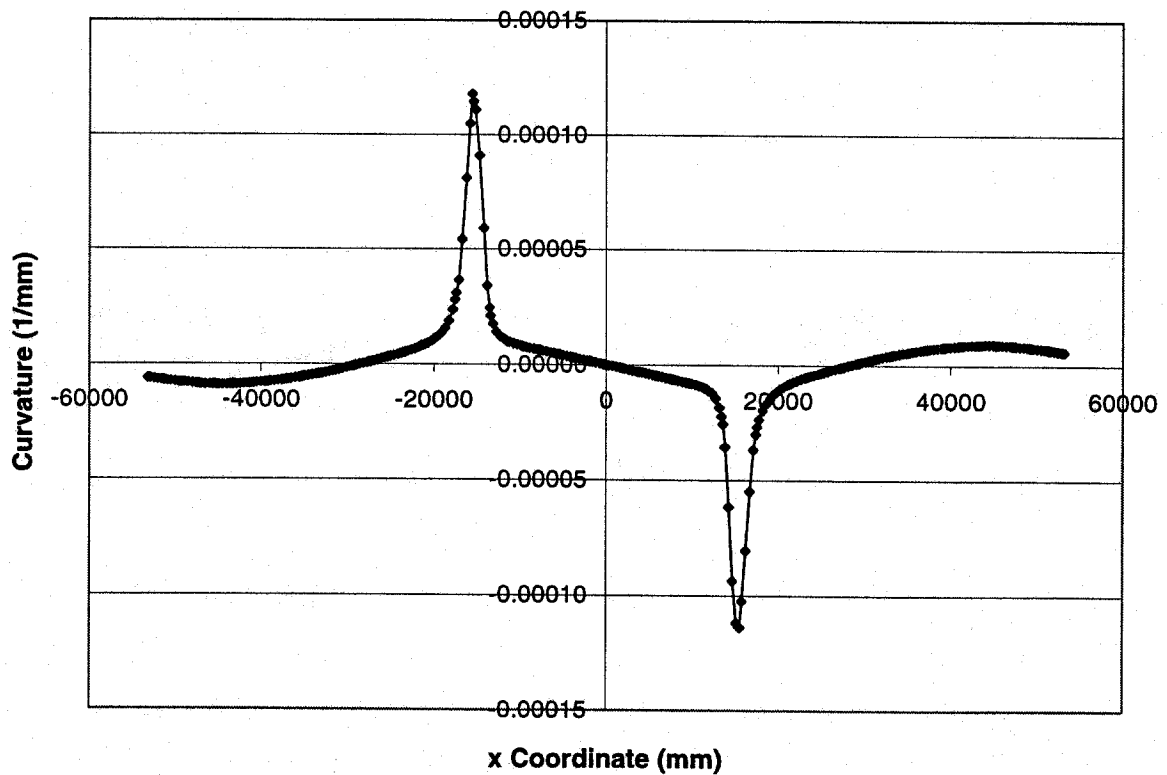Fig. 6.21 Pipe Deformed Shape at Different Temperature Differentials for Solution b8



Fig. 6.22 Variation of Curvature along the Pipe at 77.8 °C for Solution b8
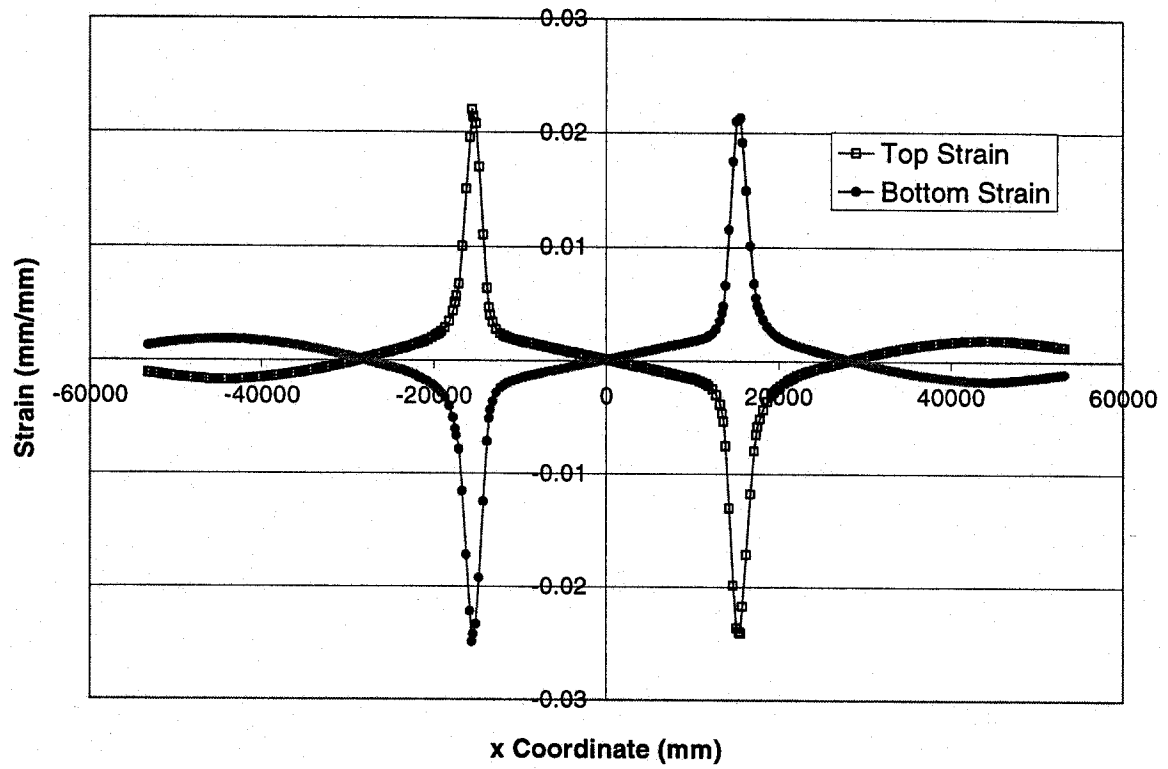
178

Fig. 6.23 Variation of Top and Bottom Strains along the Pipe at 77.8 °C for Solution b8

# CHAPTER 7. SUMMARY AND RECOMMENDATIONS

## 7.1 SUMMARY AND CONCLUSIONS

The main objective of this work was to develop a rigorous finite element model to study the behavior of buried pipelines, in general, and the thermal buckling of pipelines, in particular. The resulting finite element model was implemented in the computer program ABP (Analysis of Buried Pipelines). A summary of the study is outlined below:

1) A new two-dimensional, elastic-plastic, isoparametric $C^1$ beam element was developed that is capable of modeling large displacements and finite strains. In order to apply this element to pipeline analysis, it was equipped with features such as soil springs and internal pressure loading. An updated Lagrangian formulation was employed in the context of virtual work equation in order to establish the equilibrium equations. The $C^1$ beam element follows the Bernoulli's assumption, whereby the shear deformations are neglected. The three-node element has four degrees of freedom pre node: two displacements and two displacement derivatives in the global x and y directions. Fifth order Hermitian shape functions were developed for interpolating both coordinates and displacements in both global x and y directions.

2) It was shown that the hoop strain and the radial displacement contributions (due to internal pressure) can be dropped from the internal and external virtual work, respectively, leaving only the longitudinal effects. As a result, only the longitudinal stress and strain needed to be considered in the virtual work equation of the finite element formulation.

3) The load and stiffness contributions of internal pressure were rigorously derived and implemented in the model.

4) Since unlike traditional beam elements, the $C^1$ beam element does not use rotation as a degree of freedom, the application of concentrated moments and modeling of fixed supports (i.e., moment constraints) are not as straight-forward as they are in the case of traditional beam elements. However, the effects of concentrated moments or moment constraints were successfully broken down in terms of the derivative degrees of freedom at the nodes involved.

5) Modified arc-length method was used in order to carry out the incremental-iterative procedure for solving *applied load* problems. As an example for such problems, the classic elastica problem was analyzed. The finite element model was able to

replicate the theoretical elastica response using appropriate axial stiffness to bending stiffness ratio. This not only verified the element, but also demonstrated the power of the element as only three elements were used in the model.

6) An elastic-plastic material model developed using the von Mises yield criterion, normality flow rule, and a mixed strain-hardening rule (a mix of isotropic and kinematic hardening rules). The resulting constitutive relationship between true stress and strain measures were modified to obtain the constitutive relationship required for the pipeline-beam element in an updated Lagrangian formulation (as well in a total Lagrangian formulation).

7) A pipeline-soil interaction model was developed using soil springs on the basis of the assumption for the classical Winkler foundation. An elastic-perfectly plastic force-deformation constitutive relationship was used to model the bearing, uplift, transverse (for a horizontal analysis), and longitudinal soil springs. A second type of constitutive relationship was also implemented for the uplift spring ending with a descending (or softening) branch. This takes into account the loss of the uplift spring force as the pipe moves drastically upwards in upheaval buckling analyses.

8) A full Newton-Raphson iterative method was utilized for solving settlement problem. The pipeline-soil interaction model was verified by comparing the results of ABP for a zone settlement problem to those of PIPLIN III. Moreover, the $C^1$ beam element proved to be superior to the beam element of Zhou and Murray (1993).

9) A thermal analysis formulation was developed in order to analyze thermal buckling phenomena such as upheaval buckling and snaking. The far-field condition, simulating infinitely long continuation of the pipeline, was derived and implemented in the formulation. The thermal formulation was verified through three examples comparing the finite element results with theoretical and/or experimental counterparts.

10) Three case studies demonstrated the application of thermal analysis. The first case study was a parametric study with the initial out-of-straightness as the variant. The second and third case studies stemmed from the investigations carried out on actual pipelines having undergone thermal buckling.

## 7.2 RECOMMENDATIONS FOR FUTURE RESEARCH

Although the results of this research project satisfy most of practical applications, there is still room to expand the model to cover yet more practical cases. Furthermore,

some of the fundamental assumptions in this study can be re-examined. Some specific recommendations are outlined below:

1) The Bernoulli's assumption, whereby the shear deformations are neglected, needs to be evaluated for practical cases. This might be of more necessity for pipelines subjected to zone settlement where the settlement zone is relatively short.

2) Pipelines can undergo substantial ovalization as they bend. It might be of interest to account for ovalization, albeit in a simplified way, in the analysis.

3) The internal pressure is assumed to be an elastic loading applied at the beginning of the analysis. However, it would be of practical interest to be able to vary (increase or decrease) the internal pressure as a load step at any point during the analysis. This would require the modification of the constitutive relationships to account for the varying hoop stress.

4) The effects of the normalizing parameters used in the arc-length techniques, such as R and $\zeta$ in the constraint equation of Eq. (5.42), as well as the non-dimensionalization of the constraint equation have not been fully investigated. Further study on these issues can calibrate these factors and lead to a significant improvement in the solution efficiency.

5) The local buckling or wrinkling of the pipe due to excessive bending normally leads to significant softening of the buckled segment. A research can be performed on the inclusion of this softening effect using a method similar to the ISPDR solution technique (Zhou and Murray, 1993 and 1996).

6) An extensive parametric study is proposed to be performed on the thermal response of the pipelines by varying major variants in practical situations. This study would result in a set of graphs, from which the temperature values associated with the modes of failure can be extracted for a given pipeline. These modes of failure might be reaching the critical values of tensile and compressive strains and the emergence of the pipe out of the ground. The variants in the parametric study would include pipe size and grade, internal pressure, initial out-of-straightness, cover depth, soil density and strength parameters.

# REFERENCES

Andrew Palmer and Associates (1993). **PLUS-ONE for Windows System Manual.** Artillery House, Artillery Row, London, SW1P 1RT.

Audibert, J. M. E. and Nyman, K. J. (1977). **Soil Restraint Against Horizontal Motion of Pipes.** Journal of the Geotechnical Engineering Division, ASCE, Vol. 103, No. GT10, pp. 1119-1142.

Ballet, J. P. and Hobbs, R. E. (1992). **Asymmetric Effects of Prop Imperfections on the Upheaval Buckling of Pipelines.** Thin-Walled Structures, Vol. 13, pp. 355-373.

Bathe, K. J. (1996). **Finite Element Procedures.** Prentice Hall, Englewood Cliffs, New Jersey 07632.

Bellini, P. X. and Chulya, A. (1987), **An Improved Automatic Incremental Algorithm for the Efficient Solution of Nonlinear Finite Element Equation.** Computer and Structures, Vol. 26, No. 12, pp. 99-110.

Cappelletto, A., Tagliaferri, R., Giurlani, G., Andrei, G., Furlani, G., and Scarpelli, G. (1998). **Field Full-Scale Tests on Longitudinal Pipeline-Soil Interaction.** Proc. of Inter. Pipeline Conference IPC 1998, ASME (OMAE Division), Calgary, Alberta, Vol. 2, pp. 771-778.

CGL (Committee on Gas and Liquid Fuel Lines) (1984). **Guidelines for Seismic Design of Oil and Gas Pipeline Systems.** ASCE, pp. 150-228.

De Borst, R. (1988). **Bifurcation in Finite Element Models with a Non-Associated Flow Law.** Inter. Journal for Numerical and Analytical Methods in Geomechanics, Vol. 12, pp. 99-116.

Finch, M. (1999). **Upheaval Buckling and Floatation of Rigid Pipelines: the Influence of Recent Geotechnical Research on the Current State of the Art.** Paper OTC 10713 presented at 1999 Annual Offshore Technology Conference, Houston, May 3-6.

Hansen, J. B. (1961). **The Ultimate Resistance of Rigid Pile Against Transversal Forces.** Bulletin 12, Danish Geotechnical Institute, Copenhagen, Denmark.

Hetenyi, M. (1974). **Beams on Elastic Foundation.** The University of Michigan Press.

Hibbitt, H. D., Karlsson, B. I., and Sorensen, P. (2002). **ABAQUS User's Manual version 6.2.** Hibbitt, Karlsson, and Sorensen Inc., Pawtucket, RI 02860-4847, USA.

Hobbs, R. E. (1984). **In-Service Buckling of Heated Pipelines.** ASCE Journal of Transportation Engineering, Vol. 110, No. 2, pp. 175-189.

Hobbs, R. E. and Liang, F. (1989). **Thermal Buckling of Pipelines Close to Restraints.** Proc. of the Inter. Conf. on OMAE, Vol. V, ASME, pp. 121-127.

Hodge, P. G., Jr. **Discussion of [Prager (1956)].** Journal of Applied Mechanics, Vol. 23, pp. 482-484.

Ju, G. T. and Kyriakides, S. (1988). **Thermal Buckling of Offshore Pipelines.** ASME Journal of Offshore Mechanics and Arctic Engineering. Vol. 110, pp. 355-364.

Kerr, A. D. (1978). **Analysis of Thermal Track Buckling in the Lateral Plane.** Acta Mechanica, Vol. 30, pp. 17-50.

Klever, F. J., van Helvoirt, L. C., and Sluyterman, A. C. (1990). **A dedicated Finite-Element Model for Analyzing Upheaval Buckling Response of Submarine Pipelines.** Proc., 22$^{nd}$ Annual Offshore Technology Conference, Vol. 2, pp. 529-538.

Martinet, A. (1936). **Flambement des voies sans Joints sur Ballast et Rails de Grand Longueur (Buckling of Tracks without Joints on Ballast and Very Long Rails, in French).** Revue Generale des Chemins de Fer, Vol. 55, No. 2, pp. 212-230.

Miles, D. J. and Calladine, C. R. (1999). **Lateral Thermal Buckling of Pipelines on the Sea Bed.** Journal of Applied Mechanics, Vol. 66, Dec. 1999, pp. 891-897.

Mroz, Z. (1967). **On the Description of Anisotropic Work Hardening.** Journal of Mechanical Physics and Solids, Vol. 15, pp. 163-175.

Nielsen, N-J. R., Lyngberg, B., and Pedersen, P. T. (1990). **Upheaval Buckling Failures of Insulated Buried Pipelines: A Case Story.** Paper OTC 6488 presented at 1990 Annual Offshore Technology Conference, Houston, May 7-10.

Nyman, K. J. (1983). **Thaw Settlement Analysis for Buried Pipelines in Permafrost.** Pipelines in Adverse Environments –II, Edited by Mark Pickell, pp. 300-325.

Paulin, M. J., Philips R., Clark, J. I., Hurley, S., and Trigg, A. (1997), **Establishment of a Full-Scale Pipeline/Soil Interaction Test Facility and Results from Lateral and Axial Investigations in Sand.** Proc. of the 16$^{th}$ Inter. Conf. on OMAE, Vol. V-Pipeline Technology, ASME, pp. 139-146.

Pian, T. H. H. (1964). **Derivation of Element Stiffness Matrices by Assumed Stress Distributions.** AIAA Journal, 1964, Vol. 2, pp. 1333-1336.

Pian, T. H. H. and Tong, P. (1969). **Basis of Finite Element Methods for Solid Continua.** Int. J. Numer. Meth. Engng., 1969, Vol. 1, pp. 3-28.

Quimby, T. B. and Fitzpatrick, M. R. (1996). **Upheaval Buckling of a Pipeline in an Arctic Environment.** Proceedings of the 8th International Conference on Cold Regions Engineering. 1996, ASCE, New York, NY, USA. p 215-225.

Ramm, E. (1980). **Strategies for Tracing Nonlinear Response near Limit Points.** Europe – U.S. Workshop: "Nonlinear Finite Element Analysis in Structural Mechanics, Bochum, 1980.

Raoof, M. and Maschner, E. (1993). **Thermal Buckling of Subsea Pipelines.** Proc. of the 12th Inter. Conf. on OMAE, Vol. V-Pipeline Technology, ASME, pp. 21-29.

Raoof, M. and Maschner, E. (1994). **Vertical Buckling of Heated Offshore Pipelines.** Proc. of the 4th Inter. Offshore and Polar Engineering Conf., Osaka, Japan Vol. II, pp. 118-127.

Riks, E. (1972). **The Application of Newton's Method to the Problems of Elastic Stability.** Journal of Applied Mechanics, Vol. 39, pp. 1060-1066.

Riks, E. (1979). **An Incremental Approach to the Solution of Snapping and Buckling Problems.** Inter. Journal of Solids and Structures, Vol. 15, pp. 529-551.

Rizkalla, M., Trigg, A., Simmonds, G. (1996). **Recent Advances in the Modelling of Longitudinal Pipeline/Soil Interaction for Cohesive Soils.** Proc. of the 15th Inter. Conf. on OMAE, Vol. V-Pipeline Technology, ASME, pp. 325-332.

Row D. G., Powell, G. H., and Goodson, N. W. (1983). **Finite Element Techniques for Pipelines subjected to Extreme Loads.** Pipelines in Adverse Environments –II, Edited by Mark Pickell, pp. 474-485.

Saje, M. (1990). **A Variational Principle for Finite Planar Deformation of Straight Slender Elastic Beams.** Int. Journal of Solids and Structures, Vol. 26, No. 8, pp. 887-900.

Schweizerhof, K. H. and Wriggers, P. (1986). **Consistent Linearization for Path Following Methods in Nonlinear FE Analysis.** Computer Methods in Applied Mechanics and Engineering, North-Holland, Vol. 59, pp. 261-279.

Selvadurai, A. P. S. (1985). **Numerical Simulation of Soil-Pipeline Interaction in a Ground Subsidence Zone.** Advances in Underground Pipeline Engineering, Edited by K. Jeyaplan, pp. 311-319.

Shaw, P. K. and Bomba, J. G. (1994). **Finite-Element Analysis of Pipeline Upheaval Buckling.** Proc. of the 13th Inter. Conf. on OMAE, Vol. V-Pipeline Technology, ASME, pp. 291-296.

SSD (Structural Software Development, Inc.) (1989). **PIPLIN-III, Computer Program for Stress and Deformation Analysis of Pipelines.** 1930 Shattuck Avenue, Berkeley, California 94704, USA.

Timoshenko, S. (1936). **Theory of Elastic Stability.** McGraw-Hill Book Company, New York and London.

Trautmann, C. H. and O'Rourke, T. D. (1983). **Load-Displacement Characteristics of Pipe Affected by Permanent Earthquake Ground Movement.** Proc. Inter. Symposium on Lifeline Earthquake Engineering, Portland, Oregon, ASME, PVP-77, pp. 254-262.

Trautmann, C. H., O'Rourke, T. D., and Kulhawy, F. H. (1985). **Uplift Force-Displacement Response of Buried Pipe.** ASCE Journal of Geotechnical Engineering, Vol. 111, No. 9, pp. 1061-1075.

Trigg, A. and Rizkalla, M. (1994). **Development and Application of a Closed Form Technique for the Preliminary Assessment of Pipeline Integrity in Unstable Slopes.** Proc. of the 13th Inter. Conf. on OMAE, Vol. V-Pipeline Technology, ASME, pp. 127-139.

Vesic, A. S. (1969). **Breakout Resistance of Objects Embedded in Ocean Bottom.** Paper presented at the ASCE Ocean Engineering Conf., Miami Beach.

Wempner, G. A. (1971). **Discrete Approximations Related to Nonlinear Theories of Solids.** Inter. Journal of Solids and Structures, Vol. 7, pp. 1581-1599.

White, D. J., Barefoot, A. J., and Bolton, M. D. (2001). **Centrifuge Modelling of Thermal Buckling in Sand.** International Journal of Physical Modelling in Geotechnics, 2001, Vol. 2, pp. 19-28.

Woodward R. J., Lundgren R., and Boitano J. D. (1961). **Pile Loading Tests in Stiff Clays.** Proc. of the 5th Int. Conf. on Soil Mechanics and Foundation engineering, Paris, July 17-22, 1961, Vol. 2, pp. 177-184.

Yen, B. C., Tsao, C. H., and Hinkle, R. D. (1981). **Soil-Pipe Interaction of Heated Oil Pipelines.** ASCE Journal of Transportation Engineering, Vol. 107, No. TE1, January, pp 1-14.

Yoosef-Ghodsi, N., Kulak, G. L., and Murray, D. W. (1994). **Behavior of Girth-Welded Line Pipe,** Structural Engineering Report No. 203, Department of Civil Engineering, Univ. of Alberta, Edmonton, AB. T6G 2G7, 206 pgs.

Zhou, Z. and Murray, D. W. (1993). **Numerical Structural Analysis of Buried Pipelines.** Structural Engineering Report 181, Dept. of Civil Engineering, University of Alberta, Edmonton, Alberta.

Zhou, Z., and Murray, D.W.(1996). **Pipeline Beam Models Using Stiffness-Property-Deformation Relations**. Journal of Transportation Engineering, ASCE, Vol. 122, No.2, pp. 164-172.